Efficiency of the Benthic Microbial Methane Filter under Varying Fluid Fluxes

Dissertation

zur Erlangung des Doktorgrades in den Naturwissenschaften

--Doktor rerum naturalium--

vorgelegt der

Mathematischen-Naturwissenschaftlichen Fakultät

der Christian-Albrechts-Universität zu Kiel

Philip Steeb

Kiel 2014

Erste Gutachterin: Prof. Dr. Tina Treude

Zweiter Gutachter: PD Dr. habil. Mark Schmidt

Tag der mündlichen Prüfung: 24.04.2014

Zum Druck genehmigt: 24.04.2014

gez. Prof. Dr. Wolfgang J. Duschl, Dekan

Hiermit erkläre ich, daß die vorliegende Doktorarbeit „Efficiency of the Benthic Microbial Methane Filter under Varying Fluid Fluxes“ nach Inhalt und Form meine eigene ist, abgesehen von der Beratung meiner Betreuerin und den bezeichneten Co-Autoren der einzelnen Kapitel. Diese Arbeit wurde noch keiner Hochschule zur Prüfung vorgelegt und alle veröffentlichen Teile sind in „Publication Outline“ aufgeführt. Die Arbeit wurde unter Einhaltung der Regeln guter wissenschaftlicher Praxis der Deutschen Forschungsgemeinschaft erstellt.

_____ _____

Ort, Datum Philip Steeb

Abstract:

Marine sediments all over the world bear methane, generated from organic matter and deposited at the seafloor. By diffusion or ascending fluids the methane is transported to the sediment surface and emitted into the oceans and further into the atmosphere, where it acts as greenhouse gas. However, most of the methane is anaerobically or aerobically oxidized by microbes in the upper sediments and in the water column. One of the most important methane oxidizing processes is the anaerobic oxidation of methane (AOM) in the microbial benthic methane filter. Consortia of anaerobic methanotroph (ANME) archeae and sulfate reducing bacteria (SRB) consume the methane with sulfate as final electron acceptor. While the methane is delivered from deeper reservoirs, sulfate originates from the seawater and has to diffuse into the sediment. AOM occurs mainly in the intersection of sulfate and methane, the sulfate methane transition zone (SMTZ).

At continental margins gas hydrate bearing sediments form huge reservoirs of methane. Methane can be transported by upward migrating fluids from dewatered and dehydrated sediments. At the sediment surface, advecting fluids form so called “cold seeps”. The microbial benthic methane filter of cold seeps is well established and adapted to the flow conditions. However, increasing fluid flux can challenge the microbial benthic filter by higher methane flux and lower sulfate penetration depth, by resulted higher methane emissions.

The aim of this thesis is to study efficiency and adaptability of the benthic methane filter under non-steady state conditions. For this purpose I developed a sediment-flow-through (SLOT) system to mimic the fluid regime of the benthic methane filter and to monitor long-term incubations of undisturbed sediment cores from cold seeps under varying fluid fluxes. All experiments were performed under anoxic conditions and with two parallel sediments cores under varying fluid flow conditions. The presented thesis combines field data and experimental data from sediments of different cold seep sites and their microbial benthic methane filter.

First experiments with coastal gassy sediments from Eckernförde Bay constrain the possibility of SLOT to simulate fluid flow regimes of microbial benthic filters under fluid flux differences of one magnitude. Additionally, other seep related processes such as sulfide oxidation and precipitation were observed and prove the usefulness of the SLOT system for biogeochemical studies.

Two neighboring mounds with different steady state conditions were studied offshore Costa Rica. These mounds differ in fluid source, fluid flux as well as methane flux. Both mounds exhibit a well established microbial benthic filter which is adapted to their respective flow conditions. Fluid and methane source are reflected in the isotopic signature of authigenic carbonates, which are the archive of cold seep systems.

Field and experimental data from the Quepos Slide offshore Costa Rica were combined to study the benthic methane filter. In the experiments the microbial benthic methane filter was highly efficient and shows a good adaption within 150-170 d response time with low methane efflux within the transition. A fluid pulse with higher methane emissions reveals how fast the methane efflux can change when fluid flux is increased.

Furthermore, three different cold seep habitats from a recently discovered cold seep area at the continental margin of Chile were studied. Experiments with a bacterial mat habitat from a young seep site show a uniform fluid flow through the sediment and reveal a high adaptability of the benthic methane filter. In a clam field with high sulfide production an enormous methane efflux occured before the benthic filter was adapted to the new fluid regime. In sediments with an aerobic benthic methane filter from a tubeworm habitat, fluids were channeled by biogenic tubes. The benthic methane filter changed during the 150 d of anoxic incubation from an aerobic to an anaerobic methane sink.

In the present thesis it is demonstrated for the first time how benthic methane filters adapt to increased fluid flux. The studies reveal that beside preconditions and the intensity of the variation the sediment matrix flow conditions through the sediment is prime important for the adaptability of the benthic methane filter.

Zusammenfassung

Marine Sedimente enthalten überall auf der Welt Methan, welches aus organischem Material gebildet wurde. Dieses Methan kann durch Diffusion oder mit aufsteigenden Fluiden in die Ozeane und von dort aus weiter in die Atmosphäre gelangen, wo es als Treibhausgas wirkt. Allerdings wird das meiste Methan im Sediment als auch in der Wassersäule aerob oder anaerob oxidiert. Eine der wichtigsten Reaktionen zur Methan oxidation ist die anaerobe Methanoxidation (AOM) innerhalb des benthischen Methanfilters. Konsortien aus anaeroben methanotrophen Archaen (ANME) und sulfatreduzierende Bakterien oxidieren das Methan mit Sulfat als abschließendem Elektronenakzeptor. Während das Methan aus tieferen Speichern aufsteigt, erfolgt der Sulfatnachschub per Diffusion aus dem Meereswasser. AOM findet größtenteils in der Übergangszone von Sulfat und Methan statt, der Sulfat-Methan-Übergangszone (SMTZ).

An den Kontinentalhängen bilden Sedimente, welche Gashydrate enthalten riesige Methanspeicher. Methan kann durch aufsteigende Fluide aus entwässerten und dehydrierten Sedimenten aufwärts transportiert werden. An der Sedimentoberfläche formen diese ausströmenden Fluide so genannte „Cold Seeps“. Der benthische Methanfilter ist in diesen Cold Seeps gut ausgeprägt und an die Fließbedingungen angepasst. Erhöhte Fließgeschwindigkeiten, welche einen höheren Methanfluss sowie eine geringere Eindringtiefe des Sulfats zur Folge haben, können den benthischen Methanfilter stark strapazieren.

Das Ziel dieser Doktorarbeit ist die Effizienz und die Anpassungsfähigkeit des benthischen Methanfilters unter nicht stationären Bedingungen zu untersuchen. Aus diesem Grund habe ich ein Durchflusssystem (SLOT System) entwickelt um die Fließbedingungen des benthischen Methanfilters zu imitieren und Langzeituntersuchengen von ungestörten Sedimenten mit verschiedenen Volumenströmen aufzuzeichnen. Alle Versuche wurden unter anoxischen Bedingungen und mit zwei parallelen Sedimentkernen, welche unterschiedliche Fließbedingungen hatten, ausgeführt. Die vorliegenden Doktorarbeit vereint Feld- und Versuchsmesswerte von Cold Seep Sedimenten unterschiedlicher Standorte und ihren benthischen Methanfiltern.

Erste Versuche mit gasigen Küstensedimenten aus der Eckernförder Bucht belegen die Eignung des SLOT Systems Flussbedingungen des mikrobisch benthischen Methanfillters bei Volumenflußunterschieden von einer Größenordung zu simulieren. Zusätzlich konnten andere mit Cold Seeps verbundene Prozesse wie Sulfidoxidation und -präzipitation beobachtet werden. Dies zeigt die Nutzen des SLOT-Systems für biogeochemische Untersuchungen.

Zwei benachbarte „Mounds“ mit unterschiedlichen stationären Zuständen wurden vor Costa Rica untersucht. Diese Mounds unterschieden sich in Fluidquelle, Fluidströmung und Methanfluss. Beide enthielten einen gut ausgebildeten benthischen Methanfilter, der sich an die jeweiligen Flussbedingungen angepasst

hatte. Fluid- und Methanquellen spiegelten sich in der Isotopensignatur der autochthonen Karbonate wider, welche das Archiv der Cold Seep Geschichte darstellen.

Feld- und Versuchsergebnisse vom Quepos Slide vor Costa Rica wurden kombiniert um den benthischen Methanfilter zu untersuchen. Der mikrobielle benthische Methanfilter war sehr effizient und konnte sich mit einer Reaktionszeit von 150-170 Tagen an die geänderten Fließbedingungen anpassen. Während dieser Anpassungszeit kam es zu geringem Methanausfluss. Durch einen Fluidimpuls welcher einen hohen Methanausfluss zur Folge hatte, wurde verdeutlicht wie schnell sich der Methanausfluss ändern kann wenn das Flussvolumen ansteigt

Des Weiteren wurden drei Habitate eines kürzlich am chilenischen Kontinentalhang entdeckten Cold Seep-Gebiets untersucht. Versuche mit Sedimenten aus einem Bakterienmattenhabitat bei einer jungen Seepstelle zeigen einen gleichmäßigen Fluidfluss durch das Sediment und verdeutlichen somit eine hohe Anpassungsfähigkeit des benthischen Methanfilters. In Sedimenten aus einem Muschelfeld mit hoher Sulfidproduktion gab es einen enormen Methanausfluß bevor sich der benthische Methanfilter an die neuen Flussbedingungen angepaßt hatte. In Sedimenten mit einem aeroben Methanfilter von einen Röhrenwurmfeld wurden die Fluide durch die biogenen Röhren kanalisiert. Der benthische Methanfilter wandelte sich innerhalb von 150 Tagen anoxischer Inkubation von einer aeroben zu einer anearoben Methansenke.

In der vorliegenden Arbeit konnte zum ersten Mal gezeigt werden, wie sich benthische Methanfilter an erhöhten Fluidfluß anpassen. Die Untersuchungen zeigen, dass neben vorherigem Zustand und Grad der Veränderung auch die Sedimentmatrix und die Fließbedingungen durch das Sediment von großer Wichtigkeit für die Anpassunsfähigkeit des benthischen Methanfilters sind.

List of Content

Publication outline

The chapters 2 to 5 present publications resulting from the present thesis “Efficiency of the Benthic Microbial Methane Filter under Varying Fluid Fluxes” and each chapter is written in a form of scientific manuscripts. The chapters 2 and 3 are already accepted in peer-reviewed journals, while the chapters 4 and 5 are in preparation for submission. In the following the contributions of every manuscript are defined.

Chapter 2: A sediment flow-through system to study the impact of shifting fluid and methane flow regimes on the efficiency of the benthic methane filter

P. Steeb, P. Linke, and T. Treude
Limnology and Oceanography: Methods (accepted)

This study was initiated by T. Treude and P. Linke. The SLOT system was designed by T. Treude and developed by P. Steeb. Experiments were run by P. Steeb, including measurements and calculations. The manuscript was written by P. Steeb with input from the co-authors.

Chapter 3: Microbial activity and carbonate isotope signatures as a tool for identification of spatial differences in methane advection: A case study at the Pacific Costa Rican margin

S. Krause, P. Steeb, C. Hensen, V. Liebetrau, A. W. Dale, M. Nuzzo, and T. Treude
Biogeosciences (accepted)

This study was initiated by T. Treude, S. Krause, and C. Hensen. S. Krause and P. Steeb carried out the sampling procedure of radiotracer measurements and carbonates. Porewater measurements were performed by A. Dale and methane measurements by M. Nuzzo. Carbonate chemistry was performed by V. Liebetrau and S. Krause. Numerical

modeling was operated by C. Hensen, S. Krause, and P. Steeb. Rate measurements in the laboratory were done by P. Steeb with assistance of technicians, and turnover rates were calculated by P. Steeb. The manuscript was written by S. Krause with input of the co-authors.

Chapter 4: Efficiency and adaptability of the anaerobic benthic methane filter at Quepos Slide, offshore Costa Rica

P. Steeb, S. Krause, C. Hensen, A. W. Dale, M. Nuzzo, and T. Treude

This study was initiated by T. Treude, and P. Linke. S. Krause and P. Steeb sampled the sediments for radiotracer measurements and for the SLOT system. Porewater measurements were performed by A. Dale and methane measurements by M. Nuzzo. Numerical modeling was operated by C. Hensen, and P. Steeb. Rate measurements in laboratory were carried out by P. Steeb with assistance of technicians, and turnover rates were calculated by P. Steeb. Experiments were run by P. Steeb, including measurements and calculations. The manuscript was written by P. Steeb with input of the co-authors.

Chapter 5: Habitat depended methane efflux under varying fluid flow at the Concepción Methane Seep Area, offshore Chile

P. Steeb, P. Linke, and T. Treude

This study was initiated by T. Treude and P. Linke. Sediments for radiotracer measurements and the SLOT system were sampled by P. Steeb and T. Treude. Experiments were run by P. Steeb, including measurements and calculations. The manuscript was written by P. Steeb with input of the co-authors.

Chapter 1

Introduction to cold seep systems

Methane is an important greenhouse gas with ~25 times higher global warming potential than carbon dioxide when averaged over 100 years (Wuebbles et al. 2002; Forster et al. 2007). Marine sediments with their gas hydrates are the largest methane reservoir on Earth (Kvenvolden 1993). However, the oceans account only for 2% of global methane sources (Judd et al. 2002). Primarily responsible for this discrepancy is the benthic methane filter, a sediment zone with methane consuming microbes, where most of the methane is consumed (Reeburgh 2007).

Cold seep systems, which are areas at the seafloor with seeping fluids enriched with reduced compounds, form hot spots of the benthic filter (Levin 2005; Suess 2010). Together with hydrothermal vents, cold seeps represent oases of life in the deep sea. Both ecosystems are fueled by reduced compounds beyond sunlight, admittedly, carbon which fuels the cold seep systems is fixed by photosynthesis.

This introduction provides an overview of cold seep systems starting with the formation of methane. The second section explains fluid sources and migration, the driving force of cold seeps. In the subsequent sections gas hydrates, the benthic methane filter, and the methanotroph microbes of this ecosystem are described. In the fifth section, different seep manifestations, habitats, and reasons for temporal variations are presented. At the end, an overview of important methods to investigate cold seeps is provided followed by an explanation of the advantages of the chosen methodology for this work.

Fate of carbon in marine sediments:

In the photic zone of the oceans, the upper around 200 m water column, large amounts of carbon are fixed from the atmosphere and organic matter is formed. The organic matter sinks down in the water column and is degraded, mainly with oxygen as terminal electron acceptor. At the seafloor the organic matter is deposited. It is consecutively degraded by microbial processes using oxygen, nitrate/nitrite,

manganese, ferric iron, and sulfate as final electron acceptors (Fig. 1). When all these electron acceptors are consumed, methane can be formed by methanogenic archeae (Jørgensen 2000).

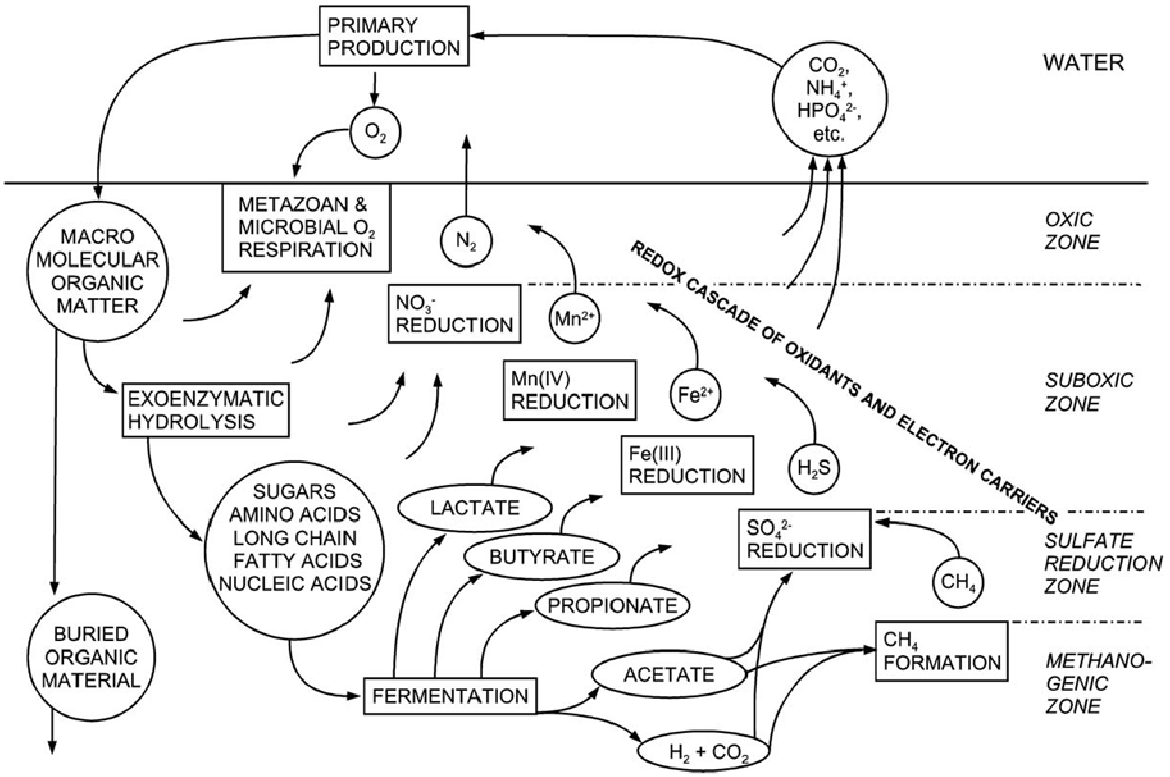

Figure 1: Pathways of organic carbon degradation in marine sediments and their relation to the geochemical zonations and the consumption of oxidants (Jørgensen 2000).

There are two pathways for methanogenesis: the most common pathway is carbonate reduction (Eqt. 1), another pathway is fermentation from acidic acid (Eqt. 2) (Thauer 1998).

$$4H_2 + HCO_3^- + H^+ \rightarrow CH_4 + 3H_2O \quad (1)$$

$$CH_3COO^- + H_2O \rightarrow CH_4 + HCO_3^{1-} \quad (2)$$

As methanogens are intolerant to oxygen, oxygen-free habitats such as anoxic sediments, swamps, rice fields, and guts of ruminates are the main sources of methane (Reeburgh 2003). In deeper sediments with higher temperature and pressure, also thermogenic methane (as well as higher hydrocarbons) is generated

by catagenesis. When olivine is hydrated and serpentinite is formed (serpentinization), hydrogen and carbon dioxide are released and can abiotically react to methane and water (Canfield et al. 2006).

Thermogenic and biogenic methane can be differentiated by their carbon isotopic composition or by intermixture of larger hydrocarbons, e.g., ethane, propane, butane et cetera. Less amounts of larger hydrocarbons and lower $\delta^{13}C$ and δD values indicate a biogenic origin and vice versa since biota always prefer the lighter and more common ^{12}C (Whiticar 1999). Up to 70% of the methane is of biotic origin (Reeburgh 2003).

Fluids: the driving force

In coastal areas fluids can result from groundwater seepage of sub-seafloor aquifers (Suess 2010). A much more important and widely spread source are fluids liberated by sediment compaction. In upwelling regions and deep sea fans, high amounts of water-loaded sediments accumulate rapidly and are compacted by the weight of the overlying sediments (Suess 2010). Compaction of sediments occurs over the whole sediment column, stronger in shallower depths where porosity decreases faster, and less pronounced in deeper parts where compaction slows down.

The convergent motion of plates at subduction zones lead to an additional lateral compaction and can result in 10 times higher fluid liberation (Saffer and Tobin 2011). Beside sediment compaction also dehydration processes and the release of bound water become important at the exposure to higher pressure and temperatures in greater depths. Dehydration processes are more common in underthrusting sediments and plates at subduction zones with higher temperature and build deep sourced fluids (Saffer and Tobin 2011).

Deep-sourced fluids are characterized by porewater freshening, elevated B and Li concentrations, higher $\delta^{18}O$ and δD values, and thermogenic hydrocarbons (Hensen et al. 2004). The most important dehydration process is the clay mineral dehydration by smectide-illite transformation at a temperature between 80-120°C (Saffer and Tobin 2011) (Fig. 2). Other less important dehydration processes occur at temperatures between 100-400°C (e.g., shale to chloritoid schist, 100–225°C; biotite-

chloritoid-garnet schist, 225–~300°C; pore collapse within basalt, ~200–400°C; zeolite to greenschist facies minerals, ~400°C) (Saffer and Tobin 2011).

Due to porewater overpressure fluids can be mobilized and ascend to the sediment surface. Drainage of sediments can be diffuse and focused (Saffer and Tobin 2011). Diffuse dewatering occurs at passive continental margins and at accretionary prisms of convergent margins and results in fluid velocities between 0.04 and 4 cm y^{-1} (Saffer and Tobin 2011). Sediment strata with low permeability lead to porewater overpressure, whereby fractures and faults with higher permeability can focus the fluid flow and drain the sediments.

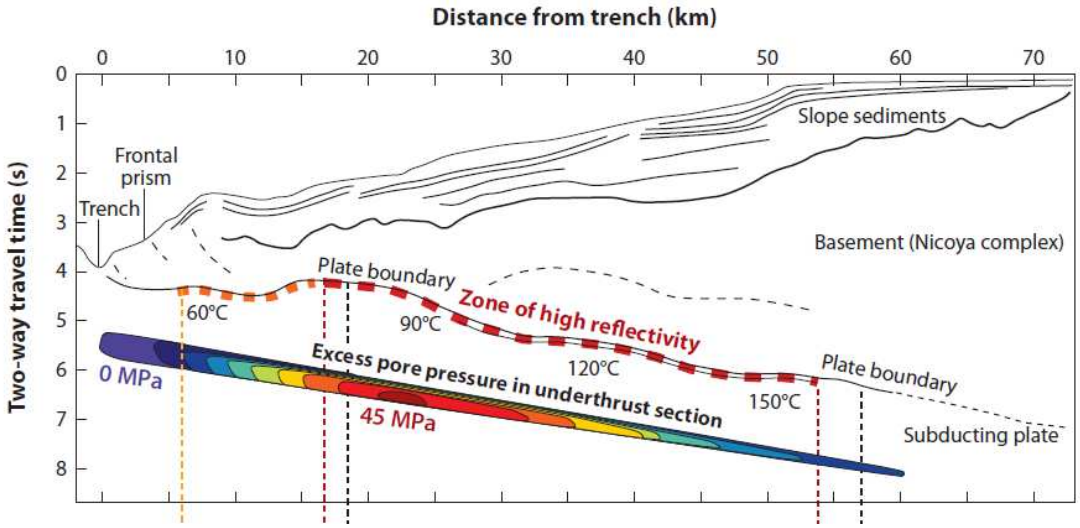

Figure 2: Drawing from the continental margin of Costa Rica and modeled pore pressure of the underthrusted plate (modified from Saffer and Tobin 2011)

At passive margins salt tectonics (Fig. 3) can cause faults which might act as pathways for rising fluids and formation of brines (Suess 2010). Continental margins at subduction zones with higher tectonic stress provide more fracture zones and faults than passive continental margin. The décollement is the boundary between underthrusting and overlaying sediments and forms the most important fault system (Ranero et al. 2008; Saffer and Tobin 2011). Fluids, dewatered along the décollement, form a mixture of deep-sourced fluids and fluids liberated by compaction from the underthrusting sediment (Fig. 4). In contrast, fluids venting through the upper plate can originate up to 90% from dehydration (Ranero et al. 2008). As a result of high tectonic stress and activity, numerous thrust faults can generate at convergent margins. Additionally, seamount subduction leads to fractures

and fluid paths (Ranero and von Huene 2000). Up to 40% of the fluids can drain through the upper plate at erosive subduction zones, while at accumulative convergent margins this pathway might be less important (Tobin and Saffer 2011).

Gas hydrates: reservoirs of methane

Methane can be trapped in gas hydrates, a crystalline, ice-like solid compound. Gas hydrates are stable within the Gas Hydrate Stability Zone (GHSZ) defined by temperature and pressure and, less important, by salinity of the porewater. While the pressure is controlled by the depth of both the water column and the overlaying sediments the temperature is driven by bottom water temperature and the geothermal gradient as a function of heat flow in the sediments.

The thickness of the GHSZ depends on bottom water temperature, geothermal gradient, and water depth around 100-500 m (Pecher et al. 2005; Piñero et al. 2013). Gas hydrate formation depends, besides the thickness of the GHSZ also on the solubility of methane, fluid flow into the GHSZ, methane generation inside the GHSZ, and therefore accumulation of organic matter (Wallmann et al. 2012).

Holocene organic matter accumulation is too low for efficient gas hydrate formation and present gas hydrates result from higher sedimentation rates of the Quaternary (Burwicz et al. 2011). The global gas hydrate inventory is assumed to be 440 – 900 GtC (Archer 2007; Burwicz et al. 2011; Wallmann et al. 2012; Piñero et al. 2013) and more than 100 evidences are found at continental margins (Pinero, Lorenzon and Kvenvolden 2007).

The GHSZ is separated by a sharp border to the free gas below, and can be detected seismically by a bottom simulated reflector (BSR). The BSR results from the sharp velocity decrease of seismic waves between the gas hydrates and free gas below (Borowski 2004).

Focused fluid flow leads to an increased heat flow and can melt gas hydrates. The BSR is disconnected at these seismic blanket zones and frequently cold seeps are located above these locations (Coffin et al. 2007).

The benthic methane filter

Upward migrating methane is oxidized by the microbial benthic methane filter (Sommer et al. 2006), aerobically (MOx) with oxygen (Eqt. 3) or anaerobically (AOM) with sulfate as terminal electron acceptor (Eqt. 4) (Reeburgh 2003). Aerobic methane oxidation is the most important pathway in the water column, the pelagic methane filter. For the benthic methane filter, AOM is the dominant pathway. It is mediated by microbes (Boetius et al. 2000), coupled to sulfate reduction and produces sulfide and bicarbonate according to the net equation (Eqt. 4).

$$CH_4 + 2O_2 \rightarrow CO_2 + 2H_2O \quad (3)$$

$$CH_4 + SO_4^{2-} \rightarrow HCO_3^- + HS^- \quad (4)$$

When methane intersects with sulfate, AOM occurs and both, methane and sulfate, are depleted and form the sulfate methane transition zone (SMTZ), sometimes also referred to as the sulfate methane interface (SMI) (Borowski et al. 1999). The depth of this zone depends on the penetration depth of sulfate, controlled by diffusion into the sediment and sulfate consumption due to sulfate reduction. Fluid flow from deeper sediments can decrease the sulfate penetration depth and push the SMTZ upwards. In the deep sea the sedimentation rate and organic matter supply are low, resulting in a deep SMTZ. In contrast, coastal regions are characterized by high deposition of organic matter with a very shallow SMTZ. At continental margins organic matter supply and sedimentation rate vary by river input and carbon fixation of the photic zone.

Above gas hydrates, methane diffuses upwards and results in SMTZs which are shallower than 50 m below seafloor (bsf) with linear methane and sulfate gradients (Borowski et al. 2000). Fluid flow from below changes the methane profile to a concave down profile and pushes the SMTZ upwards, closer to the sediment water interface. Very high fluid flow even prohibits sulfate penetration into the sediment (de Beer et al. 2006; Niemann et al. 2006b). The range of fluid flux at seep sites is very variable and ranges from 1 to more than 300 cm y^{-1} (Ranero et al. 2008). Available methane depends besides fluid flow (in cm y^{-1}) on methane concentration (in mmol l^{-1}) and both can be combined to the methane flux (in mmol m^{-2} d^{-1}). If the fluid is oversaturated, methane bubbles form, which rise upwards in the sediment and

increase the methane flux enormously (Matthews 1996). Since microbes can only oxidize dissolved methane, bubble transported methane bypasses the benthic filter and enters the water column directly (Luff and Wallmann 2003). Bubble formation, rise, velocity, and bubble induced irrigation constitute a complex issue which is beyond the scope of this thesis.

AOM-coupled sulfate reduction creates a second peak of sulfate reduction below the organoclastic sulfate reduction zone. At sites with high methane and fluid flux both zones coincide and a ratio of 1 (AOM : sulfate reduction) is reached. Since AOM is mediated by microbes $^{12}CH_4$ is preferentially oxidized and the remaining methane is enriched in $^{13}CH_4$ (Elvert et al. 1999, Whiticar 1999).

Anaerobic methanotrophs: main actors of the benthic methane filter

AOM is mediated by anaerobic methanotrophic (ANME) achaea and sulfate reducing bacteria (SRB). To date, three different ANME groups, ANME-1, ANME-2, and less frequent ANME-3 have been identified. ANME-1 and ANME-2 are associated with SRB Desulfosarina/Desulfococcus (Nauhaus et al. 2005; Knittel and Boetius 2009) and frequently form consortia, while ANME-3 is found together with Desulfobulbus (Niemann et al. 2006b). All ANME prefer a pH between 7 and 8 (de Beer et al. 2006; Knittel and Boetius 2009) and show a temperature optimum of 16 and 24°C for ANME-1 and ANME-2, respectively (Nauhaus et al. 2005). At hydrothermal vents ANME live at higher pH (9-11) (Boetius 2005) and show a decoupling of AOM and SR at temperatures above 90°C (Wankel et al. 2012). Mostly ANME-1 and ANME-2 are found together although with different population densities. ANME-2 habitats show high substrate availability (methane and sulfate) by lower sulfide concentrations (Krüger et al. 2008). Consequently ANME-2 shows up to 20 fold cell specific AOM activity (Nauhaus et al. 2005). Recently an AOM pathway with production of elemental sulfur and without the aid of SRB was shown for ANME-2 (Milucka et al. 2012).

Populations of ANME are always highest inside the SMTZ and their activity depends strongly on the methane supply. Half saturation is the substrate saturation at which the reaction rate reaches half of its maximum. For the AOM reaction, the methane

half saturation is assumed to be ~10 mmol l^{-1} (Nauhaus et al. 2002; Knittel and Boetius 2009). A sulfate concentration below 1 mmol l^{-1} can decrease AOM about 50% (Wegener and Boetius 2009). AOM yields only very low energy and only 1% of the carbon is used for biosynthesis (Knittel and Boetius 2009). Accordingly, the doubling times of the ANME are in the range of 1.1-7.5 months (Girguis et al. 2005; Nauhaus et al. 2007; Krüger et al. 2008; Meulepas et al. 2009).

Until now, an open question is how the energy is transferred between the two AOM partners. For the metabolic pathway a reverse methanogensis is assumed, based on phylogenetic similarities (Hoehler et al. 1994; Knittel and Boetius 2009).

Seeps, manifestations and habitats:

When upwards migrating fluids seep out of the sediment “cold seeps” are formed. In contrast to hydrothermal vents the fluids are colder although they are sometimes warmer than the ambient seawater. Seepage fluids from submerged aquifers can create pockmarks, a morphological depression in the seafloor (Suess 2010).

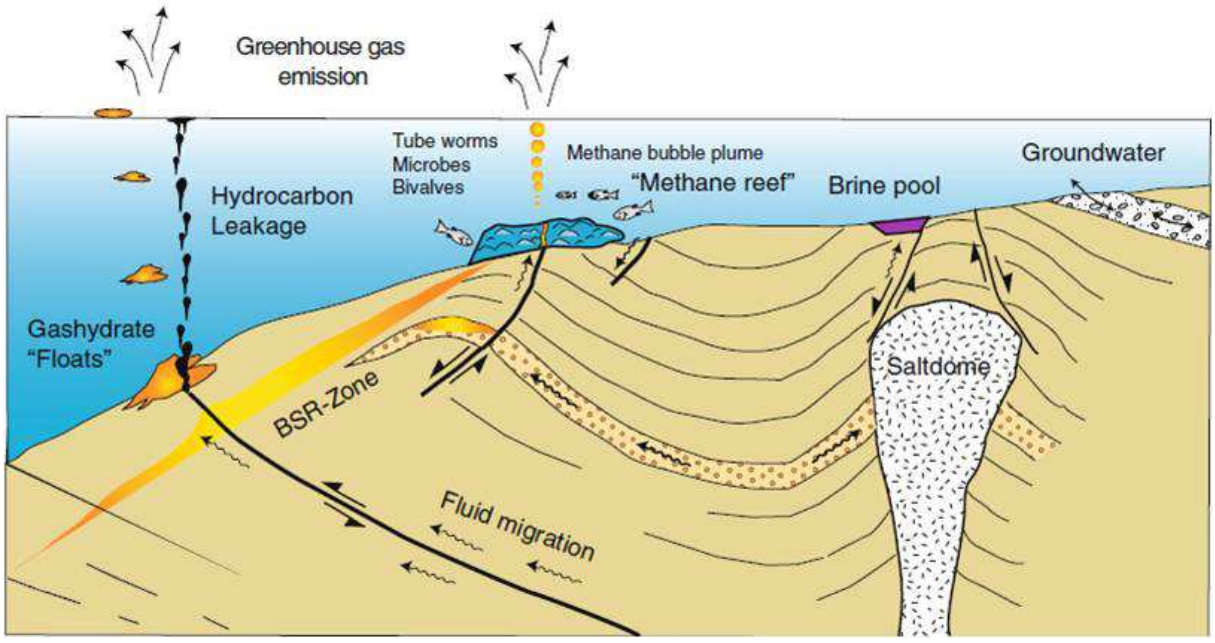

Figure 3: Seep manifestations at sedimented margins, typically passive margins. Groundwater seeps are found in coastal areas and brine pools, hydrocarbon seeps, above subsurface salt domes. Methane reefs at mid-slopes result from AOM-generated carbonate mineral precipitation. (Suess 2010)

Fluids can also be loaded with sediments and lead to mud diapirism and mud extrusions at the sediment surface (Kopf 2002). Mud mounds are elevated structures of mud breccias, often above faults, which serve as a fluid channel. When water-loaded sediments are overlaid by sediments of higher compaction, the deeper sediments can rise and build mud diapirs with large mud volcanoes at the sediment surface. These mud volcanoes are created by high sedimentation at continental margins (Niemann et al. 2006a; Lösekann et al. 2007) and deep sea fans (Feseker et al. 2010). Kopf (2002) provides a broader overview and details of mud diapirism and mud volcanoes. High fluid pressure along sediment layers with higher permeability can create slide planes for submarine landslides. Slides and scars may open structural and stratigraphical pathways for migrating fluids where seeps are generated at the sediment surface (Bohrmann et al. 2002; Mau et al. 2012; Karaca et al. 2012).

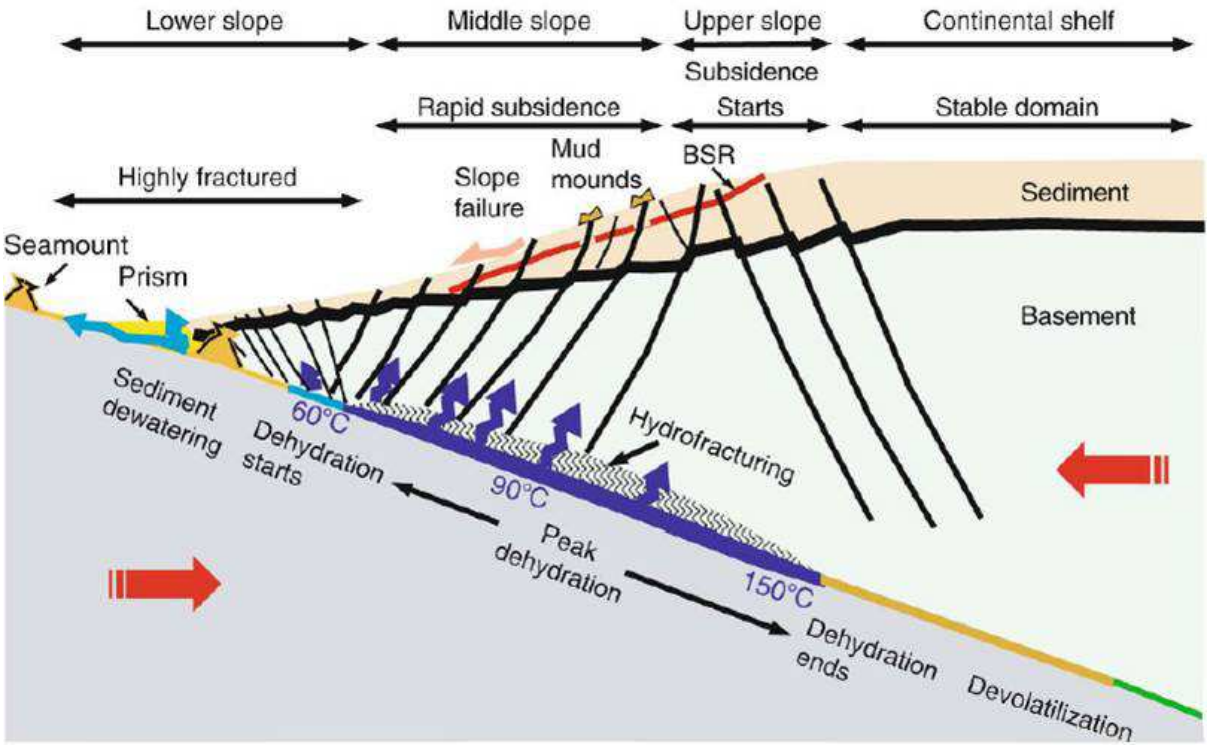

Figure 4: During plate convergence at erosive margins small accretionary prisms form at the trench, generating seeps in response to squeezing of water-rich sediments. This is followed by dehydration releasing mineral-bound water, upwards migrating and form mud mounds and seeps. Subducted volcanic seamounts can generate landslides (Suess 2010)

High methane flux and AOM rates lead to high production of bicarbonate which can precipitate as carbonates and create seep reefs. These carbonates - so called chemoherms - are abiotic authigenic carbonates with an anomalously negative

carbon isotope signature (Teichert et al. 2005). These carbonates form archives of the vent history including recent as well as fossil seeps. With stable isotope analyses it is possible to reconstruct the methane source and biomarker analyses can provide informations of past AOM activity. Chemoherms can form chimneys, which are vent structures of precipitated carbonates and growing around a fluid channel into the sediment or even into the water column (Boetius 2005; Teichert et al. 2005). Other chemoherms build large boulders or carbonate layers with downward precipitation (Liebetrau 2011).

The produced sulfide (see Eqt. 4) is an important energy source for many chemosyntrophic organisms for, e.g., bacterial mats, clam, mussels, and tubeworms. Most of the seep fauna has a negative $\delta^{13}C$ isotopic signature. Seep fauna is an important food source for higher trophic levels and builds nurseries for numerous predators like sharks and rays (Treude et al. 2012). Seep organisms oxidize sulfide with oxygen or nitrate according to Eqt. 5 and 6 (Preisler et al. 2007; Lichtschlag et al. 2010).

$$H_2S + 2O_2 \rightarrow SO_4^{2-} + 2H^+ \quad (5)$$

$$H_2S + NO_3^- + H_2O \rightarrow SO_4^{2-} + NH_4^+ \quad (6)$$

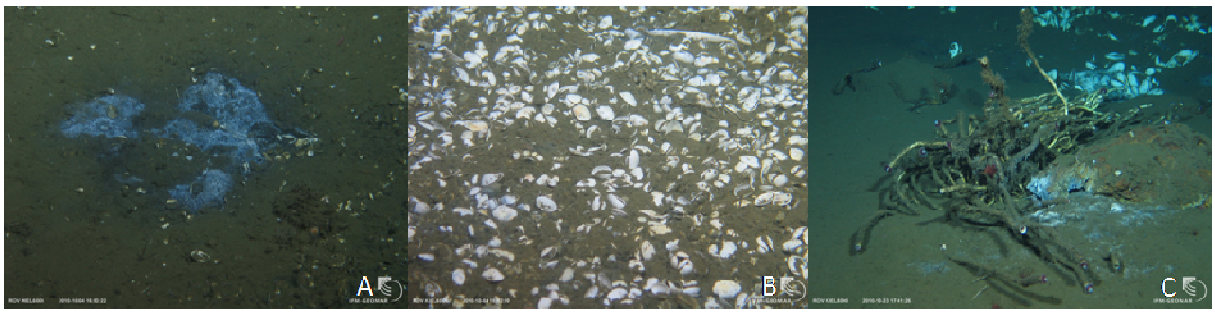

Figure 5: Chemosyntrophic organisms, bacterial mat (A), clam field (B), and tubeworms (C). Pictures: ROV KIEL 6000, on SO210 “Chilfux” cruse, offshore Chile.

The distribution of seep organisms depends on the sulfide flux and is an important indicator for methane flux and resulted AOM activity (Sahling et al. 2002). Bacterial mats live above shallow SMTZs (Treude et al. 2003; de Beer et al. 2006; Preisler et al. 2007; Lichtschlag et al. 2010), indicative for high fluid flux, and live above hot spots of AOM activity. Clams with sulfide oxidizing symbionts in their gills (e.g., Calyptogena) bioturbate and irrigate the sediment and porewater, thus increasing the sulfate flux as well as the sulfate penetration depth (Fischer et al. 2012, Tryon et al.

2002). Clams are able to reach deeper sulfide and live above deeper SMTZs and lower fluid flow and methane flux. Other seep fauna like tubeworms (Sommer et al. 2009) and Acharax are able to increase the irrigation depth down to 20 cm.

The microbial reefs of the Black Sea represent a special habitat, where methanotrophic mats create chimney-like reefs into the anoxic water column. The structures are up to 4 m high and 1 m in diameter, stabilized by interior carbonates, with rising bubbles in the porous interiors (Michaelis et al. 2002; Treude et al. 2007).

Spatial and temporal variation of methane and fluid flux:

Variations of seep activity can be related to the fluid flow velocity (in cm y^{-1}) and may change the depth of the SMTZ, or the methane supply (methane flux in mmol m^{-2} d^{-1}). If the methane concentration of the fluid stays constant, an increased fluid flow will also increase the methane flux. Transport of free gas in bubbles represents a high increase of methane flux (Luff and Wallmann 2003).

Cold seeps are created by channelized fluids and therefore represent a small-scale phenomenon. Exceptions are mud volcanoes with their huge fluid release. In their center, the highest fluid and heat flux and a shallow SMTZ are observed which dip down outwards (de Beer et al. 2006; Niemann et al. 2006b). However, fluid flow differences do not have to be distributed radially. Small-scaled and patchy spatial distribution of fluid channels are quite common at seep sites and high differences were measured in only 40 cm lateral distance (Linke et al. 2005).

Temporal variations in fluid flow and related methane flux are measured at different seep sites, by transient fluid flux as well as tidal-driven oscillation (Boles et al. 2001; Tryon et al. 2002; LaBonte et al. 2007). Transient fluids are also assumed at the décollement and other deep fluid paths (Saffer and Tobin 2011). A reason for decreased fluid flow is the sealing of veins and pores by precipitation (Liebetrau et al. 2010; Saffer and Tobin 2011). Furthermore, gas hydrate formation can block fluid paths and channels (Tryon et al. 2002).

Earthquakes can increase the pore pressure in faults and enhance the fluid flow. Furthermore, tectonic events can create new faults and new migration paths (Tryon

et al. 2002; Hensen et al. 2004; Aiello 2005; Henrys et al. 2006; Mau et al. 2007; Praeg et al. 2009; Meister et al. 2011) and reduce other fluid channels (Saffer and Tobin 2011). New fluid pathways and related heat flow can locally melt gas hydrates and may create new seep sites. Earthquakes can also trigger slope failures and yield new pressure conditions which may further destabilize gas hydrates (Ranero et al. 2008; Manga et al. 2009).

Changes in the GHSZ (thickness and depth) were generated by climate variability and related seawater temperatures and levels. Actual climate change and global warming is most pronounced in Arctic regions. Additionally, gas hydrates and GHSZ are very shallow in these regions, whereby the Arctic is most sensitive to recent gas hydrate destabilization (Buffett and Archer 2004; Biastoch et al. 2011). However, recent studies suggest gas hydrate melting is an ongoing process of the last 3 ky and assume seasonal fluctuations of gas hydrate formation and dissociation (Berndt et al. 2014).

Methods to localize, quantify, and investigate cold seeps:

In the following some common methods and their application are described. The list might not be complete and the methods themselves are not explained.

Geophysical methods are useful to identify and to map seep sites. With seismic methods the BSR, and hence, the occurrence of gas hydrates can be detected (Coffin et al. 2007; Kluesner et al. 2013). Seismological blanked zones form hints for increased heat flux and ascending fluids. With the aid of bathymetry pockmarks, mound structures and other seep manifestations can be localized and backscatter anomalies allow to identify seep carbonates (Klaucke et al. 2012). All of these geophysical methods can be deployed over wide areas and provide hints for a more specific observation or detailed sampling.

Hot spots of methane and fluid flux can be localized directly at the seafloor by observation on seep habitats and organisms with towed video camera systems (e.g., ocean floor observation system - OFOS), submersibles, or remotely operated vehicles (ROV) (Bohrmann et al. 2002; Sahling et al. 2003; Mau et al. 2006).

Mapping of the habitats enables the regionalization of fluid and methane flux, turnover rates, and methane emissions, as well as the budgeting of whole areas.

With water samples selected by CTD/rosette water samplers and analyses of their methane concentration, plumes of methane can be found in the water column and emissions can be quantified. Analyses of stable isotopes deliver hints for the methane source (e.g., Mau et al. 2012).

To determine fluid or methane flux, SMTZs, turnover rates of AOM, and respiration rates it is essential to determine porewater gradients or incubate sediments. Up to 12 m sediment cores can be sampled by gravity corer. Unfortunately, the sediment surface is disturbed by this sampling. Sampling by multicorer (MUC) provides up to eight parallel sediment cores of 80 cm length with an intact sediment surface. MUC equipped with cameras enables specific sampling of selected habitats. Porewater, methane, solid phase, and sediments for incubations (see below) can be subsampled from sediments. However, since pressure at the atmosphere is much lower than at the seafloor, methane degasses and ebullition from the sampled sediments is unavoidable which influences porewater profiles, in particular methane profiles.

Numerical transport models help to determine fluid flux from porewater anomalies and transport reaction models allow to estimate turnover rates (e.g. Hensen and Wallmann 2005; Karaca et al. 2010). Radiotracer incubation in subsamples allow to determine turnover rates of AOM and sulfate reduction (Jørgensen 1978; Kallmeyer et al. 2004; Joye et al. 2004; Treude et al. 2005).

Sediment sampling changes always the in-situ conditions and leads to artifacts and reduced methane concentrations. A solution to this dilemma is provided by in-situ measurements. Microsensors enable in-situ measurements of gaseous components such as sulfide, nitrous oxide, as well as carbon dioxide, and parameters such as pH, redox potential, and temperature, of the sediment water interface in high resolution (Wenzhöfer et al. 2000; Beer et al. 2006; Preisler et al. 2007). Benthic chambers enable measuring respiration rates directly at the seafloor (Linke et al. 2005; Sommer et al. 2006) while a chemical and aqueous transport (CAT) meter provides long-term measurements of fluid flux (Tryon et al. 2002; LaBonte et al. 2007).

To identify the kind of methanotrophs and SRB, DNA samples of the sediments are used. Catalyzed reporter deposition fluoresence in-situ hybridization (CARD-FISH) allows to quantify ANME and SRB and their proportion to the total abundance of microbes (Dapi-stained) (Pernthaler et al. 2002; Kallmeyer 2011).

Slurries of sediment and medium enable long term incubation under specific conditions (e.g., pH, temperature, inhibited reactions) in the laboratory to determine turnover rates. Under atmospheric pressure only low methane concentrations can be achieved, wherefore pressurized system were developed (Nauhaus et al. 2005; Krüger et al. 2005).

In slurry incubation concentrations of electron donors and acceptors decrease while products such as sulfide increase and inhibit the reaction. To avoid this problem, different flow-through systems were developed. They are developed to optimize the conditions for AOM or to analyze the influence of specific parameters (such as temperature, pH, pressure, methane concentration). An overview of the different systems is provided in the introduction of the next chapter (see Chapter 2). Most of these flow-through systems work with sediment slurries and optimize the supply of nutrients. Other systems allow to incubate complete sediment cores and supply the benthic filter with methane and sulfate from below under realistic flow velocities.

Objectives:

Most of the cold seeps exist since decades or centuries and contain an efficient benthic methane filter. The depth of the SMTZs depends on fluid flux to well establish the microbial community of these AOM zones. However, there are many reasons for changes in fluid flux (see spatial and temporal variation of methane and fluid flux). Enhanced fluid and related methane flux provide not only more oxidizable methane, it additionally limits the sulfate penetration depth and reduces the thickness of the benthic methane filter. Therefore, the benthic microbial methane filter is no longer under steady-state conditions and several questions appear:

How does the microbial community react on increased fluid and methane flux?

What is the efficiency of the benthic methane filter under increased fluid flow?

How is the dynamics and development of the geochemical profiles inside the sediment?

What is the response time until a new steady-state is established?

To investigate the efficiency, dynamics, and response time of a challenged benthic methane filter it is necessary to mimic the fluid regime of seep sites under realistic fluid flux conditions. In the following chapter a system and its application are described, which mimic the fluid regime of seeps under realistic varying fluid flux beyond steady-state conditions.

References:

Aiello, I. 2005. Fossil seep structures of the Monterey Bay region and tectonic/structural controls on fluid flow in an active transform margin. Palaeogeogr. Palaeoclimatol. Palaeoecol. **227**: 124–142.

Archer, D. 2007. Methane hydrate stability and anthropogenic climate change. Biogeosciences **4**: 521–544.

De Beer, D., E. Sauter, H. Niemann, N. Kaul, U. Witte, M. Schlüter, and A. Boetius. 2006. In situ fluxes and zonation of microbial activity in surface sediments of the Håkon Mosby Mud Volcano. Limnol. Oceanogr. **51**: 1315–1331.

Berndt, C., T. Feseker, T. Treude, K. Krastel, V. Liebetrau, H. Niemann, V. Bertrics, I. Dumke, K. Dünnbier, B. Ferre, C. Graves, F. Gross, K. Hissmann, V. Hühnerbach, S. Krause, K. Lieser, J. Schauer, and L. Steinle. 2014. Temporal Constrains on Hydrate-Controlled Methane Seepage off Svalbard. Science (80-.). 1.

Biastoch, A., T. Treude, and L. Rüpke. 2011. Rising Arctic Ocean temperatures cause gas hydrate destabilization and ocean acidification. Geophys. Res. … **38**: 1–5.

Boetius, A. 2005. Lost City Life. Science (80-.). **307**: 1420–1422.

Boetius, A., K. Ravenschlag, C. J. Schubert, D. Rickert, F. Widdel, A. Gieseke, R. Amann, B. B. Jørgensen, U. Witte, and O. Pfannkuche. 2000. A marine microbial consortium apparently mediating anaerobic oxidation of methane. Nature **407**: 623–6.

Bohrmann, G., K. Heeschen, C. Jung, W. Weinrebe, B. Baranov, R. Heath, V. Hu, M. Hort, and D. Masson. 2002. Widespread fluid expulsion along the seafloor of the Costa Rica convergent margin. 69–79.

Boles, J. R., J. F. Clark, I. Leifer, and L. Washburn. 2001. Temporal variation in natural methane seep rate due to tides, Coal Oil Point area, California. J. Geophys. Res. Ocean. **106**: 27077–27086.

Borowski, W. S. 2004. A review of methane and gas hydrates in the dynamic, stratified system of the Blake Ridge region, offshore southeastern North America,.

Borowski, W. S., T. M. Hoehler, M. J. Alperin, N. M. Rodriguez, and C. K. Paull. 2000. Signifficans of anaerobic methane oxidation in methane-rich sediments overlying the Blake Rich gas hydrates. Proc. Ocean Drill. Program, Sci. results **164**: 87–99.

Borowski, W. S., C. K. Paull, and I. W. Ussler. 1999. Global and local variations of interstitial sulfate gradients in deep-water, continental margin sediments: Sensitivity to underlying methane and gas hydrates. Mar. Geol. **159**: 131–154.

Buffett, B., and D. Archer. 2004. Global inventory of methane clathrate: sensitivity to changes in the deep ocean. Earth Planet. Sci. Lett. **227**: 185–199.

Burwicz, E., L. Rüpke, and K. Wallmann. 2011. Estimation of the global amount of submarine gas hydrates formed via microbial methane formation based on numerical reaction-transport modeling and a novel parameterization of Holocene sedimentation. Geochim. Cosmochim. Acta **75**: 4562–4576.

Canfield, D. E., M. T. Rosing, and C. Bjerrum. 2006. Early anaerobic metabolisms. Philos. Trans. R. Soc. Lond. B. Biol. Sci. **361**: 1819–34; discussion 1835–6.

Coffin, R., J. Pohlman, J. Gardner, R. Downer, W. Wood, L. Hamdan, S. Walker, R. Plummer, J. Gettrust, and J. Diaz. 2007. Methane hydrate exploration on the mid Chilean coast: A geochemical and geophysical survey. J. Pet. Sci. Eng. **56**: 32–41.

Elvert, M., E. Suess, D.- Kiel, and M. J. Whiticar. 1999. Anaerobic methane oxidation associated with marine gas hydrates : superlight C-isotopes from saturated and unsaturated C 20 and C 25 irregular isoprenoids. Naturwissenschaften **86**: 295–300.

Feseker, T., K. R. Brown, C. Blanchet, F. Scholz, M. Nuzzo, A. Reitz, M. Schmidt, and C. Hensen. 2010. Active mud volcanoes on the upper slope of the western Nile deep-sea fan—first results from the P362/2 cruise of R/V Poseidon. Geo-Marine Lett. **30**: 169–186.

Fischer, D., H. Sahling, K. Nöthen, G. Bohrmann, M. Zabel, and S. Kasten. 2012. Interaction between hydrocarbon seepage, chemosynthetic communities, and bottom water redox at cold seeps of the Makran accretionary prism: insights from habitat-specific pore water sampling and modeling. Biogeosciences **9**: 2013–2031.

Forster, P., V. Ramaswamy, P. Artaxo, T. Berntsen, R. Betts, D. W. Fahey, J. Haywood, J. Lean, D. C. Lowe, G. Myhre, J. Nganga, R. Prinn, G. Raga, M.

Schulz, V. Dorland, P. R.Forster, and R. Van Dorland. 2007. Changes in atmospheric constituents and in radiative forcing, p. 131–234. *In* S. Solomon, D. Qin, M. Manning, Z. Chen, M. Marquis, K.B. Averyt, M. Tignor, and H.L. Miller [eds.], Climate Change 2007: The Physical Science Basis. Contribution of Working Group I to the Fourth Assessment Report of the Intergovernmental Panel on Climate Change. Cambridge University Press,.

Girguis, P., A. Cozen, and E. DeLong. 2005. Growth and population dynamics of anaerobic methane-oxidizing archaea and sulfate-reducing bacteria in a continuous-flow bioreactor. Appl. Environ. Microbiol. **71**: 3725–3733.

Henrys, S., M. Reyners, I. Pecher, S. Bannister, Y. Nishimura, and G. Maslen. 2006. Kinking of the subducting slab by escalator normal faulting beneath the North Island of New Zealand. Geology **34**: 777.

Hensen, C., and K. Wallmann. 2005. Methane formation at Costa Rica continental margin—constraints for gas hydrate inventories and cross-décollement fluid flow. Earth Planet. Sci. Lett. **236**: 41–60.

Hensen, C., K. Wallmann, M. Schmidt, C. R. Ranero, and E. Suess. 2004. Fluid expulsion related to mud extrusion off Costa Rica—A window to the subducting slab. Geology **32**: 201.

Hoehler, T. M., M. J. Alperin, D. B. Alpert, and C. S. Martens. 1994. Field and laboratory studies of methane oxidation in an anoxic marine sediment: evidence for a methanogen sulfate reducer consortium. Global Biogeochem. Cycles **8**: 451–463.

Jørgensen, B. 2000. Bacteria and marine biogeochemistry, p. 169–206. *In* H.D. Schulz and M. Zabel [eds.], Marine Geochemistry. Springer Berlin Heidelberg.

Jørgensen, B. B. 1978. A comparison of methods for the quantification of bacterial sulfate reduction in coastal marine sediments. 1. Measurements with radiotracer techniques. Geomicrobiol. J **1**: 11–27.

Joye, S. B., A. Boetius, B. N. Orcutt, J. P. Montoya, H. N. Schulz, M. J. Erickson, and S. K. Lugo. 2004. The anaerobic oxidation of methane and sulfate reduction in sediments from Gulf of Mexico cold seeps. Chem. Geol. **205**: 219–238.

Judd, A., M. Hovland, and L. Dimitrov. 2002. The geological methane budget at continental margins and its influence on climate change. Geofluids **2**: 109–126.

Kallmeyer, J. 2011. Detection and quantification of microbial cells in subsurface sediments., p. 79–103. *In* A. Laskin, G. Gadd, and S. Sariaslani [eds.], Advances in applied microbiology. Academic Press.

Kallmeyer, J., T. G. Ferdelman, A. Weber, H. Fossing, and B. B. Jørgensen. 2004. A cold chromium distillation procedure for radiolabeled sulfide applied to sulfate reduction measurements. Limnol. Oceanogr. Methods **2**: 171–180.

Karaca, D., C. Hensen, and K. Wallmann. 2010. Controls on authigenic carbonate precipitation at cold seeps along the convergent margin off Costa Rica. Geochemistry Geophys. Geosystems **11**: 1–19.

Karaca, D., T. Schleicher, C. Hensen, P. Linke, and K. Wallmann. 2012. Quantification of methane emission from bacterial mat sites at Quepos Slide offshore Costa Rica. Int. J. Earth Sci. 1–25.

Klaucke, I., W. Weinrebe, P. Linke, D. Kläschen, and J. Bialas. 2012. Sidescan sonar imagery of widespread fossil and active cold seeps along the central Chilean continental margin. Geo-Marine Lett. , doi:10.1007/s00367-012-0283-1

Kluesner, J. W., E. A. Silver, N. L. Bangs, K. D. McIntosh, J. Gibson, D. Orange, C. R. Ranero, and R. von Huene. 2013. High density of structurally controlled, shallow to deep water fluid seep indicators imaged offshore Costa Rica. Geochemistry, Geophys. Geosystems **14**: 519–539.

Knittel, K., and A. Boetius. 2009. Anaerobic oxidation of methane: progress with an unknown process. Annu. Rev. Microbiol. **63**: 311–34.

Kopf, A. J. 2002. Significance of mud volcanism. Rev. Geophys. **40**: 1–52.

Krüger, M., M. Blumenberg, S. Kasten, A. Wieland, L. Känel, J. Klock, W. Michaelis, and R. Seifert. 2008. A novel, multi-layered methanotrophic microbial mat system growing on the sediment of the Black Sea. Environ. Microbiol. **10**: 1934–47.

Krüger, M., T. Treude, H. Wolters, K. Nauhaus, and A. Boetius. 2005. Microbial methane turnover in different marine habitats. Palaeogeogr. Palaeoclimatol. Palaeoecol. **227**: 6–17.

Kvenvolden, K. A. 1993. Gas Hydrates - Geological Perspective and Global Change. Rev. Geophys. **31**: 173–187.

LaBonte, A. L., K. K. M. Brown, and M. M. D. Tryon. 2007. Monitoring periodic and episodic flow events at Monterey Bay seeps using a new optical flow meter. J. Geophys. Res. **112**: 1–14.

Levin, L. A. 2005. Ecology of cold seep sediments: interactions of fauna with flow, chemistry and microbes. Ocean. Mar. Biol. Ann. Rev. **43**: 1–46.

Lichtschlag, A., J. Felden, and V. Brüchert. 2010. Geochemical processes and chemosynthetic primary production in different thiotrophic mats of the Håkon Mosby Mud Volcano (Barents Sea). Limnol. Ocean. **55**: 931–949.

Liebetrau, V. 2011. Geochronology, p. 413–416. *In* J. Reitner and V. Thiel [eds.], Encyclopedia of Geobiology. Springer Netherlands.

Liebetrau, V., A. Eisenhauer, and P. Linke. 2010. Cold seep carbonates and associated cold-water corals at the Hikurangi Margin, New Zealand: New

insights into fluid pathways, growth structures and geochronology. Mar. Geol. **272**: 307–318.

Linke, P., K. Wallmann, E. Suess, C. Hensen, and G. Rehder. 2005. In situ benthic fluxes from an intermittently active mud volcano at the Costa Rica convergent margin. Earth Planet. Sci. Lett. **235**: 79–95.

Lösekann, T., K. Knittel, T. Nadalig, B. Fuchs, H. Niemann, A. Boetius, and R. Amann. 2007. Diversity and abundance of aerobic and anaerobic methane oxidizers at the Haakon Mosby Mud Volcano, Barents Sea. Appl. Environ. Microbiol. **73**: 3348–62.

Luff, R., and K. Wallmann. 2003. Fluid flow, methane fluxes, carbonate precipitation and biogeochemical turnover in gas hydrate-bearing sediments at Hydrate Ridge, Cascadia Margin: numerical modeling and mass balances. Geochim. Cosmochim. Acta **67**: 3403–3421.

Manga, M., M. Brumm, and M. L. Rudolph. 2009. Earthquake triggering of mud volcanoes. Mar. Pet. Geol. **26**: 1785–1798.

Matthews, M. 1996. Migration – a view from the top, p. 139–155. *In* D. Schuhmacher and M. Abrams [eds.], Hydrocarbon migration and its near-surface expression. American Association of Petroleum Geologists Memoir.

Mau, S., G. Rehder, I. G. Arroyo, J. Gossler, and E. Suess. 2007. Indications of a link between seismotectonics and CH 4 release from seeps off Costa Rica. Geochemistry, Geophys. Geosystems **8**: 1–13.

Mau, S., G. Rehder, H. Sahling, T. Schleicher, and P. Linke. 2012. Seepage of methane at Jaco Scar, a slide caused by seamount subduction offshore Costa Rica. Int. J. Earth Sci. , doi:10.1007/s00531-012-0822-z

Mau, S., H. Sahling, G. Rehder, E. Suess, P. Linke, and E. Soeding. 2006. Estimates of methane output from mud extrusions at the erosive convergent margin off Costa Rica. Mar. Geol. **225**: 129–144.

Meister, P., M. Gutjahr, M. Frank, S. M. Bernasconi, C. Vasconcelos, and J. A. McKenzie. 2011. Dolomite formation within the methanogenic zone induced by tectonically driven fluids in the Peru accretionary prism. Geology **39**: 563–566.

Meulepas, R. J. W., C. G. Jagersma, J. Gieteling, C. J. N. Buisman, A. J. M. Stams, and P. N. L. Lens. 2009. Enrichment of anaerobic methanotrophs in sulfate-reducing membrane bioreactors. Biotechnol. Bioeng. **104**: 458–70.

Michaelis, W., R. Seifert, K. Nauhaus, T. Treude, V. Thiel, M. Blumenberg, K. Knittel, A. Gieseke, K. Peterknecht, T. Pape, A. Boetius, R. Amann, B. B. Jørgensen, F. Widdel, J. Peckmann, N. V Pimenov, and M. B. Gulin. 2002. Microbial reefs in the Black Sea fueled by anaerobic oxidation of methane. Science **297**: 1013–5.

Milucka, J., T. G. Ferdelman, L. Polerecky, D. Franzke, G. Wegener, M. Schmid, I. Lieberwirth, M. Wagner, F. Widdel, and M. M. M. Kuypers. 2012. Zero-valent sulphur is a key intermediate in marine methane oxidation. Nature **2**: 1–23.

Nauhaus, K., M. Albrecht, M. Elvert, A. Boetius, and F. Widdel. 2007. In vitro cell growth of marine archaeal-bacterial consortia during anaerobic oxidation of methane with sulfate. Environ. Microbiol. **9**: 187–96.

Nauhaus, K., A. Boetius, M. Krüger, and F. Widdel. 2002. In vitro demonstration of anaerobic oxidation of methane coupled to sulphate reduction in sediment from a marine gas hydrate area. Environ. Microbiol. **4**: 296–305.

Nauhaus, K., T. Treude, A. Boetius, and M. Krüger. 2005. Environmental regulation of the anaerobic oxidation of methane: a comparison of ANME-I and ANME-II communities. Environ. Microbiol. **7**: 98–106.

Niemann, H., J. Duarte, C. Hensen, E. Omoregie, V. H. Magalhães, M. Elvert, L. M. Pinheiro, a. Kopf, and a. Boetius. 2006a. Microbial methane turnover at mud volcanoes of the Gulf of Cadiz. Geochim. Cosmochim. Acta **70**: 5336–5355.

Niemann, H., T. Lösekann, D. de Beer, M. Elvert, T. Nadalig, K. Knittel, R. Amann, E. J. Sauter, M. Schlüter, M. Klages, J. P. Foucher, and A. Boetius. 2006b. Novel microbial communities of the Haakon Mosby mud volcano and their role as a methane sink. Nature **443**: 854–8.

Pecher, I. A., S. A. Henrys, S. Ellis, S. M. Chiswell, and N. Kukowski. 2005. Erosion of the seafloor at the top of the gas hydrate stability zone on the Hikurangi Margin, New Zealand. Geophys. Res. Lett. **32**: 3–6.

Pernthaler, A., J. Pernthaler, and R. Amann. 2002. Fluorescence In Situ Hybridization and Catalyzed Reporter Deposition for the Identification of Marine Bacteria Fluorescence In Situ Hybridization and Catalyzed Reporter Deposition for the Identification of Marine Bacteria. **68**, doi:10.1128/AEM.68.6.3094

Piñero, E., M. Marquardt, C. Hensen, M. Haeckel, and K. Wallmann. 2013. Estimation of the global inventory of methane hydrates in marine sediments using transfer functions. Biogeosciences **10**: 959–975.

Praeg, D., S. Ceramicola, R. Barbieri, V. Unnithan, and N. Wardell. 2009. Tectonically-driven mud volcanism since the late Pliocene on the Calabrian accretionary prism, central Mediterranean Sea. Mar. Pet. Geol. **26**: 1849–1865.

Preisler, A., D. de Beer, A. Lichtschlag, G. Lavik, A. Boetius, and B. B. Jørgensen. 2007. Biological and chemical sulfide oxidation in a Beggiatoa inhabited marine sediment. ISME J. **1**: 341–53.

Ranero, C., and R. von Huene. 2000. Subduction erosion along the Middle America convergent margin. Nature **404**: 748–52.

Ranero, C. R., I. Grevemeyer, H. Sahling, U. Barckhausen, C. Hensen, K. Wallmann, W. Weinrebe, P. Vannucchi, R. von Huene, and K. McIntosh. 2008.

Hydrogeological system of erosional convergent margins and its influence on tectonics and interplate seismogenesis. Geochemistry Geophys. Geosystems **9**, doi:10.1029/2007GC001679

Reeburgh, W. 2003. Global methane biogeochemistry, p. 65–89. *In* H.D. Holland and K.K. Turekian [eds.], The Atmosphere, Treatise on Geochemistry. Elsevier.

Reeburgh, W. S. 2007. Oceanic methane biogeochemistry. Chem. Rev. **107**: 486–513.

Saffer, D. M., and H. J. Tobin. 2011. Hydrogeology and Mechanics of Subduction Zone Forearcs: Fluid Flow and Pore Pressure. Annu. Rev. Earth Planet. Sci. **39**: 157–186.

Sahling, H., S. V Galkin, A. Salyuk, J. Greinert, H. Foerstel, D. Piepenburg, and E. Suess. 2003. Depth-related structure and ecological significance of cold-seep communities—a case study from the Sea of Okhotsk. Deep Sea Res. Part I Oceanogr. Res. Pap. **50**: 1391–1409.

Sahling, H., D. Rickert, R. W. Lee, P. Linke, and E. Suess. 2002. Macrofaunal community structure and sulfide flux at gas hydrate deposits from the Cascadia convergent margin, NE Pacific. Mar. Ecol. Prog. Ser. **231**: 121–138.

Sommer, S., P. Linke, O. Pfannkuche, T. Schleicher, D. Schneider v. D, a Reitz, M. Haeckel, S. Flögel, and C. Hensen. 2009. Seabed methane emissions and the habitat of frenulate tubeworms on the Captain Arutyunov mud volcano (Gulf of Cadiz). Mar. Ecol. Prog. Ser. **382**: 69–86.

Sommer, S., O. Pfannkuche, P. Linke, R. Luff, J. Greinert, M. Drews, S. Gubsch, M. Pieper, M. Poser, and T. Viergutz. 2006. Efficiency of the benthic filter: Biological control of the emission of dissolved methane from sediments containing shallow gas hydrates at Hydrate Ridge. Global Biogeochem. Cycles **20**: 1–14.

Suess, E. 2010. Marine Cold Seeps, p. 188–198. *In* K.N. Timmis [ed.], Handbook of Hydrocarbon and Lipid Microbiology. Springer Berlin Heidelberg.

Teichert, B. M. a., G. Bohrmann, and E. Suess. 2005. Chemoherms on Hydrate Ridge — Unique microbially-mediated carbonate build-ups growing into the water column. Palaeogeogr. Palaeoclimatol. Palaeoecol. **227**: 67–85.

Thauer, R. K. 1998. Biochemistry of methanogenesis: a tribute to Marjory Stephenson. Microbiology **144**: 2377–2406.

Torres, M., and J. McManus. 2002. Fluid and chemical fluxes in and out of sediments hosting methane hydrate deposits on Hydrate Ridge, OR, I: Hydrological provinces. Earth Planet. … **201**: 525–540.

Treude, T., A. Boetius, K. Knittel, K. Wallmann, and B. Barker Jørgensen. 2003. Anaerobic oxidation of methane above gas hydrates at Hydrate Ridge, NE Pacific Ocean. Mar. Ecol. Prog. Ser. **264**: 1–14.

Treude, T., S. Kiel, P. Linke, J. Peckmann, and J. Goedert. 2012. Elasmobranch egg capsules associated with modern and ancient cold seeps: a nursery for marine deep-water predators. Mar. Ecol. Prog. Ser. **437**: 175–181.

Treude, T., J. Niggemann, J. Kallmeyer, P. Wintersteller, C. J. Schubert, A. Boetius, and B. B. Jørgensen. 2005. Anaerobic oxidation of methane and sulfate reduction along the Chilean continental margin. Geochim. Cosmochim. Acta **69**: 2767–2779.

Treude, T., V. Orphan, K. Knittel, A. Gieseke, C. H. House, and A. Boetius. 2007. Consumption of methane and CO2 by methanotrophic microbial mats from gas seeps of the anoxic Black Sea. Appl. Environ. Microbiol. **73**: 2271–83.

Tryon, M. D., K. M. Brown, and M. E. Torres. 2002. Fluid and chemical fluxes in and out of sediments hosting methane hydrate deposits on Hydrate Ridge, OR, II: Hydrological provinces. Earth Planet. Sci. Lett. **201**: 541–557.

Wallmann, K., E. Pinero, E. Burwicz, M. Haeckel, C. Hensen, A. Dale, and L. Ruepke. 2012. The Global Inventory of Methane Hydrate in Marine Sediments: A Theoretical Approach. Energies **5**: 2449–2498.

Wankel, S. D., M. M. Adams, D. T. Johnston, C. M. Hansel, S. B. Joye, and P. R. Girguis. 2012. Anaerobic methane oxidation in metalliferous hydrothermal sediments: influence on carbon flux and decoupling from sulfate reduction. Environ. Microbiol. **14**: 2726–40.

Wegener, G., and A. Boetius. 2009. An experimental study on short-term changes in the anaerobic oxidation of methane in response to varying methane and sulfate fluxes. Biogeosciences **6**: 867–876.

Wenzhöfer, F., O. Holby, R. Glud, H. K. Nielsen, and J. K. Gundersen. 2000. In situ microsensor studies of a shallow water hydrothermal vent at Milos, Greece. Mar. Chem. **69**: 43–54.

Whiticar, M. J. 1999. Carbon and hydrogen isotope systematics of bacterial formation and oxidation of methane. Chem. Geol. **161**: 291–314.

Wuebbles, D. D. J., K. Hayhoe, and H. K. 2002. Atmospheric methane and global change. Earth-Science Rev. **57**: 177–210.

Chapter 2

A sediment flow-through system to study the impact of shifting fluid and methane flow regimes on the efficiency of the benthic methane filter

Abstract

The efficiency of the “benthic microbial methane filter” at marine cold seeps is controlled by diffusive sulfate supply from the overlying seawater and advective methane flux from deep reservoirs. High fluid fluxes reduce the penetration depth of sulfate and limit the filter to a very narrow zone close to the sediment-water interface. Here, we introduce a new sediment-flow-through (SLOT) system, to mimic the balance between fluid/methane flow and sulfate supply in natural sediments. SLOT enables anaerobic incubations of intact sediment cores under natural flow regimes. In addition to traditional in- and outflow sampling, geochemical parameters can be monitored along the sediment core using microsensors and rhizons. In a first test run, two cores with gassy sediments from the Eckernförde Bay (Baltic Sea) were incubated and monitored for 310 days under low (11.2 cm y^{-1}) and high fluid flow (112.1 cm y^{-1}) conditions. Rates of anaerobic oxidation of methane (AOM) were one order of magnitude higher (3.07 mmol $m^{-2} d^{-1}$) in the high flow compared to the low flow regime (0.29 mmol $m^{-2} d^{-1}$), whereas methane efflux was twice as high (0.063 and 0.033 mmol $m^{-2} d^{-1}$, respectively). Sediment profiles of sulfide, sulfate, total alkalinity, pH, redox, and other parameters offered important information on the nature and dynamics of the biogeochemical reactions in the sediment cores including methanotrophy, sulfate reduction, carbonate precipitation, and sulfide oxidation. The SLOT system proofed to be an effective device to study the temporal evolution of biogeochemical parameters in intact sediments subjected to advective fluid transport.

Introduction

Marine sediments harbor the largest methane reservoirs on earth, including methane hydrates (Burwicz et al. 2011; Wallmann et al. 2012). A fraction of this methane migrates from greater depth to the sediment surface at cold seeps and is discharged into the water column. At locations of shallow water depth and with strong emission rates, this methane can reach the atmosphere and contribute to the global greenhouse gas pool. However, the majority of marine methane is already consumed by microbial processes in the sediment and the water column (Reeburgh 2007).

To date, several metabolic pathways of microbial methane oxidation have been described, including the aerobic pathways with oxygen and several anaerobic pathways using either nitrate (Ettwig et al. 2010), iron (Beal et al. 2009), or sulfate (Boetius et al. 2000) as the terminal electron acceptor. Anaerobic oxidation of methane with sulfate (AOM) is the dominant methanotrophic pathway in marine sediments and consumes more than 80% of the methane before it reaches the water column (Hinrichs and Boetius 2002; Reeburgh 2007). On the ocean shelves and continental margins, AOM activity is mainly found in the upper 10 m of the sediment. The zone of AOM (Fig. 1) is often referred to as the “benthic methane filter” (Sommer et al. 2006). AOM is mediated by consortia of microbes, which use sulfate as electron acceptor. These consortia consist of sulfate-reducing bacteria (SRB) and anaerobic methanotrophic (ANME) archaea (Boetius et al. 2000). AOM consortia reduce sulfate and oxidize methane and generate sulfide and bicarbonate (Eq. 1):

$$CH_4 + SO_4^{2-} \rightarrow HCO_3^- + HS^- + H_2O \quad (1)$$

In a new study, Milucka et al. (2012) suggest a different reaction mechanism. In this pathway, ANME-2 archaea oxidize methane alone by producing elemental sulfur as an intermediate, which further reacts to disulfide or other polysulfides (Eq. 2):

$$7CH_4 + 8SO_4^{2-} + 4H^+ \rightarrow 4HS_2^- + 7HCO_3^- + 11H_2O \quad (2)$$

Sulfate-reducing bacteria use disulfide and disproportionate it into sulfide and sulfate in a ratio of 7:1 (Eq. 3):

$$4HS_2^- + 11H_2O \rightarrow SO_4^{2-} + 7HS^- + 5H^+ \quad (3)$$

Produced sulfate can be re-used for methane oxidation by archaea. By combining Eq. 2 and Eq. 3, the net reaction of Eq. 1 is derived.

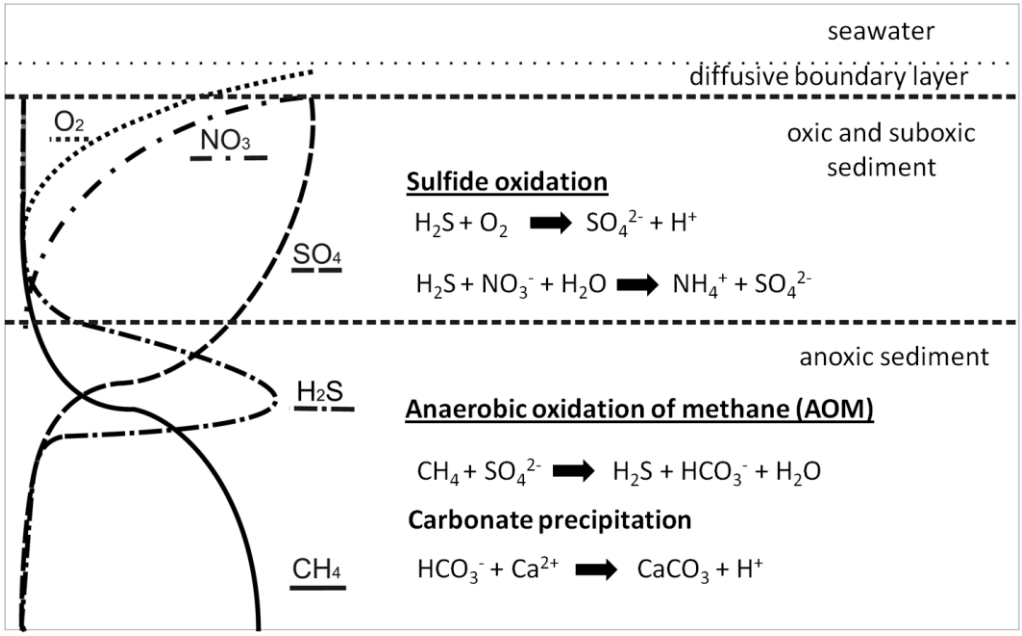

Figure 1: Schematic sketch of characteristic biogeochemical processes at cold seeps. Penetration of the electron acceptors oxygen (dotted line), nitrate (wide dash-dot line), and sulfate (dashed line). Methane (solid line) is advected with seepage fluid. Sulfide (tight dash-dot line) and bicarbonate is produced by anaerobic oxidation of methane (AOM), mediated by consortia of methanotrophic archaea and sulfate-reducing bacteria. Authigenic carbonates precipitate while sulfide is oxidized by chemoautotrophic organisms.

In sediments, the horizon where methane and sulfate are depleted simultaneously is called the sulfate-methane-transition zone (SMTZ) (Iversen and Jørgensen 1985; Knittel and Boetius 2009). In this zone, there is a marked increase in dissolved inorganic carbon (DIC) and sulfide, the products of AOM. Both products can also inhibit the reaction. Sulfide has been suggested to act as direct thermodynamic inhibitor for the AOM reaction itself, when present in high concentrations in the porewater (Treude et al. 2003; Zhang et al. 2010). Under high AOM activity, bicarbonate reacts with calcium to form authigenic carbonates (Peckmann et al. 2001): this reaction could indirectly inhibit AOM by reducing the porosity of the sediments or by blocking fluid pathways (Treude et al. 2003; Luff and Wallmann 2003; Kutterolf et al. 2008; Karaca et al. 2010), thereby retarding the supply of methane.

The depth of the SMTZ depends on the consumption rate of sulfate, the flux of methane from below (Borowski et al. 1999), and sometimes even on the activity of seep organisms (Cordes et al. 2005; Fischer et al. 2012). Apart from methanotrophy, sulfate reduction represents the most important anaerobic degradation process of organic matter in marine sediments (Jørgensen 1978); hence, the penetration depth of sulfate into sediments could additionally be dictated by organic matter input and burial rate (Borowski et al. 1999). In costal sediments, the SMTZ is often located only a few decimeters below the sea floor, due to the high consumption rate of sulfate by organoclastic sulfate reduction, while in organicpoor deep-sea sediments the depth of the SMTZ might be tens of meters below the surface (Borowski 2004). At places with advective methane supply from below, such as cold seeps and mud volcanoes, the SMTZ can be extremely shallow, even in deep-sea settings, displaying sulfate depletion within the first 10 cm (Treude et al. 2003; Niemann et al. 2006). Advective transport of fluids creates a stronger methane flux but also limits the penetration depth of sulfate. At these sites, the horizontal variability of the SMTZ depth is often very high and can vary on a decimeter scale (Treude et al. 2003; Niemann et al. 2006). Sometimes strong variability of benthic fluxes and AOM activity can be observed even within 40 cm lateral distance (Linke et al. 2005). Chemosynthetic seep fauna, such as sulfur bacteria mats, tubeworms, and clams, that are thriving on sulfide, serve as indicator for AOM activity and methane flux (Sahling et al. 2002; Torres et al. 2002; Levin et al. 2003; Treude et al. 2003; Mau et al. 2006). Aside from spatial variability, fluid flux, and associated methane supply with the attendant changes in the depth of the SMTZ, can also vary temporarily. Short-term fluid flow fluctuations can be created by blocked fluid paths, e.g., through spontaneous gas hydrate formation or carbonate precipitation (Luff et al. 2004, 2005), which force the formation of new migration pathways, or by tidal pressure changes (Tryon et al. 2002; LaBonte et al. 2007; Røy et al. 2008; Boles et al. 2001).

Fluid flow can also vary on very large temporal and spatial scales. Earthquakes can cause a pulse of strong fluid flow or create faults, which become new migration pathways for fluids (Tryon et al. 2002; Hensen et al. 2004; Aiello 2005; Henrys et al. 2006; Mau et al. 2007; Praeg et al. 2009; Meister et al. 2011). Earthquakes can also trigger slope failure, followed by mass wasting. Mass wasting on the continental slope

has been suspected to trigger methane releases from exposed gas hydrates (Ranero et al. 2008; Manga et al. 2009). Another long-term change of methane flux is postulated to be caused by global warming. Seafloor warming will decrease the stability of shallow submarine gas hydrates and increase methane fluxes (Kvenvolden 1993; LaBonte 2007). Because the Arctic Ocean is affected strongly by global warming and because gas hydrate stability is shallow compared with other oceans because of low temperatures, this region is likely to be one of the first regions to show temperature-related methane releases from gas hydrates (Buffett and Archer 2004; Biastoch et al. 2011).

The above examples illustrate that methane fluxes from the seafloor can be highly variable, both, on spatial and temporal scales. Understanding how the benthic microbial methane filter reacts to such changes with respect to growth and activity is not an easy task, because of the difficulties to both mimic natural situations in the lab or to follow adaptations in situ. There have been several previous attempts to study AOM activity and dynamics using flow-through systems, i.e., systems with a continuous flow of methane-saturated seawater through sediments, which are briefly summarized in the following paragraphs (for a direct comparison, see Table 1).

Table 1. Overview of different sediment flow- through systems and bioreactors, which were developed to investigate AOM.

Name	Type of sediment sample	Over-pressure in bar	Fluid Flow in cm yr^{-1}	Hydrologic residence time (HRT) in d	Methane (M) and sulfate (S) delivery	Task	Reference
AMIS	intact core	0.2	19-90	121.75 - 576.7	M & S from below	Microbial grow	Girgius et al. (2003, 2005)
Flow-through reactor	slurry	0.15	1500-3200	1.75 - 4.19	M & S from below	AOM efficiency	Wegener & Boetius (2009)
HP-CI/HP-MI	slurry	35.0	-	0.58	M & S mixed	Microbial kinetic	Deusner et al. (2009)
Membrane Bio-R	slurry	0.12	-	7.00	M & S mixed	Microbial grow	Meulepas (2009)
HP-Bio-R System	slurry	16.0	-	0.01 - 0.42	M & S mixed	AOM kinetic	Zhang et al. (2010)
SLOT	intact core	0.07	11-110	102.1 - 1021.0	M from below, S from top	AOM efficiency	this study

Girguis et al. (2003, 2005) developed a continuous-flow anaerobic methane incubation system (AMIS) to determine the grow rate of ANMEs. AMIS uses intact sediment cores and delivers methane-enriched seawater (including sulfate) from the bottom and seawater (including sulfate) without methane from the top. Seawater was prepared in a reactor to ensure constant methane concentration under atmospheric pressure. AOM

rates were determined in sub-samples gained during the experiment. Cell abundance of ANME organisms was determined before and after the experiment. Whereas ANME-2 revealed highest growth rates under low methane flux conditions, ANME-1 growth was faster at high methane flux.

Meulepas et al. (2009) used a flow-through membrane bioreactor under atmospheric pressure filled with sediment and supplied by artificial seawater (20 mmol L^{-1} sulfate). Methane permanently percolated through the bioreactor. Rates were determined by the turnover of $^{13}CH_4$ in incubations of suspended sediment material. After 884 days runtime, very high AOM rates (286 µmol $g_{dry\ weight}^{-1}$ d^{-1}) as well as cell doubling rates of 3.8 months were observed.

Wegener and Boetius (2009) used a flow incubation reactor under atmospheric pressure with high flow rates of artificial seawater enriched with methane to incubate sediment slurries. Starving times of 40 days were endured without causing any decrease in activity after reestablishment of methane supply. Conversely, reduced sulfate concentrations (1 mmol L^{-1}) led to a 50% decline in AOM activity.

Deusner et al. (2010) used a pressurized system (max. 35 bar), which increased concentrations of dissolved methane up to 70 mmol L^{-1} and facilitated AOM rates 10-15 fold higher compared with methane concentrations under atmospheric pressure. Beside pumps and compressor, the system contains a conditional vessel for enrichment of medium with methane and a bioreactor to incubate sediment slurries.

Zhang et al. (2010), as well, developed a high-pressure/high-methane flow-through system to prevent sulfide inhibition during incubations. The system is equipped with a conditional vessel, high pressure pumps, and an incubation vessel. In- and outflow ports provide sampling for sulfide determination.

Wankel et al. (2012) used a flow-through system similar to AMIS with a thermal gradient between 90 °C at the bottom and ~22 °C at the top to incubate hydrothermal vent sediments. Intact sediment cores were supplied with methane-enriched (2.8 mol L^{-1}) anoxic seawater medium (sulfate 28 mmol L^{-1}) from below with a fluid flow of ~330 cm y^{-1}. AOM rates were calculated based on natural concentrations of $\delta^{13}C$

methane and $\delta^{13}C$ DIC in the in- and outflow. The study suggested a decoupling of AOM from sulfate reduction at high temperatures (90 °C), which might be coupled to Fe reduction.

The above flow-through systems and bioreactors were developed to either facilitate the optimum growth condition for AOM organisms (Girguis et al. 2003; Meulepas et al. 2009) or to analyze the influence of selected factors by individually tuning the system (Wegener and Boetius 2009; Deusner et al. 2010; Zhang et al. 2010; Wankel et al. 2012). In most cases, sediment slurries instead of intact sediment cores were used (Table 1). At natural methane seeps, however, conditions are very different to such conventional artificial setups. Most importantly, methane and sulfate are supplied from different directions and with different velocities: methane advects with fluids from deeper sources, while sulfate is delivered from the overlying water column by molecular diffusion (Borowski et al. 1996). Furthermore, a change in methane supply is often correlated with an alteration of the flow regime (Tryon et al. 2002; Tryon and Brown 2004; Linke et al. 2005; LaBonte 2007; Füri et al. 2010). Thereby, the benthic methane filter is not only challenged by an increased methane supply but is further stressed by a shallowing of the penetration depth of the electron acceptor, i.e., sulfate (Niemann et al. 2006). Finally, natural (intact) sediments have very different characteristics (e.g., porosity, permeability, concentration gradients) compared with laboratory sediment slurries (homogenized sediment-seawater mixtures). The flow-through systems of Girguis et al. (2003) and Wankel et al. (2012) are, to date, the only systems that use intact sediment cores. However, the systems lack the technical feasibility to monitor biogeochemical developments inside the core over time. It was therefore the aim of the present study to develop a new system, which enables the chronological study of AOM activity and to correlate biogeochemical parameters in intact sediment cores under different fluid/methane flow regimes over the entire core length. The SLOT system facilitates a natural supply of methane and sulfate and the monitoring of biogeochemical gradients during experimentation. In a first application of the system using gassy sediments from the Eckernförde Bay, Baltic Sea (see e.g., Treude et al. 2005), we focused on the following research questions:

How does the benthic microbial methane filter and geochemical gradients respond to shifting fluid and methane flow regimes and how long is the response time until reaching steady-state conditions?

How efficiently does the benthic methane filter remove methane under increased methane supply and reduced sulfate penetration?

Materials and procedures

SLOT system

The SLOT system was designed to simulate natural seepage conditions in undisturbed sediment cores with an advective transport of methane from the bottom and a diffusive supply of sulfate from the top of the core. Fluid used to supply the electron acceptor and donors consisted of anoxic seawater culture medium for sulfate-reducing bacteria according to Widdel and Bak (2006). Anoxic sulfate-containing medium (SO_4^{2-} concentration 19 mmol L^{-1} and salinity 22 psu according to natural concentrations at the study site: Whiticar 2002; Treude et al. 2005), which served to mimic “seawater” conditions, i.e., enabling diffusive sulfate supply from the sediment surface, was methane-free. Methane-enriched medium (CH_4 concentration ~ 930 µmol L^{-1}, salinity 22 psu), which served to mimic “seepage” conditions from below, was sulfate-free. In the following, the two media will be called “seawater” and “seepage” medium according to their flow direction and composition. Seawater medium was delivered from a single reservoir with a nitrogen headspace (Fig. 2). For the supply of seepage medium, the system consisted of two connected reservoirs with a nitrogen (reservoir 1) and a methane (reservoir 2) headspace. Reservoir 2 directly delivered methane-enriched medium to the bottom of the sediment cores via peristaltic pumps (details see below). As soon as the medium level was lowered in reservoir 2, creating a slight under pressure, new medium was replenished from reservoir 1 (nitrogen headspace). In reservoir 2, medium from reservoir 1 was enriched with methane. The equilibration between the methane headspace and the medium was enhanced by letting the entering medium drop through the methane headspace.

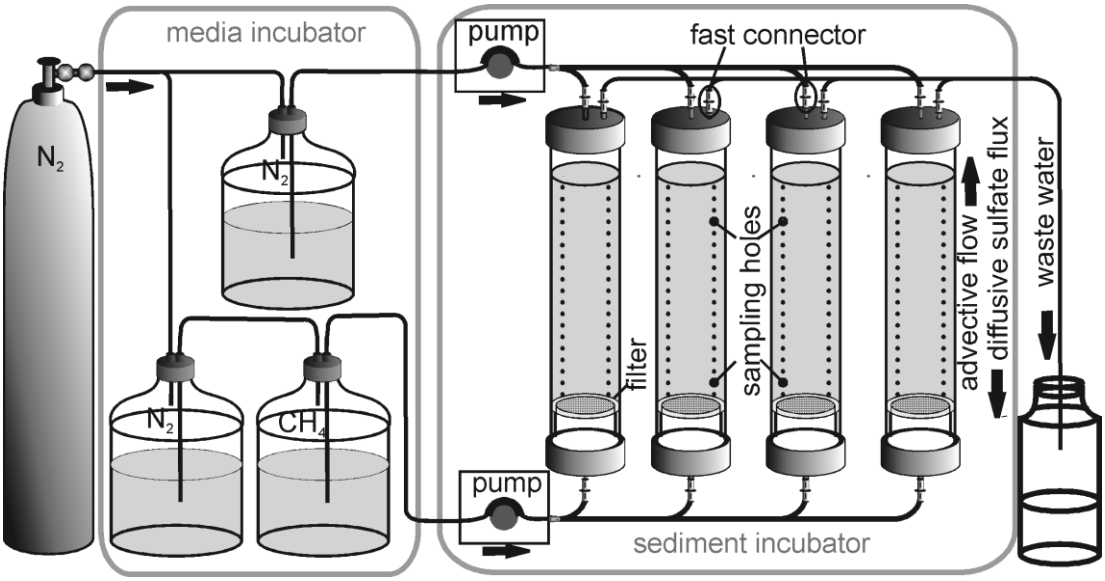

Figure 2: Schematic drawing of the SLOT system. The medium reservoirs were stored and chilled in a refrigerator chest at 10°C. The medium, which entered the core from the top, mimicked anoxic seawater. The lower medium, which was enriched with methane but sulfate-free, entered the core from the bottom and mimicked the seepage of fluid. Seep medium was enriched with methane in the CH_4 reservoir. All media were transported by pumps and through tubing. All cores were equipped with fast connectors to avoid air intrusion during disconnection and with three lines of 21 silicon-sealed holes for sampling. A glass fiber filter underneath the sediment core prevented that sediment was lost into lower parts of the SLOT system. Waste water from the outflow (top) was collected in a bottle.

To track the migration of the seepage medium inside the core, we used bromide as an inert tracer. While bromide was present in standard concentration in the seepage medium (560 µmol L^{-1}), it was present only in trace concentration (6 µmol L^{-1}) in the seawater medium. Resazurin was used as indicator for oxygen contaminations in both media (Visser et al. 1990). For further details on the composition of the media, see below (section "Experimental setup" and Table 2). All media were stored in a refrigerator chest at 10°C in the dark.

In the system, medium was transported by peristaltic pumps (Medorex TL/10E, min/max pump volume 0.1 µL min^{-1}/400 µL min^{-1}) using Santropen (autoclaveable, high flexible, very resistant) tubes (inner diameter 0.5 mm, outer diameter 1.6 mm). Between N_2 supply (gas tank), medium reservoirs and pumps as well as between pumps and sediment cores, Iso-Versenic (autoclaveable, very resistant, very low gas permeability) tubes were used (inner diameter 1 mm, outer diameter 3 mm). Tube connectors consisted of polypropylene (Brandt GmbH).

Table 2. Salt concentrations of the two different media used in the SLOT system. Seawater medium with sulfate was delivered from the top, seepage medium with methane and without sulfate from the bottom. In the last line, the gas of the medium headspace is denoted.

	Seawater medium (with SO_4^{2-})	Seepage medium (with CH_4)*
Salts	**in mmol l^{-1}**	**in mmol l^{-1}**
KBr	0.006	0.560
KCl	6.150	5.290
$CaCl_2$ $2H_2O$	6.571	6.571
$MgCl_2$ $6H_2O$	18.328	36.465
$MgSO_2$ $7H_2O$	18.137	0.000
NaCl	296.371	296.371
Medium headspace	N_2	CH_4

* $FeSO_4$ (trace element) was replaced by FeCl

Polycarbonate core liners (gastight, total length 30 cm, inner diameter 6 cm, outer diameter 6.8 cm; Fig. 3D) were equipped with three vertical lines of sampling holes (21 holes per line, diameter 4 mm, distance between sampling holes 5.8 mm), which were sealed with residue-free silicon (Aquasil, Probau). Liners were closed both at top and at bottom with a cap (Fig. 3A, B), made of polyvinyl chloride (PVC). These caps (top and bottom) had an inflow pipe with a distributor container (Fig. 3B). An outflow port (top cap only) was located behind this container. An O-ring of nitrile butadiene rubber (NBR) was located at the inner edge of the cap to seal the connection between cap and liner. At the bottom part of the liner, a filter holder (Fig. 3C) was fixed to hold a glass fiber filter (diameter 6 cm, pore size 5 µm). The filter kept sediment grains from entering the distributor container. Sediment cores were connected to the pump system by fast couplers (polypropylene, Colder Products), enabling an easy connection and disconnection of tubes without oxygen intrusion. Pumps and cores were stored in a refrigerator at 10°C and in the dark. For details on field sampling and experimental setups of the sediment cores used in the SLOT system, please see “Field sampling (Eckernförde Bay)” and “Experimental setup” below.

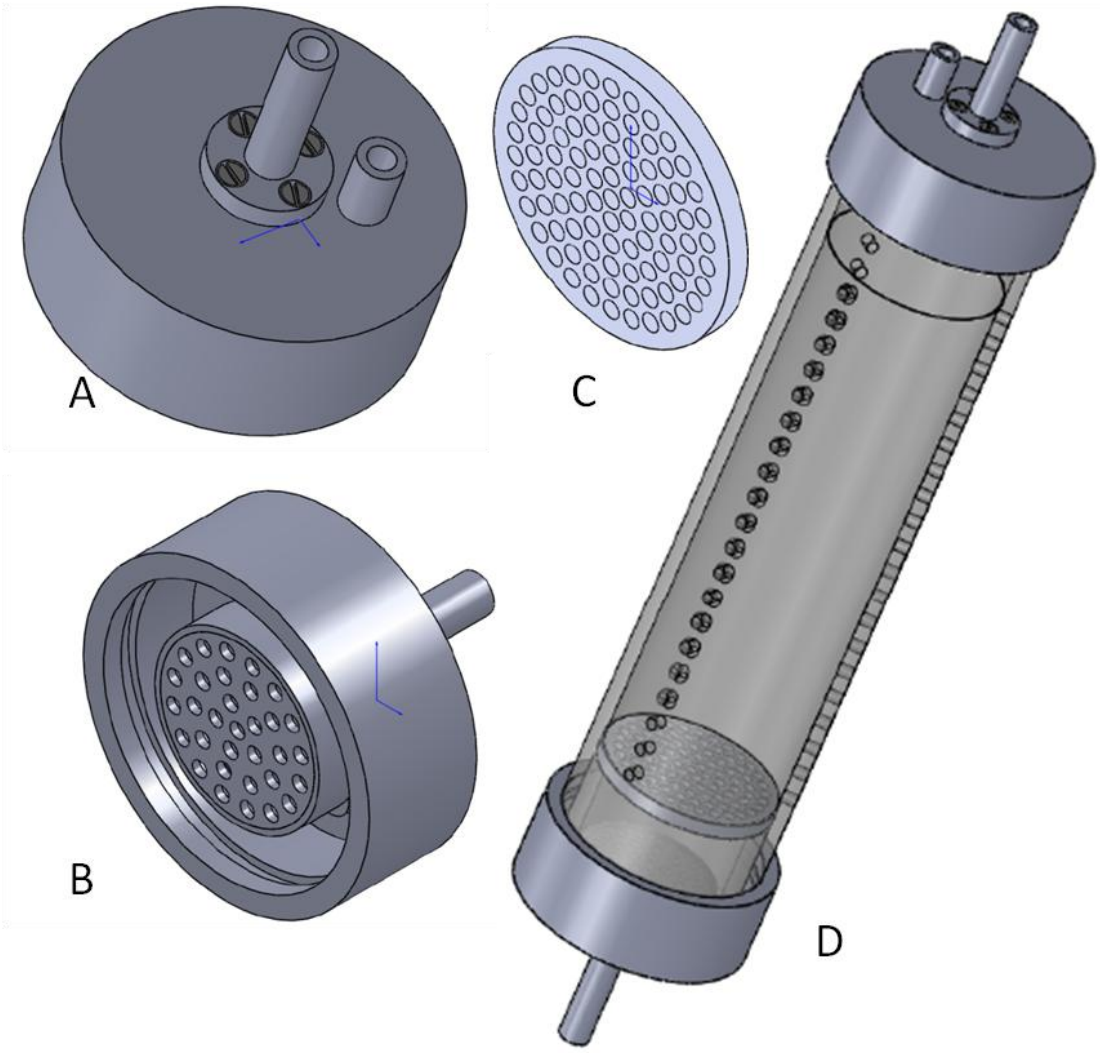

Figure 3: Single components of the SLOT liner. (A) Top cap (outside view, PVC) with inflow (middle, long, distribution container not shown) and outflow pipe (short, right), (B) Bottom cap with inflow pipe and distributor container (PVC), (C) filter holder with openings (PVC), (D) SLOT liner (polycarbonate) with three lines of sampling holes, equipped with filter holder inside (polycarbonate), top cap (in- and outflow port), and bottom cap (inflow port).

Sampling procedures and analyzes during SLOT system incubations

During incubation of the SLOT cores, silicon-filled sampling holes were used for porewater sub-sampling with rhizons (Meijboom and Noordwijk 1991) or for horizontal microsensor measurements (pH, redox potential, sulfide; Revsbech and Jørgensen 1986) at several time points over the course of the incubation (after 32, 80, 129, 169, 234, 303, and 360 days for sulfide; 169, 234, 303, and 360 days for pH; 32, 129, 169, 303, and 360 days for redox potential; total incubation time 376 days).

Porewater sampling

For porewater sampling with rhizons (Fig. 4C and 4D), the silicon was carefully removed from the sampling holes and rhizons (rhizosphere, CSS-F, length 5 cm, diameter 2.5 mm, pore size 0.2 µm), pre-wetted with autoclaved saltwater (salinity 22 psu), were slowly pushed into the sediment. Afterward, rhizones were sealed with residue-free silicon (Aquasil, Probau) around the holes and remained inside the sediment core over the entire incubation time. For repetitive porewater sampling, the first 0.5 mL residual water was removed from the rhizons and discarded. Subsequently, 1.0-1.5 mL porewater was sampled (3 mL luer-lock syringes, Becton, Dickinson and Company) and transferred to 2 mL plastic vials (safe-lock tubes, 2 mL, Eppendorf) for later analyses of total alkalinity (TA), sulfate, bromide, and chloride (see below). We calculated, according to Seeberg-Elverfeldt et al. (2005), that only a maximum of 3 mL porewater should be sampled to avoid cross sampling of adjacent depth sections.

Before porewater sampling with rhizons, the outflow medium (Fig. 4B), which leaves the system at the top, was sampled using borosilicate glass syringes (luer, 5 mL, Poulton & Graf GmbH), connected to fast couplers by a piece of Iso-Versenic tube (5 mm length, 3 mm diameter). The two inflow media (“seawater” and “seepage”) were sampled with tube connectors and borosilicate syringes (see above) directly before the fast couplers that connected the tubing to the cores. For methane samples, 2 cm^3 medium were transferred into 10 mL serum vials containing 5 cm^3 2.5% w/v NaOH. The vial was immediately closed by butyl rubber stopper. The rest (~1.5-2 cm^3) of the sample volume was stored in plastic vials (safe lock tubes, Eppendorf, 2 mL) for total alkalinity titration and ion analytics.

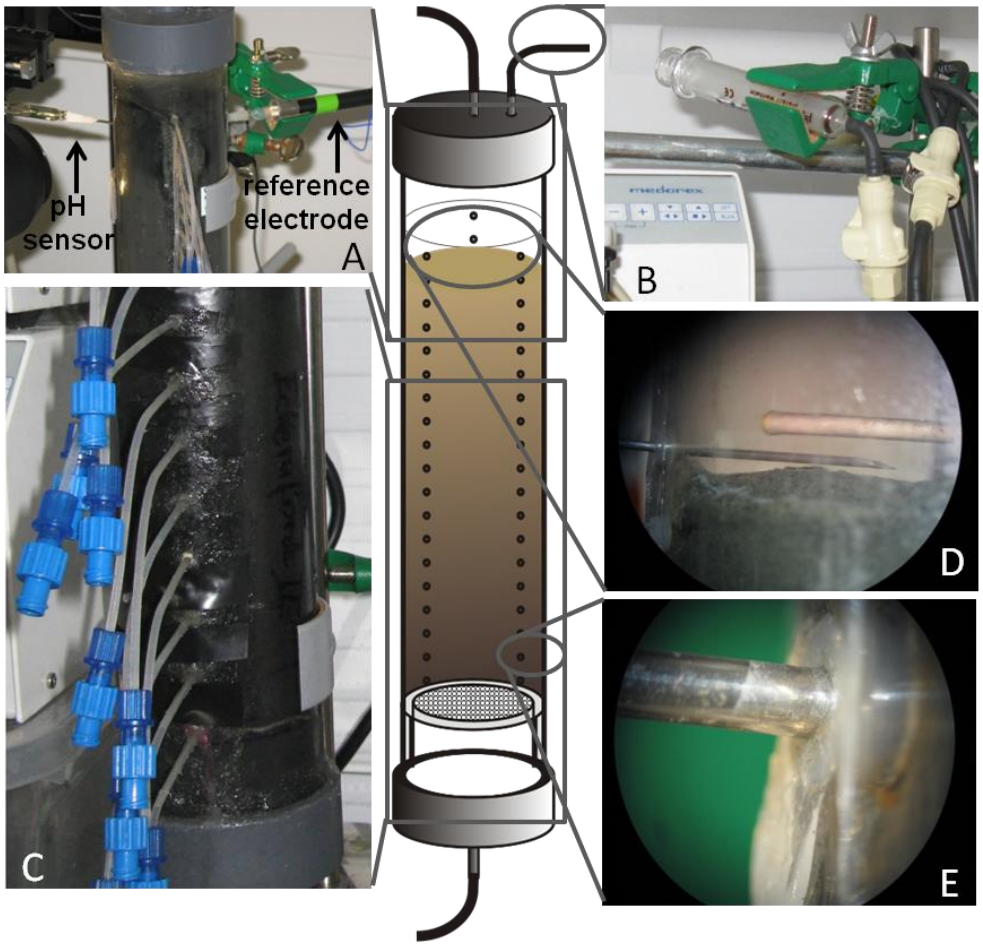

Figure 4: Sampling procedures of the SLOT cores: (a) microsensor measurement through silicon-filled sampling holes with pH needle-sensor (left) and reference needle-electrode (right); (b) outflow sampling with borosilicate syringe and fast connector; (c) microsensor and rhizone in the bottom water of the core; (d) needle-sensor penetrating a silicon-sealed sampling hole; (e) porewater sampling with rhizones through sampling holes.

Microsensor analyses

We used steel needle sensors for microsensor analyses (Revsbech and Jørgensen 1986) of geochemical parameters (pH, redox potential, sulfide) in the sediment cores (Fig. 4A, D, and E). Needle sensors are less breakable and were found to easily penetrate into the core liner through the silicon-filled holes. However, this type of sensor often has a much longer response time than normal glass sensors, depending on temperature, sensor age, and type of sediment. As the temperature of the sediment cores was close to 10 °C (stabilized by cool packs during measurements) and measurements had to be conducted at room temperature, the sensor had to adapt at each measurement point to the new temperature, which increased the response time.

Hence, sensors were allowed to adapt between 5 and 15 minutes, after penetration through the sampling holes, until a value was declared valid (at least 90 % of the response signal, t_{90}). Measurements were performed in ~ 2 cm intervals, i.e., every second sampling hole, except for the sediment-water interface, where measurements were performed directly above and below the interface. pH was measured with microsensors from Microelectrodes Inc. (MI 411 B, gauge 20). For a three-point calibration (pH 4.01, 6.89, and 9.18), standard pH buffers from Merck were used. Redox potential was measured with a sensor from Unisense, Denmark (RD-N, tip diameter 0.8 mm) or a redox needle sensor (MI-800, gauge 25, Microelectrodes Inc). The sensor was calibrated with a two point calibration of saturated quinhydron solution in buffers of pH 4 and 7. Redox potential in mV relative to the standard hydrogen electrode (SHE) was provided by the sensor manual. Hydrogen sulfide (H_2S) was measured by needle microsensors from Unisense, Denmark (H_2S-N, tip diameter 0.8 mm). The sensor was calibrated by 6 standards of NaS solutions (0, 100, 200, 500, 1000, 2000 µmol L^{-1}), prepared in an oxygen free phosphate buffer (>4 pH), with 10 % v/v TiCl. Total sulfide concentrations (including H_2S, HS^-, and S^{2-}) were calculated using H_2S concentration, pH-value, salinity, and temperature according to Jeroschewski et al. (1996). For missing pH-profiles (32, 80, 129 days runtime) a pH of 7.5 was used (media preparation pH-value).

Experiment termination and core slicing

At the end of the experiment, porewater was sampled again with rhizons (see above). This time, a larger volume (on average ~ 4.3 mL per sampling hole) for the determination of ammonium, nitrate, and sulfide samples (see analytics below) was extracted. After removal of the top and bottom caps, the core was placed on an extruder (diameter 5.8 cm). Two polycarbonate sub-cores (length 26 cm, inner diameter 2.5 cm, outer diameter 2.6 cm) were pushed into the core for the determination of sulfate reduction and anaerobic oxidation of methane (AOM) rates (see analytics below). Whereas the subcores were still inside the sediment, the sediment core was pushed outside the liner with the help of the extruder and sliced step by step into 1 cm intervals for methane sampling (2 cm^3) and 2 cm intervals for porosity (~1.5 cm^3), total CNS (subsample from porosity), and organic carbon (TOC, subsample from porosity) (see

analytics below). Additional samples were taken in 2 cm intervals for future efforts such as Catalysed Reporter Deposition Fluorescence In Situ Hybridization (CARD-FISH, 0.5 cm^3), lipid biomarker (~ 3 cm^3), and RNA/DNA (2 cm^3) analyses.

Analytical procedures

Porewater analyses

A 50 µL subsample of each porewater sample was titrated with 0.01 M HCl titrosol solution (Merck) to determine total alkalinity (TA, Ivanenkov and Lyakhin 1978) immediately after sampling using an indicator of methyl red and methylene blue and an electronic burette (876 Dosimat plus, Metrohm). The certified seawater standard IAPSO was used for calibration.

Concentrations of chloride, bromide, and sulfate (sample volume 300 µL) were determined by high performance liquid chromatography (HPLC) (Compact IC 761, Cl^-, SO_4^{2-}, conductivity detector; Br^- UV/VIS detector lambda 1010 at 230 nm). The sample was diluted 1:100 and IAPSO was analyzed as control.

Ammonium, nitrate, and total sulfide in the porewater, sampled by rhizones, were measured only at the end of the experiment. Ammonium and nitrate samples (1000 µL each) were measured by standard procedures according to Grasshoff et al. (1983). Total sulfide samples (500 µL) were analyzed by the photometric methyl blue method of Cline (1969).

Medium samples for methane analyses were taken from the in- and outflows (in total 6 times between microsensor measurement and porewater sampling; sampling after 129 d failed) using headspace-free borosilicate syringes (5 mL). Methane was determined in the headspace of the sampling vial. Therefore, 2 cm^3 sample was quickly transferred into 10 mL glass vials, filled with 5 cm^3 NaOH (2.5 %w/v) and immediately closed with butyl rubber stoppers and an aluminum crimp. Methane was analyzed by gas chromatography (Hewlett Packard Series II) with a packed column (Haye SepT, 6 ft, 3.1 mm inner diameter, 100/120 mesh, Resteck, carrier gas: He 20 mL min^{-1}, combustion gas: synthetic air 240 mL min^{-1}, H_2 20 mL min^{-1}).

AOM rates were calculated from the difference between in- and outflow methane concentrations before (303 days) and after (360 days) fluid flow swapping. For the outflow, methane concentration was multiplied by the dilution factor of the seawater medium in the overlying water column (41 and 5 for low and high flow rate, respectively). For the inflow, the methane concentration of the seepage medium was used. The difference of the two methane concentrations was then divided by the average time the fluid needed to pass the incubation chamber (hydrologic residence time 1044 and 104 days, for low and high fluid flow, respectively) and the crosssection area of the core (28.3 cm^2). The methane efflux from the cores was calculated by multiplying the outflow methane concentration by the dilution factor (see above) and the fluid flow (11.2 cm a^{-1} and 112.1 cm a^{-1}). Methane turnover rates and methane flux were converted to mmol m^{-2} d^{-1}.

Sediment parameters

Sediment methane samples were taken every centimeter immediately after core slicing by sub-sampling 2 cm^3 sediment with cut-off 3 mL PE syringes and transferring the sediment into 10 mL headspace glass vials (see above) filled with 5 mL 2.5% w/v NaOH. The samples were analyzed by gas chromatography (see above). Concentration per volume sediment was corrected for porosity to obtain methane concentration per volume porewater and to compare values with in- and outflow concentrations.

For the determination of porosity circa 2 cm^3 of sediment was weighted in a vial (pre-weighted), freeze dried, and reweighted. Porosity was calculated using the weight difference and assuming a density of 2.5 g cm^{-3} for the dry fraction.

Total C, total N, and total S were analyzed in small subsamples (ca. 20 µg) of the porosity samples (freeze dried) using a CARLO ERBA Elemental Analyzer NA 1500. TOC was determined from the difference in the C content between acidified (addition of 0.25 mmol L^{-1} HCl) and non-acidified samples. All measurements were performed in duplicates.

Radiotracer measurements

For the determination of sulfate reduction and AOM rates, in the two polycarbonate sub-cores subsampled from the main core, we used the whole core injection method for radiotracers (Jørgensen 1978). For AOM determinations, 15 µL $^{14}CH_4$ dissolved in anoxic sterile water (2 kBq, specific activity 2.28 GBq mmol^{-1}), and for sulfate reduction determinations 6 µL $^{35}SO_4^{2-}$ dissolved in sterile water (250 kBq, specific activity 37 TBq mmol^{-1}) were injected into each core, respectively, in 1 cm intervals. The sub-cores were incubated for 24 h at 10°C in the dark. After incubation, the sub-cores were sliced in 1 cm steps. The incubation was terminated by transferring the sediment into 20 mL 2.5%w/v NaOH (40 mL glass vials, rubber stopper) for AOM and into 20%w/v ZnAc (50 mL plastic centrifuge tubes) for sulfate reduction, and shaken vigorously. AOM samples were analyzed according to Treude et al. (2005) (gas chromatography, $^{14}CH_4$ combustion, and calculation) and Joye et al. (2004) ($^{14}CO_2$ trapping). Analyses of sulfate reduction samples were performed after the cold chromium distillation of Kallmeyer et al. (2004). Control samples (5 and 3 replicates for AOM and sulfate reduction, respectively) were first transferred to termination vials before the addition of tracer.

Field sampling (Eckernförde Bay)

For the first test of the SLOT system, we used gassy sediments from the Boknis Eck time series station in the Eckernförde Bay (Baltic Sea, Germany; 54°31’ N, 10°02’ E; for details, see Bange et al. 2010). Sediments (28 m water depth) in this area are characterized by a high organic carbon content (5-6%, Whiticar 2002) and an average sediment accumulation rate of 6 mm y^{-1} (Nittrouer et al. 1998). Organic carbon is mostly produced during plankton blooms (Bange et al. 2010). The sediments are gassy below the sulfate-methane transition zone (ca. >40 cm) due to high methane production rates. The produced free methane gas results in an acoustic turbidity layer (Anderson et al. 1998; Jackson et al. 1998; Richardson and Davis 1998) and causes gas bubble releases into the water column (Abegg and Anderson 1997; Boudreau et al. 2001). AOM has been described to occur in the top 30 cm of the sediments (Treude et al. 2005).

We sampled surface sediments from Boknis Eck during a day trip with the RC “Littorina” on the 23.08.2010, using a miniaturized multicorer (K.U.M.). Two multicorer cores (core liner length 62 cm, core length 32 cm, inner diameter 10 cm) were sub-sampled in a 10°C cooling room by pushing one SLOT liner (inner diameter 6.1 cm, outer diameter 7 cm, total length 30 cm, length of retrieved sediment core 20 cm) into each multicorer core. The glass fiber filter and cap used to close the core at the bottom were applied under water (artificial seawater; salinity 22 psu, aquarium salt, Tropic Marin). SLOT cores were finally dried on the outside and the connection between caps and cores were sealed with residue-free silicon. Air bubbles in the supernatant (top) and distributor container (bottom) were immediately replaced with anoxic “seawater” medium using syringes with needles applied through the silicon sealed sampling holes.

Experimental setup

The two SLOT cores from the Eckernförde Bay were installed into the SLOT system, and two different flow regimes were applied to study the response time and efficiency of AOM at different fluid and methane fluxes. Salinity of the medium was adjusted to bottom water levels at the sampling site (22 psu, Treude et al. 2005). Before starting the experiment, the cores were flushed with anoxic sulfate-enriched “seawater” medium from top to bottom for approximately 40 days (pump rate 20 µL min^{-1}, flow rate 572 cm y^{-1}, hydrologic residence time 26 days) to remove the in situ porewater and to ensure full sulfate availability throughout the core at the start of the experiment. During this flushing phase, the bottom port served as an outflow. After this phase, anoxic methane-enriched “seepage” medium was connected to the core bottom and the medium outflow was installed at the top. In the main phase of the experiment, the two cores were flushed with seepage medium from the bottom at different pump rates: 0.5 µL min^{-1} for the low flow regime (from now on abbreviated LFC for “low flow core”) and 5 µL min^{-1} for the high flow regime (from now on abbreviated HFC for “high flow core”). Using an average porosity of 0.83 and a cross-section area of 28.3 cm^2, these pump rates yielded an overall flow rate of 11.2 cm y^{-1} and 112.1 cm y^{-1}, respectively, which are at the intermediate and high level of natural seepage conditions (Torres et al. 2002; Tryon et al. 2002; Hensen et al. 2004, 2007; Linke et al. 2005). We did not apply lower flow rates, because it would take too much time (>60 months) before any effects of the

fluid migration would be measurable inside the sediment. Equally, we did not apply much higher flow rates, because it would minimize the sulfate penetration depth and push the AOM layer basically out of the sediment (Niemann et al. 2006). Furthermore, extremely high flow rates could induce channelizing of fluid flow between the core liner wall and the sediment core. We were able to avoid this effect within the range of the applied flow rates as it was later confirmed by the establishment of geochemical gradients. However, it should be kept in mind that natural inhomogeneous permeability in the sediment itself could lead to channelizing and hence to a lower residence time of the fluid and consequently to a lower efficiency of the microbial benthic methane filter (Sommer et al. 2006; Wankel et al. 2012).

At the top of the core, seawater medium was permanently pumped with 20 µL min^{-1} through the overlying water to ensure a constant sulfate concentration and the diffusion of sulfate into the sediment. After a runtime of 310 days, the flow rates of the two cores were swapped to study the response of AOM to quick changes in the flow regime. An overview of runtimes and flow rates is given in Table 3. Outflow, inflow, and vertical sampling holes were sub-sampled/measured in 1-2 month intervals as described above.

Table 3: Overview of methane flux, advective flow, and pump rate in the low and high flow core (top) as well as experimental phases and run times (bottom) under the low and high flow regime.

	low flow	**high flow**
Flux mmol CH_4 m^{-2} d^{-1}	0.285	2.847
flow of seepage medium in cm yr^{-1}	11.21	112.06
pump rate of seepage medium in µl min^{-1}	0.5	5
Experimental phase	**run time (d)**	**phase duration (d)**
pre-phase	-40 - 0	40
main phase	0 - 310	310
swapping phase	310 - 376	66

SLOT incubation results and data discussion

Evolution of geochemical gradients (day 0 to 310)

The advection of fluid from the bottom of the sediment cores was tracked via the inert tracer bromide in the seepage medium (560 µmol L^{-1}). In the low flow core (LFC, 11.2 cm y^{-1}) only a very small increase in bromide concentrations were observed in the lower part of the core (30-70 µmol L^{-1} 12 cm sediment depth; Fig. 5A, D, G, J, M, and P). In contrast, bromide concentration continuously increased from the bottom of the high flow core (HFC, 112.1 cm y^{-1}). Measurable bromide penetration started already after 32 days (Fig. 5A). After 129 days, bromide reached the sediment-water interface (112 µmol L^{-1}; Fi. 5G). In the following 132 days, a chemocline of bromide established at a depth from 3 to 8 cm (~ 230-450 µmol L^{-1}; Fig. 5J, M, and P). Sulfate profiles (Fig. 5 and 6; A, D, G, J, M, and P) generally mirrored those of bromide, indicating the displacement of resident porewater by the advecting fluid. Sulfide was initially higher in the HFC (33-505 µmol L^{-1}; Fig. 6B, E, and H) than in the LFC (20-365 µmol L^{-1}; Fig. 5B, E, and H), indicating a higher sulfate reduction activity in the first core prior to the experiment. However, during the experiment the situation changed. In the LFC sulfide accumulated, reaching a maximum of 650 µmol L^{-1} after 169 days at 19 cm (Fig. 5K) while in the HFC, sulfide appeared to be removed from the core by the advecting fluid.

Total alkalinity (TA) had an initial concentration of 30 meq L^{-1} in both the seawater and the seepage medium. During the experiment, this parameter alternated between 22 and 32 meq L^{-1} in depth and time in both cores (Fig. 5 and 6; B, E, H, K, N, and Q). Especially at the beginning of the experiment (32-129 days runtime), TA was mostly higher at the bottom of the core and decreased toward the top. With increasing runtime, stronger alternations were observed. These alternations toward either lower or higher TA values might indicate carbonate precipitation and dissolution processes, respectively (Luff and Wallmann 2003).

Initially, pH in both the seawater and the seepage mediumwas adjusted to 7.5. Nevertheless, after time, pH increased to values of 8.4 and 8.8 at the top of the LFC (Fig. 5R) and HFC (Fig. 6R), respectively; a phenomenon, which is frequently observed

at natural methane seeps (Glud et al. 2004; Beer et al. 2006) and could be assigned to sulfide oxidation by nitrate (Billerbeck et al. 2006; Preisler et al. 2007). Porewater in our experiments had a nitrate concentration of only ~ 4 µmol L^{-1} (measured after experiment termination, see below). However, the filamentous sulfur bacterium *Beggiatoa*, which is frequently found in Eckernförde Bay sediments, enriches and stores nitrate in its vacuoles (Preisler et al. 2007). The ability to store nitrate could facilitate sulfide oxidation at the sedimentwater interface of our cores even under low nitrate concentrations. At Eckernförde Bay, on average 0.16 mmol m^{-2} d^{-1} sulfide is oxidized with nitrate (Preisler et al. 2007) corresponding to 0.45 µmol d^{-1} in our system (cross area 28.3 cm^2). Sediments of the SLOT system were supplied by 0.12 µmol nitrate d^{-1} and could,

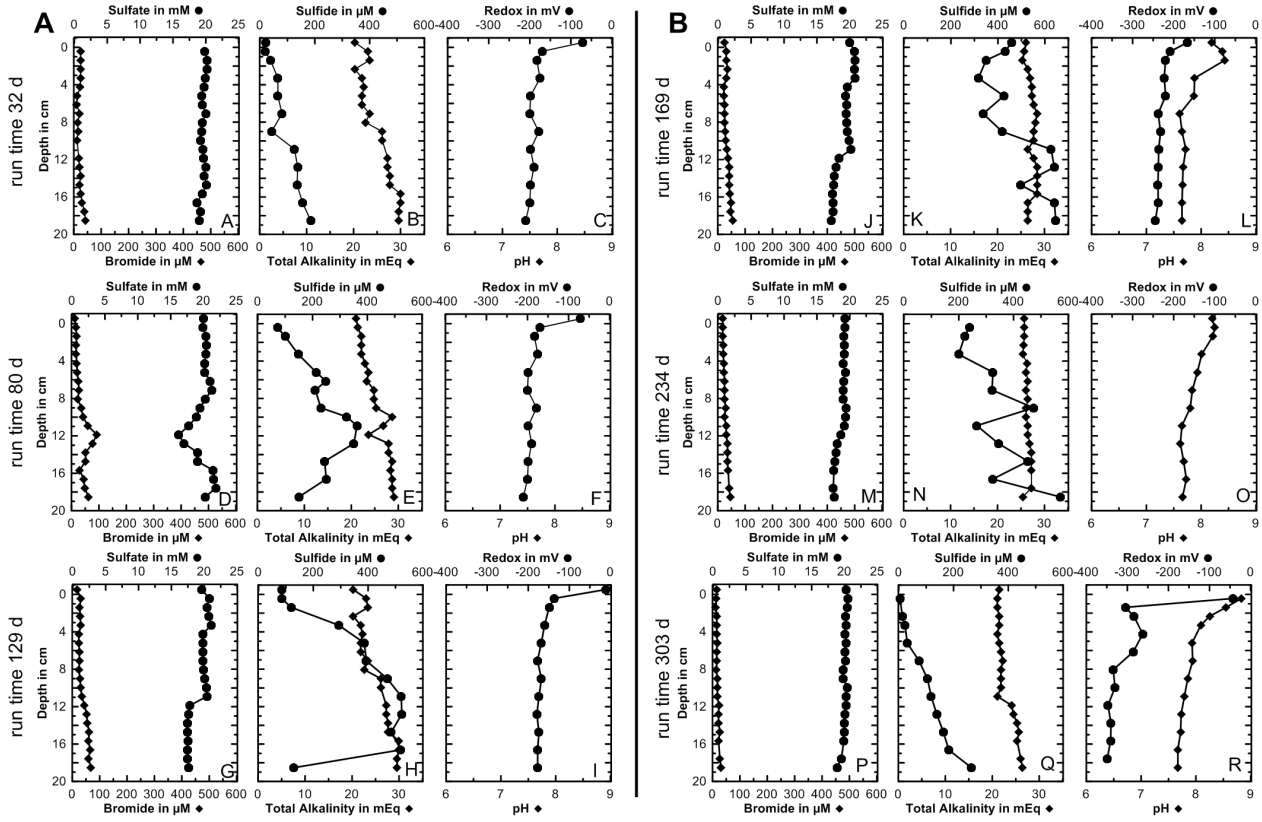

Figure 5: Geochemical parameters measured in sediment of the low flow core (LFC) from Eckernförde Bay after 32 (A, B, C), 80 (D and E), 129 (G, H, and I), 169 (J, K, L), 234 (M, N, O), and 303 (P, Q R) days of runtime. Shown are porewater profiles of sulfate, bromide (A, D, G, J, M, and P), sulfide, total alkalinity (B, E, H, K, N, and Q), redox potential (C, I, L, and R), and pH (L, O, and R).

therefore, theoretically oxidize 0.12 µmol sulfide d^{-1}, according to the dissimilatory reduction of nitrate to ammonium (Jørgensen and Nelson 2004), which is close to the referred average of Preisler et al. (2007). Below 6 cm sediment depth, pH was between

7.6 and 8.0 (Fig. 5 and 6; L, O, and R), which is often found in AOM zones (Knittel and Boetius 2009) and can be explained by precipitation of iron sulfides. Because the

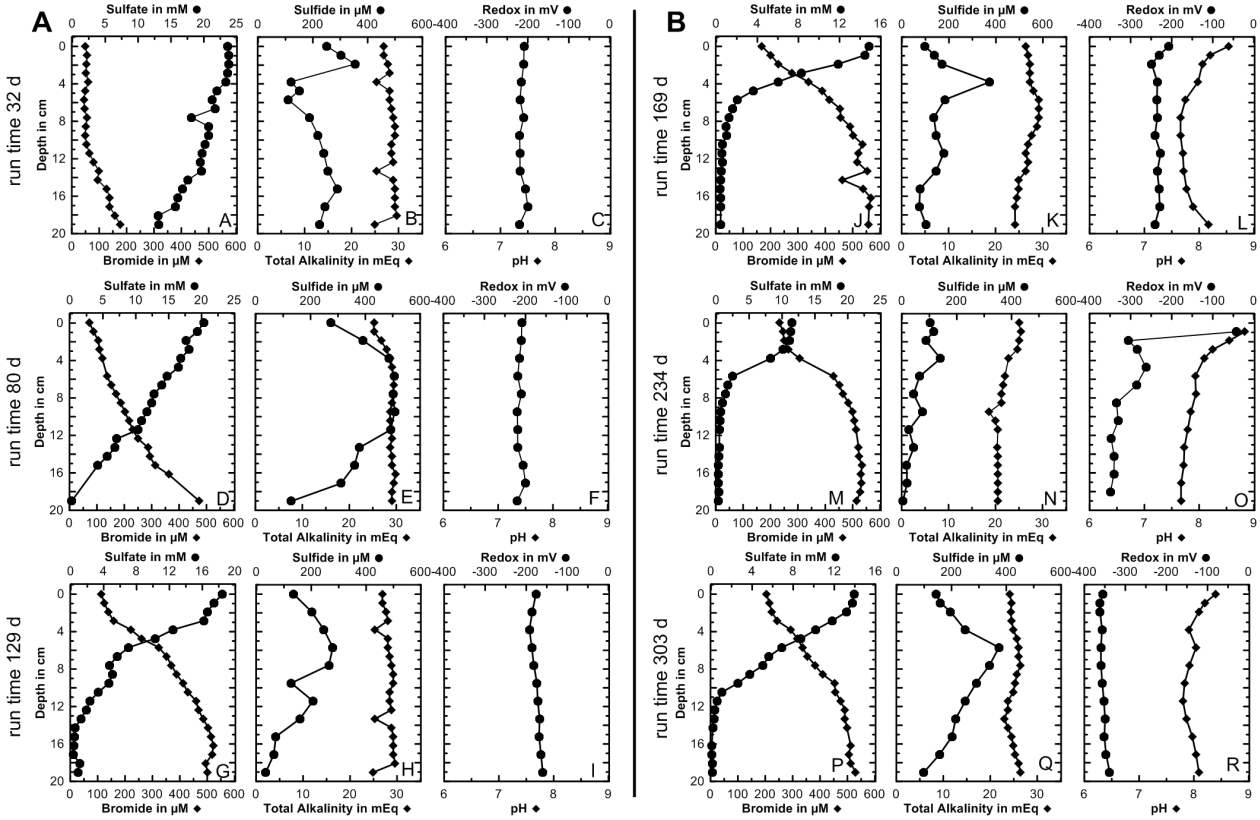

Figure 6: Geochemical parameters measured in sediment of the high flow core (HFC) from Eckernförde Bay at 32 (A, B, and C), 80 (D, and E), 129 (G, H, and I), 169 (J, K, and L), 234 (M, N, and O), and 303 (P, Q, and R) days of runtime. Porewater profiles of sulfate, bromide (A, D, G, J, M, and P), sulfide, total alkalinity (B, E, H, K, N, and Q), redox potential (C, I, L, R), and pH (L, O, and R) are shown.

sediment was constantly black colored, we could not gain any information about new precipitation of iron sulfides by visual inspections. However, sulfide iron precipitation is assumed to occur in Eckernförde Bay sediments (Preisler et al. 2007; Dale et al. 2013). Generally, the pH was higher (up to 0.3 units) in the HFC compared with the LFC, whereas the redox potential of the LFC was higher in the upper centimeters (0-2 cm, between –10 mV and –160 mV; Fig. 5C, I, and L) and lower in the deeper sediment (below 2 cm, between –150 and –245 mV). Redox values between 0-100 mV indicate a transition from anoxic to suboxic sediments and support speculated sulfide oxidation by nitrate (see above). After 303 days runtime, the redox profile was more pronounced with –47 mV (Fig. 5R) in the upper centimeter and –346 mV at the bottom of the sediment. In contrast to this, the redox profile of the HFC was generally more negative (–170 mV and

–360 mV; Fig. 6C, I, L, and R) and more evenly distributed over the whole sediment core. Increases in redox values were generally not observed or only very weak at the top of the HFC. Negative redox values in the deeper sediment layers (below 2cm) indicated reduced conditions caused by, e.g., sulfide-sulfate redox couples (Schulz 2000).

Methane concentrations measured in the bottom inflow of the seepage medium were between 771 and 1060 µmol L^{-1} (on average 930 µmol L^{-1}, ±111 SD, n = 6). Methane concentration in the top inflow of the seawater medium was not detectable. In the top outflow, methane slowly increased in the medium over the course of the experiment. This medium represents a 1:4 (HFC) and 1:40 (LFC) mixture of seepage and seawater medium. In the LFC, methane concentration in the outflow increased to a maximum of ~2.6 µmol L^{-1} (Fig. 7A) after 169 days and slightly decreased to values around 1.9 µmol L^{-1} until flow rates were swapped. A methane concentration of 2.6 µmol L^{-1} in the mixed top water column corresponds to approximately 23 µmol L^{-1} at the sediment-water interface, assuming that no methane was consumed in the water column. In the HFC, methane concentrations in the mixed supernatant water column were two times higher compared with the LFC (2.2–4.1 µmol L^{-1}, after 32–303 days runtime, respectively, Fig. 7B) corresponding to 230 µmol L^{-1} at the sediment-water interface, and continuously increased until flow rates were swapped. In the HFC, a plateau in methane concentration was not reached, but we expect the plateau to be reached after 100–200 days based on the experimental trend line. Methane effluxes calculated from methane concentration measurements reached maxima of 0.033 and 0.065 mmol $m^{-2} d^{-1}$ (Fig. 7C, D) for the LFC and HFC, respectively. The outflow contained only a small fraction of that predicted from the inflow methane concentration. If we assume that the missing methane was consumed by methanotrophs, we can estimate AOM rates of 0.29 mmol $m^{-2} d^{-1}$ and 3.15 mmol $m^{-2} d^{-1}$ (Fig. 7E, F) for the LFC and HFC, respectively.

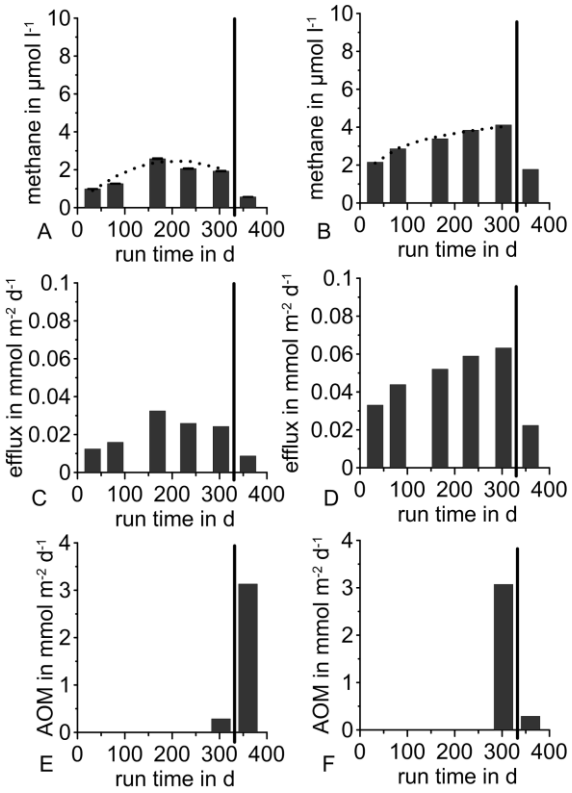

Figure 7: Methane concentration (µmol L^{-1}) in the outflow (A, B), methane efflux (mmol m^{-2} d^{-1}; C,D), and AOM rate (mmol m^{-2} d^{-1}) of the system before and after swapping: (A, C, E) low flow core (LFC) and (B, D, F) high flow core (HFC) from Eckernförde Bay. Vertical lines mark the moment of fluid flow swapping (low flow -> high flow and vice versa). Error bars (A,B) show standard deviations of three repeated gas chromatographic measurements; the first two data points represent single measurements. Dotted lines represent the trendline (low flow regime: $5 \times 10^{-6} \times t_{runtime}^{2} + 0.02\ t_{runtime} + 0.285$, $r^2 = 0.825$; high flow regime: $0.8576 \times \ln(t_{runtime}) - 0.8662$, $r^2 = 0.987$) of methane concentration development until swapping.

Evolution of geochemical gradients (day 310 to 376)

After swapping the flow velocities (11.2 cm y^{-1} was changed to 112.1 cm y^{-1} and vice versa), the reduced flow was traceable in the former HFC (from now on called the “new low flow core” = NLFC) after 40 days by a decrease in penetration of bromide at the bottom (compare Fig. 6P and Fig. 8D). Accordingly, sulfate penetrated deeper into the sediment from the overlying water column (compare Fig. 6 and Fig. 8D). In contrast, the former LFC (from now on called the “new high flow core” = NHFC) showed a pulse of bromide concentration in the lower 12 cm of up to 300 µmol L^{-1}. Consequently, sulfate decreased at these depths and reached values lower than 7 mmol L^{-1} at the bottom of the core (Fig. 8A).

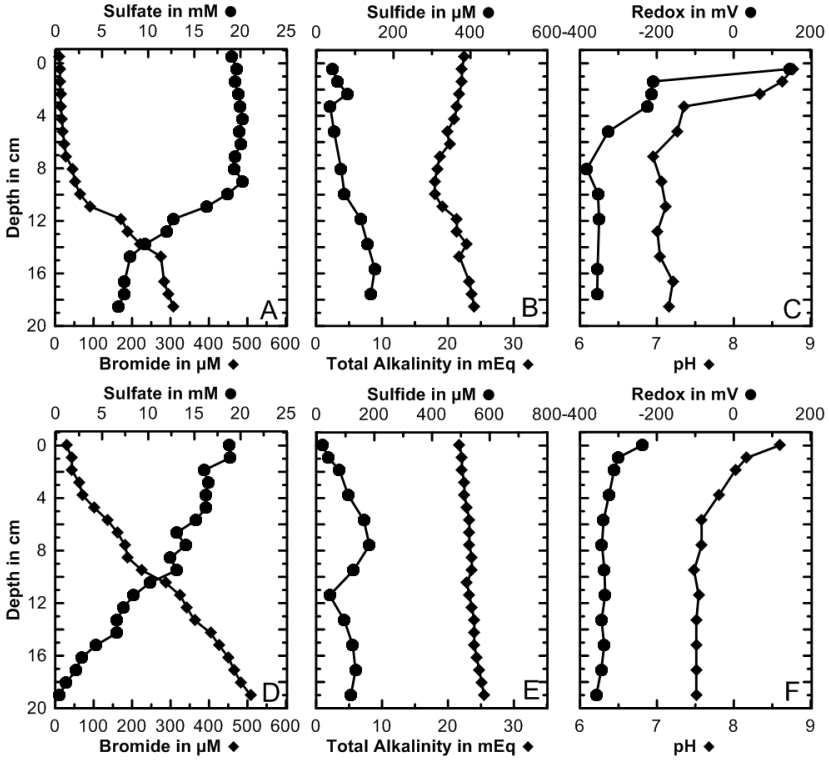

Figure 8: Geochemical parameters measured in the sediment of the new high flow core (NHFC; A-C) and new low flow core (NLFC; D-F) after 360 days runtime, i.e., 50 days after swapping of the flow rate. Shown are the porewater profiles of sulfate, bromide (A and D), sulfide, total alkalinity (B and E), redox potential, and pH (C and F).

Sulfide concentrations in the NHFC (Fig. 8B) decreased compared with the prior situation (compare Fig. 5P, 303 days runtime). In the upper part (0 to 11 cm), sulfide values ranged between 43 and 63 µmol L^{-1}, and between 73 and 151 µmol L^{-1} below 11 cm. The transition of these two sections corresponded to the steepest bromide increase from below, which delineates the interface of the upwardly migrating fluid pulse created after swapping of the flow rates. In the NLFC, two sulfide peaks (181 and 134 µmol L^{-1}) established at 8 and 17 cm sediment depth, respectively, and were separated by a minimum (44 µmol L^{-1}) at 11 cm (Fig. 8E).

TA decreased from the top of the NHFC (22.5 meq L^{-1}; Fig. 8B) to a minimum of 18 meq L^{-1} at 11 cm sediment depth. Below 11 cm, TA increased toward the bottom of the core (24 meq L^{-1}) corresponding to the slight increase of sulfide, i.e., indicating AOM activity. In the NLFC, TA increased linearly from 22.8 meq L^{-1} (Fig. 8E) at the top of the sediment to 25 meq L^{-1} at the bottom of the core.

In the NHFC core, pH was 8.77, similar to the pH value at the sediment water interface before the flow rate was increased. Below 4 cm, the pH decreased and ranged between 7.35 and 6.95 (Fig. 8C). In accordance with reduced sulfide concentration, the decrease in pH can be explained by iron sulfide precipitation (Preisler et al. 2007) (see above). In the NLFC, pH was increased to 8.60 at the top and stable around 7.5 below 6 cm sediment depth.

After swapping of the flow rates, a positive redox potential of 147 mV (Fig. 8C) at the sediment surface (0-1 cm) of the NHFC indicated the oxidation of sediment (Schulz 2000). The oxidation was probably a result of temporary oxygen intrusion, which was demonstrated by the pink color of the oxygen indicator resazurin in the supernatant water column. Below the sediment surface, redox potential decreased quickly to -200 mV at 2 cm depth and to less than –350 mV below 9 cm sediment depth. In the NLFC, redox potential was around –238 mV (Fig. 8F) close to the sediment surface and between –300 mV (2 cm) and –354 mV (bottom) in the remaining sediment core.

The methane concentration in the outflow of the SLOT system decreased in both cores 50 days after swapping the flow regimes. The reduced advective flow probably led to an eased methane transport in the NLFC (methane concentration 1.8 µmol L^{-1}; Fig. 7B, and methane efflux 0.022 mmol $m^{-2} d^{-1}$ Fig. 7D). Methane concentration in the NHFC was reduced from 1.9 to 0.6 µmol L^{-1} (Fig. 7B) and the according methane efflux was reduced from 0.029 to 0.009 mmol $m^{-2} d^{-1}$ (Fig. 7C). Here, we had rather expected an increase of methane in the outflow after increasing the methane flux. We can only speculate about the reasons for this unexpected behavior. Perhaps the incubation time was too short to allow the new methane front to reach the sediment-water interface. Another possibility may be that the sudden flow increase affected the physical properties of the sediment, for example by increasing compaction, which retarded the methane response in the outflow. AOM rates calculated via methane differences in in- and outflow were 3.132 and 0.290 mmol $m^{-2} d^{-1}$ (Fig. 7E, F) for the NHFC and NLFC, respectively.

Biogeochemical gradients in the sediment after experiment termination

After 376 days total runtime, the experiment was stopped and both cores were sliced and subsampled. Immediately before slicing, porewater was extracted to analyze for sulfate, sulfide, and nitrate concentrations.

Sulfate concentration profiles were similar in both cores, decreasing from the top (19 mmol L^{-1}) to the bottom (5.8 mmol L^{-1} and 2.2 mmol L^{-1} for the NHFC and NLFC, respectively; Fig. 9B and E). Compared with the previous measurement point 24 days earlier, sulfate was further displaced toward the top in the NHFC and penetrated deeper into the sediment in the NLFC. The sulfide profile of the NHFC showed a clear peak at 10 cm (560 µmol L^{-1}; Fig. 9C), compared with previously slightly increased sulfide values between 10-16 cm (160 µmol L^{-1}). The sulfide profile of the NLFC was similar to the previous one (maximum at 7 cm, 183 µmol L^{-1}) with a peak at 6 cm (228 µmol L^{-1}; Fig 9F). Nitrate concentrations were only measured at the bottom (3.6 and 3.7 µmol L^{-1} in the NLFC and NHFC, respectively) and at the top (4.4 µmol L^{-1} in the NLFC).

Porewater methane concentrations in the two sediment cores increased from top to bottom, i.e., from 4.5 to 21 µmol L^{-1} (Fig. 9A) in the NHFC and from 4 to 9.5 µmol L^{-1} (Fig. 9D) in the NLFC. However, even highest methane concentrations at the bottom of the cores (21 µmol L^{-1}) represented only a small fraction of the input concentration (930 µmol L^{-1}), which will be further discussed in section “Functionality of the SLOT system.”

The core from the NHFC showed no clear depth trend in sulfate reduction activity. Sulfate reduction rates fluctuated between 5.0 and 23.7 nmol cm^{-3} d^{-1} (Fig. 9B). In the NLFC, sulfate reduction was highest in the upper 9 cm (up to 28.9 nmol cm^{-3} d^{-1}, 4-5 cm; Fig. 9E) and decreased to less than 9 nmol cm^{-3} d^{-1} below. During the incubation, sulfate concentrations were relatively low below 9 cm (0.07-2 mmol L^{-1} between 129-310 days run time, Fig. 6G, J, M, and P), which likely explain the lower sulfate reduction rates in this part of the core. Another reason for the lower activity compared with the NHFC could be heterogeneous distribution of organic matter and correlated organoclastic sulfate reduction in Eckernförde Bay sediments as a result of bioturbation (Treude et al. 2005; Bertics et al. 2013). The most prominent bioturbators in Kiel Bight are polychaetes (Graf et al. 1983; Meyer-Reil 1983). These and other organisms add to the

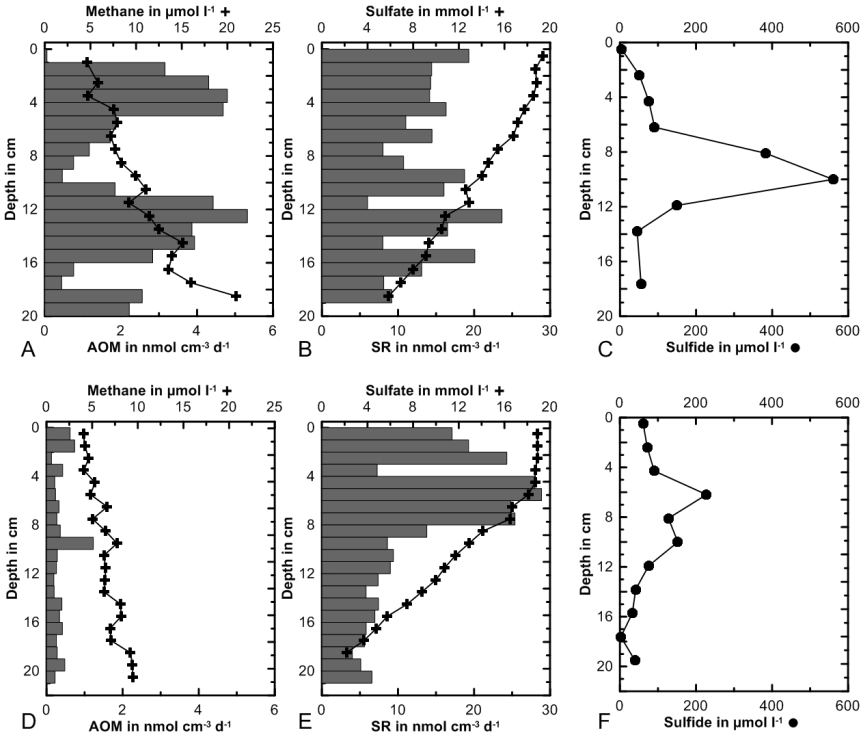

Figure 9: Biogeochemical parameters in the new high flow core (NHFC; AC) and new low flow core (NLFC; D-F) after slicing (376 days runtime). Porewater profiles of methane (A, D, cross), sulfate (B, E, cross), sulfide (C, F, dots), and results of the radiotracer measurements of AOM (A, D, bars) and sulfate reduction (SR) (B, E, bars) are shown.

heterogeneous distribution of organic matter in the sediment, which is retained after sediment sampling (Bertics et al. 2013; Dale et al. 2013). Furthermore, the death of infauna after deoxygenation could provide additional inhomogeneously distributed sources of organic matter inside the core. Calculated areal rates of sulfate reduction integrated over the entire sediment depth were similar for both cores: 2.6 mmol m^{-2} d^{-1} in the NHFC (0-19 cm) and 2.7 mmol m^{-2} d^{-1} in the NLFC (0-21 cm). In general, AOM rates were found to be much lower compared with sulfate reduction. AOM rates were 0.06-5.32 nmol cm^{-3} d^{-1} (Fig. 9A) and 0.13-1.23 nmol cm^{-3} d^{-1} (Fig. 9E) in the NHFC and NLFC, respectively. Areal AOM rates were 0.5 and 0.1 mmol m^{-2} d^{-1}, respectively. A high ratio of sulfate reduction to AOM rates might reflect a high proportion of organoclastic sulfate reduction in the cores (see above). Generally, sulfate reduction and AOM rates were lower by almost an order of magnitude relative to those measured in previous studies in Eckernförde Bay (4.1-10.5 mmol m^{-2} d^{-1} sulfate reduction, 0.5-1.5 mmol m^{-2} d^{-1} AOM for the upper 25 cm, Treude et al. 2005). The sediments used in our experiment were sampled from 0-21 cm below sea floor (bsf), which is slightly above the

reported main AOM zone of 20 to 25 cmbsf (Treude et al. 2005). Hence, lower AOM rates might be correlated with a lower initial abundance of AOM organisms in the sediment. We think that a significant enrichment of ANME microbes over the entire core was not likely, because activity and growth was probably restricted to a very narrow SMTZ. Other experiments report doubling times of ANMEs between 1.1-7.5 months, but these were achieved under ideal methane/sulfate conditions (Girguis et al. 2005; Nauhaus et al. 2007; Krüger et al. 2008; Meulepas et al. 2009).

Sediment porosity decreased from the top (0.88 in both cores) to the bottom (0.78 and 0.82; Fig. 10C and F) of the NHFC and NLFC, respectively, and were similar to values determined in previous studies (Treude et al. 2005; Bertics et al. 2013; Dale et al. 2013). Total carbon (TC) was mostly controlled by the organic fraction (TOC) (Fig. 10A and D). Inorganic carbon (TIC) sources constituted only a minor component of the TC (0.02-0.33% w/w). One exemption was the depth section 5-11 cm in the NHFC, where TIC revealed a distinct peak of 0.57% w/w. This carbonate accumulation might have been present before the experiment. However, porewater profiles of bromide and sulfate from the 360 days runtime indicated that the experimentally created seepage front was located at 11 cm depth (Fig. 8A), indicating the zone of highest AOM activity, which could cause precipitation of authigenic carbonates. On average, the TIC content was higher in the NHFC (0.208 ± 0.162% w/w) compared with the NLFC (0.071 ± 0.034% w/w).

Total sulfur (TS) contents were on average lower in the NHFC (1.36 ± 0.23% w/w; Fig. 10B) compared with the NLFC (1.618 ± 0.13% w/w; Fig 10E), and was constant over the entire depth in both cores, except for a peak in the lower part (1.93% w/w, 15 cm, NHFC; 1.90% w/w, 19 cm NLFC). TS values of 1.5-2% w/w were high, but common for sediments with high C-org contents (Leventhaler 1983, 1995, Rullköter 2006). The differences in TS between cores may be indicative of precipitation of metal sulfides caused by high sulfate reduction rates in the NLFC.

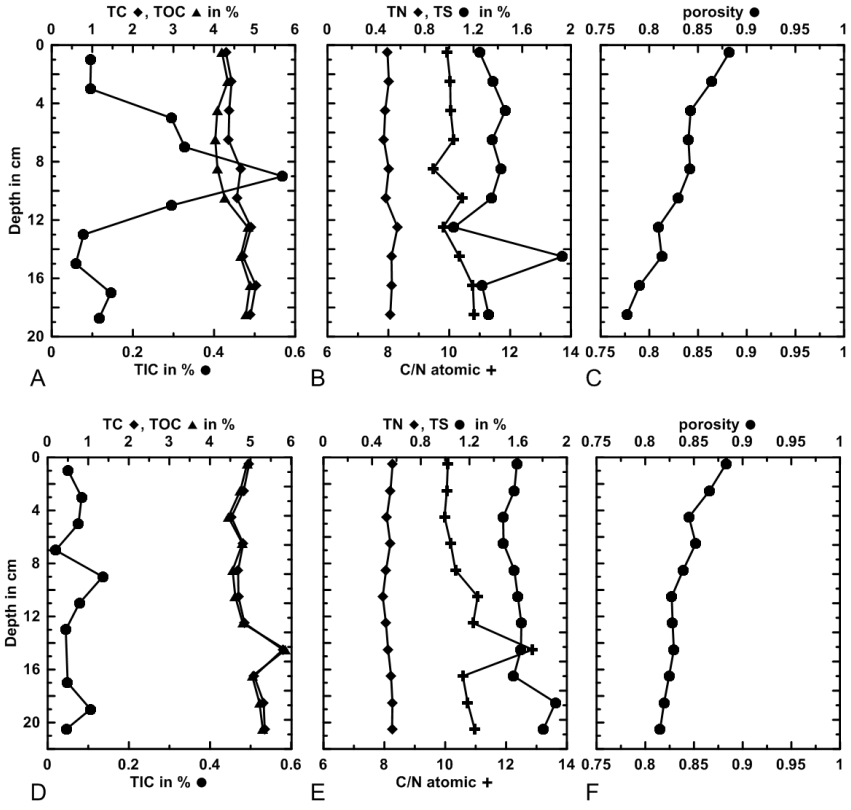

Figure 10: Sediment solid phase parameters measured in the sediment core of the new high flow core (NHFC; A-C) and new low flow core (NLFC; D-F): (A and D) Total carbon content (TC), total organic carbon content (TOC), total inorganic carbon content (TIC) in %w/w of the dry weight; (B and E) total nitrogen (TN), total sulfur (TS) in %w/w of the dry weight, C/N ratio; (C and F) porosity of the sediment.

Total nitrogen (TN) and C/N values were relatively consistent over depth in both cores (Fig. 10B and E). TN was between 0.46 and 0.59, and the C/N values were between 9.5-10.8 with an exemption value of 12.8 at 15 cm in the NLFC, which was the result of a corresponding high TOC value. TN and C/N values were in accordance with ex situ data from the first 2 m sediment depth of a previous study at Eckernförde Bay (Whiticar 2002).

Assessment

Functionality of the SLOT system

The aim of the present study was to develop a sediment flow-through system to mimic natural fluid flow conditions found at methane seeps using intact sediment cores, and to enable continuous measurements of biogeochemical parameters over the entire core to

monitor the evolution of parameters associated with changes in fluid and methane flux. Overall, the system revealed good functionality and performance. Rhizones and microsensors provided an easy method to sample and measure changes and reactions inside the core, enabling a monitoring of various parameters during the experiments. With the pumping system, the balance between diffusion of “seawater” and advective transport of seepage medium was successfully adjusted. With this approach, it was possible to mimic real seep conditions. The two reservoir systems provided a relatively simple approach to supply almost methane-saturated media, similar to the study of Wegener and Boetius (2009).

By tracking the bromide tracer, we demonstrated that (a) methane-enriched seepage fluid was successfully advected from the bottom of the core, (b) seepage fluid migrated and dispersed trough the pore space like under natural conditions without system-induced channelizing, and (c) seepage and seawater medium developed a chemocline, representative for a sulfate-methane transition zone, inside the sediment. It should be highlighted that in natural sediments, fluid transport is rarely homogenous, due to heterogeneities in pore space, size, and distribution. Increased fluid flow may reinforce different fluid pathways inside the sediment and result in higher permeability. However, fluid flow through the sediments of both cores appeared relatively homogenous, indicated by the development of steep porewater gradients. Only one sulfate profile (NHFC, Fig. 5D) indicated a fluid bypass after 80 days, which later disappeared again, probably temporarily caused by the sampling procedures with rhizones. Each sampling procedure with either microsensors or rhizones may cause disturbances in the system. Hence, it was fundamental to find optimal sample intervals and volumes, between which the system was able to “recover” after sampling. However, not only the individual sampling volumes per depth section but also the total amount of porewater collected over the entire core, seems to influence the profile of dissolved parameters. For instance, when in total 96 cm^3 porewater were withdrawn from the NLFC directly before core slicing (376 days), the sulfate penetration depth was higher and the chemocline was flattened (Fig. 8D) compared with the previous sampling (Fig. 9E), indicating that the total sample volume was too high leading to a smoothening of the profiles. We calculated a dilution of 1:0.2 (porewater : seawater medium) for the entire core and this

sampling procedure. The smoothening effect was assumed to be less pronounced during the normal (39 cm^3 porewater volume) sampling procedure (dilution 1:0.08). The dilution effect can be especially strong in the upper centimeter of the core, where the replacing fluid is directly drawn from the overlying seawater causing an increase in sulfate penetration.

Methane measured in samples taken after core slicing could not confirm the input methane concentration (930 µmol L^{-1}), which entered the sediment cores at the bottom. Sampling procedures, including porewater extraction and long sampling times during core slicing, probably facilitated major losses of methane before fixation of samples. The use of rhizones could have different effects on dissolved methane concentrations in the sediment core. First, it is possible that disproportional high amounts of methane were lost due to degassing by the underpressure generated during rhizon sampling. Second, the withdrawal of too large porewater sample volumes (see above), at the end of the experiment, probably diluted the methane profile, especially since fluid could only be replenished from the overlying methane-free seawater medium (connection to seepage medium was closed). We can exclude that methane was lost between the inflow (fast connector) and the sediment core, i.e., in the distribution container. No leaks were detected in this intercept, which was tested by applying under- and overpressure. The distribution container had a volume of ~ 90 mL and was located directly below the filter, which separated the core from the medium. Even during porewater extraction, no oxygen intrusion at the caps or through liner and silicon was observed (confirmed by resazurin). Hence, a methane loss through this pathway seems implausible.

In our approach, AOM rates were derived from in- and outflow differences of methane concentrations during incubations, i.e., before (303 days) and after (360 days) swapping of the flow rates, and additionally via radiotracer measurements after termination of the experiment (376 days). In comparison, AOM rates measured with radiotracers in the NHFC and NLFC, respectively, at day 376 reached only ~16% and ~35% of the rates determined at day 360 via in- and outflow. Lower AOM rates derived from radiotracer measurements could be a result of methane losses during porewater sampling (see above), which caused lower methane concentrations and hence lower methane turnover (Nauhaus et al. 2002). It might, therefore, be more reliable to use the AOM rates that

were calculated from the difference of methane in in- and outflow samples, which remained unaffected by this artifact. Alternatively, the volume of porewater sampling could be reduced, to avoid methane losses, or the time between final porewater and sediment sampling could be increased to allow the system to reestablish the original methane gradient. However, for the NHFC, it should be considered that AOM rates calculated via in- and outflow could also be overestimated, because the applied runtime was probably insufficient for the new methane front to reach the sediment surface (hydrological residence time of the fluid = 104.5 days). A longer runtime after swapping is, therefore, recommendable.

Comparison with previous systems

Previous systems were developed to investigate the growth rate of AOM-related microbes (Girguis et al. 2003; Meulepas et al. 2009), the kinetics of the AOM reaction (Wegener and Boetius 2009; Deusner et al. 2010; Zhang et al. 2010; Wankel et al. 2012) or to enrich samples with methanotrophs (Meulepas et al. 2009). These systems idealized, and sometimes optimized, the conditions for microbial activity. Hence, in previous systems, higher turnover rates were expected. Technical differences between the present and previous systems are (1) hydrostatic pressure and related methane concentrations, (2) supply direction of methane and sulfate, (3) sample type (slurry or intact sediments), (4) steady-state or non–steady-state conditions.

Some of the referred systems incubated under high hydrostatic pressure (Deusner et al. 2010; Zhang et al. 2010), and thereby, produced higher methane concentrations. Consequently, AOM rates were much higher under these conditions compared with our study. However, high-pressure systems with gases require high security standards and complicate subsampling. Porewater extractions and microsensor measurements from pressurized intact sediment cores are, to our knowledge, still not feasible.

In all of the previous systems, sulfate and methane were supplied in one direction, which was different from the natural settings and could mask effects of high fluid flow or thermodynamic limitations of reactants. Only Wegener and Boetius (2009) investigated limitations of sulfate and methane, but still in one flow direction.

With the exemption of the AMIS (Girguis et al. 2003) and the thermal system by Wankel et al. 2010, most previous systems used homogenized sediment slurries for their surveys. Meulepas et al. (2009), Deusner et al. (2010), and Zhang et al. (2010) additionally stirred their incubation to provide ideal substrate supply. This approach is optimal for studying physiological characteristics of AOM organisms but not for studying activity and responses under natural sediment conditions. In AMIS, intact natural sediment cores were used; however, admittedly these cores were periodically disturbed by the sampling procedures for rate and other determinations. In our system, disturbances of the sediment structure were kept to a minimum by the use of thin microsensors and permanently installed rhizones.

In the present study, a non–steady-state situation was in the focus, i.e., the direct response of anaerobic methanotrophs to changes in the fluid regime in their natural sedimentary environment was investigated. Only the pulse experiment of Wegener and Boetius (2009) and the AMIS of Girguis et al. (2005) created non–steady-state conditions, however, the response of the AOM community and related biogeochemical processes could not be followed inside the cores of these systems.

Most importantly, all previous systems share the limitation that only the in- and outflow ports of the system can be sampled and analyzed. Hence, these systems basically represent black boxes, because biogeochemical developments inside the reaction chamber or sediment core remain unknown. Our investigation with the SLOT system revealed that conditions inside sediment cores were inhomogeneous and changed with time, and highlight the importance of monitoring educts (sulfate) and products (sulfide and TA) of AOM, as well as directly related parameters such as pH and redox potential. Besides AOM, many other reactions are indirectly connected to methane or fluid flow in-seep sediments. These reactions include the precipitation of authigenic carbonates (Luff and Wallmann 2003; Han et al. 2004; Karaca et al. 2010) and metal sulfides (Morse et al. 2002; Orcutt et al. 2011), changes in porosity and permeability (Tenthorey and Scholz 1998; Zhang et al. 2010), as well as sulfide oxidation (Glud et al. 2004; Beer et al. 2006; Preisler et al. 2007). Specifically, sulfide oxidation by chemoautotrophic organisms can change the supply of sulfate (Glud et al. 2007), as well as the depth of the SMTZ (Preisler et al. 2007). All these effects are missed without monitoring

porewater and sediment parameters over the entire sediment core. Herefore, the SLOT system provides a more realistic view on these effects and offers new opportunities to study such processes in depth to answer these long-standing questions.

Comments and recommendations

Here, we highlight some important characteristics of the SLOT system and provide recommendations for future rebuilds and developments.

Bromide is a suitable tracer for the advecting fluid for many reasons: (1) it is easy to analyze with other anions by ion chromatography, hence no additional sample is needed; (2) it is a natural component of the seawater, but to our knowledge no essential nutrient (microbially inert); (3) it does not change any parameters in the seepage medium (in case of salinity it is replaced with chloride). Monitoring porewater migration via bromide further helps to make a decision about the total runtime and termination of the experiment.

The SLOT system stimulates a lot more processes than only AOM. Especially, alterations in TA profiles indicate precipitation and dissolution processes. To better use this parameter for the monitoring of AOM and sulfate reduction dynamics, the initial TA concentration (~30 meq L^{-1}) in the medium could be reduced to seawater level (~2.3 meq L^{-1}).

Consistency of the medium composition over the course of the entire experiment is a prerequisite for correct budgeting. During our experiments, we observed the precipitation of crystals (probably $CaCO_3$ and metal sulfides) in the medium as well as fluctuations of methane (± 110 μmol L^{-1}) and probably sulfide concentrations. These fluctuations can influence the budgets of the system and might change the media conditions, for e.g., pH by carbonate precipitation. An advanced stirred or percolated media reservoir would be an useful improvement for the system, similar to the systems of Deusner et al. (2010), Zhang et al. (2010), Wankel et al. (2012), and Girguis et al. (2003, 2005). Stirred media can prevent precipitation of salts, carbonates and metal sulfides, while percolation warrants better homogenous methane dissolution.

The installed sampling holes (4 mm diameter) allow a subsampling of small sediment sub-samples during experiments, which could enable the investigation of changes in the microbial community structure or cell abundance over the course of the experiment via molecular analyses. However, because this approach could change sediment properties and stimulate fluid channelizing, it is not advisable to use it together with advective transport experiments.

Many other applications for the SLOT system are possible. For example, other benthic seepage systems could be simulated, e.g., seepage of brines, hydrothermal fluids, or petroleum. Anoxic seawater could be exchanged by oxygenated seawater to investigate the full spectrum of biogeochemical reactions at the sediment-water interface. Additionally, sediment cores could be installed without advective fluid flow to study, e.g., the fate of organic matter or oil spills that settle on the sediment surface. Seawater media of the system can be altered easily to study, e.g., the effects of different electron acceptors like nitrate, manganese, or iron.

Acknowledgments

We thank the crew of the RC "Littorina" for technical support during sediment collection. We further thank the Technology and Logistic Centre at GEOMAR as well as S. Reischke for support during the technical realization of the SLOT system. Special thanks go to B. Domeyer, A. Bleyer, and R. Suhrberg for analytical support. K. Kretschmer is thanked for support during system maintenance. R. Schmitz-Streit is thanked for scientific input during the development of the system. This project was financed through the Collaborative Research Center (SFB) 574 "Volatiles and Fluids in Subduction Zones" and the Cluster of Excellence "The Future Ocean" funded by the German Research Foundation (DFG). This publication is contribution no. 269 of the SFB 574 “Volatiles and Fluids in Subduction Zones” at Kiel University.

References:

Abegg, F., and A. L. Anderson. 1997. The acoustic turbid layer in muddy sediments of Eckernförde Bay, Western Baltic: methane concentration, saturation and bubble characteristics. Marine Geology **137**: 137–147.

Aiello, I. W. 2005. Fossil seep structures of the Monterey Bay region and tectonic/structural controls on fluid flow in an active transform margin. Palaeogeography, Palaeoclimatology, Palaeoecology **227**: 124–142.

Anderson, A. L., F. Abegg, J. Hawkins, M. E. Duncan, and A. P. Lyons. 1998. Bubble populations and acoustic interaction with the gassy floor of Eckernförde Bay. Continental Shelf Research **18**: 1807–1838.

Bange, H., K. Bergmann, H. Hansen, A. Kock, R. Koppe, F. Malien, and C. Ostrau. 2010. Dissolved methane during hypoxic events at the Boknis Eck time series station (Eckernförde Bay, SW Baltic Sea). Biogeosciences **7**: 1279–1284.

Beal, E. J., C. H. House, and V. J. Orphan. 2009. Manganese- and iron-dependent marine methane oxidation. Science **325**: 184–187.

Beer, D. De, E. Sauter, and H. Niemann. 2006. In situ fluxes and zonation of microbial activity in surface sediments of the Håkon Mosby Mud Volcano. Limnology and Oceanography **51**: 1315–1331.

Bertics, V. J., C. R. Löscher, I. Salonen, A. W. Dale, R. A. Schmitz, and T. Treude. 2013. Occurrence of benthic microbial nitrogen fixation coupled to sulfate reduction in the seasonally hypoxic Eckernförde Bay, Baltic Sea. Biogeosciences **10**: 1243–1258.

Biastoch, A., T. Treude, L. H. Rüpke, U. Riebesell, C. Roth, E. B. Burwicz, W. Park, M. Latif, C. W. Böning, G. Madec, and K. Wallmann. 2011. Rising Arctic Ocean temperatures cause gas hydrate destabilization and ocean acidification. Geophysical Research Letters **38**: 1–5.

Billerbeck, M., U. Werner, L. Polerecky, E. Walpersdorf, D. de Beer, and M. Huettel. 2006. Surficial and deep pore water circulation governs spatial and temporal scales of nutrient recycling in intertidal sand flat sediment. Marine Ecology Progress Series **326**: 61–76.

Boetius, A., K. Ravenschlag, C. J. Schubert, D. Rickert, F. Widdel, A. Gieseke, R. Amann, B. B. Jørgensen, U. Witte, O. Pfannkuche, and B. B. Jorgensen. 2000. A marine microbial consortium apparently mediating anaerobic oxidation of methane. Nature **407**: 623–626.

Borowski, W., C. Paull, and W. Ussler. 1996. Marine pore-water sulfate profiles indicate in situ methane flux from underlying gas hydrate. Geology **24**: 655–658.

Borowski, W. S. 2004. A review of methane and gas hydrates in the dynamic, stratified system of the Blake Ridge region, offshore southeastern North America. Chemical Geology **205**: 311–346.

Borowski, W. S., C. K. Paull, and I. W. Ussler. 1999. Global and local variations of interstitial sulfate gradients in deep-water, continental margin sediments: Sensitivity to underlying methane and gas hydrates. Marine Geology **159**: 131–154.

Boudreau, B. P., B. S. Gardiner, and B. D. Johnson. 2001. Rate of growth of isolated bubbles in sediments with a diagenetic source of methane. Limnology and Oceanography **46**: 616–622.

Buffett, B., and D. Archer. 2004. Global inventory of methane clathrate: sensitivity to changes in the deep ocean. Earth and Planetary Science Letters **227**: 185–199.

Burwicz, E., L. Rüpke, and K. Wallmann. 2011. Estimation of the global amount of submarine gas hydrates formed via microbial methane formation based on numerical reaction-transport modeling and a novel parameterization of Holocene sedimentation. Geochimica et Cosmochimica Acta **75**: 4562–4576.

Cline, J. 1969. Spectrophotometric determination of hydrogen sulfide in natural waters. Limnology and Oceanography **14**: 454–458.

Cordes, E. E., M. a Arthur, K. Shea, R. S. Arvidson, and C. R. Fisher. 2005. Modeling the mutualistic interactions between tubeworms and microbial consortia. PLoS biology **3**: e77.

Dale, A., P. Regnier, and P. Van Cappellen. 2006. Bioenergetic controls on anaerobic oxidation of methane (AOM) in coastal marine sediments: A theoretical analysis. American Journal of Science **306**: 246–294.

Dale, A. W., V. J. Bertics, T. Treude, S. Sommer, and K. Wallmann. 2013. Modeling benthic-pelagic nutrient exchange processes and porewater distributions in a seasonally-hypoxic sediment: evidence for massive phosphate release by Beggiatoa? Biogeosciences **10**: 629–651.

Deusner, C., V. Meyer, and T. G. Ferdelman. 2010. High-pressure systems for gas-phase free continuous incubation of enriched marine microbial communities performing anaerobic oxidation of methane. Biotechnology and Bioengineering **105**: 524–33.

Ettwig, K. F., M. K. Butler, D. Le Paslier, E. Pelletier, S. Mangenot, M. M. M. Kuypers, F. Schreiber, B. E. Dutilh, J. Zedelius, D. de Beer, J. Gloerich, H. J. C. T. Wessels, T. van Alen, F. Luesken, M. L. Wu, K. T. van de Pas-Schoonen, H. J. M. Op den Camp, E. M. Janssen-Megens, K.-J. Francoijs, H. Stunnenberg, J. Weissenbach, M. S. M. Jetten, and M. Strous. 2010. Nitrite-driven anaerobic methane oxidation by oxygenic bacteria. Nature **464**: 543–8.

Fischer, D., H. Sahling, K. Nöthen, G. Bohrmann, M. Zabel, and S. Kasten. 2012. Interaction between hydrocarbon seepage, chemosynthetic communities, and bottom water redox at cold seeps of the Makran accretionary prism: insights from habitat-specific pore water sampling and modeling. Biogeosciences **9**: 2013–2031.

Füri, E., D. R. Hilton, M. D. Tryon, K. M. Brown, G. M. McMurtry, W. Brückmann, and C. G. Wheat. 2010. Carbon release from submarine seeps at the Costa Rica fore arc: Implications for the volatile cycle at the Central America convergent margin. Geochemistry Geophysics Geosystems **11**, doi:10.1029/2009GC002810

Girguis, P. R., A. E. Cozen, and E. F. Delong. 2005. Growth and Population Dynamics of Anaerobic Methane-Oxidizing Archaea and Sulfate-Reducing Bacteria in a. Applied and Environmental microbiology **71**: 3725–3733.

Girguis, P. R., V. J. Orphan, S. J. Hallam, and E. F. Delong. 2003. Growth and Methane Oxidation Rates of Anaerobic Methanotrophic Archaea in a Continuous-Flow Bioreactor. Applied and Environmental Microbiology **69**: 5472–5482.

Glud, R. N., P. Berg, H. Fossing, and B. B. Jørgensen. 2007. Effect of the diffusive boundary layer on benthic mineralization and O2 distribution: A theoretical model analysis. Limnology and Oceanography **52**: 547–557.

Glud, R. N., S. Rysgaard, T. Fenchel, and P. H. Nielsen. 2004. A conspicuous H2S-oxidizing microbial mat from a high-latitude Arctic fjord (Young Sound, NE Greenland). Marine Biology **145**: 51–60.

Graf, G., R. Schulz, R. Peinert, and L. Meyer-Reil. 1983. Benthic response to sedimentation events during autumn to spring at a shallow water station in the Western Kiel Bight I. Analyses of processes om a community level. Marine Biology **77**: 235–246.

Grasshoff, K., M. Erhardt, and K. Kremling. 1983. Methods of seawater analysis, Wiley-VCH, Weinheim.

Han, X., E. Suess, H. Sahling, and K. Wallmann. 2004. Fluid venting activity on the Costa Rica margin: new results from authigenic carbonates. International Journal of Earth Sciences **93**: 596–611.

Henrys, S., M. Reyners, I. Pecher, S. Bannister, Y. Nishimura, and G. Maslen. 2006. Kinking of the subducting slab by escalator normal faulting beneath the North Island of New Zealand. Geology **34**: 777.

Hensen, C., M. Nuzzo, E. Hornibrook, L. M. Pinheiro, B. Bock, V. H. Magalhães, and W. Brückmann. 2007. Sources of mud volcano fluids in the Gulf of Cadiz—indications for hydrothermal imprint. Geochimica et Cosmochimica Acta **71**: 1232–1248.

Hensen, C., K. Wallmann, M. Schmidt, C. R. Ranero, and E. Suess. 2004. Fluid expulsion related to mud extrusion off Costa Rica—A window to the subducting slab. Geology **32**: 201.

Hinrichs, K., and A. Boetius. 2002. The Anaerobic Oxidation of Methane: New Insights in Microbial Ecology and Biogeochemistry, p. 457–477. *In* G. Wefer, B. Billett, D. Hebbeln, B.B. Jørgensen, M. Schlüter, and T.C.E. Van Weering [eds.], Ocean margin systems. Springer-Verlag Berlin Heidelberg.

Ivanenkov, V. N., and Y. I. Lyakhin. 1978. Determination of total alkalinity in seawater, p. 110–114. *In* O.K. Bordovsky and V.N. Ivanenkov [eds.], Methods of Hydrochemical Investigations in the Ocean. Nauka.

Iversen, N., and B. B. Jørgensen. 1985. Anaerobic methane oxidation rates at the sulfate-methane transition in marine sediments from Kattegat and Skagerrak (Denmark). Limnology and Oceanography **30**: 944–955.

Jackson, D., K. Williams, T. F. Wever, C. T. Friedrichs, and L. D. Wright. 1998. Sonar evidence for methane ebullition in Eckernförde Bay. Continental Shelf Research **18**: 1893–1915.

Jeroschewski, P., C. Steuckart, and M. Kühl. 1996. An amperometric microsensor for the determination of H2S in aquatic environments. Analytical Chemistry **68**: 4351–4357.

Jørgensen, B. B. 1978. A comparison of methods for the quantification of bacterial sulfate reduction in coastal marine sediments. Geomicrobiology Journal 37–41.

Jørgensen, B. B., and D. Nelson. 2004. Sulfide oxidation in marine sediments: Geochemistry meets microbiology, p. 63–81. *In* J.P. Amend, K.J. Edwards, and T.W. Lyons [eds.], Sulfur Biogeochemistry - Past and Present. Geological Society of America.

Joye, S. B., A. Boetius, B. N. Orcutt, J. P. Montoya, H. N. Schulz, M. J. Erickson, and S. K. Lugo. 2004. The anaerobic oxidation of methane and sulfate reduction in sediments from Gulf of Mexico cold seeps. Chemical Geology **205**: 219–238.

Kallmeyer, J., T. G. Ferdelman, A. Weber, H. Fossing, B. B. Jørgensen, and M. M. Microbiology. 2004. A cold chromium distillation procedure for radiolabeled sulfide applied to sulfate reduction measurements. Limnology and Oceanography: Methods **2**: 171–180.

Karaca, D., C. Hensen, and K. Wallmann. 2010. Controls on authigenic carbonate precipitation at cold seeps along the convergent margin off Costa Rica. Geochemistry Geophysics Geosystems **11**: 1–19.

Knittel, K., and A. Boetius. 2009. Anaerobic oxidation of methane: progress with an unknown process. Annual review of microbiology **63**: 311–34.

Krüger, M., M. Blumenberg, S. Kasten, A. Wieland, L. Känel, J. Klock, W. Michaelis, and R. Seifert. 2008. A novel, multi-layered methanotrophic microbial mat system growing on the sediment of the Black Sea. Environmental Microbiology **10**: 1934–1947.

Kutterolf, S., V. Liebetrau, T. Mörz, A. Freundt, T. Hammerich, and D. Garbe-Schönberg. 2008. Lifetime and cyclicity of fluid venting at forearc mound structures determined by tephrostratigraphy and radiometric dating of authigenic carbonates. Geology **36**: 707.

Kvenvolden, K. A. 1993. Gas Hydrates - Geological Perspective and Global Change. Reviews of Geophysics **31**: 173–187.

LaBonte, A. 2007. Monitoring periodic and episodic flow events at Monterey Bay seeps using a new optical flow meter. Journal of Geophysical Research **112**: 1–14.

Lei, X., H. Fujimaki, Y. Lu, Z. Zhang, and T. Maekawa. 2007. Ammonia removal from pretreated methane fermentation effluent through a soil trench system: a column experiment. Chemosphere **66**: 2077–86.

Levin, L. A., W. Ziebis, G. G. F. Mendoza, V. A. Growney, M. D. Tryon, K. M. Brown, C. Mahn, J. M. Gieskes, and A. E. Rathburn. 2003. Spatial heterogeneity of macrofauna at northern California methane seeps: influence of sulfide concentration and fluid flow. Marine Ecology Progress Series **265**: 123–139.

Linke, P., K. Wallmann, E. Suess, C. Hensen, and G. Rehder. 2005. In situ benthic fluxes from an intermittently active mud volcano at the Costa Rica convergent margin. Earth and Planetary Science Letters **235**: 79–95.

Luff, R., J. Greinert, K. Wallmann, I. Klaucke, and E. Suess. 2005. Simulation of long-term feedbacks from authigenic carbonate crust formation at cold vent sites. Chemical Geology **216**: 157–174.

Luff, R., and K. Wallmann. 2003. Fluid flow, methane fluxes, carbonate precipitation and biogeochemical turnover in gas hydrate-bearing sediments at Hydrate Ridge, Cascadia Margin: numerical modeling and mass balances. Geochimica et Cosmochimica Acta **67**: 3403–3421.

Luff, R., K. Wallmann, and G. Aloisi. 2004. Numerical modeling of carbonate crust formation at cold vent sites: significance for fluid and methane budgets and chemosynthetic biological communities. Earth and Planetary Science Letters **221**: 337–353.

Manga, M., M. Brumm, and M. L. Rudolph. 2009. Earthquake triggering of mud volcanoes. Marine and Petroleum Geology **26**: 1785–1798.

Mau, S., G. Rehder, I. G. Arroyo, J. Gossler, and E. Suess. 2007. Indications of a link between seismotectonics and CH 4 release from seeps off Costa Rica. Geochemistry, Geophysics, Geosystems **8**: 1–13.

Mau, S., H. Sahling, G. Rehder, E. Suess, P. Linke, and E. Soeding. 2006. Estimates of methane output from mud extrusions at the erosive convergent margin off Costa Rica. Marine Geology **225**: 129–144.

Meijboom, F., and M. Noordwijk. 1991. Rhizon soil solution samplers as artificial roots. *Root Ecology and us Pratical Application, 3 ISRR SymposiumWien*. 794–795.

Meister, P., M. Gutjahr, M. Frank, S. M. Bernasconi, C. Vasconcelos, and J. a. McKenzie. 2011. Dolomite formation within the methanogenic zone induced by tectonically driven fluids in the Peru accretionary prism. Geology **39**: 563–566.

Meulepas, R. J. W., C. G. Jagersma, J. Gieteling, C. J. N. Buisman, A. J. M. Stams, and P. N. L. Lens. 2009. Enrichment of anaerobic methanotrophs in sulfate-reducing membrane bioreactors. Biotechnology and Bioengineering **104**: 458–70.

Meyer-Reil, L. 1983. Benthic response to sedimentation events during autumn to spring at a shallow water station in the Western Kiel Bight II. Analysis of benthic bacterial populations. Marine Biology **77**: 247–256.

Milucka, J., T. G. Ferdelman, L. Polerecky, D. Franzke, G. Wegener, M. Schmid, I. Lieberwirth, M. Wagner, F. Widdel, and M. M. M. Kuypers. 2012. Zero-valent sulphur is a key intermediate in marine methane oxidation. Nature **2**: 1–23.

Morse, J., D. Gledhill, K. Sell, and R. Arvidson. 2002. Pyritization of iron in sediments from the continental slope of the northern Gulf of Mexico. Aquatic Geochemistry **8**: 3–13.

Nauhaus, K., A. Boetius, M. Krüger and F. Widdel. 2002. In vitro demonstration of anaerobic oxidation of methane coupled to sulphate reduction in sediment from marine gas hydrate area. Environ. Microbiol. **4**(5): 298-305.

Nauhaus, K., M. Albrecht, M. Elvert, A. Boetius, and F. Widdel. 2007. In vitro cell growth of marine archaeal-bacterial consortia during anaerobic oxidation of methane with sulfate. Environmental Microbiology **9**: 187–96.

Niemann, H., T. Lösekann, D. de Beer, M. Elvert, T. Nadalig, K. Knittel, R. Amann, E. J. Sauter, M. Schlüter, M. Klages, J. P. Foucher, and A. Boetius. 2006. Novel microbial communities of the Haakon Mosby mud volcano and their role as a methane sink. Nature **443**: 854–8.

Nittrouer, C. A., G. R. Lopez, L. D. Wright, S. J. Bentley, A. F. D. Andrea, C. T. Friedrichs, N. I. Craig, and C. K. Sommerfield. 1998. Oceanographic processes and the preservation of sedimentary structure in Eckernförde Bay , Baltic Sea. Continental Shelf Research **18**: 1689–1714.

Orcutt, B. N., J. B. Sylvan, N. J. Knab, and K. J. Edwards. 2011. Microbial ecology of the dark ocean above, at, and below the seafloor. Microbiology and Molecular Biology Reviews **75**: 361–422.

Peckmann, J., a Reimer, U. Luth, C. Luth, B. . Hansen, C. Heinicke, J. Hoefs, and J. Reitner. 2001. Methane-derived carbonates and authigenic pyrite from the northwestern Black Sea. Marine Geology **177**: 129–150.

Praeg, D., S. Ceramicola, R. Barbieri, V. Unnithan, and N. Wardell. 2009. Tectonically-driven mud volcanism since the late Pliocene on the Calabrian accretionary prism, central Mediterranean Sea. Marine and Petroleum Geology **26**: 1849–1865.

Preisler, A., D. de Beer, A. Lichtschlag, G. Lavik, A. Boetius, and B. B. Jørgensen. 2007. Biological and chemical sulfide oxidation in a Beggiatoa inhabited marine sediment. The ISME journal **1**: 341–53.

Ranero, C. R., I. Grevemeyer, H. Sahling, U. Barckhausen, C. Hensen, K. Wallmann, W. Weinrebe, P. Vannucchi, R. von Huene, and K. McIntosh. 2008. Hydrogeological system of erosional convergent margins and its influence on tectonics and interplate seismogenesis. Geochemistry Geophysics Geosystems **9**, doi:10.1029/2007GC001679

Reeburgh, W. S. 2007. Oceanic methane biogeochemistry. Chemical reviews **107**: 486–513.

Revsbech, N., and B. Jørgensen. 1986. Microelectrodes: Their Use in Microbial ecology K.C. Marshall [ed.]. Advances in Microbial Ecology **9**: 293–352.

Richardson, M., and A. Davis. 1998. Modeling methane-rich sediments of Eckernförde Bay. Continental Shelf Research **18**: 1671–1688.

Røy, H., J. S. Lee, S. Jansen, and D. de Beer. 2008. Tide-driven deep pore-water flow in intertidal sand flats. Limnology and Oceanography **53**: 1521–1530.

Sahling, H., D. Rickert, R. Lee, P. Linke, and E. Suess. 2002. Macrofaunal community structure and sulfide flux at gas hydrate deposits from the Cascadia convergent margin, NE Pacific. Marine Ecology Progress Series **231**: 121–138.

Schulz, H. D. 2000. Redox Measurements in Marine Sediments, p. 235–246. *In* J. Schüring, H.D. Schulz, J. Böttcher, and W.H.M. Duijnisveld [eds.], REDOX: Fundamentals, Processes, and Applications. Springer Berlin.

Seeberg-Elverfeldt, J., M. Schlüter, T. Feseker, and M. Kölling. 2005. Rhizon sampling of pore waters near the sediment-water interface of aquatic systems. Limnology and Oceanography: Methods **3**: 361–371.

Sommer, S., O. Pfannkuche, P. Linke, R. Luff, J. Greinert, M. Drews, S. Gubsch, M. Pieper, M. Poser, and T. Viergutz. 2006. Efficiency of the benthic filter: Biological control of the emission of dissolved methane from sediments containing shallow gas hydrates at Hydrate Ridge. Global Biogeochemical Cycles **20**: 1–14.

Tenthorey, E., and C. Scholz. 1998. Precipitation sealing and diagenesis: 1. Experimental results. Journal of Geophysical Research **103**: 23,951–23,967.

Torres, M., J. McManus, D. Hammond, M. A. de Anglis, K. Hesschen, S. Colbert, M. D. Tryon, K. Brown, and E. Suess. 2002. Fluid and chemical fluxes in and out of sediments hosting methane hydrate deposits on Hydrate Ridge, OR, I: Hydrological provinces. Earth and Planetary Science Letters **201**: 525–540.

Treude, T., A. Boetius, K. Knittel, K. Wallmann, and B. B. Jørgensen. 2003. Anaerobic oxidation of methane above gas hydrates at Hydrate Ridge, NE Pacific Ocean. Marine Ecology Progress Series **264**: 1–14.

Treude, T., M. Krüger, A. Boetius, and B. Jørgensen. 2005. Environmental control on anaerobic oxidation of methane in the gassy sediments of Eckernförde Bay(German Baltic). Limnology and Oceanography **50**: 1771–1786.

Tryon, M., K. Brown, and M. Torres. 2002. Fluid and chemical flux in and out of sediments hosting methane hydrate deposits on Hydrate Ridge, OR, II: Hydrological processes. Earth and Planetary Science Letters **201**: 541–557.

Tryon, M. D., and K. M. Brown. 2004. Fluid and chemical cycling at Bush Hill: Implications for gas- and hydrate-rich environments. Geochemistry Geophysics Geosystems **5**: 1–7.

Visser, W., W. a Scheffers, W. H. Batenburg-van der Vegte, and J. P. van Dijken. 1990. Oxygen requirements of yeasts. Applied and environmental microbiology **56**: 3785–92.

Wallmann, K., E. Pinero, E. Burwicz, M. Haeckel, C. Hensen, A. Dale, and L. Ruepke. 2012. The Global Inventory of Methane Hydrate in Marine Sediments: A Theoretical Approach. Energies **5**: 2449–2498.

Wankel, S. D., M. M. Adams, D. T. Johnston, C. M. Hansel, S. B. Joye, and P. R. Girguis. 2012. Anaerobic methane oxidation in metalliferous hydrothermal sediments: influence on carbon flux and decoupling from sulfate reduction. Environmental microbiology **14**: 2726–40.

Wegener, G., and A. Boetius. 2009. An experimental study on short-term changes in the anaerobic oxidation of methane in response to varying methane and sulfate fluxes. Biogeosciences **6**: 867–876.

Whiticar, M. J. 2002. Diagenetic relationships of methanogenesis , nutrients, acoustic turbidity , pockmarks and freshwater seepages in Eckernförde Bay. Marine Geology **182**: 29–53.

Widdel, F., and F. Bak. 2006. The Prokaryotes, p. 3352–3378. *In* M. Dworkin, S. Falkow, E. Rosenberg, K.-H. Schleifer, and E. Stackebrandt [eds.], The Prokaryotes, A Handbook on the Biology of Bacteria. Springer US.

Zhang, Y., J.-P. Henriet, J. Bursens, and N. Boon. 2010. Stimulation of in vitro anaerobic oxidation of methane rate in a continuous high-pressure bioreactor. Bioresource technology **101**: 3132–8.

Chapter 3:

Microbial activity and carbonate isotope signatures as a tool for identification of spatial differences in methane advection: a case study at the Pacific Costa Rican margin

Abstract

The forearc of the convergent margin offshore Costa Rica is a region characterized by strong advection of methane-charged fluids causing the formation of ubiquitous cold seeps (mounds). Presented here are the first measurements of microbial anaerobic oxidation of methane (AOM) and sulfate reduction (SR) rates in sediments from two mounds (11 and 12), applying radiotracer techniques in combination with numerical modelling. In addition, analysis of microbial, methane-dependent carbonate $\delta^{18}O$, $\delta^{13}C$, and $^{87}Sr/^{86}Sr$ signatures constrained the origin of the carbonate-precipitating fluid. Average rates of microbial activities differed by a factor of ~5 to 6 between Mound 11 (AOM 140.71 (±40.84 SD) mmol m^{-2} d^{-1}, SR 117.25 (±82.06 SD) mmol m^{-2} d^{-1}) and Mound 12 (AOM 22.37 (±0.85 SD) mmol m^{-2} d^{-1}, SR 23.99 (±5.79 SD) mmol m^{-2} d^{-1}). Modelling results yielded upward fluid advection velocities of 200 cm yr^{-1} at Mound 11 and 15 cm yr^{-1} at Mound 12. Analysis of oxygen and carbon isotope variations of authigenic carbonates from the two locations revealed more enriched (heavier) values for Mound 11 ($\delta^{18}O$: 3.18 to 6.15‰; $\delta^{13}C$: −14.14 to −29.56‰) compared to Mound 12 ($\delta^{18}O$: 3.09 to 4.48‰; $\delta^{13}C$:−39.53 to −48.98‰). The variation of carbonate $^{87}Sr/^{86}Sr$ indicated considerable admixture of deep-source fluid at Mound 11, while seawater $^{87}Sr/^{86}Sr$ characteristics prevailed at Mound 12 during precipitation. The present study is in accordance with previous work supporting considerable differences of methane flux between the two mounds. It also strengthens the hypothesis of a dominant deep fluid source with thermogenic methane at Mound 11 versus a shallow source of biogenic methane at Mound 12. The results demonstrate that measurements of methane-driven microbial activity in combination with numerical modelling are a valid tool for constraining recent methane fluxes in the study area. In addition, the analysis of methane-derived

authigenic carbonates provides an independent line of evidence for long-term fluid contribution to the porewater chemistry of shallow sediments in the study area.

Introduction

Fluid emanation at the seafloor is a common feature occurring in forearcs of convergent margins. The most important mechanisms that create fluid overpressuring and expulsion are tectonic compression, rapid burial of underconsolidated sediments, the release of mineral-bound water, the formation of gas from the biogenic or thermogenic breakdown of organic material, and the dissolution of gas hydrates (Kopf 2002; Saffer and Tobin 2011). Compressional release of porewater and the release of mineral-bound water from subducting sediments are thought to play a major role in terms of fluid cycling in the forearc of the Costa Rican margin (Hensen et al. 2004; Ranero et al. 2008).

When these fluids exit the sediment surface, they form what is commonly known as cold seeps. Cold-seep systems can be associated with different geological structures such as crater-like structures (pockmarks) or mud extrusions (mounds, volcanoes) (Judd et al. 2002). These systems are often characterized by authigenic carbonate concretions of micritic crystal morphology (Naehr et al. 2007), produced by microbial anaerobic oxidation of methane (AOM) in the sediment (e.g. Bohrmann and Greinert 1998; Greinert et al. 2001; Suess 2010).

The prerequisite for microbial-related authigenic carbonates at cold seeps is the advection of methane (CH_4). In marine sediments, methane is formed either as the result of microbial (biogenic methane) or thermal (thermogenic methane) degradation of organic matter (Schoell 1988; Thauer 1998). Thermogenic methanogenesis is either facilitated by (1) pyrolysis of organic matter or (2) water–rock interaction, resulting in different carbon isotope signatures compared to biogenic methane formation (Whiticar 1999).

In anoxic sediments, methane removal is mediated by microbial, sulfate (SO_4^{2-})-dependent AOM (Boetius et al. 2000). The general reaction of AOM is (Barnes and Goldberg 1976)

$$\mathrm{CH_4 + SO_4^{2-} \rightarrow HCO_3^- + HS^- + H_2O}$$

AOM and sulfate reduction (SR) increase porewater alkalinity, producing bicarbonate (HCO_3^-), which can dissociate into carbonate (CO_3^{2-}). In the case of supersaturation, carbonate minerals may form, predominantly with Ca^{2+} ions (Peckmann et al. 2001). The chemical and isotopic composition of authigenic carbonate provides information regarding the fluids present at the site of precipitation (Peckmann et al. 2001; Naehr et al. 2007). Therefore, authigenic carbonates represent a suitable archive of the palaeohydrological and geological settings present during precipitation.

Here, we report the first rate measurements of AOM and SR as well as carbonate mineralogy and isotopy from two adjacent mud extrusions (Mound 11 and 12) located at the subduction zone forearc off the Pacific Costa Rican coast. In addition, a numerical model, constraining fluxes of the main chemical species in the porewater, is presented. An accessory data set of strontium isotopic signatures from carbonates obtained during previous cruises is also included, representing a supporting indicator for potentially different fluid sources and their contribution to mineral composition during precipitation. Both mound structures have been extensively studied (e.g. Hensen et al. 2004; Schmidt et al. 2005; Mavromatis et al. 2012), focusing on either individual geological or biogeochemical aspects. Here, we directly compare the geochemical situation of the two mounds and characterize differences, especially emphasizing methane advection and resulting microbial activity applying on-board techniques.

Material and methods

Geological settings and study sites

The Middle American Trench is a large-scale subduction zone with a length of 2750 km located off the south-western coast of Central America. Offshore Costa Rica, the trench is formed by the eastward subduction of the oceanic Cocos Plate beneath the Caribbean Plate. A characteristic feature of this trench is the subduction of seamounts and ridges (Ranero and von Huene 2000). As these structures are thrusted into and below the continental plate, subduction of material may cause fractures in the upper plate and overlying shelf sediments through which fluids rise towards the surface (Ranero et al. 2008).

Chapter 3: Costa Rica mounds

Fluid emanation off Costa Rica predominantly occurs at bathymetric elevations, so-called mounds, which are ubiquitous and composed of authigenic carbonates, mud extrusions, and hemipelagic sediments (Hensen and Wallmann 2005). The present study focuses on the two neighbouring mounds, Mound 11 and 12 (Fig. 1 and 2), which are situated northeast of the Osa Peninsula (Bohrmann and Greinert 1998; Greinert et al. 2001) at water depths of ~1000m (Klaucke et al. 2008).

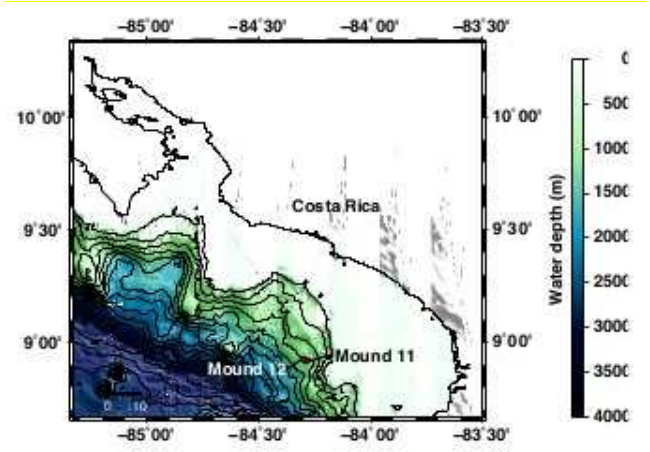

Figure 1: Bathymetric map of the Pacific continental slope of Costa Rica; locations Mound 11 and Mound 12 are shown.

Mound 11 is located at 08°55'20'' N and −84°18'14''W and has two summits that are ~300m apart and ~250m in diameter (Klaucke et al. 2008). Previous investigations, including sediment sampling and video survey, showed that the surface of Mound 11 consists of fine-grained sediment with mats of sulfur bacteria (Mörz et al. 2005; Schmidt et al. 2005; Mau et al. 2006).

Mound 12 is located about 1 km north of Mound 11 and is characterized by a differing geological morphology, including a solitary summit with a diameter of ~800m (Klaucke et al. 2008). Sediment sampling and video surveys of the sediment surface revealed fine-grained sediment and typical cold-seep features, such as mats of sulfur-oxidizing bacteria, fields of chemosymbiotic vesicomyid clams, and carbonate precipitates (Linke et al. 2005; Mau et al. 2006).

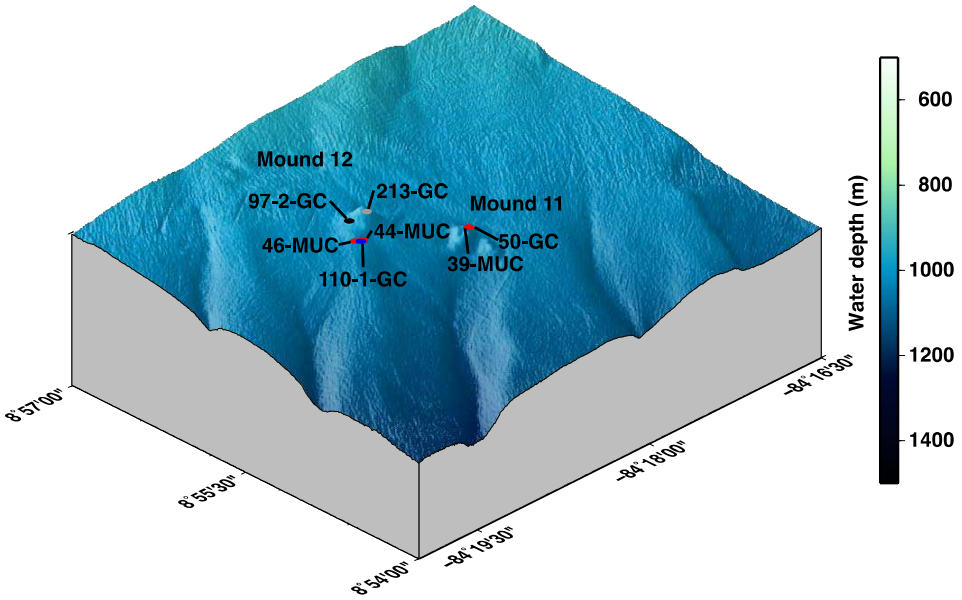

Figure 2: 3-D relief map of the study area offshore of Costa Rica showing stations at Mound 11 and 12 sampled during expeditions SO206 (red), SO173 (blue), M66 (grey), and M54 (black).

Sediment and carbonate sampling

Sediment samples from Mound 11 and 12 were obtained during the research expedition SO206 (June 2010) on board the German RV *Sonne*. Stations for sediment recovery on both mounds were situated at water depths of 1000–1010m (Table 1). Samples were collected with a gravity corer (GC) (barrel length 6 m) and a video-guided multicorer (MUC) consisting of eight core liners per deployment, each 60 cm long and 10 cm in diameter. MUC sampling was performed at locations with microbial mats of filamentous sulfur-oxidizing bacteria visible on the sediment surface, indicating areas of high methane flux (Treude et al. 2003; Torres et al. 2004). The obtained carbonates from GC and MUC samples varied in size from centimetres to decimetres, forming irregular, elongated, and flattened nodules. The carbonate nodules were picked from GC and MUC cores using gloves, wrapped in aluminium foil, and subsequently stored at −20 ℃. Two bivalve shell fragments found within sediment from SO206- 39 (MUC) were sampled in the same way. In addition, strontium isotopy of carbonate samples obtained from Mound 11 and 12 during three previous cruises SO173/4 (September 2003) on board the RV *Sonne*, M66/3a (October–November 2005), and M54/3a (September

2002) on board the RV *Meteor* (Table 1) were also used in this study. An overview of carbonate samples taken from GC and MUC cores is given in Table 2.

Table 1. Overview of sampled stations at Mound 11 and 12 during cruises SO206 SO173/4, M66/3a, and M54/3a.

Site	Station	Instrument	Lat. (N°)	Long. (W°)	Water depth (m)
Mound 11	SO206-38	GC	8° 55.36′	-84° 18.22′	1016
Mound 11	SO206-39	TV-MUC	8° 55.34′	-84° 18.23′	1005
Mound 11	SO206-50	GC	8° 55.33′	-84° 18.23′	1003
Mound 11	M54-155	GC	8° 55.36′	-84° 18.23′	1018
Mound 12	SO206-44	TV-MUC	8° 55.69′	-84° 18.79′	1007
Mound 12	SO206-46	TV-MUC	8° 55.72′	-84° 18.83′	1009
Mound 12	M54-97-2	GC	8° 55.90′	-84° 18.70′	1001
Mound 12	SO173 110-1	GC	8° 55.74′	-84° 18.81′	1008
Mound 12	M66-213	GC	8° 55.85′	-84° 18.60′	980

Core processing for porewater extraction

The GC obtained at station SO206-50 (length 300 cm) was sectioned into 1m intervals and cut in half vertically. One half was stored at 4℃, serving as archive, whilst the other half was used for sediment and porewater sampling. Nine samples for porewater extraction were obtained at 30–45 cm intervals over a total length of 300 cm. From each MUC cast (Mound 11, SO206-39; Mound 12, SO206-44 and 46), one core was assigned for sediment porewater analysis and sampled at 10 discrete 1 cm depth intervals from the surface down to the bottom of the core.

Table 2. List of carbonate samples from Mound 11 and 12 used for mineralogy and stable isotope analysis of carbonates. Samples from SO173, M66, and M54 were used for $^{87}Sr/^{86}Sr$ and $\delta^{13}C$ analysis (cmbsf = centimetres below seafloor).

Site	Station	Depth (cmbsf)
Mound 11	SO206-38	172-185
Mound 11	SO206-39	8
Mound 11	SO206-39	10-12
Mound 11	SO206-39	11
Mound 11	SO206-39	20-25
Mound 11	SO206-39	26-30
Mound 11	SO206-39, shell	25
Mound 11	SO206-39, shell	26-30
Mound 11	M54-155 A	90
Mound 11	M54-155 B	100
Mound 12	SO206-44	5-8
Mound 12	SO206-46	6-7
Mound 12	SO173-110-1	50-60
Mound 12	M66-213	0
Mound 12	M54-97-2	353
Mound 12	M54 97-2	353

Porewater analysis

Porewater was extracted from sediments using a pressure filtration system (argon 3–4 bar, 0.2 µm regenerated cellulose filters). Retrieved porewater was analysed on board for total alkalinity (TA) and total dissolved sulfide concentrations. Additional porewater samples were stored frozen for further measurements on land.

For TA determination, 1 mL of porewater was titrated manually with 0.01M HCl using an open cell and a Metrom Titrino plus titration unit. A methyl red–methylene blue solution with the following composition was used as indicator: sodium salt of methyl red (37 mg)

was mixed with 1.19 mL of 0.1 M NaOH and dissolved in 80 mL of ethanol (96%) (solution 1). Methylene blue (10 mg) was dissolved in 10 mL of ethanol (96%) (solution 2). Both solutions were mixed (80 mL of solution 1 and 4.8 mL of solution 2) to obtain a greenish-brown product. IAPSO standard seawater was used for TA calibration. Hydrogen sulfide concentration measurements were carried out photometrically after Cline (1969). For sulfide calibration, Titrisol® standard 0.1 N $Na_2S_2O_3$ was used. For sulfate measurements, porewater samples were acidified with ultra-purified HNO_3 (65%) and cooled to 4 °C until further use. Sulfate and chloride concentrations were determined using ion chromatography (METHROM 761) at GEOMAR laboratory, Kiel. The determination of main and trace elements was carried out using atomic emission spectroscopy with inductively coupled plasma atomic emission spectroscopy (ICP-AES) (JY 170 ULTRACE) at GEOMAR, Kiel.

Methane was stripped on board from sediments according to the method of McAullife (1971). Sediment plugs were recovered using clean, disposable 10 mL polypropylene syringes with the end removed. The sediment plug was immediately transferred to a 30 mL glass vial filled with 10 mL of 10% aqueous potassium chloride (KCl) solution. The vial was sealed and vigorously shaken to disaggregate the mud and to stop all bacterial activity (Bowes and Hornibrook 2006). The sample was stored upside down to minimize potential gas exchange with the atmosphere and allowed to equilibrate with the vial headspace for 48 h. The gas was then extracted with a syringe while injecting an equivalent amount of 10% KCl solution. A blank sample (air equilibrated with 10% KCl solution) was taken for background corrections. The KCl solution was not acidified so as to avoid production of CO_2 by dissolution of carbonate minerals. The headspace gas was injected into either 10 or 20 mL sterile serum vials filled (bubble-free) with acidified (pH 1), 10% KCl solution to terminate any microbial activity, whilst displacing an equivalent amount of solution. The vials were stored upside down until analysis. The methane concentration was determined on board by gas chromatography coupled to a flame ionization detector (GC-FID) using a Shimadzu GC14A instrument fitted with a Restek Rt® Alumina Bond/KCl capillary column (50 m, 0.53 mm ID) operated at 60 °C. N_2 was used as a carrier gas.

Sediment sampling for ex situ microbial turnover rates of methane and sulfate

Immediately after retrieval of the MUC, six replicate polycarbonate push cores (three for AOM rates, three for SR rates; inner diameter 26 mm, length 25 cm) were sampled from pristine surface sediment from one MUC liner. Open ends of push cores were sealed tightly with rubber stoppers, avoiding air entrapment. Sediment from gravity corers was sampled with six 5 mL glass tubes, closed with syringe puncheons, and dipped in Antifoam® to enable a better gliding. In addition, 10 controls (5 mL each) were sampled from anoxic sediment of the same core (GC or MUC) using 5 mL syringes with cut-off tips. For sampling with glass tubes or syringes, the puncheons were pushed to the open ends and placed on the sediment. While the puncheons remained in place, the glass tubes or syringes were pushed forward into the sediment. After retraction, open ends of glass tubes and syringes were sealed tightly with rubber stoppers for anoxic incubation. Subsequently, incubations with radiotracers were carried out in the closed glass vials.

Anaerobic oxidation of methane (AOM)

On board, radioactive methane ($^{14}CH_4$ dissolved in water, 15 µL injection volume, activity 1–2 kBq, specific activity 2.28 GBq $mmol^{-1}$) was injected into replicate push cores at 1 cm intervals according to the whole-core injection method of Jørgensen (1978). Alternatively, radioactive methane was injected through the rubber stoppers into sediment sampled from GC cores. After tracer injection, the push cores or glass tubes were incubated at in situ temperature (8 ℃) for 24 h in the dark. Subsequently, microbial activity was terminated by sectioning 1 cm intervals of sediment into 40 mL glass vials filled with 20 mL of sodium hydroxide (2.5%w/w). All sediment from a glass tube was transferred into a 40 mL glass vial with sodium hydroxide. Vials were closed immediately after sediment transfer and shaken vigorously before storage. Controls were first transferred into sodium hydroxide before addition of radiotracer. At GEOMAR, AOM rates were determined after Treude et al. (2005) (gas chromatography, $^{14}CH_4$ combustion, and calculation) and Joye et al. (2004) ($^{14}CO_2$ trapping).

Sulfate reduction (SR) rates

Sampling, injection, and incubation conditions were identical to that of the AOM samples. The injected radiotracer was radioactive sulfate ($^{35}SO_4^{2-}$ dissolved in water, 6 µL injection volume, activity 200 kBq, specific activity 37 TBq $mmol^{-1}$). After 24 h, microbial activity was terminated by sectioning 1 cm intervals of sediment into 50 mL plastic centrifuge vials filled with 20 mL of zinc acetate (20%w/w). Controls were first transferred into zinc acetate before addition of radiotracer. SR rates were determined using the cold-chromium distillation method by Kallmeyer et al. (2004).

X-ray diffraction and isotope analysis of carbonates

Carbonate samples and bivalve shell fragments were dried at 37 ℃ for 12 h and gently cleaned of sediment remains. The top surface from each carbonate piece was scoured over an area of ~5 mm x 5 mm, after which a small cavity was drilled to yield mineral powder. The powder was analysed for mineralogy using X-ray diffraction (Philips Xray diffractometer PW 1710 with monochromatic CoKα, 40 kV, 35 mA, 0.01° s^{-1}) between 2 and 70 2θ (incident angle). The resulting spectra were analysed using the software XPowder® (XPowder, Spain). Quantitative analyses of the spectra were carried out by the reference intensity ratios (RIR) method with a precision of approximately 5%. In order to calculate the molar percentage of $MgCO_3$ of magnesian calcite, the d-104 calcite peak shift was determined after Goldsmith et al. (1961). The standard error was about ±1 mol% $MgCO_3$ content according to lab standards (Mavromatis et al. 2012).

From each homogenized carbonate powder sample (see above), an aliquot of 10 mg was separated for carbon $\delta^{13}C$ and oxygen $\delta^{18}O$ stable isotope analysis. A fraction (approximately 1 mg) was dissolved by water-free phosphoric acid at 73 ℃ in a “Carbo-Kiel” (Thermo Fischer Scientific Inc.) online carbonate preparation line, and measured for carbon and oxygen stable isotope ratios with a MAT 253 mass spectrometer (Thermo Fischer Inc.). The $\delta^{13}C$ and $\delta^{18}O$ values are reported as permil deviation from laboratory standard referred to the VPDB (Vienna Pee Dee belemnite) scale. The standard deviations given are based on replicate analyses (n = 7) of the laboratory standard. External reproducibility was 0.032‰ for $\delta^{13}C$ and 0.054‰ for $\delta^{18}O$ (1-σ values).

The $\delta^{18}O$ values of carbonates are strongly dependent on the temperature at which precipitation occurred and also on the $\delta^{18}O$ signature of the surrounding liquid phase. In order to constrain the hydrological conditions during the precipitation, the equilibrium $\delta^{18}O$ values for the different carbonate phases with water were calculated for present local seafloor conditions, i.e. a bottom-water temperature of 8 ℃ (derived from measurements during SO206) and $\delta^{18}O$ of + 0.2‰ (SO206-39 (MUC) bottom water). The equilibrium fractionation factor for ^{18}O between calcite and water was calculated according to Kim and O'Neil (1997):

$$1{,}000 \ln \alpha_{calcite-water} = 18.03 * 10^3 T^{-1} - 32.42$$

with temperature, T, in kelvin. The equilibrium $\delta^{18}O$ value for magnesian calcite and water was calculated by applying a correction factor of 0.06‰ for each mol% of $MgCO_3$ (Tarutani et al. 1969). The equation of Grossman and Ku (1986) was used for calculating the $\delta^{18}O$ equilibrium fractionation factor between aragonite and water:

$$T(°C) = 21.8 - 4.69(\delta^{18}O_{aragonite} - \delta^{18}O_{water})$$

The $\delta^{18}O$ equilibrium fractionation factor between dolomite and water was calculated after Fritz and Smith (1970):

$$1{,}000 \ln \alpha_{dolomite-water} = 2.62 * 10^6 T^{-2} + 2.17$$

In addition, strontium, oxygen, and carbon isotope data of visually selected carbonate-dominated nodule fragments of millimetre size obtained from Mound 11 and 12 during previous cruises (listed in Table 2) are reported in this study. The strontium data were applied as a potential indicator of different fluid sources and their contribution during precipitation.

For strontium isotope analysis, samples were leached with 2.25 N HNO_3 to ensure complete dissolution of carbonate phases. The average concentration of strontium in terrigenous sediments is 240 ppm (Capo et al. 1998), while marine carbonates contain at least by a factor of 5 to 30 more (Dasch 1969; Bayon et al. 2007). As the samples were carbonate dominated, the contribution of strontium from etched and partially dissolved terrigenous material was considered to be of minor impact.

Strontium isotope ratios were determined by thermal ionization mass spectrometry (TIMS) after chemical separation by cation exchange chromatography using Sr-specific resin (Eichrom). Reported strontium isotope data are normalized to a $^{87}Sr/^{86}Sr$ ratio of 0.710248 for NIST 987 according to McArthur et al. (1998). IAPSO standard seawater was measured as a reference for modern seawater $^{87}Sr/^{86}Sr$, giving a value of 0.709176. During the present study, the analytical precision of samples was higher than the external reproducibility of $\pm 1.5\times10^{-5}$ (2σ). Only sample SO173 110-1-a (Table 6) showed a lower precision (2.1×10^{-5} 2σ).

Numerical modelling of measured data

A simple one-dimensional transport–reaction model similar to previously published approaches (Schmidt et al. 2005; Hensen and Wallmann 2005; Wallmann et al. 2006; Dale et al. 2010) was formulated to simulate the measured porewater profiles of Cl^-, SO_4^{2-}, CH_4, total hydrogen sulfide, (TH_2S, ~H_2S + HS^-), HCO_3^-, and Ca^{2+} in the three MUC cores and one gravity core (Table 3). The model was primarily used to quantify upward flow velocities, benthic fluxes, and rates of AOM and $CaCO_3$ precipitation. Processes considered include porewater advection and irrigation (non-local exchange), sediment accumulation, and molecular diffusion of dissolved species. Organic matter degradation was not simulated as its rate is assumed to be insignificant compared to methane-related SR and AOM (Wallmann et al. 2006; Karaca et al. 2010).

A partial differential equation based on the classical approach for early diagenesis (Berner 1980) was used to simulate the steady-state concentrations and fluxes:

$$\phi(x) \cdot \frac{\partial C(x)}{\partial t} = \frac{\partial(\phi(x) \cdot D_{sed}(x) \cdot \frac{\partial C(x)}{\partial x})}{\partial x} - \frac{\partial(\phi(x) v(x) C(x))}{\partial x} + \phi(x) \cdot R(x)$$

where $C(x)$ is the concentration of dissolved species in pore fluids (mmol l^{-1}), t is the time (yr), x is the sediment depth (cm), $\phi(x)$ is the sediment porosity, $D_{sed}(x)$ is the molecular diffusion coefficient in sediments ($cm^2\ yr^{-1}$), $v(x)$ is the advection velocity of pore fluid ($cm\ yr^{-1}$), and $R(x)$ represents the sum of all reactions considered in the simulated sediment domain.

Table 3. Summary of model input parameters and boundary conditions used for numerical modelling of biogeochemical processes at Mound 11 and 12.

	Mound 11, SO206-39	Mound 11, SO206-50	Mound 12, SO206-44	Mound 12, SO206-46	unit	constraint
Model parameter values						
Length core	35.5	290	13	9	cm	measured
Length of simulated sediment column	100	500	100	100	cm	pre-defined
Number of model layers	200	120	200	200	-	pre-defined
Temperature (*T*)	8	8	8	8	°C	measured
Salinity (*S*)	35	35	35	35	PSU	measured
Pressure	101	101	101	101	bar	measured
Porosity at sediment surface (ϕ_{top})	0.84	0.65	0.76	0.82	1	measured
Porosity at infinite sediment depth(ϕ_{bot})	0.66	0.68	0.68	0.68	1	fitted
Attenuation coefficient for porosity decrease with depth (*const*)	0.04	0	0.12	0.16	cm^{-1}	fitted
Burial velocity at depth (ω_{bot})	0.02	0.02	0.02	0.02	cm yr^{-1}	pre-defined*
Fluid flow at the sediment/ water interface (v_{top})	200	1.2	15	15	cm yr^{-1}	fitted
Kinetic constant for the anaerobic oxidation of methane (k_{AOM})	15000	200	6400	1000	$mmol^{-1}$ cm^3 yr^{-1}	fitted
Kinetic constant for $CaCO_3$ precipitation (k_{ca})	50000	0.85	80	500	yr^{-1}	fitted
Kinetic constant for H_2S removal from pore water (k_{res})	0.01	0.0005	0	0	mmol cm^{-3} yr^{-1}	fitted
Attenuation coefficient for decrease in H_2S removal rate (*remS*)	0.01	0	0.00002	0	cm^{-1}	fitted
Non-local mixing coefficient (α')	500	1.2	50	250	yr^{-1}	fitted
Depth of irrigated layer (x_{mix})	1	20	3	0	cm	fitted
Irrigation parameter (w_{mix})	1.7	30	0.8	2	cm	fitted
Pore water concentration upper/lower boundary						
BW SO_4^{2-}/BS SO_4^{2-}	27/0	28.5/0	28.5/0	28.5/0	mM	measured
BW CH_4/BS CH_4	0.00001/75	0.00001/85	0.00001/85	0.00001/85	mM	measured
BW Cl^-/BS Cl^-	548/200	550.5/10	557.5/550	550.5/550	mM	measured
BW HCO_3^-/BS HCO_3^-	2.3/4.5	4.0/0	2.3/30	2.3/30	mM	calculated
BW Ca^{2+}/ BS Ca^{2+}	10.18/9.20	10.5/10.0	10.4/6.0	10.42/8.54	mM	measured
BW total sulfide/ BS total sulfide	0.001/0.0	0.001/1.0	0.001/0.0	0.001/0.0	µM	measured

BW indicates concentrations of dissolved species at the upper boundary of the model column, whereas BS represent concentrations at the bottom of the sediment column. *Hensen et al (2005) & Karaca et al. (2010)

Due to compaction, sediment porosity decreases with depth and can be approximated by

$$\phi(x) = \left(\phi_{top} - \phi_{bot}\right) \cdot e^{(-\mathrm{const} \cdot x)} + \phi_{bot}$$

where ϕ_{top} is the porosity at the upper boundary and const (cm^{-1}) is the attenuation coefficient for the decrease of porosity with depth.

The velocity of pore fluid advection through sediments consists of a downward component due to burial and compaction and an upward component due to fluid advection from depth:

$$v(x) = \frac{\omega_{bot} \cdot \phi_{bot} - v_{top} - \phi_{top}}{\phi(x)},$$

where ω_{bot} is the sedimentation rate at the lower boundary (cm yr^{-1}), ϕ_{bot} is the porosity at the lower boundary, and v_{top} (cm yr^{-1}) is the upward-directed fluid velocity at the sediment surface.

Temperature-dependent molecular diffusion coefficients of dissolved species were calculated according to Boudreau (1997) and corrected for tortuosity:

$$D_{sed}(x) = \frac{D_0}{1 - \ln(\phi(x))^2},$$

where D_0 is the molecular diffusion coefficient in seawater at the in situ temperature.

Admixing of bottom water into the upper sediment column is a process which is typically observed in seep environments and has been ascribed to various processes such as density-driven formation of convection cells or irrigation through bubble ebullition (Henry et al. 1996; Haeckel et al. 2007; Chuang et al. 2013). In general, these processes can be simulated by including a non-local mixing term (Boudreau and Marinelli 1994; Schmidt et al. 2005):

$$R_{mix}(x) = \alpha(x) \cdot (C(x) - C(0))$$

$$\alpha(x) = \frac{\alpha'}{(1 + e^{(x - x_{mix})/w_{mix}})}$$

where $\alpha'(x)$ (yr^{-1}) is the depth-dependent irrigation coefficient, α (yr^{-1}) is a site-specific irrigation coefficient (yr^{-1}), ($C(x)-C(0)$) is the difference in solute concentration between seawater and sediment, x_{mix} (cm) is the depth of the mixed layer and w_{mix} (cm) represents the thickness of the transition layer between irrigated and non-irrigated sediment layers.

Methane is oxidized with sulfate during AOM, resulting in the production of hydrogen sulfide and bicarbonate:

$$CH_4 + SO_4^{2-} \rightarrow HCO_3^- + HS^- + H_2O.$$

The rate of AOM (R_{AOM}, mmol $cm^{-3}\,yr^{-1}$) was calculated using a bimolecular rate law:

$$R_{AOM}(x) = k_{AOM} \cdot [SO_4^{2-}] \cdot [CH_4],$$

where k_{AOM} is the kinetic constant for the anaerobic oxidation of methane (in $mol^{-1}\,cm^3\,yr^{-1}$).

In order to produce fits to porewater profiles of dissolved hydrogen sulfide, precipitation of iron sulfides is assumed using Eq. (13) as suggested by (Wallmann et al. 2008)

$$H_2S + {}^{2}/_{5}\,Fe_2O_3 \rightarrow {}^{2}/_{5}\,FeS_2 + {}^{1}/_{5}\,FeS + {}^{1}/_{5}\,FeO + H_2O\,,$$

The general depth-dependent function of sulfide removal from pore fluid ($R_{Sprec}(x)$) is defined as

$$R_{Sprec}(x) = \frac{[H_2S]}{K_{SP} + [H_2S]} \cdot k_{reS} \cdot e^{(-remS \cdot x)}\,,$$

where K_{SP} is a kinetic constant for sulfide removal in mmol cm^{-3}, k_{reS} is the kinetic constant for total sulfide removal from pore fluids in mmol cm^{-3} yr^{-1}, and remS is the attenuation coefficient for the decrease in sulfide removal rate with depth in cm^{-1}.

Rates of $CaCO_3$ precipitation were derived by fitting the model curve to the porewater Ca^{2+} profile:

$$R_{Ca}(x) = k_{Ca} \cdot \left(Ca_{meas}(x) - Ca_{mod}(x)\right),$$

An analytical function was fit through the data ($Ca_{meas}(x)$). The rate of $CaCO_3$ precipitation is thus a function of the concentration difference between Ca^{2+} calculated in the model during each depth interval and time step ($Ca_{mod}(x)$) and the measured Ca^{2+} ($Ca_{meas}(x)$). Precipitation rates were adjusted by varying the rate constant k_{Ca} (in yr^{-1}). Precipitation of $CaCO_3$ consumes two moles of bicarbonate per mole of Ca^{2+}:

$$Ca^{2+} + 2HCO_3^- \rightarrow CaCO_3 + CO_2 + H_2O$$

The loss of HCO_3^- during precipitation of $CaCO_3$ and the production of HCO_3^- and HS^- during AOM strongly affect porewater total alkalinity (TA). Neglecting minor porewater constituents such as $B(OH)_4^-$, TA can be defined as

$TA = HCO_3^- + 2\ CO_3^{2-} + HS^-$.

At prevailing pH values between 7 and 8, HCO_3^- contributes more than 90% to the carbonate alkalinity (CA) and HS^- dominates TH_2S, and as such a simplified alkalinity approxomation can be performed considering only these two major species:

$TA = HCO_3^- + HS^-$

This approach is not meant to substitute a full representation of the carbonate system. Instead, the comparison between measured and modelled alkalinity and hydrogen sulfide profiles provides a constraint on chosen AOM and $CaCO_3$ precipitation rates.

At the upper and lower boundary of the model column, constant concentrations of dissolved species were prescribed (Dirichlet boundary conditions). The individual bottomwater concentrations of chemical species were defined as upper boundary conditions (0 cm) for each of the four modelled cores. Chemical species concentrations at the base of the cores served as lower boundary conditions. The upper and lower boundary conditions as well as other model parameters are summarized in Table 3.

Reliable measurements of dissolved methane were not available since most of the dissolved methane is typically lost during core retrieval (e.g. Hensen et al. 2007). Because all modelled cores indicate methane saturation at some depth below the zone of sulfate penetration, methane concentrations at the lower boundary were defined by calculating the (temperature-, pressure-, and chlorinity-dependent) solubility with respect to gas hydrate stability (Tishchenko et al. 2005) for each core separately.

Central finite differences were applied to approximate the spatial derivatives of the partial differential equations (PDEs). The NDSolve object of Mathematica® version 7.0 (method-of-lines technique) was used to solve the resulting systems of ordinary differential equations (ODEs).

Results

Porewater chemistry and microbial turnover rates

Biogeochemical profiles obtained at Mound 11, stations SO206-39 (MUC) and SO206-50 (GC) respectively (Fig. 3) revealed considerable differences regarding the vertical position of the sulfate–methane transition zone (SMT) and the location of peak microbial turnover rates of methane and sulfate (Fig. 3a, e). The sediment core from SO206-39 showed a strong decline of sulfate from a surface concentration of 27.4 mmol SO_4^{2-} L^{-1} to < 0.5 mmol l^{-1} within the first 6 cm below seafloor (cmbsf). Methane concentration increased from 2 mmol CH_4 L^{-1} at 21 cmbsf to 17.9 mmol CH_4 L^{-1} at 7.5 cmbsf. Towards

the surface, values further declined to 0.6 mmol $CH_4\,L^{-1}$. The SMT was located at ~5 cmbsf. Sulfate concentration at station SO206-50 (GC) decreased from a surface concentration of 27.5 mmol $SO_4^{2-}\,L^{-1}$ to < 0.5 mmol $SO_4^{2-}\,L^{-1}$ at 150.5 cmbsf. Methane declined from 5.1 mmol $CH_4\,L^{-1}$ at the bottom of the core (290 cmbsf) to 1.9 mmol $CH_4\,L^{-1}$ at 210 cmbsf. At a sediment depth of 190 cmbsf methane concentration steeply increased to 20.9 mmol $CH_4\,L^{-1}$, followed by a sharp decline to a surface concentration of 0.06 mmol $CH_4\,L^{-1}$. The SMT at station SO206-50 was located at ~125 cmbsf, i.e. considerably deeper compared to SO206-39.

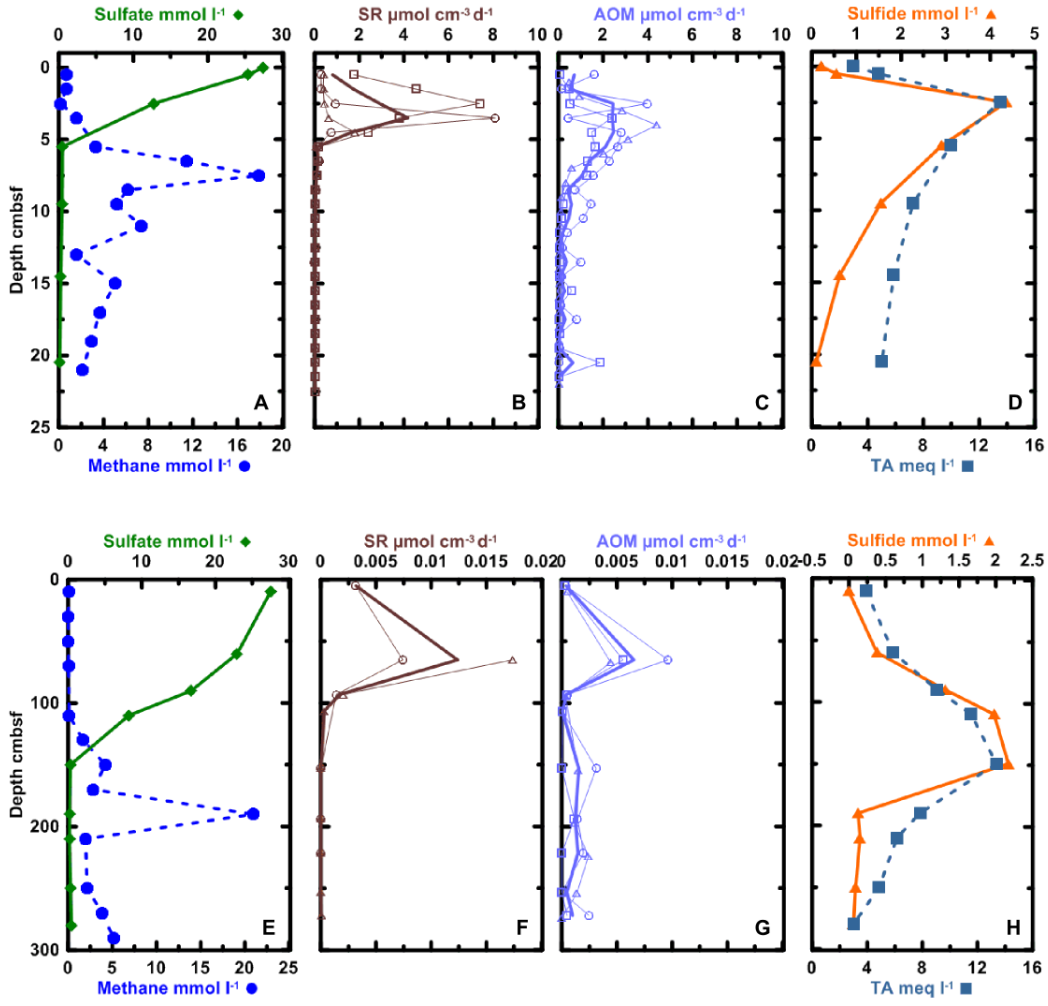

Figure 3: Mound 11 porewater profiles for sulfate, methane, sulfide, and total alkalinity (TA) as well as rates of sulfate reduction (SR) and anaerobic oxidation of methane (AOM). (A–D): SO206-39 (MUC) (covered by sulfur bacteria mat); (E–H): SO206-50 (GC). For SR and AOM profiles of individual replicates (fine lines with symbols) average profiles (bold lines without symbols) are given. Note the difference in depth (cmbsf) between station SO206-50 (GC) and stations SO206-39, 44, and 46 (MUC).

At Mound 11, AOM and SR rates from SO206-39 showed peak values of 4.4 µmol CH_4 cm^{-3} d^{-1} and 8.1 µmol SO_4^{2-} cm^{-3} d^{-1}, respectively, between 2 and 5 cmbsf (Fig. 3b, c). Corresponding integrated average areal rates (0–10 cm) were 140.71 (±40.84 SD, n = 3) mmol CH_4 m^{-2} d^{-1} for AOM and 117.25 (±82.06 SD, n = 3) mmol SO_4^{2-} m^{-2} d^{-1} for SR (Table 4). At SO206-50, maximum rates for AOM and SR reached 0.01 µmol CH_4 cm^{-3} d^{-1} and 0.017 µmol SO_4^{2-} cm^{-3} d^{-1}, respectively, at 65 cmbsf (Fig. 3f, g). Corresponding areal rates, integrated over the sampled core length (290 cm), yielded average values of 4.76 (±2.21 SD, n = 3) mmol CH_4 m^{-2} d^{-1} for AOM and 45.48 (±53.67 SD, n = 2) mmol SO_4^{2-} m^{-2} d^{-1} for SR. Despite the differences in AOM and SR rates of stations SO206-50 and SO206-39, maximum sulfide (2.3 and 4.4 mmol L^{-1}) and total alkalinity (2.1 and 4.2 meq L^{-1}) levels were of the same order of magnitude in both cores (Fig. 3d, h). In contrast to SO206-50 the curvatures of sulfide and TA at SO206-39 showed a concave shape below the SMT.

Table 4. Ex situ determined rates of anaerobic oxidation of methane (AOM) and sulfate reduction (SR) obtained from SO206 MUC sediment cores, in comparison with previous studies. Modelled AOM rates and benthic fluxes are also presented. All rates are expressed in mmol m^{-2} d^{-1}. Standard deviations (SD) are given.

Site	Station	AOM	SR	Depth of integration (cm)	AOM	CaCO3 precipitation	SO_4^{2-}*	CH_4*	HCO_3^-*	Ca^{2+}*	Simulated core length (cm)
		measured			modeled						
Mound 11	SO206-39	140.71 (± 40.84 SD)	117.25 (± 82.06 SD)	0-10	143.69	6.52	143.82	-201.63	-151.43	-35.82	100
Mound 11	SO206-50	4.76 (± 2.21 SD)	45.48 (± 53.67 SD)	0-270	1.62	0.61	1.62	-0.30	-0.40	0.40	500
Mound 12	SO206-44	22.37 (± 0.85 SD)	23.99 (± 5.79 SD)	0-10	22.23	2.35	22.24	-4.28	-26.89	0.48	100
Mound 12	SO206-46	10.68 (± 3.53 SD)	64.97 (± 6.79 SD)	0-10	16.16	1.53	16.16	-12.45	-23.21	-1.35	100
Mound 12[1]		16.11		0-10							
Mound 11modeled[2]		9.64		0-27.5							
Hydrate Ridge[3]		99.00 (± 102.00 SD)	65.00 (± 58.00 SD)	0-10							
Håkon Mosby[4]		19.45 (± 5.48 SD)		0-10							

[1]Linke et al., 2000; [2]Karaca et al., 2010; [3]Treude et al., 2003; [4]Niemann et al., 2006
* total benthic flux, negative values indicate upward flux from sediment into the water column, while positive values represent downward flux from the water column into the sediment

At Mound 12, the sulfate and methane concentration profiles differed between the two stations SO206-44 (MUC) and SO206-46 (MUC) (Fig. 4a, e). At station SO206-44, sulfate decreased gradually from surface concentrations of 28.4 to 4.2 mmol SO_4^{2-} L^{-1} between 5 and 7 cmbsf. Below this depth, sulfate concentration declined to 1.4 mmol SO_4^{2-} L^{-1} at the core bottom (13 cmbsf). Methane concentrations in SO206-44 sediment varied considerably over the entire core length of 20 cm. At the surface, methane concentration was 3.5 mmol CH_4 L^{-1}, followed by an increase to ~14 mmol CH_4 L^{-1}

between 2.5 and 6.5 cmbsf. Below this depth, methane concentration varied between 1 and 12 mmol L^{-1}. Due to the presence of massive carbonate layers in the sediment, core liner penetration at station SO206-46 was limited to 12–15 cmbsf. Here, sulfate declined from surface concentrations of 28.3 mmol SO_4^{2-} L^{-1} to 11.5 mmol SO_4^{2-} L^{-1} at 9 cmbsf. Methane increased from 1.3 to 19.1 mmol CH_4 L^{-1} between 11 and 9 cmbsf, declining steeply to < 0.2 mmol CH_4 L^{-1} towards the sediment surface.

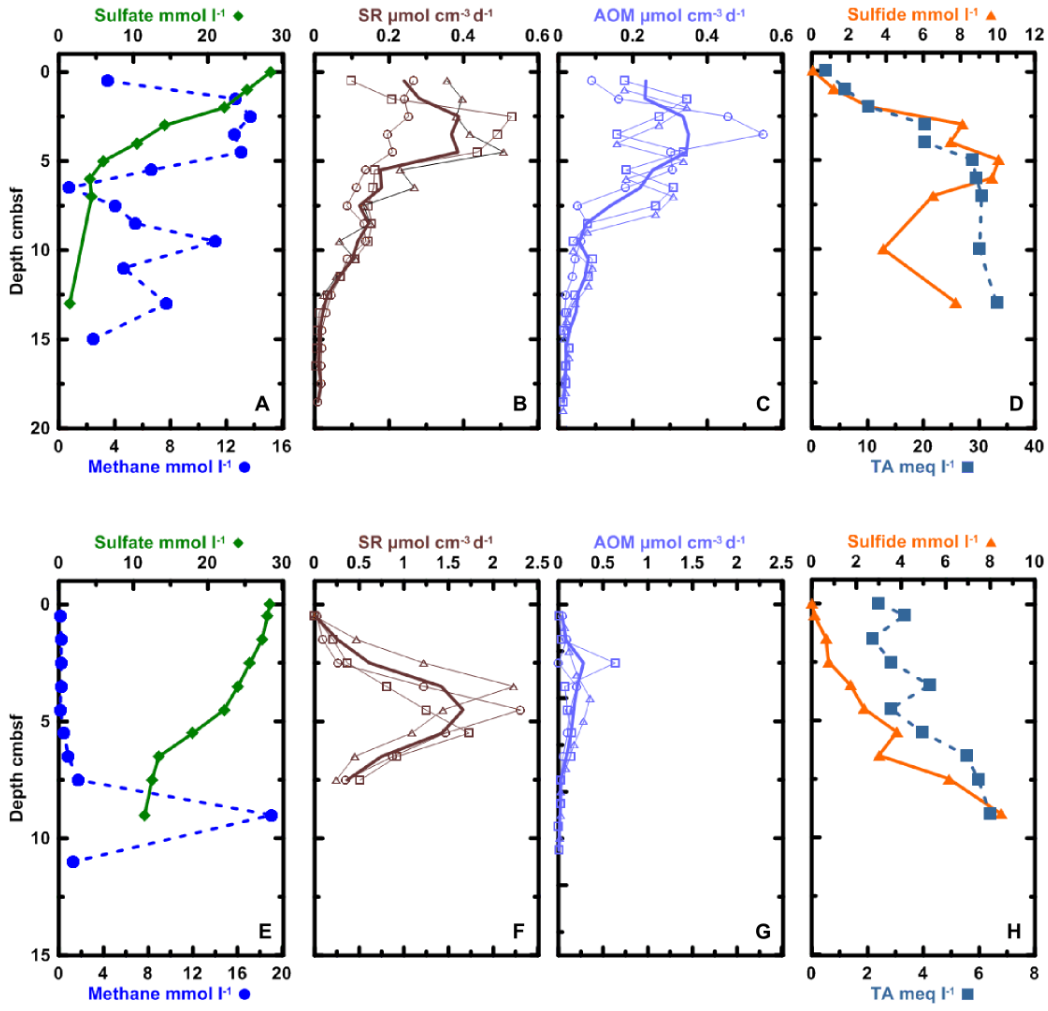

Figure 4: Mound 12 porewater profiles for sulfate, methane, sulfide, and total alkalinity (TA) as well as sediment rates of sulfate reduction (SR) and anaerobic oxidation of methane (AOM). (A–D): SO206-44 (MUC) (covered by sulfur bacteria mat); (E–H): SO206-46 (MUC) cores (covered by bacterial mat). For SR and AOM profiles of individual replicates (fine lines with symbols), average profiles (bold lines without symbols) are given.

Highest rates for AOM and SR at Mound 12 were measured between 2 and 5 cmbsf at both stations. At station SO206-44, peak values of 0.58 µmol CH_4 cm^{-3} d^{-1} and 0.52 µmol SO_4^{2-} cm^{-3} d^{-1} were measured (Fig. 4b, c). Integrated average areal rates of the top 10

cm yielded 22.37 (±0.85 SD, n = 3) mmol CH_4 m^{-2} d^{-1} and 23.99 (±5.79 SD, n = 3) mmol SO_4^{2-} m^{-2} d^{-1} for AOM and SR, respectively (Table 4). At station SO206-46, microbial rates were slightly higher, reaching maximum values of 0.65 µmol CH_4 cm^{-3} d^{-1} (AOM) and 2.30 µmol cm^{-3} d^{-1} (SR) (Fig. 4f, g). Corresponding average areal rates were 10.68 (±3.53 SD, n = 3) for AOM and 64.97 (±6.79 SD, n = 3) for SR.

Numerical modelling results

The advective fluid flow velocity and AOM and calcium carbonate precipitation rates were determined by fitting the model to the porewater data. Parameter values and boundary conditions used for simulations (Table 3) yielded good fits to the measured porewater profiles (see supplementary information, Figs. 1S–4S). Considerable deviations between model results and porewater data occurred only for methane and hydrogen sulfide profiles, as measured concentrations were lower than simulated values. This discrepancy is caused by the loss of methane and hydrogen sulfide due to outgassing during core retrieval and has been reported before (Hensen et al. 2007; Karaca et al. 2010).

The depth-integrated AOM rates differed considerably between the two cores obtained at Mound 11 (SO206-39 (MUC) and SO206-50 (GC)) (Table 4). For station SO206- 39 an AOM rate of 143.69 mmol CH_4 m^{-2} d^{-1} (integrated from 0 to 100 cm sediment depth) was calculated. In contrast, at station SO206-50 the modelled AOM rate (integrated from 0 to 500 cm sediment depth) was two orders of magnitude lower (1.62 mmol CH_4 m^{-2} d^{1}). The two stations at Mound 12 (SO206-44 (MUC), SO206-46 (MUC)) showed modelled AOM rates (each integrated from 0 to 100 cm sediment depth) of 22.23 and 16.16 mmol CH_4 m^{-2} d^{-1}, respectively. At stations SO206-39 and SO206-50 (Mound 11) depth-integrated calcium carbonate precipitation rates varied between 6.52 and 0.61 mmol $CaCO_3$ m^{-2} d^{-1}, respectively, while the two stations from Mound 12 showed values of 2.35 (SO206-44) and 1.53 mmol Ca^{2+} m^{-2} d^{-1} (SO206- 46).

According to model results, considerable differences of sediment–water column total fluxes of the dissolved chemical species occurred between the two mounds (Table 4). Due to the 1:1 stoichiometry of methane and sulfate consumption during AOM, the total influx of sulfate from the water column into the sediment was in accordance with the

depth-integrated AOM rates at the four stations with highest sulfate fluxes at station SO206-39 (Mound 11) and SO206-44 (Mound 12) of 143.82 and 22.24 mmol SO_4^{2-} m^{-2} d^{-1}, respectively (Table 4). The calculated methane flux yielded negative values for all stations, indicating an upward-directed flux inside the sediment. The two stations at Mound 11 showed contrasting values for methane flux, ranging from 201.63 (SO206-39) to 0.30 mmol CH_4 m^{-2} d^{-1} (SO206-50). Furthermore, the two stations at Mound 12 largely differed in upward methane flux, showing values of 4.28 and 12.45 mmol CH_4 m^{-2} d^{-1}, respectively. Modelled total flux of dissolved inorganic carbon – after accounting for AOM and carbonate precipitation – showed bicarbonate (HCO_3^-) export from the sediment into the water column at both mounds (Table 4). In accordance to fluid flow and AOM rate, highest bicarbonate flux was found at station SO206-39 (Mound 11, 151.43 mmol C m^{-2} d^{-1}), while the corresponding flux rate at the neighbouring station SO206-50 was considerably lower (0.40 mmol HCO_3^- m^{-2} d^{-1}). At the two stations at Mound 12, total upward bicarbonate flux ranged between 26.89 (SO206-44) and 23.21 mmol C m^{-2} d^{-1} (SO206-46). Modelled flux rates of calcium showed an upward flux into the sediment of 35.82 and 1.35 mmol Ca^{2+} m^{-2} d^{-1} at stations SO206-39 (Mound 11) and SO1206-46 (Mound 12), respectively. In contrast, stations SO206-50 (Mound 11) and SO206-44 (Mound 12) were characterized by downward calcium fluxes of 0.40 and 0.48 mmol Ca^{2+} m^{-2} d^{-1}, respectively.

Carbonate mineralogy and isotopic composition

The carbonate nodules obtained during the SO206 cruise were composed of a matrix consisting of carbonate-cemented sediment with carbonate contents varying between 52 and 61 wt%. Encountered carbonate shapes varied from elongated structures, some of which exceeded 12 cm in length, to roundish nodules of < 1 to 4 cm diameter. The two shell fragments showed carbonate contents of 17 and 31 wt%. The mineralogy of the carbonate nodules from Mound 11 was largely dominated by magnesian calcite, representing 42 to 49 wt% of the total sample mass, and aragonite (10– 13 wt% of the total sample mass) (Table 5). In one sample at station SO206-39, magnesian calcite occurred together with dolomite. Another Mound 11 sample showed aragonite as the sole carbonate mineral present. In contrast to the carbonate nodules, the two shell fragments most likely belonging to the vesicomyid family were mainly characterized by

aragonite and calcite. Carbonate samples from Mound 11 were characterized by $\delta^{13}C$ values ranging from −29.56 to −14.14‰ (±0.03 SD) (Table 5, Table 6, Fig. 5). Corresponding $\delta^{18}O$ values varied between 3.18 and 6.15‰ (±0.05 SD). Isotopic signatures of the two bivalve shell fragments deviated from the authigenic carbonate samples, with $\delta^{18}O$ being lower (3.55–3.96‰) (±0.05 SD) and $\delta^{13}C$ values being considerably higher (−9.61 to −6.98‰) (±0.03 SD). The two samples from Mound 11 collected during cruise M54 were characterized by varying contents of aragonite and calcite (Table 6). In addition, the carbonate-dominated leachates (2.25 N HNO_3) of these samples showed $^{87}Sr/^{86}Sr$ ratios (0.708829 and 0.709049), which were considerably lower than for modern seawater (Table 6).

Table 5. Mineralogy and stable isotope composition of carbonate samples from Mound 11 and 12 (cruise SO206). Italicized samples indicate bivalve shell fragments. The standard deviation (SD) of lab standard is given.

Site	Station	Depth (cmbsf)	Total carbonate (wt%)	Magnesian calcite (wt%)	mol% of $MgCO_3$	Calcite (wt%)	Aragonite (wt%)	Dolomite (wt%)	$\delta^{13}C$	SD	$\delta^{18}O$	SD
Mound 11	SO206-38	172-185	54	44	14		10		-27.14	0.03	5.65	0.05
Mound 11	SO206-39	8	60	49	13		12		-26.21	0.03	5.87	0.05
Mound 11	SO206-39	10-12	58	48	15			11	-21.20	0.03	4.72	0.05
Mound 11	SO206-39	11	53	42	13		11		-27.49	0.03	5.71	0.05
Mound 11	SO206-39	20-25	58	46	15		13		-29.56	0.03	6.15	0.05
Mound 11	SO206-39	26-30	48				48		-29.01	0.03	5.85	0.05
Mound 11	*SO206-39, shell*	*25*	*17*	*6*	*12*	*7*	*11*		*-6.98*	0.03	*3.55*	0.05
Mound 11	*SO206-39, shell*	*26-30*	*31*			*12*	*19*		*-9.61*	0.03	*3.96*	0.05
Mound 12	SO206-44	5-8	55	33	15		13		-48.98	0.03	4.15	0.05
Mound 12	SO206-46	6-7	54	39	15	27			-45.70	0.03	4.48	0.05

The two carbonate samples from Mound 12, obtained during SO206, also consisted mainly of magnesian calcite (Table 5). In comparison to Mound 11, the mass of magnesian calcite was smaller, ranging from 33 to 39 wt%. The two samples also differed amongst each other; one contained magnesian calcite and calcite, the other magnesian calcite and aragonite. In contrast, Mound 12 samples from cruises M54, M66, and SO173 were largely dominated by aragonite (Table 6). The carbon and oxygen isotopic signatures of carbonate samples obtained from Mound 12 were in general more negative than at Mound 11. Values for $\delta^{13}C$ ranged from −48.98 to

Table 6. List of $^{87}Sr/^{86}Sr$ ratios, $\delta^{13}C$, and $\delta^{18}O$ of carbonate-dominated fragments from Mound 11 and 12 carbonates obtained during cruises M54, M66, and SO173. Second standard error (2σ) and standard deviations (SD) are given.

Site	Station	Depth (cmbsf)	$^{87}Sr/^{86}Sr$	2σ	$\delta^{13}C$	SD	$\delta^{18}O$	SD	Aragonite (wt%)	Calcite (wt%)
Mound 11	M54-155 A	155	0.708829	1.4E-05	-14.14	0.02	3.18	0.09	10	90
Mound 11	M54-155 B	155	0.709049	7.0E-06	-15.57	0.02	4.22	0.04	70	30
Mound 12	M54-97-2 A	353	0.709167	7.5E-06	-46.28	0.02	3.56	0.04	> 98	< 2
Mound 12	M54-97-2 B	353	0.709164	6.1E-06	-46.87	0.02	3.62	0.04	> 98	< 2
Mound 12	M66-3 213 A	0	0.70909	7.0E-06	-39.53	0.02	4.13	0.04	95	5
Mound 12	M66-3 213 B	0	0.709158	8.0E-06	-42.46	0.02	3.96	0.04	> 98	< 2
Mound 12	SO173 110-1a	50-60	0.709114	2.1E-05	-49.13	0.02	3.29	0.04	90	10
Mound 12	SO173 110-1b	50-60	0.709098	8.0E-06	-48.61	0.02	3.24	0.04	> 98	< 2
Mound 12	SO173 110-1	50-60	0.709088	7.0E-06	-47.50	0.02	3.09	0.04	> 98	< 2
Mound 12	SO173 110-1	50-60	0.709097	6.0E-06	-48.58	0.02	3.27	0.04	> 98	< 2
Modern seawater*			0.709176	1.5E-05						

* IAPSO standard seawater was used to represent modern seawater $^{87}Sr/^{86}Sr$ ratio

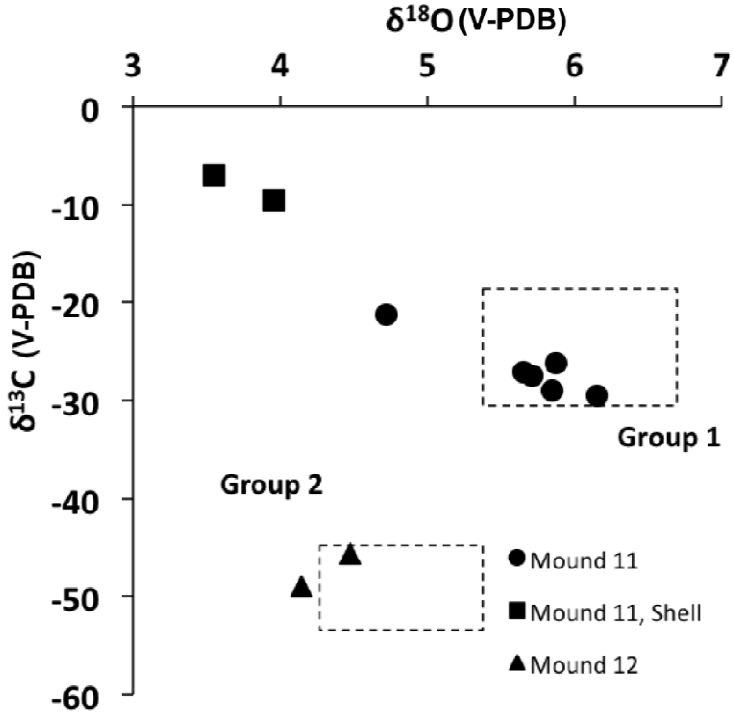

Figure 5: $\delta^{13}C$ vs. $\delta^{18}O$ plot of carbonate material sampled from various locations during SO206 (solid symbols). The grouping was based on isotopic, petrographic, mineralogical, and morphological similarities according to (Han et al. 2004). All values refer to the VPDB scale.

−39.53‰ (±0.03 SD) (Table5 and 6), $\delta^{18}O$ ranged between 3.09 and 4.48‰ (±0.05 SD). In contrast to Mound 11, the carbonate samples collected from Mound 12 generally showed higher $^{87}Sr/^{86}Sr$ ratios (0.709088 to 0.709167), ranging close to the value for modern seawater (0.709176) (Table 6). The composition of magnesian calcite was rather homogeneous in all samples from the two mounds, with a $MgCO_3$ content ranging between 12 and 16 mol%. The results for mineralogy and isotopic composition of sampled carbonates are compiled in Table 5 and 6.

Discussion

In the present study, considerable differences of microbial AOM and SR activity as well as in $\delta^{18}O$, $\delta^{13}C$, and $^{87}Sr/^{86}Sr$ isotopic signatures of carbonates from surface sediment samples of the two neighbouring mounds are indicative of different fluid contributions. In the following sections the differences in microbial activity and carbonate isotopic signatures between Mound 11 and 12 will be discussed.

Microbial activity

Measured areal AOM and SR rates obtained from Mound 11 were up to one order of magnitude higher compared to Mound 12, and were in the same order of rates reported for high-advective cold-seep systems such as Hydrate Ridge (Treude et al. 2003)and Håkon Mosby Mud Volcano (Niemann et al. 2006) (Table 4). To our knowledge, areal measured AOM rates of Mound 11 (SO206-39) exceed values that have been published for marine cold-seep locations so far (e.g. Treude et al. 2003; Joye et al. 2004; Krüger et al. 2005). AOM and SR rates at the Mound 11 station SO206- 50 were considerably lower than at SO206-39, illustrating the strong spatial heterogeneity in fluid flow often encountered at seep locations. Especially the individual replicates for SR rates at SO206-50 showed largely deviating values, explaining the standard deviation exceeding 100%.

The observed difference in AOM and SR rates between the two mounds might be due to different advective transport velocities of methane charged fluid. Previous reactive-transport modeling (Mound 11) (Karaca et al. 2010) and benthic flux chamber experiments (Mound 12) (Linke et al. 2005) yielded maximum fluid flow at Mound 11 as high as 200 cm yr^{-1} at the centre of the seep (within microbial mat patches), while only

approximately 10 cm yr^{-1} was calculated for Mound 12. In contrast to these previous investigations, the present study derived fluid flow velocities of the two mounds from a comprehensive data set acquired during a single cruise. As the same methodological approach was applied for both locations, measured and modelled results can be compared directly.

The applied modelling approach indicated an advective fluid flow 13 times larger at Mound 11 than Mound 12. The fluid velocity constrained using the numerical transport–reaction model at Mound 11 (SO206-39) was 200 cm yr^{-1}, which is the same value as determined by Karaca et al. (2010) at this site. As the samples of the present study were obtained from a different geographical position at Mound 11, the observed difference is likely to reflect the spatial variability at this location. The modelled depth-integrated areal AOM rate for Mound 11 (station SO206-39) was similar to the measured rate (Table 4). Thus, the modelling approach is suitable to describe the rate of methane turnover and related biogeochemical processes at this station. The modelled AOM rate for station SO206-50 was approximately 66% lower than the measured one. Considering that the measured AOM rate at SO206-50 had a standard deviation of approximately 54%, the measured and modelled results were still in good agreement.

For both stations at Mound 12, best-fit model results were obtained using a fluid flow velocity of 15 cm yr^{-1}. Linke et al. (2005) (16 cm yr^{-1}) and Karaca et al. (2010) (10 cm yr^{-1}) yielded similar results, which indicate that spatial variation of fluid advection is less pronounced than at Mound 11. As for Mound 11, measured and modelled areal AOM rates were generally similar for Mound 12. However, the measured AOM rate for station SO206-46 was approximately 51% lower than predicted by the model. The data used to constrain the model were obtained from the same multiple corer deployment but using different cores from those used for rate measurements. Therefore, it may be that variations of AOM activity between individual MUC cores could explain the observed differences between measured and modelled areal AOM rates at both mounds.

Previous studies of seep sites at Hydrate Ridge showed considerable lateral sediment heterogeneity regarding AOM activity (Treude et al., 2003), which can also be assumed for the region off Costa Rica (Hensen et al. 2004; Schmidt et al. 2005; Linke et al. 2005).

However, spatial heterogeneity of AOM activity is not accounted for in the current model approach, as it assumed that concentrations and consequently reaction rates only vary with sediment depth. Therefore, the deviation of measurement- and model-based AOM rate for station SO206-46 does not necessarily indicate that model accuracy was insufficient to describe the methane-related biogeochemical processes at Mound 12, but rather illustrates the spatial heterogeneity of sedimentary AOM activity.

It should be mentioned that the observed difference in AOM and SR rates between the two mounds, measured here in surface sediments covered by thick sulfur bacteria mats, illustrates the wide range of methane turnover that can be connected with this type of chemosynthetic habitat. Sulfur bacteria are capable of oxidizing sulfide (Jørgensen and Nelson 2004), and are typically present at localities of high anaerobic methane turnover (Treude et al., 2003). Consequently, the sulfate, produced by microbial sulfide oxidation, is partially introduced into the sediment, thus adding to the amount of sulfate originating from seawater. The process of sulfide oxidation is not explicitly resolved in the model; however, it is mimicked by intense non-local transport of sulfate into the sediment; that is, sulfide oxidation occurs on top of the sediment column. Regardless of the ultimate source of sulfate (re-oxidation or bottom water), shallow downward mixing of bottom water is required to obtain measured AOM rates at Mound 11 and is also suggested by shallow concave-down type sulfate profile of the MUC core porewater (SO206-39) at this location. The variability of AOM rates underneath sulfur bacteria mats observed in our study calls for caution with respect to extrapolation of methane turnover rates based on visual seafloor observations.

Carbonate mineralogy and isotope systematics

The authigenic carbonates from Mound 11 and 12 are a direct result of methane-dependent microbial activity. Measurements and modelling of the current microbial methane and sulfate turnover can be utilized to constrain ongoing methane advection. In addition, the carbonate archive provides indications for the long-term fluid advection of the past.

The majority of carbonate nodules, obtained during SO206, were largely characterized by Mg-rich calcite as the dominant carbonate phase, followed by aragonite, thus

representing typical seep carbonates (Han et al. 2004; Pierre et al. 2012). However, one carbonate sample from Mound 11 showed aragonite as the sole carbonate phase present (48 wt% of the total sample). The chemical situation at which aragonite or magnesian calcite is primarily formed is not well constrained (Burton 1993), but there is evidence that the combination of the carbonate saturation state and the Mg/Ca ratio in solution largely define the carbonate precipitate mineralogy (De Choudens-Sánchez and González 2009). In addition, Burton and Walter (1987) showed that a low bottom-water temperature of about 2.5 ℃ may favour calcite precipitation. Furthermore, magnesian calcite could have replaced highly metastable aragonite (Pierre et al. 2012). The occurrence of dolomite in one of the Mound 11 carbonate nodules might be the result of locally enhanced microbial activity of sulfate-reducing bacteria (Pierre et al. 2012; Krause et al. 2012).

In order to constrain the prevailing fluid sources during precipitation, the equilibrium $\delta^{18}O$ values for the present carbonate phases and bottom water were calculated. Based on the bottom-water conditions used (8 ℃, +0.2 $\delta^{18}O$), the equilibrium $\delta^{18}O$ values for calcite, magnesian calcite, dolomite, and aragonite with water were 1.5, 2.4, 5.1, and 3.1‰, respectively. Considering the dominant carbonate phases of the samples, the measured $\delta^{18}O$ values apparently exceeded the equilibrium values for bottom water (Table 5). However, the $\delta^{18}O$ value of one shallow sample from Mound 11, including magnesian calcite and dolomite, was close to the equilibrium $\delta^{18}O$ values for dolomite. Therefore, it cannot be excluded that carbonate from this sample formed under considerable influence of bottom water. In contrast, the higher $\delta^{18}O$ values of the remaining carbonates from Mound 11 indicate that precipitation occurred under considerable influence of a deep-source fluid, which is enriched in ^{18}O (Mavromatis et al. 2012). According to Hensen et al. (2004), the observed positive $\delta^{18}O$ values of deep-source fluids from the study area are the result of clay-mineral dehydration at temperatures between 85 and 130 ℃ at ~12 km depth and subsequent upward fluid transport. The two bivalve shell fragments were close to the equilibrium $\delta^{18}O$ value for aragonite bottom water, indicating that synthesis of the shell indeed occurred in the bottom water. The two carbonate samples obtained from Mound 12 also showed higher $\delta^{18}O$ values than the equilibrium values for the dominant carbonate phases (Table 5).

Yet, in comparison to Mound 11, the $\delta^{18}O$ values of Mound 12 carbonates were closer to the equilibrium values, indicating that deep-source fluid was present during precipitation, but to a lesser extent than at Mound 11.

In comparison to Mound 12, carbonate nodules at Mound 11 were less depleted in $\delta^{13}C$, suggesting methane of thermogenic origin predominantly present during concretion formation (Schmidt et al., 2005). In principal, the $\delta^{13}C$ values encountered in Mound 11 carbonates could also originate from organic matter degradation (Curtis 1987). However, organic matter degradation is assumed to be a negligible sink for sulfate and a source of methane compared to SR and AOM fuelled by upward advection of methane-rich fluids in the study area (Wallmann et al. 2006; Karaca et al. 2010). Therefore, thermogenic methane is considered a primary inorganic carbon source in Mound 11 sediments. In contrast, methane of biogenic origin from a shallower source might have been causative for strongly depleted $\delta^{13}C$ in Mound 12 carbonates (Hensen and Wallmann 2005).

Han et al. (2004) identified five types of authigenic carbonate associated with fluid vents on the Costa Rica margin based on morphological, petrographic, and stable isotope criteria (referred to the PDB scale): chemoherm carbonates, seepage-associated concretions, gas-hydrate-associated concretions, as well as calcareous and dolomitic concretions. Regarding the isotopic composition, carbonate samples obtained for Mound 11 and 12 during the SO206 cruise can be divided into two groups (Fig. 5). Group 1 was comprised of Mound 11 carbonates samples, while group 2 included samples from Mound 12. Carbonates from group 1 were characterized by $\delta^{18}O$ values between 5.6 and 6.7‰. Corresponding $\delta^{13}C$ values ranged from −21 to −29‰. According to the carbonate classification mentioned above, group 1 carbonate isotope composition is indicative of gas-hydrate-associated concretions ($\delta^{18}O$ 5.2 to 6.8‰, $\delta^{13}C$ −18.6 to −29.8‰; Han et al., 2004). This type of carbonate is characterized by layered Mg-rich calcite and aragonite precipitated into spaces previously occupied by gas hydrates before dissociation (Bohrmann et al. 2002; Suess 2002). Bivalve shell material from Mound 11 was mainly composed of aragonite and organic components. Corresponding values of $\delta^{13}C$ showed an isotopic signature considerably higher compared to the carbonates (−6.9 and −9.7‰), indicating shell formation in seawater with atmospheric CO_2 as a carbon source (Emrich et al. 1970). The carbonates from group 2 had a lower

$\delta^{18}O$ signature (4.1–4.5‰), while depletion of ^{13}C was stronger compared to group 1 (−39 to −49‰). According to Han et al. (2004), carbonates of group 2 are typical for seepage-associated concretions ($\delta^{18}O$ 4.3 to 5.4‰, $\delta^{13}C$ −44.6 to −53.0‰). This type of carbonate occurs at or near the seafloor, forming small, individual carbonate blocks, concretions, and crusts of high Mg calcite.

The $^{87}Sr/^{86}Sr$ signature of the carbonate samples varied between the two mounds depending on the aragonite/calcite ratio (Table 6). The aragonite-dominated samples from Mound 12, representing 90 to > 98 wt% of the present carbonate, generally showed $^{87}Sr/^{86}Sr$ signatures in the range of modern seawater or slightly lower. Considering the variation of the $^{87}Sr/^{86}Sr$ encountered in carbonates from Mound 12, two groups can be distinguished (Fig. 6). One group, consisting of five samples, encompasses $^{87}Sr/^{86}Sr$ ratios slightly lower than modern seawater, represented by IAPSO standard seawater. The difference of $^{87}Sr/^{86}Sr$ between this group and IAPSO standard seawater was larger than the second standard error (2σ) of 1.5×10^{-5} for IAPSO standard seawater. Therefore, it can be assumed that fluid, although to a small extend, contributed to the porewater during carbonate precipitation. Carbonates from this group were retrieved from 50 to 60 cmbsf, with the exception of one sample (M66-3 213 B), which was collected from the sediment surface. Consequently, precipitation of these carbonates occurred under seawater conditions with minor fluid contribution. In contrast, the three remaining carbonate samples showed $^{87}Sr/^{86}Sr$ ratios similar to modern seawater, indicating precipitation under seawater conditions. Two of these carbonates were collected from 353 cmbsf, and one from the sediment surface.

In contrast, Mound 11 carbonate samples showed considerably lower $^{87}Sr/^{86}Sr$ ratios. This difference correlated with the amount of calcite present, as the 90 wt% calcitedominated sample showed a lower $^{87}Sr/^{86}Sr$ ratio compared to the sample containing 30 wt% calcite. The observed lower $^{87}Sr/^{86}Sr$ ratio, compared to seawater, of Mound 11 carbonates formed under considerable influence of deep-source fluid, exposed to the weathering of abundant volcanic ashes in the sediment (Silver et al. 2000; Soeding et al. 2003; Kutterolf et al. 2008). The $^{87}Sr/^{86}Sr$ of Mound 11 carbonates were slightly higher than reported porewater values of 0.708699 (23.5 cmbsf) (Scholz et al. 2010). In contrast, Mound 12 carbonates presumably precipitated under hydrological

conditions dominated by seawater. The observed difference in the $^{87}Sr/^{86}Sr$ ratio provides independent evidence that the authigenic carbonates at Mound 11 were formed under influence of advecting fluid, while Mound 12 carbonates formed in a seawater environment with only small contributions of ascending fluid.

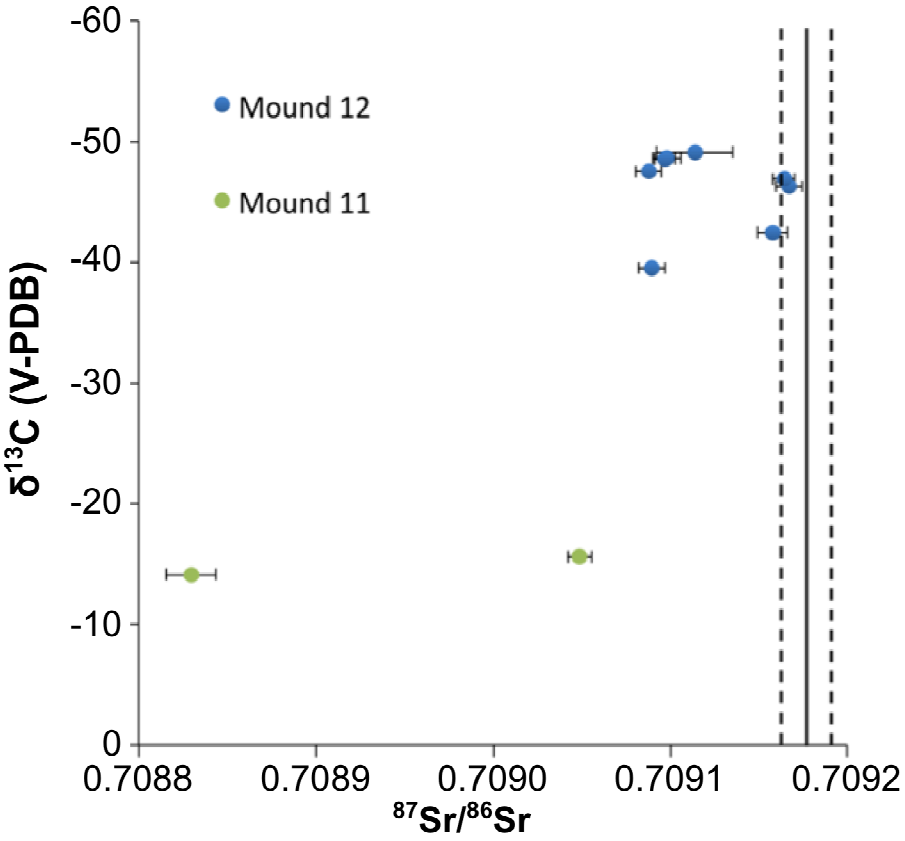

Figure 6: $\delta^{13}C$ vs. $^{87}Sr/^{86}Sr$ ratios of carbonate material sampled during cruises SO173/4, M66/3a, and M54/3a. Two standard deviations (2σ) of individual $^{87}Sr/^{86}Sr$ measurements are given. The solid line indicates the measured $^{87}Sr/^{86}Sr$ ratio of IAPSO standard seawater; the dotted lines represent 2σ. The standard deviation of $\delta^{13}C$ measurements was 0.02‰ (symbols larger than error bars).

According to sediment petrographic interpretation, dating of volcaniclastic layers and uranium–thorium dating of carbonates from the two locations (Kutterolf et al. 2008), Mound 11 is considered to be currently active, implying that it has been expelling fluids and, potentially, mud onto the surrounding seafloor for at least the last 15 ka. In contrast, pelagic surface sediments (131 cm thickness) at Mound 12 indicate that vertical mud transport has been inactive for the last 5 ka (Kutterolf et al. 2008). The rate measurements presented in this study demonstrated recent methane-related microbial activity at both mounds. Consequently, Mound 12 also has to be considered as a site of

active fluid venting, delivering sufficient methane to support related microbial activity. The present study demonstrated that fluid and methane migration at Mound 12 showed spatial variations, and therefore sampling of surface sediments could recover either pelagic or seep sediments, depending on where sampling instruments were deployed. During video surveys of Mound 12 surface sediments, we discovered both areas displaying chemosynthetic communities as well as areas devoid of such, which indicates heterogeneous fluid migration.

As both mounds are situated on the same fault zone, ascending fluids may originate from the same source (Mavromatis et al. 2012). Due to past or ongoing tectonic processes, the fluid pathway of Mound 12 might have been compromised, reducing deep-source fluid advection at this location. The slightly lighter $\delta^{18}O$ values of Mound 12 carbonates suggest that fluids at this location represent a mixture of deep-source fluid with bottom water. In contrast, carbonate $\delta^{13}C$ values indicated that fluids at Mound 11 are primarily charged with deep-source thermogenic methane.

Summary

Methane-charged fluid advection is causative for high microbial activity in surface sediments of the two neighbouring mounds, Mound 11 and 12, located at the Pacific continental margin off Costa Rica. Anaerobic oxidation of methane (AOM) and sulfate reduction (SR) rates determined ex situ in surface sediments were one order of magnitude higher at Mound 11 compared to Mound 12. Differences in carbonate stable isotope composition and $^{87}Sr/^{86}Sr$ signatures of the two mounds indicated that ascending fluid at Mound 11 originated from a deep source transporting primarily thermogenic methane. In contrast, advecting fluids at Mound 12 were less prominent and primarily charged with biogenic methane from a shallower source. Our study demonstrated that direct measurements of microbial AOM and SR activity, in combination with numerical modelling and carbonate archives analysis, provide a suitable ground-truthing tool to support geophysical measurements in order to constrain spatial variations of methane-charged fluid flow at the Costa Rica continental margin.

References

Barnes, R., and E. Goldberg. 1976. Methane production and consumption in anoxic marine sediments. Geology **4**: 297–300.

Bayon, G., C. Pierre, J. Etoubleau, M. Voisset, E. Cauquil, T. Marsset, N. Sultan, E. Le Drezen, and Y. Fouquet. 2007. Sr/Ca and Mg/Ca ratios in Niger Delta sediments: Implications for authigenic carbonate in cold seep environments. Mar. Geol. **241**: 93–109.

Berner, R. A. 1980. Early Diagenesis – A Theoretical Approach, Princeton University Press.

Boetius, A., K. Ravenschlag, C. J. Schubert, D. Rickert, F. Widdel, A. Gieseke, R. Amann, B. B. Jørgensen, U. Witte, O. Pfannkuche, and B. B. Jorgensen. 2000. A marine microbial consortium apparently mediating anaerobic oxidation of methane. Nature **407**: 623–626.

Bohrmann, G., and J. Greinert. 1998. Authigenic carbonates from the Cascadia subduction zone and their relation to gas hydrate stability. **18**: 647–650.

Bohrmann, G., K. Heeschen, and C. Jung. 2002. Widespread fluid expulsion along the seafloor of the Costa Rica convergent margin. Terra … **14**: 69–79.

Boudreau, B. P. 1997. Diagenetic Models and their Implementation: Modelling Transport and Reactions in Aquatic Sediments, Springer Verlag.

Boudreau, B. P., and R. L. Marinelli. 1994. A modelling study of discontinuous biological irrigation. J. Mar. Res. **52**: 947–968.

Bowes, H. L., and E. R. C. Hornibrook. 2006. Emission of highly 13C depleted methane from an upland blanket mire. Geophys. Res. Lett. **33**: 1–4.

Burton, E. A. 1993. Controls on marine carbonate cement mineralogy: Review and reassessment. Chem. Geol. **105**: 163–179.

Burton, E. A., and L. M. Walter. 1987. Relative precipitation rates of aragonite and Mg calcite from seawater: temperature or carbonate ion control? Geology **15**: 111–114.

Capo, R. C., B. W. Stewart, and O. A. Chadwick. 1998. Strontium isotopes as tracers of ecosystems processes: Theory and methods. Geoderma **82**: 197–225.

De Choudens-Sánchez, V., and L. A. González. 2009. Calcite and aragonite precipitation under controlled instantaneous supersaturation: elucidating the role of CaCO3 saturation state and Mg/Ca ratio on calcium carbonate polymorphism. J. Sediment. Res. **79**: 363– 376.

Chuang, P.-C., A. W. Dale, K. Wallmann, M. Haeckel, T. F. Yang, N.-C. Chen, H.-C. Chen, H.-W. Chen, S. Lin, C.-H. Sun, C.-F. You, C.-S. Horng, Y. Wang, and S.-H. Chung. 2013. Relating sulfate and methane dynamics to geology: Accretionary prism offshore SW Taiwan. Geochemistry, Geophys. Geosystems **14**: 2523–2545.

Cline, J. 1969. Spectrophotometric determination of hydrogen sulfide in natural waters. Limnol. Oceanogr. **14**: 454–458.

Curtis, C. 1987. Mineralogical Consequences of Organic Matter Degradation in Sediments: Inorganic/Organic Diagenesis, p. 108–123. *In* Marine Clastic Sedimentology. Springer Netherlands.

Dale, A. W., S. Sommer, M. Haeckel, K. Wallmann, P. Linke, G. Wegener, and O. Pfannkuche. 2010. Pathways and regulation of carbon, sulfur and energy transfer in marine sediments overlying methane gas hydrates on the Opouawe Bank (New Zealand). Geochim. Cosmochim. Acta **74**: 5763–5784.

Dasch, E. J. 1969. Strontium isotopes in weathering profiles, deep-sea sediments, and sedimentary rocks. Geochim. Cosmochim. Ac. **33**: 1521–1552.

Emrich, K., D. H. Ehhalt, and J. C. Vogel. 1970. Carbon isotope fractionation during the precipitation of calcium carbonate. Earth Planet. Sci. Lett. **8**: 363–371.

Fritz, P., and D. C. W. Smith. 1970. The isotopic composition of secondary dolomites. Geochim. Cosmochim. Acta **34**: 1167–1173.

Goldsmith, J. R., D. L. Graf, and H. C. Heard. 1961. Lattice constants of Carbonates, the calcium-magnesium. Am. Miner. **46**: 453–457.

Greinert, J., G. Bohrmann, and E. Suess. 2001. Gas hydrate-associated carbonates and methane-venting at Hydrate Ridge: classification, distribution, and origin of authigenic lithologies. Geophys. Monogr. Ser.

Grossman, E. L., and T. L. Ku. 1986. Carbon and oxygen isotope fractionation in biogenic aragonite: temperature effects. Chem. Geol. **59**: 59–74.

Haeckel, M., B. P. Boudreau, and K. Wallmann. 2007. Bubble-induced porewater mixing: A 3-D model for deep porewater irrigation. Geochim. Cosmochim. Acta **71**: 5135–5154.

Han, X., E. Suess, H. Sahling, and K. Wallmann. 2004. Fluid venting activity on the Costa Rica margin: new results from authigenic carbonates. Int. J. Earth Sci. 596–611.

Henry, P., X. Le Pichon, S. Lallemant, S. Lance, J. B. Martin, J. P. Foucher, A. Fiala-Médioni, F. Rostek, N. Guilhaumou, V. Pranal, and M. Castrec. 1996. Fluid flow in

and around a mud volcano field seaward of the Barbados accretionary wedge: Results from Manon cruise. J. Geophys. Res. **101**: 297–323.

Hensen, C., M. Nuzzo, E. Hornibrook, L. M. Pinheiro, B. Bock, V. H. Magalhães, and W. Brückmann. 2007. Sources of mud volcano fluids in the Gulf of Cadiz—indications for hydrothermal imprint. Geochim. Cosmochim. Acta **71**: 1232–1248.

Hensen, C., and K. Wallmann. 2005. Methane formation at Costa Rica continental margin—constraints for gas hydrate inventories and cross-décollement fluid flow. Earth Planet. Sci. Lett. **236**: 41–60.

Hensen, C., K. Wallmann, M. Schmidt, C. R. Ranero, and E. Suess. 2004. Fluid expulsion related to mud extrusion off Costa Rica—A window to the subducting slab. Geology **32**: 201.

Jørgensen, B. B. 1978. A comparison of methods for the quantification of bacterial sulfate reduction in coastal marine sediments. 1. Measurements with radiotracer techniques. Geomicrobiol. J **1**: 11–27.

Jørgensen, B. B., and D. C. Nelson. 2004. Sulfi de oxidation in marine sediments : Geochemistry meets microbiology. 63–81.

Joye, S. B., A. Boetius, B. N. Orcutt, J. P. Montoya, H. N. Schulz, M. J. Erickson, and S. K. Lugo. 2004. The anaerobic oxidation of methane and sulfate reduction in sediments from Gulf of Mexico cold seeps. Chem. Geol. **205**: 219–238.

Judd, A., M. Hovland, and L. Dimitrov. 2002. The geological methane budget at continental margins and its influence on climate change. Geofluids **2**: 109–126.

Kallmeyer, J., T. G. Ferdelman, A. Weber, H. Fossing, and B. B. Jørgensen. 2004. A cold chromium distillation procedure for radiolabeled sulfide applied to sulfate reduction measurements. Limnol. Oceanogr. Methods **2**: 171–180.

Karaca, D., C. Hensen, and K. Wallmann. 2010. Controls on authigenic carbonate precipitation at cold seeps along the convergent margin off Costa Rica. Geochemistry Geophys. Geosystems **11**: 1–19.

Kim, S. T., and J. R. O'Neil. 1997. Equilibrium and nonequilibrium oxygen isotope effects in synthetic carbonates. Geochim. Cosmochim. Acta **61**: 3461–3475.

Klaucke, I., D. G. Masson, C. J. Petersen, W. Weinrebe, and C. R. Ranero. 2008. Multifrequency geoacoustic imaging of fluid escape structures offshore Costa Rica: Implications for the quantification of seep processes. Geochemistry Geophys. Geosystems **9**: 1–16.

Kopf, A. J. 2002. Significance of mud volcanism. Rev. Geophys. **40**: 1–52.

Krause, S., V. Liebetrau, S. Gorb, M. Sanchez-Roman, J. a. McKenzie, and T. Treude. 2012. Microbial nucleation of Mg-rich dolomite in exopolymeric substances under anoxic modern seawater salinity: New insight into an old enigma. Geology **40**: 587–590.

Krüger, M., T. Treude, H. Wolters, K. Nauhaus, and A. Boetius. 2005. Microbial methane turnover in different marine habitats. Palaeogeogr. Palaeoclimatol. Palaeoecol. **227**: 6–17.

Kutterolf, S., V. Liebetrau, T. Mörz, A. Freundt, T. Hammerich, and D. Garbe-Schönberg. 2008. Lifetime and cyclicity of fluid venting at forearc mound structures determined by tephrostratigraphy and radiometric dating of authigenic carbonates. Geology **36**: 707.

Linke, P., K. Wallmann, E. Suess, C. Hensen, and G. Rehder. 2005. In situ benthic fluxes from an intermittently active mud volcano at the Costa Rica convergent margin. Earth Planet. Sci. Lett. **235**: 79–95.

Mau, S., H. Sahling, G. Rehder, E. Suess, P. Linke, and E. Soeding. 2006. Estimates of methane output from mud extrusions at the erosive convergent margin off Costa Rica. Mar. Geol. **225**: 129–144.

Mavromatis, V., R. Botz, M. Schmidt, V. Liebetrau, and C. Hensen. 2012. Formation of carbonate concretions in surface sediments of two mud mounds, offshore Costa Rica: a stable isotope study. Int. J. Earth Sci. , doi:10.1007/s00531-012-0843-7

McArthur, J. M., M. F. Thirlwall, M. Engkilde, W. J. Zinsmeister, and R. J. Howarth. 1998. Strontium isotope profiles across K/T boundary sequences in Denmark and Antarctica. Earth Planet. Sci. Lett. **160**: 179–192.

McAullife, C. 1971. GC Determination of solutes by multiple phase equilibration Chemical Technolgy. Chem. Technolgy **1**: 46–51.

Mörz, T., N. Fekete, A. J. Kopf, W. Brueckmann, S. Kreiter, V. Huehnerbach, D. G. Masson, D. A. Hepp, M. Schmidt, S. Kutterolf, H. Sahling, F. Abegg, V. Spiess, E. Suess, and C. R. Ranero. 2005. Styles and productivity of mud diapirism along the Middle American Margin, Part II, Mound Culebra and Mounds 11 and 12, in Mud volcanoes, geodynamics and seismicity, G. Martinelli and B. Panahi [eds.]. Springer Netherlands.

Naehr, T. H., P. Eichhubl, V. J. Orphan, M. Hovland, C. K. Paull, W. Ussler, T. D. Lorenson, and H. G. Greene. 2007. Authigenic carbonate formation at hydrocarbon seeps in continental margin sediments: A comparative study. Deep Sea Res. Part II Top. Stud. Oceanogr. **54**: 1268–1291.

Niemann, H., T. Lösekann, D. de Beer, M. Elvert, T. Nadalig, K. Knittel, R. Amann, E. J. Sauter, M. Schlüter, M. Klages, J. P. Foucher, and A. Boetius. 2006. Novel

microbial communities of the Haakon Mosby mud volcano and their role as a methane sink. Nature **443**: 854–8.

Peckmann, J., a Reimer, U. Luth, C. Luth, B. . Hansen, C. Heinicke, J. Hoefs, and J. Reitner. 2001. Methane-derived carbonates and authigenic pyrite from the northwestern Black Sea. Mar. Geol. **177**: 129–150.

Pierre, C., M.-M. Blanc-Valleron, J. Demange, O. Boudouma, J.-P. Foucher, T. Pape, T. Himmler, N. Fekete, and V. Spiess. 2012. Authigenic carbonates from active methane seeps offshore southwest Africa. Geo-Mar. Lett. **32**: 501–513.

Ranero, C., and R. von Huene. 2000. Subduction erosion along the Middle America convergent margin. Nature **404**: 748–52.

Ranero, C. R., I. Grevemeyer, H. Sahling, U. Barckhausen, C. Hensen, K. Wallmann, W. Weinrebe, P. Vannucchi, R. von Huene, and K. McIntosh. 2008. Hydrogeological system of erosional convergent margins and its influence on tectonics and interplate seismogenesis. Geochemistry Geophys. Geosystems **9**, doi:10.1029/2007GC001679

Saffer, D. M., and H. J. Tobin. 2011. Hydrogeology and Mechanics of Subduction Zone Forearcs: Fluid Flow and Pore Pressure. Annu. Rev. Earth Planet. Sci. **39**: 157–186.

Schmidt, M., C. Hensen, T. Mörz, C. Müller, I. Grevemeyer, K. Wallmann, S. Mau, and N. Kaul. 2005. Methane hydrate accumulation in “Mound 11” mud volcano, Costa Rica forearc. Mar. Geol. **216**: 83–100.

Schoell, M. 1988. Multiple origins of methane in the earth. Chem. Geol. **71**: 1–10.

Scholz, F., C. Hensen, Z. Lu, and U. Fehn. 2010. Controls on the 129I/I ratio of deep-seated marine interstitial fluids: “Old” organic versus fissiogenic 129-iodine. Earth Planet. Sci. Lett. **294**: 27–36.

Silver, E., M. Kastner, A. Fisher, J. Morris, K. McIntosh, and D. Saffer. 2000. Fluid flow paths in the Middle America Trench and Costa Rica margin. Geology **28**: 679–682.

Soeding, E., K. Wallmann, E. Suess, and E. Fluh. 2003. FS Meteor cruise report M 54/2-3:Caldera-Curacao.

Suess, E. 2002. Gashydrat – Eine Verbindung aus Methan und Wasser. Nov. Ac. Lc. **85**: 123–146.

Suess, E. 2010. Marine Cold Seeps, p. 188–198. *In* K.N. Timmis [ed.], Handbook of Hydrocarbon and Lipid Microbiology. Springer Berlin Heidelberg.

Tarutani, T., R. N. Clayton, and T. K. Mayeda. 1969. The effect of polymorphism Fractionation, and magnesium substitution of oxygen isotope between calcium carbonate and water. Geochim. Cosmochim. Acta **33**: 987–996.

Thauer, R. K. 1998. Biochemistry of methanogenesis: a tribute to Marjory Stephenson. Microbiology **144**: 2377–2406.

Tishchenko, P., C. Hensen, K. Wallmann, and C. S. Wong. 2005. Calculation of the stability and solubility of methane hydrate in seawater. Chem. Geol. **219**: 37–52.

Torres, M. E. E., K. Wallmann, A. M. M. Tréhu, G. Bohrmann, W. S. W. S. Borowski, and H. Tomaru. 2004. Gas hydrate growth, methane transport, and chloride enrichment at the southern summit of Hydrate Ridge, Cascadia margin off Oregon. Earth Planet. Sci. Lett. **226**: 168–175.

Treude, T., A. Boetius, K. Knittel, K. Wallmann, and B. Barker Jørgensen. 2003. Anaerobic oxidation of methane above gas hydrates at Hydrate Ridge, NE Pacific Ocean. Mar. Ecol. Prog. Ser. **264**: 1–14.

Treude, T., M. Krüger, A. Boetius, and B. Jørgensen. 2005. Environmental control on anaerobic oxidation of methane in the gassy sediments of Eckernfoerde Bay(German Baltic). Limnol. Oceanogr. **50**: 1771–1786.

Wallmann, K., G. Aloisi, M. Haeckel, P. Tishchenko, G. Pavlova, J. Greinert, S. Kutterolf, and A. Eisenhauer. 2008. Silicate weathering in anoxic marine sediments. Geochim. Cosmochim. Acta **72**: 2895–2918.

Wallmann, K., M. Drews, G. Aloisi, and G. Bohrmann. 2006. Methane discharge into the Black Sea and the global ocean via fluid flow through submarine mud volcanoes. Earth Planet. Sci. Lett. **248**: 545–560.

Whiticar, M. J. 1999. Carbon and hydrogen isotope systematics of bacterial formation and oxidation of methane. Chem. Geol. **161**: 291–314.

Chapter 4

Efficiency and Adaptability of the Benthic Methane Filter at Quepos Slide, Offshore Costa Rica

Philip Steeb[1]*, Stefan Krause[1], Peter Linke[1], Christian Hensen[1], Andrew W. Dale[1], Marianne Nuzzo[2], Tina Treude[1]*

[1]GEOMAR Helmholtz Centre for Ocean Research Kiel, Wischhofstrasse 1-3, D-24148 Kiel, Germany

[2]LNEG, Marine Geology Department, Alfragide, Portugal & Institute Dom Luiz, University of Lisbon, Lisbon, Portugal. Now at Integrated Geochemical Interpretation, Ltd. (UK)

*Corresponding Author: psteeb@geomar.de, ttreude@geomar.de

Working Title: Quepos Slide SLOT System

Abstract:

Large amounts of methane are delivered by fluids through the erosive forearc of the convergent margin offshore Costa Rica and lead to the formation of cold seeps at the sediment surface. Besides mud extrusion, many cold seeps are created by massive landslides induced by seamount subduction or fluid migration. Most of the dissolved methane reaching the seafloor at cold seeps is oxidized within the benthic microbial methane filter by anaerobic oxidation of methane (AOM). Measurements of AOM and sulfate reduction, as well as, numerical modeling of porewater profiles, reveal a highly active and efficient benthic filter at Quepos Slide site; a huge landslide on the continental slope between the Nicoya and Osa Peninsula. Integrated areal rates of AOM range from 12.87 ± 5.98 mmol m^{-2} d^{-1} to 45.15 ± 11.48 mmol m^{-2} d^{-1} and only 1 to 2.5% of the delivered methane was released into the water column.

Additionally, two parallel sediment cores were used for in vitro experiments in a recent developed Sediment-Flow-Through (SLOT) system to simulate an increased fluid and methane flux. The benthic methane filter revealed a high adaptability to

increased fluid flow and recovered the previous efficiency of methane oxidation within 150-170 d response time.

Introduction

Organic carbon accumulation at continental margins can lead to the formation of large methane reservoirs through its biological or thermogenic breakdown (Judd et al. 2002). Stored methane gas may be transported upwards together with ascending fluids or by molecular diffusion to form gas hydrate layers within the gas hydrates stability zone (GHSZ) (Torres et al. 2004; Burwicz et al. 2011; Wallmann et al. 2012). The release of methane-charged fluids at the sediment-water interface creates so called “cold seeps” (Judd et al. 2002; Suess 2010). Within the surface sediment, a majority of the methane is consumed by the anaerobic oxidation of methane (AOM) (Hinrichs and Boetius 2002). AOM is coupled to sulfate reduction and produces bicarbonate and sulfide. The reaction is mediated by a consortia of anaerobic methanotrophic (ANME) archaea and sulfate-reducing bacteria (SRB) (Boetius et al. 2000). Recent studies propose that some ANME can reduce sulfate without the aid of SRB (Milucka et al. 2012). Additionally, the use of other electron acceptors such as Mn, Fe (Beal et al. 2009), or nitrate (Ettwig et al. 2010) is also possible. However, sulfate is the most abundant electron acceptor in seawater and AOM coupled to sulfate reduction is, to our knowledge, by far the most important anaerobic pathway for methane oxidation (Reeburgh 2007). The sediment zone, in which methane and sulfate overlap, is called the sulfate-methane transition zone (SMTZ). The depth of the SMTZ is dependent on (1) sulfate depletion resulting from organic matter degradation, (2) the flux of methane from below the SMTZ (3) the advective fluid flow rate (Treude et al. 2003; Orcutt et al. 2011). The SMTZ can be located as deep as 160 meters below the seafloor (mbsf) at continental margins and sometimes even at 300 mbsf in the deep sea (Borowski et al. 1999). In coastal sediments, the SMTZ is influenced by an enhanced supply of organic matter and, subsequently, it is often located close to the sediment-water interface compared to sediments in greater water depths (Hinrichs and Boetius 2002). At seepage sites, advective fluid flow pushes the SMTZ closer to the surface and reducing it to sometimes only tens of centimeters below the seafloor (cmbsf) (Treude et al. 2003; Niemann et al. 2006; Krause et al. 2014). At the center of the Hakon Mosby Mud Volcano, high advective fluid flow even

inhibits sulfate penetration into the sediment (de Beer et al. 2006; Niemann et al. 2006), resulting in the absence of a SMTZ. In general, the depth of the SMTZ can determine which seep organisms can access the produced sulfide. As a result, prevailing communities can be used as indicators of seepage intensity (Sahling et al. 2002; Levin 2003; Treude et al. 2003; Mau et al. 2006; Fischer et al. 2012).

Subduction zones represent large-scale systems of sediment and element recycling at continental margins. Fluids are mobilized by the compaction of subducted sediments or by clay mineral dehydration (Hensen et al. 2004; Tryon et al. 2010) and ascend along faults to the sediment surface, transporting methane and other hydrocarbons. When the fluids are highly enriched in hydrocarbon gases and meet adequate pressure-temperature conditions, gas hydrates may precipitate (Hensen and Wallmann 2005). Gas hydrates sometimes block fluid paths (Tryon et al. 2002; Minami et al. 2012) and change the composition of fluids flowing through the GHSZ. Alternatively, dissociating gas hydrates act as additional sources for methane and fluids (Kvenvolden 2002), or dilute fluids by freshening (Hesse et al. 2000; Hensen et al. 2004).

In this study, we present the first direct rate measurements of AOM and sulfate reduction for Quepos Slide and compare the measurements with modeled rates. Since methane is an important greenhouse gas, it is of prime interest how much methane the microbial benthic methane filter can consume and how fast the methane filter can adapt to new flow conditions. To answer this particular question, we performed laboratory experiments with undisturbed seep sediments from Quepos Slide and subjected them to different flow conditions. For this part of the study, we used a newly developed Sediment-Flow-Through system referred to as SLOT (Steeb et al. submitted), which mimics natural fluid-flow regimes.

Geological Setting: At the Middle American Trench, the Cocos Plate in the north and Nazca Plate in the south are subducted below the Caribbean Plate at a velocity of 8.8 cm yr^{-1} (Syracuse and Abers 2006). At the Middle American Trench, seep features like mud volcanoes, mud diapirs, and pockmarks are very abundant. More than 40 seeps have been identified at the central Costa Rican Pacific Trench, on average one seep every 4 km (Sahling et al. 2008). Recent high-resolution mapping revealed even greater seep density in this region (Kluesner et al. 2013). Between the

Nicoya (north) and Osa (south) Peninsula, seamounts from the Nasca Plate are subducted (Ranero and von Huene 2000), resulting in slope failures and huge landslides or scarps (e. g., Jaco Scarp, BGR landslide, GEOMAR landslide; Harders et al. 2011; Ranero et al. 2008). Landslide-induced seeps are created by opening new structural and stratigraphical fluid pathways (Ranero et al. 2008; Mau et al. 2012) or by gas hydrate dissociation resulting from altered pressure and temperature conditions.

Fluids and related methane flux can vary spatially, temporally, in origin, compositions, and velocity. Temporal variations can be caused by gas hydrate formation and dissociation or triggered by earthquakes, which are frequent in this active subduction zone.

The “dissimilar” twin mounds, “Mound 11” and “Mound 12”, located at 1000 m water depth, half-way between the Nicoya and Osa Peninsula, have been extensively investigated to assess the controls on temporal and spatial difference in fluid flow regimes and fluid sources. The mounds are located approximately 600 m apart in the same fault zone, although they differ in activity, fluid flow (Hensen et al. 2004; Linke et al. 2005; Karaca et al. 2010; Krause et al. 2014), fluid origin (Hensen et al. 2004; Han et al. 2004; Schmidt et al. 2005), and microbial activity (Krause et al. 2014). Individual mound histories of the last 10^5 yr can be characterized by high active phases of up to 50 kyr in duration interrupted by phases of inactivity (Kutterolf et al. 2008). Besides this long-term variability, very short periods of increased fluid flow have been identified. Füri et al. (2010) indicated a two-month-long fluid pulse with increased advective flow from 5 cm yr^{-1} to 20 cm yr^{-1} at Mound 11 in October 2005. In the water column of this region very different methane concentrations were detected in the year 2003 and 2004, presumably caused by an earthquake in June 2003 (Mau et al. 2007).

The research area of the present study, the Quepos Slide, is located south of the twin Mounds 11 and 12. This landslide is approximately 9.5 km wide and 8 km long (Harder 2011). The translational slide has a headwall of 160 m and the slide head is located at ~400 m below sea level (mbsl) in the Eastern Pacific oxygen minimum zone (OMZ; between 250 -550 m water depth; Bohrmann et al. 2002). Four tongues of the landslide can be identified, which reach down to ~800 water depth (Bohrmann

et al. 2002; Harders et al. 2011), indicating three subsequent events following the initial slide (Harders et al. 2011). The Quepos Slide was most likely caused by seamount subduction (Harders et al. 2011). Along the toe, fluids and gas can migrate from hydrates inside the GHSZ. Chemosynthetic organisms are abundant, with bacterial mats present throughout, while authigenic carbonates and clams can be found at deeper areas and at the toe of the slide (Bohrmann et al. 2002). Directly below the headwall, the sediments are covered by bacterial mats (Bohrmann et al. 2002; Sahling et al. 2008; Karaca et al. 2012). At Quepos Slide fluid flows vary between 1 and 40 cm yr^{-1} and AOM has been modeled to vary between 1.5 and 42.1 mmol m^{-2} d^{-1} (Karaca et al. 2012). According to the model, 53% (~316 x 10^3 mol yr^{-1}) of the methane is oxidized by the highly active benthic microbial methane filter, while 47% (280 x 10^3 mol yr^{-1}) is released into the water column. An elevated methane concentration of 72 nmol l^{-1} was observed in the seawater directly above the slide head, compared to 0-2 nmol l^{-1} in the bulk water (Bohrmann et al. 2002).

Methods

Surface sediments from Quepos Slide were obtained by a video-guided multi-corer (TV-Muc) during the GEOMAR research cruise SO206 of the German research vessel RV Sonne. Two sites (SO206-29, SO206-31) from the headwall of Quepos Slide, both of which were covered by bacterial mats, were sampled (Table 1). All subsampling procedures were performed on board at 4°C immediately after obtaining the sediments. Three replicate cores of each TV-Muc were used for (1) porewater analyses, (2) *ex situ* AOM and sulfate reduction rate determinations, and (3) methane concentration determination. Additionally, two replicate cores of SO206-31(Muc) were sub-sampled for laboratory experiments (sediment flow-through system, see below).

Table 1: Sampling sites of the Quepos Slide, SMTZ in cm below seafloor (bsf).

Station	Latitude (S)	Longitude (W)	Water depth m	Depth of SMTZ cmbsf
SO206-St29	-8°51.29'	-84°12.60'	402	12.5 - 22.5
SO206-St31	-8°51.12'	-84°13.06'	399	5.0 - 15.0

Porewater measurement (ex situ): Porewater of the ex situ samples were extracted by a pressure-filtration system performed with argon. Total alkalinity (TA) was analyzed onboard via titration (Ivanenkov and Lyakhin 1978). Sulfide was determined photometrically by methylene blue method (Cline 1969). Sub-samples for the determination of sulfate, chloride, and bromide were frozen and analyzed at GEOMAR (Kiel, Germany) by ion chromatography (Compact IC 761) upon return. Further porewater sampling and analytical procedures are described in detail by Krause et al. (2014).

Methane (ex situ): For methane determination, 10 cm^3 of sediment was transferred to glass vials filled with 10 ml 10% KCl for poisoning and headspace equilibration. Methane concentrations were measured onboard using a Shimadzu GC14A gas chromatograph fitted with a Restek® Alumina Bond capillary column and operated with nitrogen as carrier gas.

Microbial rate measurement (ex situ): Ex situ turnover rates of sulfate reduction and AOM were determined by radiotracer techniques. For both sulfate reduction and AOM, three replicate polycarbonate tubes (26 mm inner diameter, 250 mm length) were sub-sampled from one MUC core and incubated by whole core incubation (Jørgensen 1978). Additional bulk sediment was sampled to produce controls. Fifteen µl $^{14}CH_4$ (1–2 kBq dissolved in anoxic, sterile water; specific activity 22.28 GBq $mmol^{-1}$), and 6 µl $^{35}SO_4^{2-}$ (200 kBq dissolved in water; specific activity 37 TBq $mmol^{-1}$), was injected into the sediment AOM and sulfate reduction cores, respectively, at a vertical resolution of 1 cm; the cores were then incubated for 24 h in the dark at in situ temperature (8°C). After incubation, the sediment core was sliced in 1-cm intervals and the sediments was added to 20 ml NaOH (2.5% w/v, 40 ml glas vials with rubber stopper) for AOM, and to 20 ml zinc acetate (20% w/v, 50 ml plastic vials) for sulfate reduction. For controls (five each), 5 cm^3 sediment were transferred into the respective chemicals before the tracer was added (see above). AOM was determined according to Treude et al (2005) (GC and Combustion) and Joye et al. (2004) ($^{14}CO_2$ trapping). Sulfate reduction was determined using the cold chromium distillation method after Kallmeyer et al. (2004).

Numerical Model approach: Porewater profiles and AOM turnover rates were modeled using a one-dimensional transport reaction model, previously used and

described by Krause et al. (2014). Calcification was not of interest in this study, hence the kinetic constant of Ca-carbonate precipitation was set to zero (no carbonate precipitation). Because the sampling sites were located above the GHSZ (Wallmann et al. 2012), methane concentrations were calculated using an applicable model based on Tishchenko et al. (2005), which was also previously used by Karaca et al. (2012). Table x provides an overview of fitted, measured, and calculated parameters of the model.

Sediment-Flow-Through System: The response of the sediment to changes in fluid and methane fluxes was studied using a newly developed Sediment-Flow-Through (SLOT)-system (Steeb et al. 2014)which mimics natural flow conditions with diffusive supply of sulfate to the sediment surface and advective methane supply from the bottom of the core. The system enables continuous monitoring of geochemical gradients inside the sediment as well as in the in- and outflow. For SLOT experiments, two replicate multicorer cores from station SO206-31 were sub-sampled with specific SLOT liners (Steeb et al. 2014), closed with rubber stoppers, and sealed with electrical tape for transport. At GEOMAR, filters (glass fiber, Whatman GF/F) were applied at the bottom of the sediment core and at the lower and upper cap, as previously described in Steeb et al. (2014).

Two different seawater media were used in the SLOT-incubations. One medium, resembling "seawater", was amended with natural sulfate concentration (28.0 mM) and was delivered to the sediment from top by diffusion. The other medium, resembling "seepage" fluid, carried dissolved methane (965 ± 180 µM) and was sulfate-free. Seepage medium was delivered to the cores by advection from the bottom. Both media were based on the sulfate reducer medium developed by (Widdel and Bak 2006). In the “seepage” medium, $MgSO_4$ was replaced by MgCl. Both media were anoxic, with a pH adjusted to 7.5, and a salinity of 35. Bromide served as an inert tracer and was present only in the methane-loaded seepage medium (800 µmol l^{-1}). Hence, the depth where bromide and sulfate concentrations overlapped was interpreted as the SMTZ. Medium composition and the gas headspace composition of the reservoirs are summarized in Table 2.

SLOT experiments were performed with sediment cores under two different flow regimes: one with relatively low advective fluid flow (10.6 cm yr^{-1}), here further

referred as the low flow core (LFC), and one with a 10-fold higher advective fluid flow (106.3 cm yr^{-1}), further referred as the high flow core (HFC). Fluid flow velocities at Quepos Slide has been determined previously by modeling (1 – 40 cm yr^{-1}; Karaca et al. 2012). Neighboring seeps exhibit similar or even higher (up to 200 cm yr^{-1}) advective flow rates (Hensen et al. 2004; Linke et al. 2005; Karaca et al. 2010; Krause et al. 2014).

Table 2: Salt concentrations of the two different media used in the SLOT-System. Seawater medium with sulfate was delivered from the top, seepage medium with methane and without sulfate from the bottom. In the last line, the gas in the medium headspace is denoted.

	Seawater medium (with SO_4^{2-})	**Seepage medium (with CH_4)***
Salts	**in mmol l^{-1}**	**in mmol l^{-1}**
KBr	0.006	0.756
KCl	8.050	8.050
$CaCl_2$ $2H_2O$	10.000	10.00
$MgCl_2$ $6H_2O$	27.890	55.490
$MgSO_2$ $7H_2O$	27.600	0.000
NaCl	451.000	451.000
Medium headspace	N_2	CH_4

* $FeSO_4$ (trace element) was replaced by FeCl

The applied fluid flow rates were strong enough to observe considerable changes within the time frame of one year and were not too strong to reduce the sulfate penetration depth to less than 1 cm.

Table 3: Overview of methane flux, advective flow, and pump rate in the low and high flow core (top) as well as experimental phases and run times (bottom) under the low and high flow regime.

methane flux	**low flow**	**high flow**
in mmol m^{-2} d^{-1}	0.42	4.2
advective flow in cm yr^{-1}	10.6	106.3
pumping rate µl min-1	0.4	4
Hydrological Residence Time (HRT)	1080	108
running time in d	**total time**	**phase time**
pre-run	-40 - 0	40
main run	0 - 260	260
swapped run	260 - 350	90

In the initial preparation phase of the experiment (40 days), the outflow of the system was located at the bottom of the core and only methane-free seawater medium was

pumped from top to bottom to establish a homogeneous sulfate distribution and anoxic conditions throughout the entire sediment column. In the subsequent first experimental phase, the outflow was located at the top of the core and seawater medium was delivered to overlying seawater at a pump rate of 20 µl min^{-1}. Henceforward, sulfate was transported into the sediment core solely via diffusion. From the bottom, seepage medium was supplied at 0.5 µl min^{-1} (LFC) and 5 µl min^{-1} (HFC). With an average inflow methane concentration of 965 ± 180 µmol l^{-1} in the seepage medium, a methane flux of 0.28 and 2.81 mmol m^{-2} d^{-1} was calculated for the LFC and HFC core, respectively. Applied methane concentrations and resulting fluxes were considerably lower compared to in situ conditions (after Tishchenko et al. 2005; Karaca et al. 2012), since cores were not pressurized. After 260 d the first experimental phase was finished and pump rates were swapped from low to high flow, and vice versa, marking the beginning of the second and last experimental phase. After 316 d, the experiment was terminated and the cores were sliced and sub-sampled for further analyses.

Geochemical parameters during SLOT experimentation: During the SLOT experiments, geochemical parameters were measured in 1-cm depth intervals throughout the sediment core. In addition, also the in- and out-flowing fluids were monitored. Sulfide concentrations, pH, and redox potential were measured with microsensors (sulfide needle sensor, H_2S-N, tip diameter 0.8 mm, Unisense; pH, MI 411 B, Gauge 20, Microelectrodes Inc.; redox potential needle sensors, MI-800, Gauge 25, Microelectrodes Inc.). Porewater samples for the determination of sulfate, bromide, and total alkalinity (1.5-2 ml) concentration analysis were obtained using pre-installed rhizones (CSS-F, length 5 cm, diameter 2.5 mm, pore size 0.2 µm, rhizosphere). The in- and outflow of both cores were sampled with glass syringes for the determination of sulfate, bromide, total alkalinity and methane concentration. All sampling and measurement proceedings for the experiment are described in detail by Steeb et al. (2014).

Experiment termination and final sampling: At the end of the experiment porewater was sampled for sulfide (0.5 ml), sulfate, bromide and total alkalinity (1.5 ml). Sulfide was analysed after Cline (1969), sulfate and bromide by ion chromatography (Compact IC 761, Cl^-, SO_4^{2-}, conductivity detector; Br^- UV/VIS detector lambda 1010 at 230 nm) and total alkalinity by titration (876 Dosimat plus,

Metrohm, Ivanenkov and Lyakin 1978). Nitrate and ammonium (2 ml) were only sampled at the end of the experiment and analysed by photometric methods following Grasshoff et al. (1983).

After the final porewater sampling from the SLOT cores, sediment sub-samples of each core were taken. For radiotracer determinations of AOM and sulfate reduction, two sub-cores (polycarbonate, length 260 mm, inner diameter 26 mm) were collected from each SLOT core and treated after the protocols mentioned above. For determination of methane concentrations, each SLOT sediment core was sampled in 1 cm intervals (2 cm^3 volume sub-samples) using cut-off syringes (3 ml, PE). The sediment samples were transferred into glass vials (13ml) with 5 ml 2.5% w/v NaOH. Vials were closed with butyl rubber stoppers and shaken directly after sampling. Methane was analyzed by gas chromatography (Hewlett Packard Series II) with a packed column (Haye SepT, 6 ft, 3.1 mm inner diameter, 100/120 mesh, Resteck, carrier gas: He 20 ml min^{-1}, combustion gas: synthetic air 240 ml min^{-1}, H_2 20 ml min^{-1}).

The remaining sediment was sampled in 2-cm depth intervals. For porosity measurements, approximately 2 cm^3 samples were obtained using cut-off syringes (3 ml, PE), transferred to pre-weighted vials, and weighed, before and after the sample was freeze-dried. Porosity was then calculated by the difference in weight (Dalsgaard et al. 2000). Sub-samples of the dried sediment were used to determine total carbon (TC), total nitrogen (TN), total sulfur (TS) and total organic carbon (TOC) of the solid phase. TC, TN, TS, and TOC were analyzed using a CARLO ERBA Elemental Analyzer NA 1500. For TOC determination, inorganic carbon was removed by adding hydrochloric acid. From the difference between TC and TOC, total inorganic carbon (TIC) was calculated. All analyses of the solid phase were carried out in duplicate. The detailed sampling procedure and subsequent analytical procedures are described in Steeb et al. (2014).

Methane emission from the sediment was calculated by multiplying the out-flow methane concentrations with the dilution factor (41 and 5 for LFC and HFC, respectively) and the fluid flow (10.6 and 106.3 cm yr^{-1} for LFC and HFC, respectively) according to Steeb et al. (2014). AOM rates were calculated from the

difference between in- and outflow methane concentrations before (258 d) and after (316 d) fluid flow velocity change according to Steeb et al. (2014).

Results:

Ex situ profiles

Both MUC cores (SO206-29 and SO-206-31) were sampled in ~ 400 m water depth from sediments covered with bacterial mats, which are indicative for high methane fluxes (Torres et al. 2002; Treude et al. 2003).

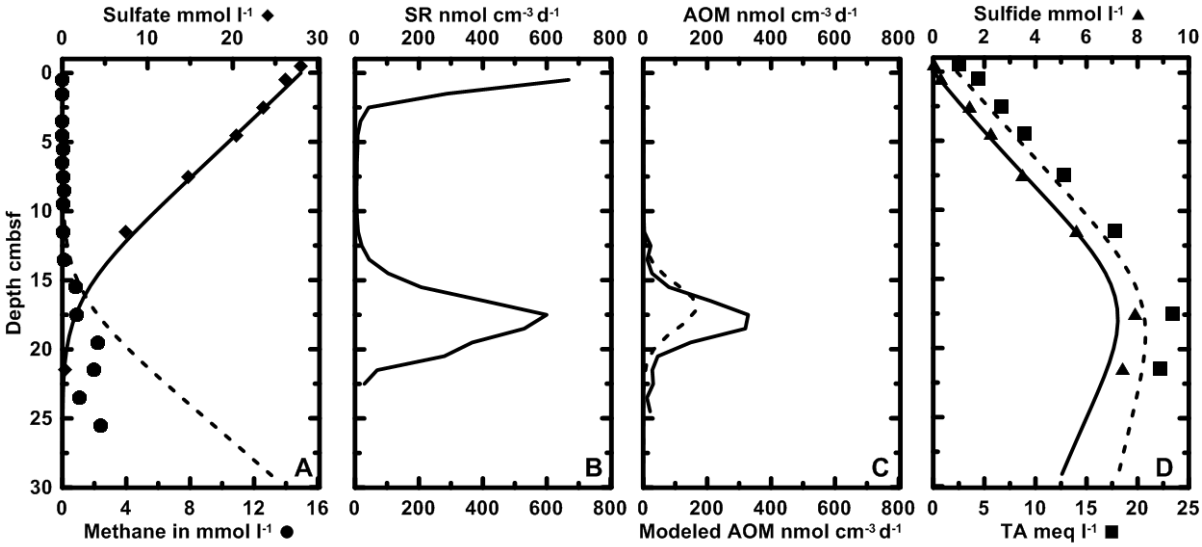

Figure 1: Depth profiles of measured and modeled porewater parameters as well as microbial turnover rates for SO206-29 (MUC), sampled from 402 m water depth. A) measured (dots) and modeled sulfate concentrations (solid line) as well as measured (diamonds) and modeled (dashed line) methane concentrations, (B) average measured sulfate reduction rates (bold line), C) average measured AOM (bold line), as well as modeled AOM rates (dashed line), D) measured (triangles) and modeled sulfide concentration (solid line), measured (squares) and modeled (dashed line) total alkalinity.

At station SO-206-29, sulfate decreased from 28 mmol l^{-1} at the sediment surface to zero at the bottom of the core (26 cm below sea floor (cmbsf)) (Fig. 1A). Conversely, methane concentrations were low (0.0 – 0.1 mmol l^{-1}) in the upper 15 cmbsf and increased below this zone to a maximum of 2.4 mmol l^{-1} at the bottom (Fig. 1A). Accordingly, the sulfate-methane transition zone was located at approximately 17.5 cmbsf. Two maxima of sulfate reduction rates were identified in one of the replicate cores at the top (up to 1821 nmol cm^{-3} d^{-1}) and between 12.5 and 22.5 cmbsf (up to 879 nmol cm^{-3} d^{-1}) (Fig. 1B). AOM coincided with the second sulfate reduction

maxima and reached rates up to 569 nmol cm^{-3} d^{-1} (Fig. 1C). Sulfide and total alkalinity (TA) increased from the top (0.0 mmol l^{-1} and 2.5 meq l^{-1}, respectively) to a maximum within the SMTZ (7.9 mmol l^{-1} and 23.4 meq l^{-1}, respectively, at 17.5 cm sediment depth), (Fig. 1D). Areal rates integrated over 0-15 cmbsf were similar between AOM (on average 12.87 ± 5.98 mmol m^{-2} d^{-1}) and sulfate reduction (on average 13.38 ± SD 13.61 mmol m^{-2} d^{-1}) with a ratio of 0.96 (AOM:sulfate reduction), respectively.

Best fit for the model resulted in a fluid flow of 2.5 cm yr^{-1} and an areal AOM rate of 5.4 mmol m^{-2} yr^{-1} (Table 4). In total, more than 99% of the methane was oxidized by AOM and only 1% was released to the seawater. Fitted porewater profiles and AOM rates are shown in Fig. 1.

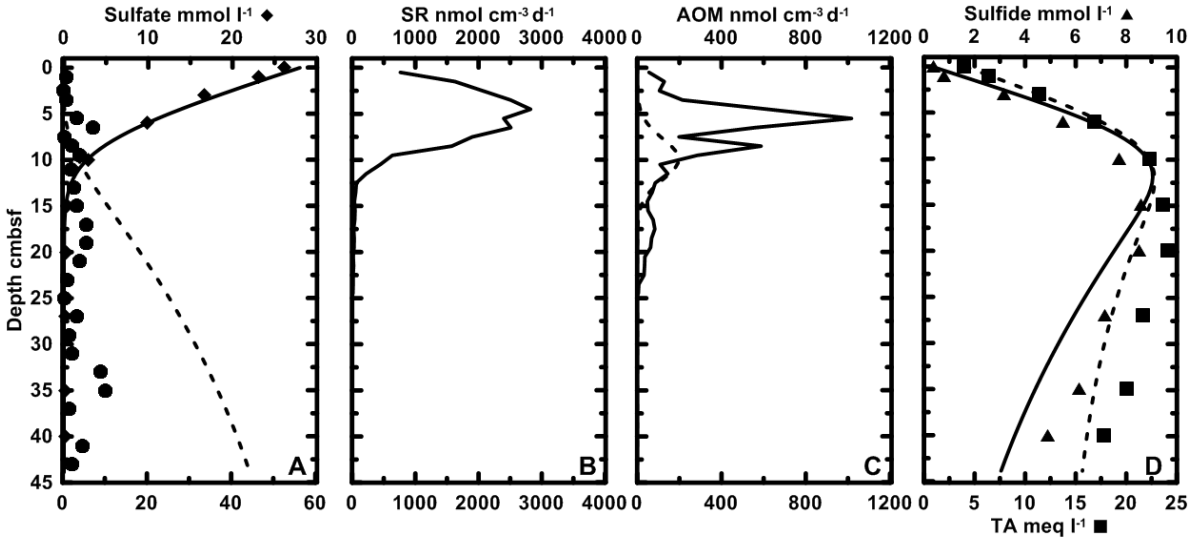

Figure 2: Porewater and modeled profiles and turnover rates of SO206-31Muc sampled in 401 m water depth. A) Sulfate concentration of the porewater (dots) , and methane concentration of the sediment (diamonds), modeled sulfate (solid line) and methane (dashed line)concentration B) three replicates of sulfate reduction rates (thin lines and symbols) and the average (bulk line), C) three replicates of AOM rates (thin lines and symbols), the average (bulk line), and modeled AOM (dashed line), D) sulfide (triangles), total alkalinity (squares) concentrations, and modeled sulfide (solid line) and total alkalinity (dashed line).

In the second core, SO206-31, sulfate decreased to 0 mmol l^{-1} within the first 15 cm sediment depth and considerable methane concentrations (> 3.4 mmol l^{-1}) were observed at 5 cmbsf (Fig. 2A). The observed maximum methane concentration was 10.2 mmol l^{-1} (20.5 cmbsf). Accordingly, the SMTZ was located at approximately 5 - 15 cmbsf. Sulfate reduction and AOM occurred between 0 and 12.5 cmbsf with a sulfate reduction maximum (12052 nmol cm^{-3} d^{-1}) at the top of the SMTZ (~2.5

cmbsf) and an AOM maximum (1400 nmol cm^{-3} d^{-1}) in the upper part of the SMTZ (5.5 cm cmbsf) (Fig. 2B, C). Highest sulfide and TA concentrations were measured within the SMTZ between 10 and 15 cmbsf (8.6 mmol l^{-1} and 24.1 meq l^{-1}, respectively) (Fig. 2D). Integrated areal sulfate reduction rates over 0-15 cm (218.90 ± 159.80 mmol m^{-2} d^{-1}) were around 5 times (AOM: SR = 0.21) higher compared to the integrated areal rates of AOM (45.15 ± 11.48 mmol m^{-2} d^{-1}) of the same depth.

Table 4: Summary of model input parameters used for numerical modeling of biogeochemical processes at Quepos Slide and major model results

Parameter	Quepos Slide SO206-St29	Quepos Slide SO206-St31	Unit	Parameter source
Model parameter values				
Length core	32	44	cm	measured
Length of simulated column	150	150	cm	fitted
Number of model layers	200	200		fitted
Temperature	8	8	°C	measured
Salinity	35	35	PSU	measured
Pressure	41	41	bar	measured
Porosity at sediment surface	0.95	0.93		measured
Porosity at inbfinity sediment depth	0.74	0.70		fitted
Attenuation coefficient for porosity decrase with depth	0.04	0.04	cm^{-1}	fitted
Coefficient for tortuosity calculation	1	1		fitted
Burial velocity at depth	0.02	0.02	cm yr^{-1}	fitted
Fluid flow at the sediment water interface	3.5	4	cm yr^{-1}	fitted
Kinetic for AOM	10000	20000	cm $mmol^{-1}$ yr^{-1}	fitted
Kinetic constant for $CaCO_3$ precipitation	0	0	yr^{-1}	fitted
Density of porewater	1.03184	1.03184		calculated
Density of dry solids in sediment	2.5	2.5	g cm^{-3}	assumed
Kinetic constant for H_2S removal from porewater	0.001	0.0005	mmol cm^{-3} yr^{-1}	fitted
Attenuation coefficient for decrease in H2S removal rate	0.0001	0.00005	cm^{-1}	fitted
Non-local mixing coefficient	0	100	yr^{-1}	fitted
Depth of irrigated layer	1	0.2	cm	fitted
Width of irrigated layer	1	0.2	cm	fitted
Porewater concentration upper/lower boundary				
Bottom water / Bottom sediment SO_4^{2-}	28.00 / 0.00	28.00 / 0.00	mmol l^{-1}	measured
Bottom water / Bottom sediment CH_4	0.00 / 61.00	0.00 / 61.00	mmol l^{-1}	calculated*
Bottom water / Bottom sediment Cl^-	553.00 / 350.00	548.00 / 320.00	mmol l^{-1}	measured
Bottom water / Bottom sediment HCO_3^-	2.30 / 12.00	2.30 / 14.00	mmol l^{-1}	measured
Bottom water / Bottom sediment TH_2S	0.00 / 0.00	0.03 / 0.00	mmol l^{-1}	measured
Model Results				
Methane flux at sediment bottom	5.95	6.41	mmol m^{-2} d^{-1}	modeled
Methane Efflux at sediment water interface	0.00	0.00	mmol m^{-2} d^{-1}	modeled
Percentage of consumed methane	100	100	%	modeled
Anaerobic oxdation of methane	5.95	6.41	mmol m^{-2} d^{-1}	modeled

*Calculated after Tishchenko et al. 2005

In comparison, modeled AOM rates were generally lower than the measured ones. Using a fitted fluid flow of 6 cm yr^{-1} the corresponding modeled areal AOM rate was 5 times lower (9.3 mmol m^{-2} d^{-1}) than the areal rate obtained by radiotracer incubations. Around 2.5% of the methane flux was estimated to be released from the sediment

into the water column. Fitted porewater profiles and modeled AOM rates are shown in Fig. 2.

SLOT incubation experiments

Main phase of the Experiment (0-260 d runtime):

The LFC core

In the low flow regime core (LFC) incubations, bromide concentration, which was used as a tracer to track the seepage medium, was always very low and near the quantification limit (20 µmol l^{-1}). Values increased only weakly in the lowest 5 cm of the core reaching a maximum of 45 µmol l^{-1} after 49 d (Fig. 3D). Sulfate, which was delivered from the top by diffusion, decreased only minimal at the bottom of the core (27.2 mmol l^{-1}), which was in accordance with a small increase in bromide (up to ~45 µmol l^{-1}) in this section, confirming a slow advection of methane-enriched seepage medium. After 105 d, sulfate levels stabilized around 26 mmol l^{-1} at the bottom of the core and did not further decrease during the low flow phase.

In the first 105 d, **sulfide concentrations** of the LFC core varied between 23 and 300 µmol l^{-1} over depth with a maximum between 9 - 11 cm (Fig. 3B, E, H). After 171 d, a sulfide peak (920 µmol l^{-1}, Fig. 3K) occurred at 0.26 cm sediment depth, while no sulfide was detected in the overlaying water. Below the peak, sulfide varied between 300 and 500 µmol l^{-1}. Thirty days later (201 d runtime), maximum sulfide concentrations up to 230 µmol l^{-1} were observed between 1.5 and 10.7 cm sediment depth (Fig. 3N). After 258 d, directly before changing from low to high fluid flow, maximum sulfide concentrations were 115 µmol l^{-1} at 4.5-5.5 cmbsf (Fig. 3Q) and decreased to a minimum of 36 µmol l^{-1} near the sediment-water interface.

TA was predominantly lower inside the cores than in the media (30 meq l^{-1}). During the LFC, TA continuously decreased over the time from ~30 to ~24 meq l^{-1} below ~9 cm (Fig. 3B, E, H, K). After 171 d, TA varied between 28.7 and 21.7 meq l^{-1}. Directly before the change of fluid flow (258 d), TA increased from the top (23.3 meq l^{-1}) to the bottom (26.7 meq l^{-1}; Fig. 3Q).

Initial **redox potential** of the LFC was -50 mV at the top and around -150 mV below 2 cm sediment depth (Fig. 3C). After 49 d, the redox potential became more negative

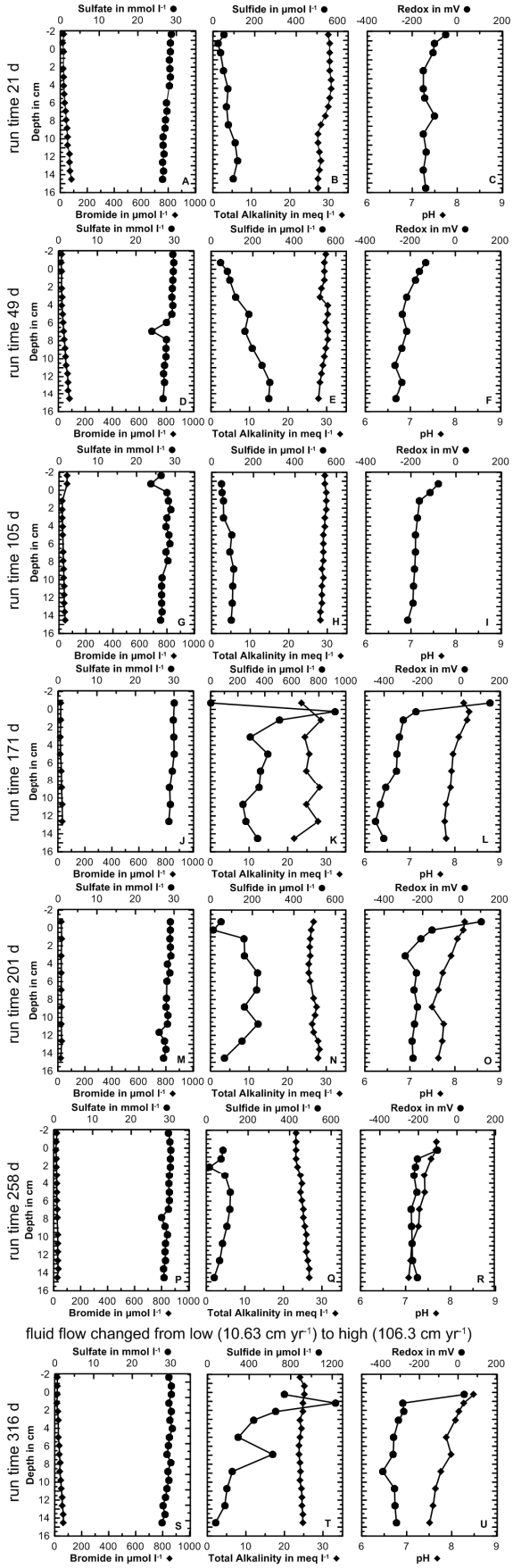

Figure 3: Geochemical parameters measured in the sediment of the low flow regime (LFC) core from Quepos Slide after 21 (A, B, C), 49 (D and E), 105 (G, H, and I), 171 (J, K, L), 202 (M, N, O), and 258 (P, Q, R) days of runtime. Shown are porewater profiles of sulfate, bromide (A, D, G, J, M, P), sulfide, total alkalinity (B, E, H, K, N, Q), redox potential (C, F, I, L, O, R) and pH (I, L, O, R).

(-130 mV at top and between -160 to -270 mV below, Fig. 3F); after 105 d, the redox potential increased to -80 mV at the top (Fig. 3I). Between 171 and 202 d of runtime, the overlaying water of the core showed a pink color caused by the oxygen indicator resazurin (Visser et al. 1990). At the same time, redox potential was positive (between 150 and 100 mV) at the sediment water interface (Fig. 3L, O), probably resulted by oxygen intrusion. Nevertheless, free oxygen would result redox potential above 350 mV (Schulz 2000), therefore oxygen was only temporally available. Deeper inside the sediment redox values between -200 and -400 mV were reached (Fig 3L, O).

Directly before changing the fluid flow (258 d), the redox potential of the LFC was -100 mV in the overlaying water and around -200 mV inside the sediment (Fig. 3R).

After 171 d runtime, **pH** was highest at the sediment-water interface (8.2, Fig. 3L) and around 7.6 deeper in the sediment. Immediately before fluid flow change (258 d) pH decreased from 7.6 at the top to 7.1 at the bottom of the core (Fig. 3R).

Methane concentrations of the out-flow in LFC started at 1.5 µmol l^{-1} (29 d) and increased to 2.5 µmol l^{-1} after 105 d before decreasing again to 0.9 µmol l^{-1} after 258 d (Fig. 5). The calculated efflux of methane followed the trend of methane concentrations. The LFC methane efflux varied between 0.0111 and 0.0296 mmol m^{-2} d^{-1} and calculated AOM rates from the difference of in- and out-flow were 0.304 mmol m^{-2} d^{-1}, direct before the swapping of the fluid flow.

The HFC core:

In the high flow regime (HFC) core, bromide quickly appeared after 21 d (400 µmol l^{-1}) at the bottom of the core (Fig. 4A). Bromide concentration continuously increased from the bottom towards the top of the core until a chemocline developed between 4 and 10 cm sediment depth after 105 d (Fig. 4G). This chemocline persisted during the remaining experiment and moved slowly upwards reaching a zone between 1 and 6 cm depth after 258 d, Fig. 4A, D). Sulfate concentrations during the HFC period were opposite to the bromide distribution and coincided with the chemocline. Sulfate continuously decreased at the bottom of the core reaching the minimum concentration (0.2 mmol l^{-1}) after 201 d (Fig. 4M). Simultaneously, sulfate was more

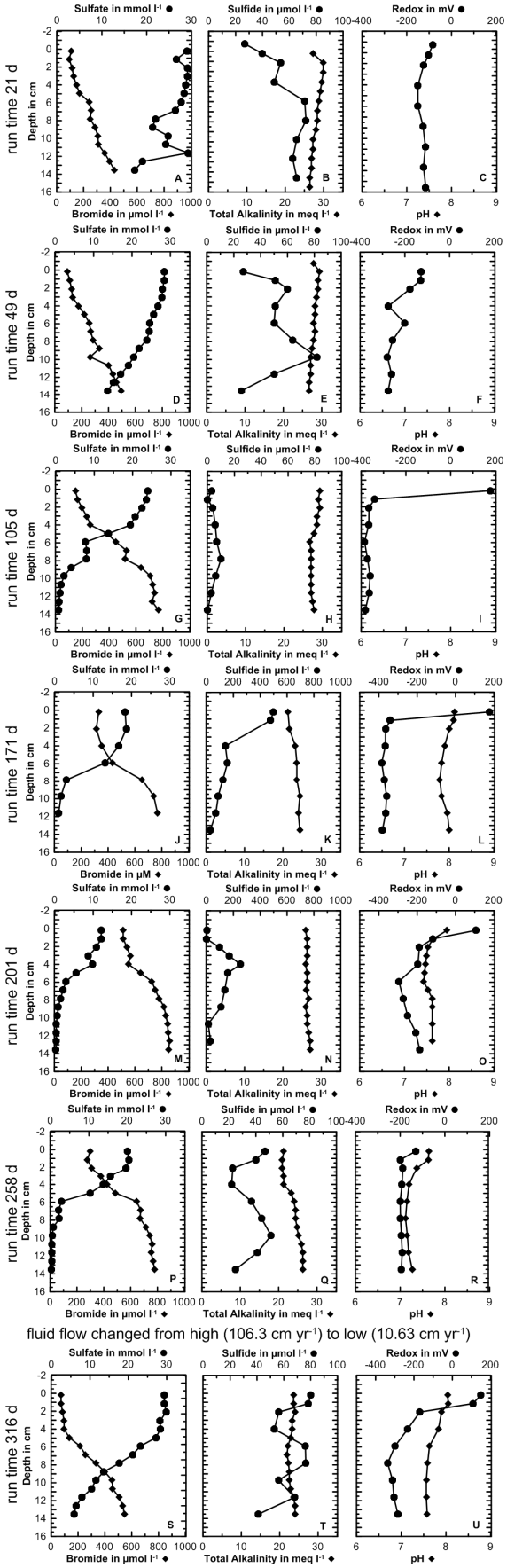

Figure 4: Geochemical parameters measured in sediment of the high flow regime core (HFC) from Quepos Slide after 21 (A, B, C), 49 (D and E), 105 (G, H, and I), 171 (J, K, L), 202 (M, N, O), and 258 (P, Q, R) days of runtime. Shown are porewater profiles of sulfate, bromide (A, D, G, J, M, P), sulfide, total alkalinity (B, E, H, K, N, Q), redox potential (C, F, I, L, O, R) and pH (I, L, O, R).

and more displaced from the bottom to the top of the core, decreasing from 28.5 mmol l^{-1} to 12 mmol l^{-1} at the sediment-water interface.

Sulfide concentrations were considerably lower compared to the LFC. In the beginning (21 d), sulfide increased from the top (27 µmol l^{-1}) to 6 cm sediment depth (70 µmol l^{-1}) within the SMTZ (Fig. 4B) and was constant at this level below 6 cm sediment depth. In the following months, sulfide decreased below 20 µmol l^{-1} (105 d) and increased rapidly after 171 d runtime at the top of the core to more than 500 µmol l^{-1} (Fig. 4K). In the following months sulfide concentrations decreased again at first to maximum values of 300 µmol l^{-1} (4 cm sediment depth, 202 d runtime) and to less than 60 µmol l^{-1} after 258 d (Fig. 4Q).

TA of the HFC core showed similar trends as the LFC core. In the beginning (21 d), TA decreased from 29 to 30 meq l^{-1} at the top of the core to 26 – 27 meq l^{-1} at the bottom (Fig. 4B, E, H). After 171 d, this distribution reversed with TA increasing from the top of the core to the bottom, from 21 - 26 meq l^{-1} to 24 – 27 meq l^{-1} (Fig. 4K).

Redox potential of the HFC core was, similar to the LFC core, highest at the sediment-water interface and in the overlaying water and lowest at larger depths of the core. Initially (21 d) redox potential was -85 mV at the sediment water interface and between -100 and -150 mV in the sediment (Fig. 4C). Over time, redox potential in the sediment became more negative, reaching an ultimate value of up to -385 mV (Fig. 4I, L). Between 105 to 202 d runtime, the overlaying water turned pink and showed redox potentials from 100 to 200 mV (Fig. 4Q), indicating oxygen contaminations in the core. Directly before flow exchange, the redox potential was negative again with -120 mV in the overlaying water and around -200 mV in the rest of the core (Fig. 4R).

Similar to the LFC core, the pH was highest at the top and lower inside the sediment (8.1 – 7.8 after 171 d and 8.0 – 7.4 after 202 d; Fig. 4L and O). Direct before fluid flow change (258 d) pH was decreased to 7.6 at the top and to 7.1-7.3 inside the sediment (Fig. 4R).

Methane concentration in the HFC outflow was initially 7.5 µmol l^{-1} and then decreased to 1.7 µmol l^{-1} during the next 200 d. After 258 d run time, methane concentration in the outflow increased again to 2.8 µmol l^{-1}. Efflux of the HFC ranged

from 0.0248 up to 0.1091 mmol m^{-2} d^{-1} and calculated AOM were 3.114 mmol m^{-2} d^{-1} direct before the swapping of the fluid flow (258 d).

After fluid flow swapping (260-350 d runtime):

After 260 d, the fluid flow in the cores was changed from low to high and vice versa.

NHFC (former LFC) core

In the new high flow regime core (NHFC) sulfate and bromide concentrations did not change considerably over the entire runtime (316 d). TA remained constant at 25 meq l^{-1} (Fig. 3T). Sulfide concentrations were highest at 0.3 cm sediment depth (1230 µmol l^{-1}) and first decreased steeply followed by a more steady increase (below 3 cm) with the exception of a second maximum (625 µmol l^{-1}) at 5 cm. At the bottom of the core, a sulfide concentration of in maximum 75 µmol l^{-1} was reached. Redox potential was positive (31 mV) in the overlaying water and between -280 and -330 mV within

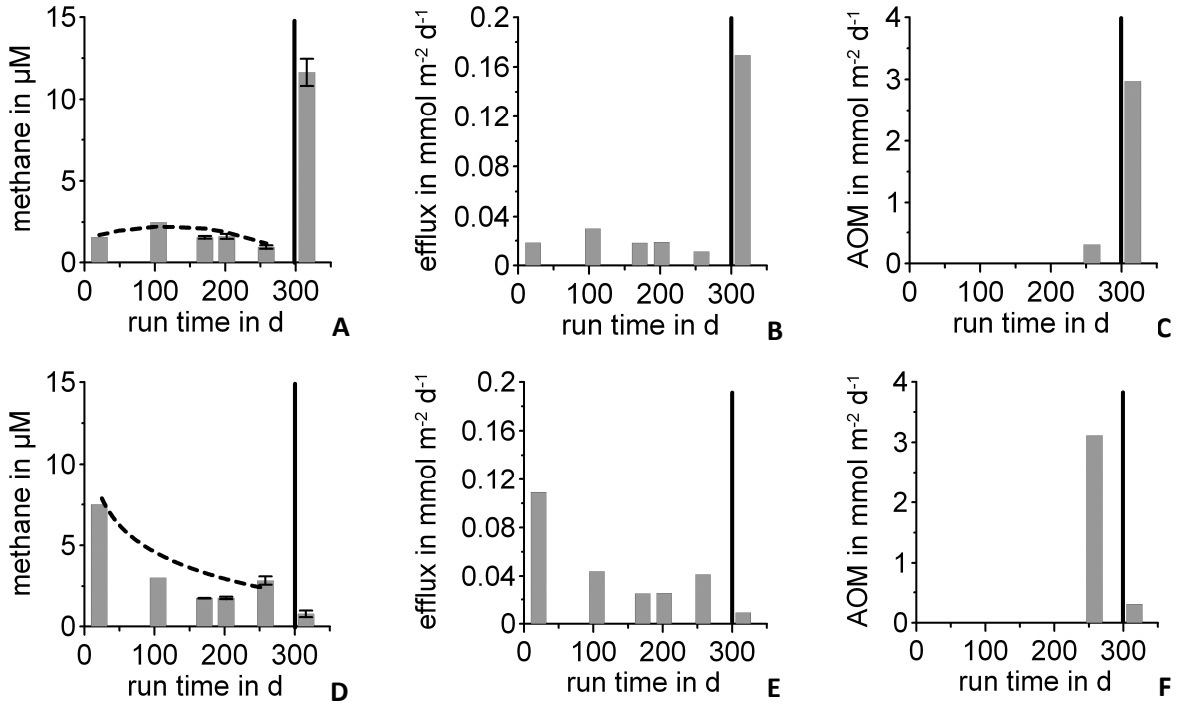

Figure 5: Methane concentration (µmol l^{-1}) in the outflow (A, B), methane efflux (mmol m^{-2} d^{-1}; C,D), and calculated AOM rate (mmol m^{-2} d^{-1}; E, F) of the system before and after fluid flow swapping: (A, C, E) low flow regime core (LFC), and (B, D, F) high flow regime core (HFC) from Quepos Slide. Vertical lines mark the moment of fluid flow swapping (low flow → high flow and vice versa at 258 d runtime). Error bars (A, B) show standard deviations of three repeated gas chromatographic measurements; the first two data points represent single measurements. Dotted lines represent the trendline (low flow regime: $5x10^{-6} * t_{runtime}^2 + 0.02\ t_{runtime} + 0.285$, $r^2 = 0.825$; high flow regime: $0.8576 * \ln(t_{runtime}) - 0.8662$, $r^2 = 0.987$) of methane concentration development until swapping.

the sediment (Fig. 3U). The pH decreased from 8.49 to 7.51 between the sediment-water interface and the bottom of the core.

Methane concentration of the outflow increased considerably after 316 d total run time from 0.93 to 11 µmol l^{-1}. Calculated methane effluxes were 0.17 mmol m^{-2} d^{-1} and corresponding AOM rates were 3.00 mmol m^{-2} d^{-1}.

NLFC (former HFC) core

In the new low flow regime core (NLFC), sulfate penetrated deeper and bromide ascended less into the sediment, as compared to the profile prior to fluid flow change (Fig. 4S). Sulfide concentrations remained low, between 50 and 80 µmol l^{-1}, and TA varied between 23 and 25 meq l^{-1} (Fig. 4T). Redox potential was positive (150 mV) at the sediment water interface and the upper sediment (Fig. 4U). Inside the sediment, redox decreased to values between -200 to -400 mV. The pH profile decreased from 8.05 in the overlaying water and the sediment-water interface down to 7.55 below 6 cm sediment depth.

Methane concentrations in the outflow declined from 2.8 to 0.7 µmol l^{-1}. Calculated methane effluxes were 0.009 mmol m^{-2} d^{-1} and corresponding AOM rates were 0.306 mmol m^{-2} d^{-1}.

Experiment termination and final sampling:

After 350 d runtime, the experiment was terminated, porewater was sampled, and the sediment sub-sampled for further analyses. In both cores, methane concentrations determined after experiment termination were only a minor fraction of the original in-flow concentration (939 µmol l^{-1}), which was attributed to methane losses during porewater extraction (Steeb et al. 2014). Methane concentrations varied between 2 and 4 µmol l^{-1} with a slight increase towards the bottom of the core (Fig. 6A). Sulfate concentrations decreased only slightly from 29.5 mmol l^{-1} at the top to 26.2 mmol l^{-1} at the bottom of the core (Fig. 6B). Sulfide increased from 50 mmol l^{-1} at the sediment surface (0.3 cm) to a maximum of 125 µmol l^{-1} at 6 cm and decreased to 80 µmol l^{-1} at the bottom of the core (Fig. 6C). AOM rates determined by radiotracer techniques show highest values between 4 to 10 cm sediment depth (0.50 – 0.91 nmol cm^{-3} d^{-1}) and, apart from that, increased by trend from the top (0.10 nmol cm^{-3} d^{-1}) to bottom

(0.33 nmol cm^{-3} d^{-1}). Areal rates integrated over the entire sediment core (0-15 cm) were 0.043 and 2.31 mmol m^{-2} d^{-1} for AOM and sulfate reduction, respectively.

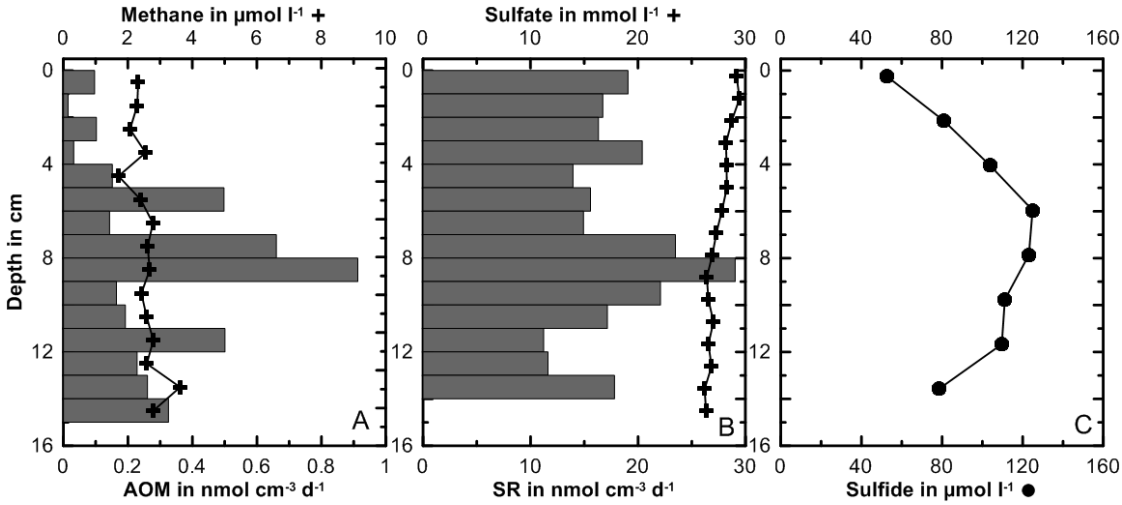

Figure 6: Biogeochemical parameters in the new high flow core (NHFC) after slicing (358 d runtime). Porewater profiles of methane (A, D, cross), sulfate (B, E, crosses), sulfide (C, F, dots), and results of the radiotracer measurements of AOM (A, D, bars) and sulfate reduction (SR) (B, E, bars) are shown.

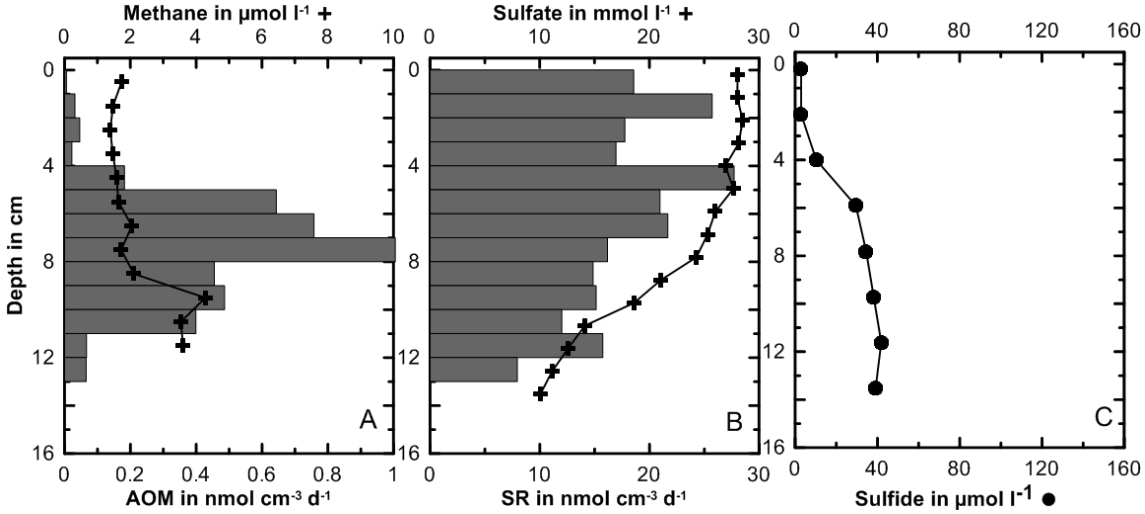

Figure 7: Biogeochemical parameters in the new low flow core (NLFC) (A - C) after slicing (358 d runtime). Porewater profiles of methane (A, D, cross), sulfate (B, E, crosses), sulfide (C, F, dots), and results of the radiotracer measurements of AOM (A, D, bars) and sulfate reduction (SR) (B, E, bars) are shown.

In the original HFC (=NLFC) core, methane concentrations remained consistently low at around 2-4 µmol l^{-1} (Fig. 7A). Sulfate was between 27 – 28.5 mmol l^{-1} within the upper first 6 cm and then decreased to 10 mmol l^{-1}below this depth (Fig. 7B). Consistent with the steepest decrease in sulfate, sulfide increased to a maximum of 42 µmol l^{-1}. Highest AOM rates determined with radiotracer techniques were detected between 5 and 11 cm (0.4 - 1 nmol cm^{-3} d^{-1} Fig. 7A). Sulfate reduction rates ranged from 16.95 to 27.71 nmol cm^{-3} d^{-1} in the upper sediment (0 - 6 cm depth) and

decreased to 7.96 nmol cm^{-3} d^{-1} at the bottom, which corresponded to a simultaneous decrease in sulfate, at the bottom of the core (Fig. 6A). Areal rates integrated over the entire sediment depth (14 cm) were 0.042 and 2.49 mmol m^{-2} d^{-1} for AOM and sulfate reduction, respectively.

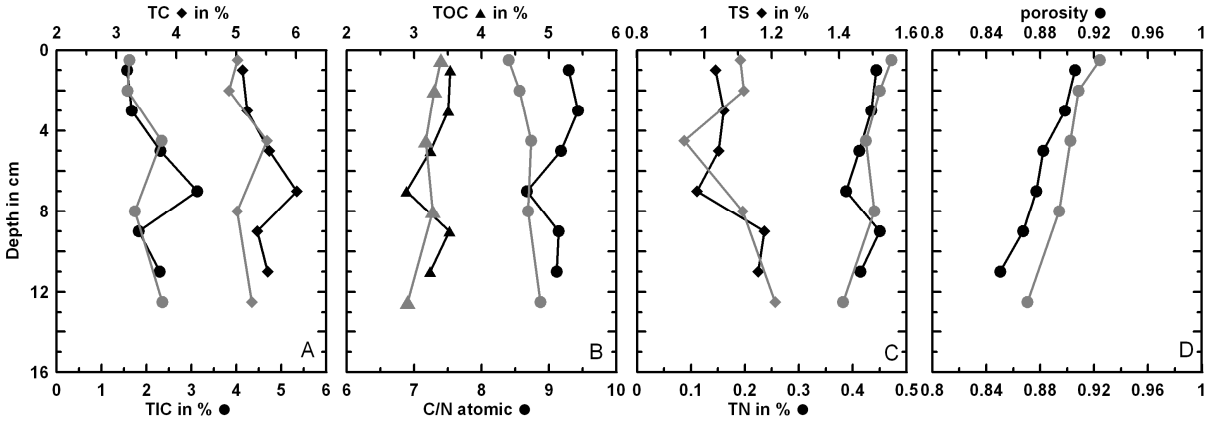

Figure 8: Sediment solid phase parameters measured in the sediment of the ex-situ data of the SO206-31Muc core (grey) compared to the (A, B, C, D) original low flow core (LFC = NHFC). Total carbon content (TC), and total inorganic carbon content (TIC) in % w/w of the dry weight(A, E); atomic C/N ratio and total organic carbon content (TOC) in % w/w of the dry weight (B, F); total nitrogen (TN), total sulfur (TS) in % w/w of the dry weight (C, G); porosity of the sediment (D, H).

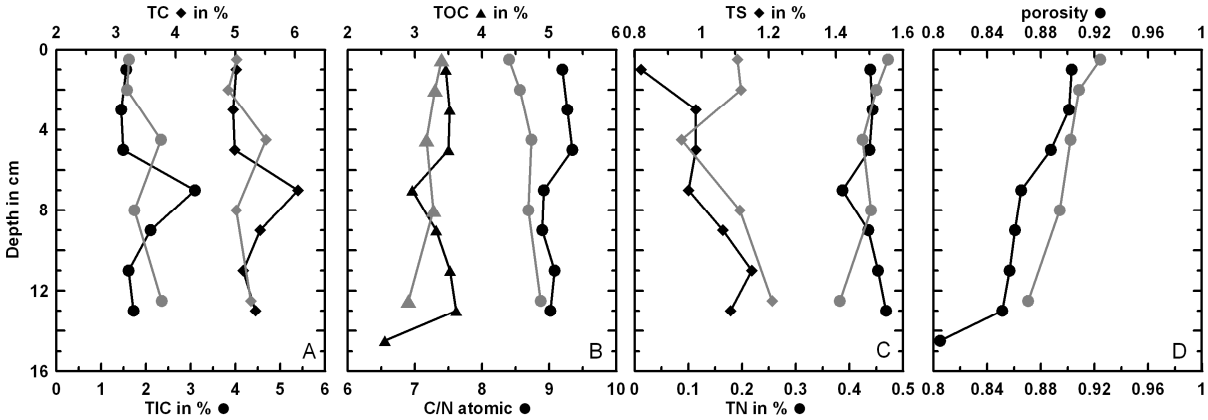

Figure 9: Sediment solid phase parameters measured in the sediment of the ex-situ data of the SO206-31Muc core (grey) compared to the (A, B, C, D) original high flow core (HFC = NLFC). Total carbon content (TC), and total inorganic carbon content (TIC) in % w/w of the dry weight(A, E); atomic C/N ratio and total organic carbon content (TOC) in % w/w of the dry weight (B, F); total nitrogen (TN), total sulfur (TS) in % w/w of the dry weight (C, G); porosity of the sediment (D, H).

The TC contents were similar in both, the NHFC and NLFC core, and varied between 5.0 and 5.4% w/w (Fig. 8A, Fig. 9A). A carbon peak (6% w/w, 7 cm sediment depth) resulted from higher TIC (3.0 -3.6% w/w) in both cores. TOC (2.90 – 3.62% w/w) of the NHFC and NLFC did not differ considerable from ex situ data (2.91–3.40% w/w). Atomic C/N ratios were higher in both flow-through cores (8.67 – 9.43) compared to ex situ data (7.61 – 8.88). In the experiment cores (NHFC and NLFC), TS was slightly lower (0.82 – 1.18), than in the ex-situ data (0.94 - 1.3% w/w), especially in

the upper region of the original HFC core (0.84 to 1.11% w/w for NHFC and ex situ data, respectively) and showed in contrast to the ex-situ no minimum at 4.5 cm sediment depth (Fig. 8C; Fig. 9C).

Discussion:

Fluid seepage and related processes and their impact on porewater gradients:

Quepos Slide sediment cores that were studied ex situ, exhibited a SMTZ and AOM peaks within the upper 20 cm of the sediment. We therefore assume that the most active zone of the benthic methane filter was captured by our SLOT experiments (core length 14-16 cm). During the experiments, the depth of the SMTZ was controlled by fluid flow and shifted over time. We defined the SMTZ as the zone which sulfate, provided by the seawater medium from the top, and bromide, used as tracer for the methane-loaded medium seepage from below, overlapped. Fluid flow velocity in the low flow regime core (LFC, 10.6 cm yr^{-1}) was similar to modeled flow based on our ex situ data (6-16 cm yr^{-1}). In the high flow regime core (HFC, 106 cm yr^{-1}), the fluid flow was ten times higher compared to our modeled data and also higher than other values published for Quepos Slide (1-40 cm yr^{-1}, Karaca et al. 2012); however, the flow was still in the range of neighboring seeps (0.1 – 200 cm yr^{-1}, Hensen et al. 2004; Linke et al. 2005; Karaca et al. 2010; Krause et al. 2014). During the entire LFC experiment (before and after fluid flow swapping) no SMTZ developed. The missing evolution of a SMTZ was probably the result of a high hydrological residence time of the fluid (1080 d for the LFC and 108 d for the NHFC), i.e., the average time for the fluids to pass the entire sediment core. Nevertheless, small amounts of the seepage fluid obviously passed through the entire sediment, probably facilitated through channeling, as demonstrated by the presence of methane in the outflow. From the bromide concentration in the outflow, the fraction of total emitted seepage medium in relation to the total inflow volume of seepage medium was calculated. This fraction increased from 0% to 2.5% in the last phase of the low flow regime and further increased to 4% after the system was changed to high flow. Radiotracer measurements after experiment termination revealed low AOM activity over the entire core with highest turnover between 7 and 9 cm sediment depth, while methane concentrations stayed continuously low around 2-3 µmol l^{-1}

over the entire core (see sampling artifacts, chapter Results: Experiment termination and final sampling). In the HFC the SMTZ and related AOM activity was much more pronounced. The SMTZ rose from 14 cm (max. depth) to above 6 cm, and fell down to 10 cm sediment depth during the subsequent low flow phase. During the first phase, fluids and SMTZ showed continuous migration, which was fast initially and became slower towards the end. The relatively stable depth of the SMTZ at the end of the first experiment phase (0 - 260 d) indicated the transition to a steady-state situation. Highest AOM rates, determined by radiotracer measurements after experiment termination, were found within this SMTZ (6-10 cm sediment depth).

Sulfide concentrations of the HFC were generally highest in the expected SMTZ. In the LFC, sulfide peaks were relatively broad and not so distinct, which was probably the result of a broad dispersive mixing layer between seepage and seawater medium. Due to the low fluid flow, higher sulfide concentrations evolved in the LFC as compared to the HFC, where sulfide was basically flushed-out before it was able to accumulate. In the LFC experiments, sulfide concentrations fluctuated over time. While the increase in sulfide concentration was most likely correlated with enhanced sulfate reduction, a decrease could be caused either by the precipitation of metal sulfides and/or by microbial oxidation of sulfide (chemosynthesis). Precipitation of sulfide is correlated with a drop in pH (Glud et al. 2007; Preisler et al. 2007), as it was observed in our study. For the microbial oxidation of sulfide, nitrate or oxygen is needed. In accordance with a redox potential of less than 300 mV, free oxygen was only temporally available (if at all) in the overlaying water due to an artifact. Moreover, sulfide oxidation with oxygen would result in a drop in pH; conversely, pH increased in the surface sediments. In contrast, sulfide oxidation via nitrate to ammonium results in an increase in pH and was observed at the sediment-water interface of seeps system (de Beer et al. 2006). Nitrate availability in the seawater medium was limited (~4 µmol l^{-1}). Nevertheless, sulfide-oxidizing bacteria as *Beggiatoa* or *Thioploca* can accumulate nitrate in their vacuoles to oxidize sulfide (Fossing et al. 1995; Preisler et al. 2007). Furthermore, when sampled our sediment cores were covered by sulfide-oxidizing bacterial mats. Since oxygen concentration in the bottom water is negligible in this OMZ, nitrate appears to be the most attractive electron acceptor for these sulfide oxidizers.

Microbial turnover rates and efficiency of the benthic methane filter:

Integrated areal AOM rates (45.15 ± 11.48 mmol m^{-2} d^{-1}) of the ex-situ radiotracer measurements were in the upper range of previous modeled data (2.6 – 42.1 mmol m^{-2} d^{-1}) and moderate to high compared to other seep systems (Treude et al. 2003; Krause et al. 2014). In the SLOT experiments, the methane flux (0.3 – 2.8 mmol m^{-2} d^{-1}) was lower compared to modeled flux (9.7 – 24.8 mmol m^{-2} d^{-1}) and previously modeled data (4.4 - 93.1 mmol m^{-2} d^{-1}, Karaca et al. 2012). However, they are still in the range of published values for methane fluxes at seeps of this region (Mau et al. 2006). In agreement with the lower methane flux in the SLOT experiment, AOM rates determined from the difference between in and outflow were much lower than ex-situ measurements (~0.31 and ~3.12 mmol m^{-2} d^{-1} in the LFC and HFC, respectively). Radiotracer measurements revealed AOM peaks within the SMTZ of the HFC (4-10 cmbsf). A broader distribution of AOM was found in the LFC, while similar integrated rates suggest the same potential for AOM.

While in a previous study the methane consumption efficiency was estimated to range between 23 and 96% of the total methane flux (Karaca et al. (2012), the efficiency in our study was around 99% for both ex situ sampling and experimental setup (under the assumption of steady state conditions directly before fluid change). One possible explanation for the partial disagreement in efficiency with earlier studies could be variability of methane fluxes in this highly heterogeneous area. While Karaca et al. (2012) provided a high sampling density of different habitat types (20 sediment cores from the same seep site), only two randomly chosen sites were sampled in our study, and only one was used for the experiment. Another explanation could be temporal variability of fluid and methane flux. Previous samplings were conducted up to 10 years prior to our study. Methane flux as well as microbial activity could easily change during this time (Mau et al. 2007; Füri et al. 2010). A drop in methane flux would probably enhance the efficiency of the benthic methane filter. For example, in our experiment, methane flux was 2-33-times lower compared to the model of Karaca et al. (2012) due to technical limitations (hydrostatic pressure), resulting in a high efficiency of the benthic microbial methane filter, even though at a relatively high fluid flux.

Radiotracer measurements after experiment termination revealed higher levels of sulfate reduction compared to AOM rates, which is probably due to organic matter degradation coupled to sulfate reduction. Increased C/N ratios after the experiment termination compared to the ex-situ data (Fig. 8B; Fig. 9B) support this assumption, because fresh organic matter with high nitrogen content is preferred by microbes, leading to high C/N values during advanced organic matter degradation (Whiticar 2002). Around 80% of the sulfate reduction in ex-situ measurement of SO206-St31 resulted from organic matter degradation. Since the cores were obtained within an OMZ, sulfate reduction is supposedly the most important pathway for organic matter degradation (Jørgensen 1977; Sørensen et al. 1979; Bohlen et al. 2011).

Response time of the microbial benthic methane filter:

In the outflow of the LFC, methane concentrations increased only little and decreased after 202 d (directly before fluid flow swapping) to the initial concentration. In contrast, methane concentrations in the outflow the HFC core were high (7.5 µmol l^{-1}) at the beginning (29 d) and decreased quasi-exponentially to concentrations of ~2 µmol l^{-1} after 171 d. In the same time interval, the fraction of methane-loaded fluid at the sediment-water interface, calculated from the tracer (bromide) concentrations, changed from 13% to 34%, (Fig. 4A, J). From the delivered methane (125.5 and 376.4 µmol l^{-1}) 30% and 98%, respectively, was oxidized. This period can be interpreted as the response time of the benthic microbial methane filter in the sediments of Quepos Slide. After fluid flow change, the efflux of methane was suddenly reduced to only 27% (0.7 µmol l^{-1}) in the former HFC (=NLFC), while the efflux in the former LFC (=NHFC) increased rapidly to 1257% (11.6 µmol l-1). Based on bromide concentrations, the fraction of the seepage medium in the outflow of the NHFC was 4%, which should theoretically equal 14.1 µmol l^{-1} methane in the outflow. Compared to methane concentrations directly measured in the outflow, only 17.5% of the inflow methane was oxidized and 82.5% was emitted.

These results indicate how a sudden event like an earthquake could result in an abrupt increase in methane efflux. Mau et al. (2006) attributed fluctuations of methane concentrations in the water column, which occurred between autumn 2002 and 2003 at the Costa Rican seeps, to an earthquake in June 2002. It was not specified if the increased methane flux resulted from increased fluid flow, or simply

from bubble release or if it was a continuous increase of methane flux or just a transient effect.

The experiments of the present study clearly show that the benthic microbial methane filter is able to react within a relatively brief time of 5-6 month to increased methane fluxes and responds with the development of a much shallower and condensed AOM zone. Even if methane fluxes and methane concentrations were four times higher, as expected in-situ according to modeled methane fluxes that were based on ex-situ data, the benthic microbial methane filter might be able to respond quickly, if a methanotrophic community is already fully established. Outside of seep habitats, where microbial benthic methane filter are either absent or in deeper sediment zones, the adaption might take much more time, since the doubling rate of the microbes involved is in the order of a few months (Girguis et al. 2005; Nauhaus et al. 2007; Krüger et al. 2008; Meulepas et al. 2009). Mau et al. (2007) observed a reduction of methane emissions in the water column above the earthquake-impacted seepage area by 50-90% in a period of one year. In our experiments, only ~170 d were needed for the benthic microbial methane filter to adapt to the new flow regime. It is not clear if the subsequent reduction of methane emissions observed by Mau et al. (2007) was the result of an ephemeral pulse of methane flux or by the adaption of the microbial benthic methane filter. Our results indicate that at least both situations are conceivable.

Another scenario, in which the benthic methane filter could be confronted with an increase in methane flux, could be seafloor warming and subsequent destabilization of gas hydrates as a result of climate change (Buffet and Archer 2004). Due to retarded heat flux into deeper sediment layers, dissociation of considerable gas hydrate volumes probably require hundreds to thousands of years (Biastoch et al. 2011). We show that an established microbial benthic methane filter could compensate slow increases in methane flux. Only "pristine" sediments, which are virtually devoid of methanotrophs are expected to show long adaptations periods of up to several years or even decades (Dale et al. 2008) due to slow growth rates of the anaerobes (Girguis et al. 2005; Nauhaus et al. 2007; Goffredi et al. 2008).

Conclusion:

Radiotracer rate measurements of AOM on surface sediments of the Quepos Slide, a cold seep at the pacific coast of Costa Rica, revealed a highly efficient benthic methane filter, which was in agreement with the applied numerical model. Additionally, in vitro experiments with intact sediment cores using a sediment-flow-through system demonstrated that methane emissions under enhanced fluid flow, compared to modeled in-situ conditions, were efficiently compensated (99% oxidation) by the benthic methane filter after a 150 – 170 d response period. These results show, how established benthic methanotrophic microbial communities could react to pulses in fluid and methane flow, induced by, e.g., by earthquakes, or dissociating gas hydrates, and how fast they would adapt to the new flow regime.

Acknowledgments:

We thank the captain and the crew of R/V *Sonne* and all staff members who supported work onboard. Special thanks go to B. Domeyer, A. Bleyer, R. Ebbinghaus, R. Surberg, E. Corrales-Cordero, and E. Pinero for support during porewater analyzes. K. Kretschmer is thanked for support during system maintenance. K. Kretchmer, J. Farkas, and J. Hommer are thanked for support during radiotracer analyzes. This project was financed through the Collaborative Research Center (SFB) 574 "Volatiles and Fluids in Subduction Zones" and the Cluster of Excellence "The Future Ocean" funded by the German Research Foundation (DFG).M. Nuzzo was funded by the Portuguese Science and Technology Foundation post-doctoral fellowship FCT-SFRH/BPD/44598/2008 and her work is a contribution of FCT grant PTDC/PTDC/MAR/118443/2010.

References:

De Beer, D., E. Sauter, H. Niemann, N. Kaul, U. Witte, M. Schlüter, and A. Boetius. 2006. In situ fluxes and zonation of microbial activity in surface sediments of the Håkon Mosby Mud Volcano. Limnol. Oceanogr. **51**: 1315–1331.

Boetius, A., K. Ravenschlag, C. J. Schubert, D. Rickert, F. Widdel, A. Gieseke, R. Amann, B. B. Jørgensen, U. Witte, O. Pfannkuche, and B. B. Jorgensen. 2000. A marine microbial consortium apparently mediating anaerobic oxidation of methane. Nature **407**: 623–626.

Bohlen, L., A. W. Dale, S. Sommer, T. Mosch, C. Hensen, A. Noffke, F. Scholz, and K. Wallmann. 2011. Benthic nitrogen cycling traversing the Peruvian oxygen minimum zone. Geochim. Cosmochim. Acta **75**: 6094–6111.

Bohrmann, G., K. Heeschen, and C. Jung. 2002. Widespread fluid expulsion along the seafloor of the Costa Rica convergent margin. Terra … **14**: 69–79.

Borowski, W. S., C. K. Paull, and I. W. Ussler. 1999. Global and local variations of interstitial sulfate gradients in deep-water, continental margin sediments: Sensitivity to underlying methane and gas hydrates. Mar. Geol. **159**: 131–154.

Burwicz, E., L. Rüpke, and K. Wallmann. 2011. Estimation of the global amount of submarine gas hydrates formed via microbial methane formation based on numerical reaction-transport modeling and a novel parameterization of Holocene sedimentation. Geochim. Cosmochim. Acta **75**: 4562–4576.

Cline, J. 1969. Spectrophotometric determination of hydrogen sulfide in natural waters. Limnol. Oceanogr. **14**: 454–458.

Dale, A. W., P. Van Cappellen, D. R. Aguilera, and P. Regnier. 2008. Methane efflux from marine sediments in passive and active margins: Estimations from bioenergetic reaction–transport simulations. Earth Planet. Sci. Lett. **265**: 329–344.

Dalsgaard, T., L. P. Nielsen, V. Brotas, P. Viaroli, G. Underwood, D. Nedwell, K. Sundbäck, S. Rysgaard, A. Miles, M. Bartoli, L. Dong, D. C. O. Thornton, L. D. M. Ottosen, G. Castaldelli, and N. Risgaard-Petersen. 2000. Sediment Characteristics, p. 53–54. *In* Protocol Handbook for NICE- Nitrogen Cycling in Esturies: a project under EU research programme: Marine Science and Technology (MAST III). National Environmental Research Institute.

Ettwig, K. F., M. K. Butler, D. Le Paslier, E. Pelletier, S. Mangenot, M. M. M. Kuypers, F. Schreiber, B. E. Dutilh, J. Zedelius, D. de Beer, J. Gloerich, H. J. C. T. Wessels, T. van Alen, F. Luesken, M. L. Wu, K. T. van de Pas-Schoonen, H. J. M. Op den Camp, E. M. Janssen-Megens, K.-J. Francoijs, H. Stunnenberg, J. Weissenbach, M. S. M. Jetten, and M. Strous. 2010. Nitrite-driven anaerobic methane oxidation by oxygenic bacteria. Nature **464**: 543–8.

Fischer, D., H. Sahling, K. Nöthen, G. Bohrmann, M. Zabel, and S. Kasten. 2012. Interaction between hydrocarbon seepage, chemosynthetic communities, and bottom water redox at cold seeps of the Makran accretionary prism: insights from habitat-specific pore water sampling and modeling. Biogeosciences **9**: 2013–2031.

Fossing, H., V. Gallardo, and B. Jørgensen. 1995. Concentration and transport of nitrate by the mat-forming sulphur bacterium Thioploca. Nature **374**: 714–715.

Füri, E., D. R. Hilton, M. D. Tryon, K. M. Brown, G. M. McMurtry, W. Brückmann, and C. G. Wheat. 2010. Carbon release from submarine seeps at the Costa Rica fore arc: Implications for the volatile cycle at the Central America convergent margin. Geochemistry, Geophys. Geosystems **11**, doi:10.1029/2009GC002810

Girguis, P., A. Cozen, and E. DeLong. 2005. Growth and population dynamics of anaerobic methane-oxidizing archaea and sulfate-reducing bacteria in a continuous-flow bioreactor. Appl. Environ. Microbiol. **71**: 3725–3733.

Glud, R. N., P. Berg, H. Fossing, and B. B. Jørgensen. 2007. Effect of the diffusive boundary layer on benthic mineralization and O2 distribution: A theoretical model analysis. Limnol. Oceanogr. **52**: 547–557.

Goffredi, S. K., R. Wilpiszeski, R. Lee, and V. J. Orphan. 2008. Temporal evolution of methane cycling and phylogenetic diversity of archaea in sediments from a deep-sea whale-fall in Monterey Canyon, California. ISME J. **2**: 204–20.

Grasshoff, K., M. Erhardt, K. Kremling, and C. Revised. 1983. Methods of seawater analysis, Wiley-VCH, Weinheim.

Han, X., E. Suess, H. Sahling, and K. Wallmann. 2004. Fluid venting activity on the Costa Rica margin: new results from authigenic carbonates. Int. J. Earth Sci. **93**: 596–611.

Harders, R., C. R. Ranero, W. Weinrebe, and J. H. Behrmann. 2011. Submarine slope failures along the convergent continental margin of the Middle America Trench. Geochemistry Geophys. Geosystems **12**, doi:10.1029/2010GC003401

Hensen, C., and K. Wallmann. 2005. Methane formation at Costa Rica continental margin—constraints for gas hydrate inventories and cross-décollement fluid flow. Earth Planet. Sci. Lett. **236**: 41–60.

Hensen, C., K. Wallmann, M. Schmidt, C. R. Ranero, and E. Suess. 2004. Fluid expulsion related to mud extrusion off Costa Rica—A window to the subducting slab. Geology **32**: 201.

Hesse, R., S. K. Frape, P. K. Egeberg, and R. Matsumoto. 2000. Stable Isotope Studies (Cl, O, and H) of Interstitial Waters from Site 997, Blake Ridge Gas Hydrate Field, West Atlantic. Proc. Ocean Drill. Program, Sci. results **164**: 129–137.

Hinrichs, K., and A. Boetius. 2002. The anaerobic oxidation of methane: new insights in microbial ecology and biogeochemistry, p. 457–477. *In* G. Wefer, D. Billet, D. Hebbeln, B. Jørgensen, M. Schlüter, and T. Van Weering [eds.], Ocean Margin Systems. Springer-Verlag Berlin Heidelberg.

Ivanenkov, V. N., and Y. I. Lyakhin. 1978. Determination of total alkalinity in seawater, p. 110–114. *In* O.K. Bordovsky and V.N. Ivanenkov [eds.], Methods of Hydrochemical Investigations in the Ocean. Nauka Publ. House.

Jørgensen, B. B. 1977. The Sulfur Cycle of a Coastal Marine Sediment (Limfjorden, Denmark). Limnol. Oceanogr. **22**: 814–832.

Jørgensen, B. B. 1978. A comparison of methods for the quantification of bacterial sulfate reduction in coastal marine sediments. 1. Measurements with radiotracer techniques. Geomicrobiol. J **1**: 11–27.

Joye, S. B., A. Boetius, B. N. Orcutt, J. P. Montoya, H. N. Schulz, M. J. Erickson, and S. K. Lugo. 2004. The anaerobic oxidation of methane and sulfate reduction in sediments from Gulf of Mexico cold seeps. Chem. Geol. **205**: 219–238.

Judd, A., M. Hovland, and L. Dimitrov. 2002. The geological methane budget at continental margins and its influence on climate change. Geofluids **2**: 109–126.

Kallmeyer, J., T. G. Ferdelman, A. Weber, H. Fossing, and B. B. Jørgensen. 2004. A cold chromium distillation procedure for radiolabeled sulfide applied to sulfate reduction measurements. Limnol. Oceanogr. Methods **2**: 171–180.

Karaca, D., C. Hensen, and K. Wallmann. 2010. Controls on authigenic carbonate precipitation at cold seeps along the convergent margin off Costa Rica. Geochemistry Geophys. Geosystems **11**: 1–19.

Karaca, D., T. Schleicher, C. Hensen, P. Linke, and K. Wallmann. 2012. Quantification of methane emission from bacterial mat sites at Quepos Slide offshore Costa Rica. Int. J. Earth Sci. 1–25.

Kluesner, J. W., E. A. Silver, N. L. Bangs, K. D. McIntosh, J. Gibson, D. Orange, C. R. Ranero, and R. von Huene. 2013. High density of structurally controlled, shallow to deep water fluid seep indicators imaged offshore Costa Rica. Geochemistry, Geophys. Geosystems **14**: 519–539.

Krause, S., P. Steeb, C. Hensen, V. Liebetrau, A. W. Dale, M. Nuzzo, and T. Treude. 2014. Microbial activity and carbonate isotope signatures as a tool for identification of spatial differences in methane advection: a case study at the Pacific Costa Rican margin. Biogeosciences **11**: 507–523.

Krüger, M., M. Blumenberg, S. Kasten, A. Wieland, L. Känel, J. Klock, W. Michaelis, and R. Seifert. 2008. A novel, multi-layered methanotrophic microbial mat system growing on the sediment of the Black Sea. Environ. Microbiol. **10**: 1934–47.

Kutterolf, S., V. Liebetrau, T. Mörz, A. Freundt, T. Hammerich, and D. Garbe-Schönberg. 2008. Lifetime and cyclicity of fluid venting at forearc mound structures determined by tephrostratigraphy and radiometric dating of authigenic carbonates. Geology **36**: 707.

Kvenvolden, K. 2002. Methane hydrate in the global organic carbon cycle. Terra Nov. **14**: 302–306.

Levin, L. A. 2003. Oxygen Minimum Zone Benthos : Adaption and Community. Ocean. Mar. Biol. an Annu. Rev. **41**: 1–45.

Linke, P., K. Wallmann, E. Suess, C. Hensen, and G. Rehder. 2005. In situ benthic fluxes from an intermittently active mud volcano at the Costa Rica convergent margin. Earth Planet. Sci. Lett. **235**: 79–95.

Mau, S., G. Rehder, I. G. Arroyo, J. Gossler, and E. Suess. 2007. Indications of a link between seismotectonics and CH 4 release from seeps off Costa Rica. Geochemistry, Geophys. Geosystems **8**: 1–13.

Mau, S., G. Rehder, H. Sahling, T. Schleicher, and P. Linke. 2012. Seepage of methane at Jaco Scar, a slide caused by seamount subduction offshore Costa Rica. Int. J. Earth Sci. , doi:10.1007/s00531-012-0822-z

Mau, S., H. Sahling, G. Rehder, E. Suess, P. Linke, and E. Soeding. 2006. Estimates of methane output from mud extrusions at the erosive convergent margin off Costa Rica. Mar. Geol. **225**: 129–144.

Meulepas, R. J. W., C. G. Jagersma, J. Gieteling, C. J. N. Buisman, A. J. M. Stams, and P. N. L. Lens. 2009. Enrichment of anaerobic methanotrophs in sulfate-reducing membrane bioreactors. Biotechnol. Bioeng. **104**: 458–70.

Milucka, J., T. G. Ferdelman, L. Polerecky, D. Franzke, G. Wegener, M. Schmid, I. Lieberwirth, M. Wagner, F. Widdel, and M. M. M. Kuypers. 2012. Zero-valent sulphur is a key intermediate in marine methane oxidation. Nature **2**: 1–23.

Minami, H., K. Tatsumi, A. Hachikubo, S. Yamashita, H. Sakagami, N. Takahashi, H. Shoji, Y. K. Jin, A. Obzhirov, N. Nikolaeva, and A. Derkachev. 2012. Possible variation in methane flux caused by gas hydrate formation on the northeastern continental slope off Sakhalin Island, Russia. Geo-Marine Lett. **32**: 525–534.

Nauhaus, K., M. Albrecht, M. Elvert, A. Boetius, and F. Widdel. 2007. In vitro cell growth of marine archaeal-bacterial consortia during anaerobic oxidation of methane with sulfate. Environ. Microbiol. **9**: 187–96.

Niemann, H., T. Lösekann, D. de Beer, M. Elvert, T. Nadalig, K. Knittel, R. Amann, E. J. Sauter, M. Schlüter, M. Klages, J. P. Foucher, and A. Boetius. 2006. Novel microbial communities of the Haakon Mosby mud volcano and their role as a methane sink. Nature **443**: 854–8.

Orcutt, B. N., J. B. Sylvan, N. J. Knab, and K. J. Edwards. 2011. Microbial ecology of the dark ocean above, at, and below the seafloor. Microbiol. Mol. Biol. Rev. **75**: 361–422.

Preisler, A., D. de Beer, A. Lichtschlag, G. Lavik, A. Boetius, and B. B. Jørgensen. 2007. Biological and chemical sulfide oxidation in a Beggiatoa inhabited marine sediment. ISME J. **1**: 341–53.

Ranero, C., and R. von Huene. 2000. Subduction erosion along the Middle America convergent margin. Nature **404**: 748–52.

Ranero, C. R., I. Grevemeyer, H. Sahling, U. Barckhausen, C. Hensen, K. Wallmann, W. Weinrebe, P. Vannucchi, R. von Huene, and K. McIntosh. 2008.

Hydrogeological system of erosional convergent margins and its influence on tectonics and interplate seismogenesis. Geochemistry Geophys. Geosystems **9**, doi:10.1029/2007GC001679

Reeburgh, W. S. 2007. Oceanic methane biogeochemistry. Chem. Rev. **107**: 486–513.

Sahling, H., D. G. Masson, C. R. Ranero, V. Hühnerbach, W. Weinrebe, I. Klaucke, D. Bürk, W. Brückmann, and E. Suess. 2008. Fluid seepage at the continental margin offshore Costa Rica and southern Nicaragua. Geochemistry, Geophys. Geosystems **9**: 1–22.

Sahling, H., D. Rickert, R. W. Lee, P. Linke, and E. Suess. 2002. Macrofaunal community structure and sulfide flux at gas hydrate deposits from the Cascadia convergent margin, NE Pacific. Mar. Ecol. Prog. Ser. **231**: 121–138.

Schmidt, M., C. Hensen, T. Mörz, C. Müller, I. Grevemeyer, K. Wallmann, S. Mau, and N. Kaul. 2005. Methane hydrate accumulation in “Mound 11” mud volcano, Costa Rica forearc. Mar. Geol. **216**: 83–100.

Sørensen, J., B. Jørgensen, and N. Revsbech. 1979. A comparison of oxygen, nitrate, and sulfate respiration in coastal marine sediments. Microb. Ecol. **5**: 105–115.

Steeb, P., P. Linke, and T. Treude. 2014. A sediment flow-through system to study the impact of shifting fluid and methane flow regimes on the efficiency of the benthic methane filter. Limnol. Oceanogr. Methods **12**: 25–45.

Suess, E. 2010. Marine Cold Seeps, p. 188–198. *In* K.N. Timmis [ed.], Handbook of Hydrocarbon and Lipid Microbiology. Springer Berlin Heidelberg.

Syracuse, E. M., and G. a. Abers. 2006. Global compilation of variations in slab depth beneath arc volcanoes and implications. Geochemistry, Geophys. Geosystems **7**: 1–18.

Tishchenko, P., C. Hensen, K. Wallmann, and C. S. Wong. 2005. Calculation of the stability and solubility of methane hydrate in seawater. Chem. Geol. **219**: 37–52.

Torres, M. E. E., K. Wallmann, A. M. M. Tréhu, G. Bohrmann, W. S. W. S. Borowski, and H. Tomaru. 2004. Gas hydrate growth, methane transport, and chloride enrichment at the southern summit of Hydrate Ridge, Cascadia margin off Oregon. Earth Planet. Sci. Lett. **226**: 168–175.

Torres, M., J. McManus, D. Hammond, M. A. de Anglis, K. Hesschen, S. Colbert, M. D. Tryon, K. Brown, and E. Suess. 2002. Fluid and chemical fluxes in and out of sediments hosting methane hydrate deposits on Hydrate Ridge, OR, I: Hydrological provinces. Earth Planet. Sci. Lett. **201**: 525–540.

Treude, T., A. Boetius, K. Knittel, K. Wallmann, and B. Barker Jørgensen. 2003. Anaerobic oxidation of methane above gas hydrates at Hydrate Ridge, NE Pacific Ocean. Mar. Ecol. Prog. Ser. **264**: 1–14.

Tryon, M., K. Brown, and M. Torres. 2002. Fluid and chemical flux in and out of sediments hosting methane hydrate deposits on Hydrate Ridge, OR, II: Hydrological processes. Earth Planet. Sci. Lett. **201**: 541–557.

Tryon, M. D., C. G. Wheat, and D. R. Hilton. 2010. Fluid sources and pathways of the Costa Rica erosional convergent margin. Geochemistry, Geophys. Geosystems **11**: n/a–n/a.

Visser, W., W. a Scheffers, W. H. Batenburg-van der Vegte, and J. P. van Dijken. 1990. Oxygen requirements of yeasts. Appl. Environ. Microbiol. **56**: 3785–92.

Wallmann, K., E. Pinero, E. Burwicz, M. Haeckel, C. Hensen, A. Dale, and L. Ruepke. 2012. The Global Inventory of Methane Hydrate in Marine Sediments: A Theoretical Approach. Energies **5**: 2449–2498.

Whiticar, M. J. 2002. Diagenetic relationships of methanogenesis , nutrients, acoustic turbidity , pockmarks and freshwater seepages in Eckernförde Bay. Mar. Geol. **182**: 29–53.

Widdel, F., and F. Bak. 2006. Gram-negative mesophilic sulfate-reducing bacteria, p. 3352–3378. *In* M. Dworkin, S. Falkow, E. Rosenberg, K.-H. Schleifer, and E. Stackebrandt [eds.], The Prokaryotes. Springer US.

Chapter 5

Habitat depended methane efflux under varying fluid flow at the Concepción Methane Seep Area, Offshore Chile

Steeb, P.[1]*, Linke, P. [1], Treude, T. [1]*

[1] Helmholtz Centre for Ocean Research Kiel (GEOMAR), Wischhofstr. 1-3, 24148 Kiel, Germany

*Corresponding authors: psteeb@geomar.de, ttreude@geomar.de

Abstract

Within subduction zones of active continental margins, large amounts of methane can be mobilized by dewatering processes and transported to the seafloor along migration pathways. Before the methane is emitted to the water column, most of it is oxidized within the benthic methane filter by anaerobic oxidation of methane (AOM). AOM depend on sulfate supply from the seawater, the terminal electron acceptor. Fluid flux can shallow the sulfate penetration depth and forms therefore a key factor for the efficiency of the benthic methane filter.

In a recently discovered seep area located western of Concepción (Chile), surface sediments from different habitats were sampled to study the efficiency of the benthic methane filter. Porewater chemistry was analyzed and turnover rates of methane and sulfur were determined by radiotracer techniques. Additional, in vitro experiments with a recently developed Sediment-Flow-Through (SLOT) system were performed to challenge the benthic methane filter by increased fluid flux.

A bacterial mat habitat from a young seep site with moderate AOM areal rates (20.5±0.3 mmol m^{-2} d^{-1}) revealed a high adaptable benthic methane filter. The second habitat was a field of dead clams with moderate AOM rates

(16.9±0.3 mmol m^{-2} d^{-1}) and high sulfide concentrations. The in vitro experiments showed, how a methane and fluid pulse could change in sulfide excess which could initiate a sudden death of the seep fauna. The last habitat was a tubeworm field with an aerobic benthic methane filter (8.7±5.3 mmol m^{-2} d^{-1}), which changed in 150 d of oxygen-free incubation, into an efficient anaerobic benthic methane filter.

Introduction

Marine sediments at continental margins with their gas hydrate bearing sediments form huge reservoirs of methane (Kvenvolden 1993). Methane can migrate by diffusion or by mobilized fluids to the sediment surface and, through the water column, further to the atmosphere, where it acts as important greenhouse gas. However, most of the methane is already oxidized at the sediment surface, in the benthic methane filter (Sommer et al. 2006). The most important reaction within this methane sink is the anaerobic oxidation of methane (AOM). The methane is oxidized with sulfate as terminal electron acceptor and produces sulfide and bicarbonate (Boetius et al. 2000; Knittel et al. 2003; Treude et al. 2003) according the to the following net equation (1).

$$CH_4 + SO_4^{2-} \rightarrow HCO_3^- + HS^- + H_2O \quad (1)$$

While methane is delivered from deep reservoirs by advecting fluids, sulfate is supplied from the seawater by diffusion. The interface where methane and sulfate overlap in the sediment is called the sulfate methane transition zone (SMTZ) (Iversen and Jørgensen 1985). The depth of the SMTZ depends beside the sulfate reduction rate (Borowski et al. 1999) and methane flux (Borowski 2004), on advecting fluids through the sediment (Luff and Wallmann 2003; Mau et al. 2007).

At convergent continental margins, porewater is mobilized not only by sediment accumulation and compaction, but also from clay mineral dehydration and compaction by the underthrusted sediments (Hensen et al. 2004; Saffer and Tobin 2011). Seismic activity at subduction zones form faults and can focus upwards migrating fluids (Saffer and Tobin 2011). Gas hydrates influence methane and fluid flux, since they represent a methane reservoir on the one hand and can block fluid paths on the other hand (Tryon et al. 2002). By sufficient organic matter supply large

amounts of methane can accumulate and form widespread gas hydrate deposits owing to the optimum pressure-temperature conditions within the gas hydrate stability zone (GHSZ) (Kvenvolden 1993; Hester and Brewer 2009; Burwicz et al. 2011; Wallmann et al. 2012). At the bottom of the GHSZ, free methane is accumulated below dense gas hydrate layers. This interface can be detected seismically by the bottom simulated reflector (BSR) (Archer 2007). Heated focused fluids can locally change the GHSZ and generate gaps into the BSR, so called “wiped out” zones. Above this wiped out zones ascending fluids reach the sediment-water interface and form “cold seeps”, a common feature at continental margins (Judd et al. 2002; Levin 2005; Suess 2010). At cold seeps, the SMTZ is typically relatively shallow, as a result of fluid advection and high amounts of methane which are transported into the benthic methane filter. Accumulating sulfide feeds chemosynthetic organism (e.g., free-living sulfur bacteria as well as symbiont tubeworms, clams, and mussels) at the sediment surface. This seep fauna serves as indicator for methane flux and fluid advection (e.g., Mau et al. 2006; Sahling et al. 2003; Treude et al. 2003). Bacterial mats cover sediments with SMTZs only several cm below the seafloor and indicate hot spots of AOM and fluid flux. Clams can reach deeper sulfide and colonize at sites with less fluid flux and can increase the sulfate penetration depth by bio-irrigation. Tubeworms are found at less active sites and their “roots” reach deep into the sediment (Sahling et al. 2002).

Bicarbonate production from AOM increases carbonate alkalinity in the sediment and thereby facilitates the precipitation of sometimes voluminous authigenic carbonate deposits. These deposits represent a long-term sink for methane-derived carbon and archives seepage history (Liebetrau et al. 2010).

Geological setting of the study area

The Chilean coast is part of the Andes subduction system, where the Nasca Plate subducts beneath the South American Plate with a velocity of 66 mm yr^{-1} (Angermann et al. 1999). Between Miocene and Pliocene the Chilean convergent margin has changed from erosionary to accresionary subduction during the last 1-6 Ma, triggered by increased terrestrial input from the development of the Patagonian ice sheet (Kukowski and Oncken 2006; Melnick and Echtler 2006). The subduction trench is filled with 1.5-2 km sediment (Völker 2006). The upper part (0-1 km depth) of the sediment is frontally accreted caused by the overriding plate, while the lower

part (1-2 km depth) is underthrusting the forearc in a subduction channel (Geersen et al. 2011).

High amounts of low-weathered riverine input (Lamy et al. 1998; Scholz et al. 2013) are major deposits besides variable amounts of volcanic ashes (Lucassen et al. 2010). High amounts of organic matter produced in the nutrient-rich euphotic zone (Arntz and Fahrbach 1991) constantly deposit to the seafloor resulting in an organic carbon content of 2 - 4% in the sediment (Schubert and Nielsen 2000; Treude et al. 2005b; Niggemann et al. 2007).

Upwelling occurs in localized cells at the Chilean coast (Morales et al. 1996; Iriarte et al. 2000). In southern Chile, upwelling and the related formation of an oxygen minimum zone (OMZ) is a seasonal phenomena restricted to the summer. High rates of sulfate reduction occur over the entire continental margin of Chile (Thamdrup and Canfield 1996; Ferdelman et al. 1997; Treude et al. 2005b; Niggemann et al. 2007) and is estimated to account for up to almost 100% of the organic matter degradation within the OMZ (Thamdrup and Canfield 1996). In general, sulfate reduction off Chile increases from north to south (Niggemann et al. 2007) and with water depth (Thamdrup and Canfield 1996; Ferdelman et al. 1997; Treude et al. 2005b). Inside diffusive SMTZs, sulfate reduction is mostly fueled by methane (Treude et al. 2005b).

Offshore Concepción at around 36°S, the Concepción Methane Seep Area (CMSA) is located between 600 and 1000 m below sea level (mbsl). This area was first discovered after noticing the abundant presence of chemotrophic and chemosymbiotic organisms (Sellanes et al. 2004, 2010; Zapata-Hernández et al. 2014). Backscatter anomalies show widespread occurrence of authigenic carbonates of both recent and fossil seep sites (Klaucke et al. 2012). Increased heat flow was detected above without or weak bottom simulating reflector (BSR) was detected in a ~11 km long seismic NW-SE transect (Grevemeyer et al. 2006). The BSR becomes shallower upslope. Piston coring revealed SMTZ between 30 and 1000 cm, with shallowest depths above the wipe out zones (Coffin et al. 2007). Samples from this transect and from a gas hydrate mound show sulfate-reducing bacteria within the SMTZ, as compared to sediment layers above and below (Hamdan et al. 2008). Low fluid flux (0.08-0.18 cm yr^{-1}) was determined for CMSA sediment, and methane has mostly biogenic origins with sometimes small fractions of thermogenic gas (Scholz et al. 2013).

Earthquakes are very common at convergent margins and can induce fluid and methane flow (Grevemeyer et al. 2006; Mau et al. 2007). The Chilean convergent margin represents one of the most active seismic areas and just recently (27. Feb. 2010) one of the strongest known earthquakes (Mw 8.8 Maule Earthquake) occurred, with its epicenter just ~100 km north of Concepción (Völker et al. 2011 references there in). On a cruise just 7 month after this earthquake we investigated the efficiency of the microbial benthic methane filter as well as the response of induced fluid flow and methane flux, in this region

In the present study we determined for the first time methane turnover rates in surface sediments from different chemosynthetic habitats within the CMSA and analyzed related geochemical parameters. We experimentally studied the efficiency of the microbial benthic methane filter and its response to sudden changes in fluid and methane flux. The experiments were realized by applying fluid flow to sediment cores over a period of 6 months using a recently developed sediment flow through (SLOT) system (Steeb et al. 2014).

Methods

Sediment sampling: During the CHIFLUX cruise (SO210) of the German research vessel “Sonne”, surface sediments from different cold seep habitats (a bacterial mat, a clam field, and a tubeworm field) were sampled with different push cores deployed by the Remotely Operated Vehicle (ROV) "Kiel 6000", GEOMAR, Shilling Robotics). Four sediment cores were taken from each station. One core was used for the extraction and analyses of porewater, as well as the determination of methane concentration and sediment porosity. A second core was used for the determination of microbial methane oxidation and sulfate reduction. Two sediment cores were sampled with special SLOT-liners (length 30 cm, i.d. 6 cm, Steeb et al. 2014) for *in vitro* experiments at GEOMAR, Kiel, Germany. Three different types of chemosynthetic habitats were sampled (see below): (a) sediments covered by dense mats of free-living, filamentous sulfur bacteria ("bacterial mat habitat"), (b) sediments occupied by epibenthic chemosymbiotic clams ("clam field habitat"), and (c) sediments inhabited by chemosymbiotic frenulate tubeworms ("tubeworm field

habitat"). After recovery, sediment cores were transferred to a 4°C cold room for immediate subsampling.

Habitat description:

Characteristics of all sampling sites are summarized in Table 1. Soft sediments were typical for the entire area of the *bacterial mat* site, without indications of massive authigenic carbonate accumulations. Sometimes black spots instead of sulfur bacteria mat were observed at the sediment surface, indicating sulfide consumption by iron in the sediment (Treude et al. 2009).

Table 1: Sampling sites of the of three sediment types, sampled all by push cores deployed by ROV. integrated area rates of AOM and sulfate reduction (SR) are calculated for the upper 15 cm. For the tubeworm sediment, no SMTZ can be determined and AOM rates are methane oxidation rates.

Station	Habitate	Latitude (S)	Longitude (W)	Water depth (bsl) m	Depth of SMTZ cm	AOM mmol m^{-2} d^{-1}	SR mmol m^{-2} d^{-1}	AOM : SR
SO210-St42	Bacteria mat	- 36:28.241	- 73:40.727	707	0 - 5	20.5 ± 0.33	24.2 ± 4.01	0.85
SO210-St25	Clam field	- 36:22.857	- 73:42.767	689	5 - 12.5	16.9 ± 6.48	57.0 ± 35.61	0.30
SO210-St88	Pogonophorean	- 36:22.871	- 73:42.588	685	N. A.	8.67 ± 5.28	0.31 ± 0.05	27.97

In the area of the clam and tubeworm field, open cracks in the seafloor and sediment depressions were observed, indicating seismic activity. The clam field habitat, localized in a slight depression, was densely covered by clam shells mainly of *Calyptogena gallardoi*. Beside *C. gallardoi*, many other seep organisms such as the clam *Tyrasira* spp. and mussels, probably Acharax spp., were identified. All ROV videographs and grab samples revealed exclusively dead clams. Surrounding massive carbonate boulders in the vicinity of the clam field were populated by vestimentiferan tubeworms (*Lamellibrachia sp*.) and revealed an age of 4.6-5.6 kyr (V. Liebetrau, pers. comm.) according to $^{230}Th/^{234}U$ dating. Almost 2 µmol l^{-1} methane was detected in the bottom water directly above the clam field (Linke 2011). Inside the clam-field sediment young, micritic authigenic carbonates were found. The tubeworm field, was populated by a dense colony of frenulate tubeworms. Tubes protruded into the water column and extended at least 13 cm (the maximum sampling depth) into the sediment. The very soft and fluffy surface sediment had a bright color, indicating full oxidation. Protruding tubes were covered with organic particles,

Figure 1: Sampled habitats at the CMSA, bacterial mat (A, B), clam field (C, D), tubeworm field (E, F), recent crack in the seafloor (G) next to the sampling sites of the clam and tubeworm field. On the right sampling with push cores deployed by ROV “Kiel 6000” (B, D, F). Pictures: ROV “Kiel 6000” on the cruse SO210, Chiflux, October 2010.

probably as a result of sediment-trapping attributes, and were grazed by demersal deep-sea shrimps.

Biogeochemical determinations onboard: *Porewater sampling.* Porewater was extracted by a porewater squeeze with argon pressure of 3 to 5 bar and filtered with

a 0.2 µm cellulose acetate membrane filter. Anions like SO_4^{2-}, Cl^- and Br^- were analyzed by ion chromatography (IC, METROHM 761 Compact), sulfide was determined photometrically by the Cline (1969) method according to Grasshoff et al. (1983), and total alkalinity (TA) was determined by titration with 0.02 M HCl (Ivanenkov and Lyakhin 1978). All porewater extraction and analytics were performed onboard.

Methane concentration. Three ml of sediment were sub-sampled with cut-off syringes (PE, 10 ml) and transferred into glass vials containing 9 ml 1M NaOH. Vials were immediately closed with rubber stoppers and shaken thoroughly to stop microbial activity and to equilibrate methane with the headspace. The headspace was analyzed onshore using a GC (CE 8000 TOP gas chromatograph) equipped with a 30 m capillary column (Restek Q-PLOT, 0.32 mm) and a flame ionization detector (FID).

Sediment porosity and CNS content. Small sediment sub samples were transferred in pre-weighted plastic cups and closed gastight. Onshore the samples were weighted, freeze dried, and re-weighted, to calculate the porosity. Subsamples of this sediment sample were later used to determine total carbon (TC), total organic carbon (TOC), total nitrogen (TN), and total sulfur (TS) using Carbo Erba Element Analyzer (NA1500). TOC was determined after adding 1M HCl to get rid of the carbonate. Total inorganic carbon (TIC) was calculated from the difference between TC and TOC.

Microbial turnover rates. For the determination of AOM and sulfate-reduction rates three sub cores (length 30 cm, diameter 2.6 cm, polycarbonate) each (six total) were sampled from one push core. Through small silicon filled holes, 15 µl $^{14}CH_4$ (1–2 kBq dissolved in anoxic, sterile water; specific activity 22.28 GBq mmol-1), and 6 µl $^{35}SO_4^{2-}$ (200 kBq dissolved in water; specific activity 37 TBq mmol-1), were injected into the sediment of the AOM and sulfate reduction cores, respectively, at a vertical resolution of 1 cm; according to whole-core incubation of (Jørgensen 1978). After 24 h incubation under *in situ* temperature in the dark, the sub cores were sliced in cm intervals. AOM samples were transferred into glass vials (50 ml) containing 20 ml 2.5% w/v NaOH, immediately closed with rubber stoppers, and shaken thoroughly, to stop all microbial activity. Sulfate reduction samples were transferred into 50 ml plastic centrifuge vials containing 25 ml 20% w/v Zn-acetate, closed, and shaken

thoroughly. Controls (five for AOM, three for sulfate reduction) were first transferred into NaOH and Zn-acetate solution, respectively, before the tracer addition. AOM rates were determined according to Treude et al. (2005) (CH_4 determination, combustion, and calculation) and Joye et al. (2004) (CO_2 trapping). Sulfate reduction rates were determined according to Kallmeyer et al. (2004).

***In vitro* experimentations:** To challenge the benthic microbial methane filter and to follow its response to different fluid and methane fluxes, a newly developed Sediment Flow Through (SLOT) system was used (Steeb et al. 2014). The SLOT system mimics natural fluid and methane seepage through intact sediment cores and facilitates the step-wise monitoring of vertical porewater gradients as well as in- and out-put parameters over the course of the experiment. After experiment termination, further parameters, such as AOM and sulfate reduction rates, can be determined in the sediment core.

SLOT system functionality. The SLOT system is working with two different media, representing the seawater and the fluid, both modified sulfate reducer media after Widdel and Bak (2006). Artificial anoxic seawater was delivered to the top of the core. Anoxic, sulfate-free, and methane enriched medium, representing the fluid, was pumped in the core from below. The salt concentrations of the different media are summarized in Table 2.

Table 2: Salt concentrations of the two different media used in the SLOT-System. Seawater medium with sulfate was delivered from the top, seepage medium with methane and without sulfate from the bottom. In the last line, the gas of the medium headspace is denoted.

	Seawater medium (with SO_4^{2-})	**Fluid medium (with CH_4)***
Salts	**in mmol l^{-1}**	**in mmol l^{-1}**
KBr	0.800	0.756
KCl	8.050	8.050
$CaCl_2$ $2H_2O$	10.000	10.00
$MgCl_2$ $6H_2O$	27.890	55.490
$MgSO_2$ $7H_2O$	27.600	0.000
NaCl	451.000	451.000
Medium headspace	N_2	CH_4

* $FeSO_4$ (trace element) was replaced by FeCl

The outflow was located at the top, whereby the sulfate from the artificial seawater could penetrate into the sediment only by diffusion. Both media were prepared with

salt concentrations of seawater (except sulfate), a pH of 7.5, and a TA concentration of 2-4 meq l^{-1}. Before the cores were connected to the system, the rubber stoppers were removed, a filter was distributed below the sediment, and caps with in- and out-flow ports were placed on top and bottom. One line of silicon sealed sampling holes was equipped with rhizons for porewater extraction. Preperation of the sediment cores is described in Steeb et al. (2014).

SLOT sampling measurements: SLOT enables porewater measurement and sampling over the entire experiment. Sulfide, pH, and redox potential was measured by needle microsensors (Revsbech and Jørgensen 1986), pricked through the silicon sealed sampling holes into the sediment. Sulfate, bromide, chloride and TA were determined in porewater, extracted with the aid of preinstalled rhizons (rhizosphere, CSS-F, length 5 cm, diameter 2.5 mm, pore size 0.2 µm).Sulfate and Bromide were analyzed by IC (METROHM 761 Compact, sulfate by conductivity detector, Bromide by UV/VIS detector lambda 1010 at 230 nm), and TA by titration (see above, Ivanenkov and Lyakhin 1978). In- and outflow were sampled by connecting borosilcate glass syringes on fast couplers of the in- and outflow (Steeb et al. 2014) for ion concentrations (SO_4^{2-}, Br^-, TA, see above) and methane. Methane subsamples (2 ml) were transferred into glass vials containing 5 ml 2.5% w/v NaOH, closed immediately with butyl rubber stopper, and shaken. The headspace of the samples was analyzed by gas chromatography (Hewlett Packard Series II) with a packed column (Haye SepT, 6 ft, 3.1 mm inner diameter, 100/120 mesh, Resteck, carrier gas: He 20 ml min^{-1}, combustion gas: synthetic air 240 ml min^{-1}, H_2 20 ml min^{-1}).

At the end of the experiment, the rhizons were removed, the caps opened and two sub core tubes for rate measurement were pressed into the sediment. Turnover rates of AOM and sulfate reduction were analyzed according to the onboard proceedings (see above), with one replicate each. Sediment for controls (5 for AOM, 3 for sulfate reduction) was collected from sediments beside the sub cores. Remaining sediment was sampled in 1 cm intervals for methane (2 cm^3 sediment in 5 ml 2.5% w/v NaOH, see above), and sliced in 2 cm intervals for porosity (see above). TC, TOC, TIC, TN, and TS were analyzed from small subsamples of the freeze dried porosity samples (see above). All sampling and measurement proceedings are described in Steeb et al. (2014).

Experiment procedure:

In a pre-phase (22 d) only the seawater inflow from above was connected and the outflow was located at the bottom of the core, to set all geochemical gradients to equal, constant conditions. After this pre-phase both, seawater (from the top) and seepage (from the bottom) media were connected and the outflow was located at the top of the core. Two different flow regimes for each habitat were applied (i) with a moderated advective flow, further called low flow core (LFC), (ii) high advective fluid flow, further called high flow core (HFC). The pumping rate for the seawater was set to 20 µl min^{-1} in all cores. Pumping rates of the fluid were 4 µl min^{-1} for the LFC and 8 µl min^{-1} for the HFC. Different porosities of the cores result different advective flow rates and related methane fluxes, all listed in table 3.

Calculations: *Methane concentrations*. Methane samples collected from the in- and outflow were analyzed at different time points. Samples analyzed immediately after sampling showed consistently higher methane levels compared to samples that were stored up to twelve months prior to analyze. Since repeated measurements revealed a linear correlation between methane losses and time (R^2 0.97), methane concentrations determined at later time points were corrected by the estimated loss.

Table 3: Overview of pumping rates, dilution factors, advective fluid flows, hydrological residence times, methane fluxes and runtime of the experiment, for the three different habitats used in SLOT-system under low (LFC) and high (HFC) fluid flow conditions.

	Bacterial Mat		Clam Field		Pogonophorean Field	
	LFC	HFC	LFC	HFC	LFC	HFC
Pumpin Rate Seawater (above) in µl min^{-1}	20	20	20	20	20	20
Pumpin Rate Fluid (below) in µl min^{-1}	4	8	4	8	4	8
Dilution Factor in the Bottom Water	6.0	3.5	6.0	3.5	6.0	3.5
Fluid Flow in cm yr^{-1}	118.1	232.4	112.7	229.8	114.5	232.3
Hydrological Residence Time (HRT) in d	111	56	114	56	113	56
Methane Flux in mmol m^{-2} d^{-1}	3.234	6.364	3.087	6.291	3.134	6.359
Runtime of the Experiment in d	138		144		151	

AOM rates determined from in- and outflow methane. Aside from radiotracer measurements, AOM rates were calculated from the difference between the methane concentration in the in- and outflow of the system. For the outflow, methane concentration was multiplied by the dilution factor of the seawater medium in the overlying water column (6 and 3.5 for low and high flow rate, respectively). For the inflow, the methane concentration of the seepage medium was used. The difference of the two methane concentrations was then divided by the average time the fluid

needed to pass the incubation chamber (hydrologic residence time – HRT, Table 3) and the cross-section area of the core (28.3 cm²). The methane efflux from the cores was calculated by multiplying the outflow methane concentration by the dilution factor (Table 3) and the fluid flow (Table 3). Turnover rates and methane efflux were converted to mmol m^{-2} d^{-1}.

Results

Field data:

Bacterial Mat: Sediments from the bacterial mat were black from the surface to 5 cm below seafloor (bsf), and dark gray between 5 and 12 cmbsf. The rest of the sediment core (down to 23 cmbsf) was bright gray interspersed with black spots. Gas bubbles were observed between 2 and 20 cmbsf with highest concentration and size between 2 and 12 cmbsf.

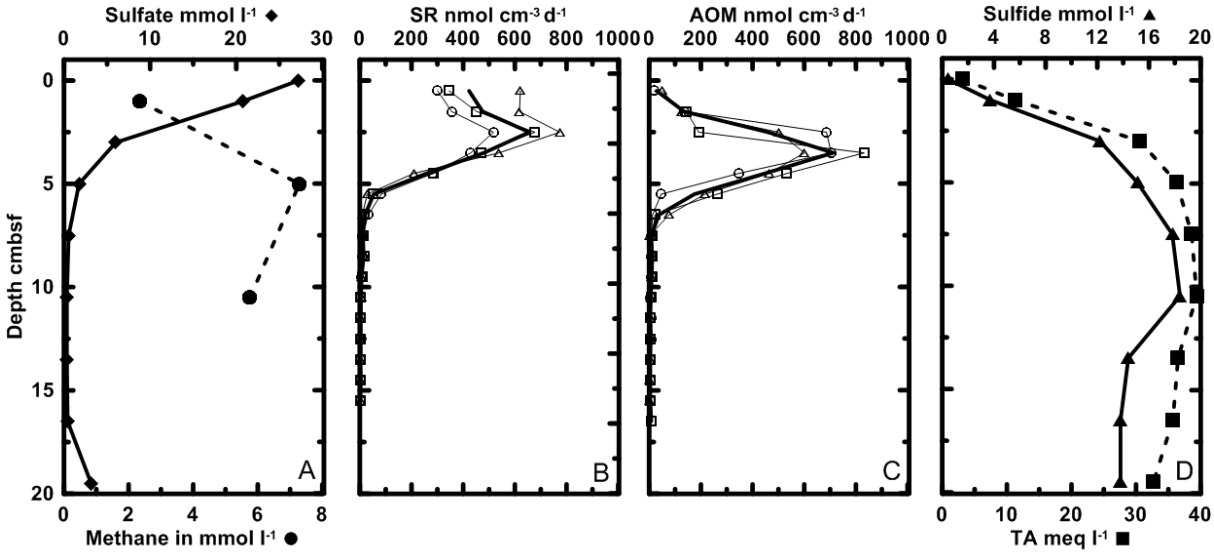

Figure 2: Porewater profiles of SO210-St42 and turnover rates at 707 m water depth of a bacterial mat. Shown are A) sulfate (dot) and methane (diamond) concentrations, B) three replicates of sulfate reduction and their average (bulk line), C) three replicates of AOM rates and their average (bulk line),D) sulfide and total alkalinity concentration in relation to the sediment depth below seafloor (bsf).

The sediment of the entire core was very soft; below 10 cmbsf white clam shell fractures were found sporadically. Sulfate was depleted from 27.3 mmol l^{-1} in the bottom water, to 0.5 mmol l^{-1} at 7.5 cmbsf. Methane increased from the top (2.33 mmol l^{-1}) to 5 cm (7.3 mmol l^{-1}) and revealed a shallow SMTZ in the first 10 cm

(Fig. 2A). Sulfate reduction rates were highest in the first 5 cmbsf with a maximum at 2.5 cmbsf (660 ± 130 nmol cm^{-3} d^{-1}), and close to zero below 7.5 cmbsf (Fig. 2B). AOM rates were almost zero at the sediment surface and increased to a maximum (712 ± 116 nmol cm^{-3} d^{-1}) at 3 cmbsf. Similar to sulfate reduction, AOM rates were zero below 7.5 cmbsf. Areal rates integrated over 0-15 cmbsf were 24.16 ± 4.02 mmol m^{-2} d^{-1} for sulfate reduction and 20.53 ± 0.33 mmol m^{-2} d^{-1} for AOM. Sulfide and total alkalinity (TA) increased simultaneously (Fig. 2D) from 0.42 mmol l^{-1} sulfide (3.1 meq l^{-1}, TA) at the sediment surface, to a maximum of 18.4 mmol l^{-1} sulfide (39.5 meq l^{-1}, TA) at 10.5 cmbsf. Below 11 cmbsf, the concentrations decreased slightly to 13.8 mmol l^{-1} and 32.7 meq l^{-1} for sulfide and TA, respectively. Porosity and solid phase parameters of the bacterial mat, clam field and tubeworm field sediments (e.g., TC, TIC, TOC, TN, TS, C/N) are described below for direct comparison with data generated from the *in vitro* experiment.

Clam field: The first two cmbsf of the sediment core were brown-green followed by a black layer down to 8 cmbsf. Below 8 cmbsf, the sediment got brighter with the depth. Gas bubbles were distributed over in the entire core. Sulfate concentration was 27.6 mmol l^{-1} in the bottom water and decreased only slightly to 23.7 mmol l^{-1} in the first 5 cmbsf. Below 5 cmbsf, sulfate strongly depleted to 4.7 mmol l^{-1} at 7.5 cmbsf and depleted further down to 12.5 cmbsf (1.3 mmol l^{-1}). Methane was 0.19 mmol l^{-1} at the top of the core and increased successively to 6.6 mmol l^{-1} at 16 cmbsf (Fig. 3A). Sulfate reduction occurred mostly between 2.5 and 12.5 cmbsf, with a maximum of 963 ± 885 nmol cm^{-3} d^{-1} at 5 cmbsf. AOM rates were slightly lower between 2.5 – 10 cmbsf with a maximum of 313 ± 105 nmol cm^{-3} d^{-1}.

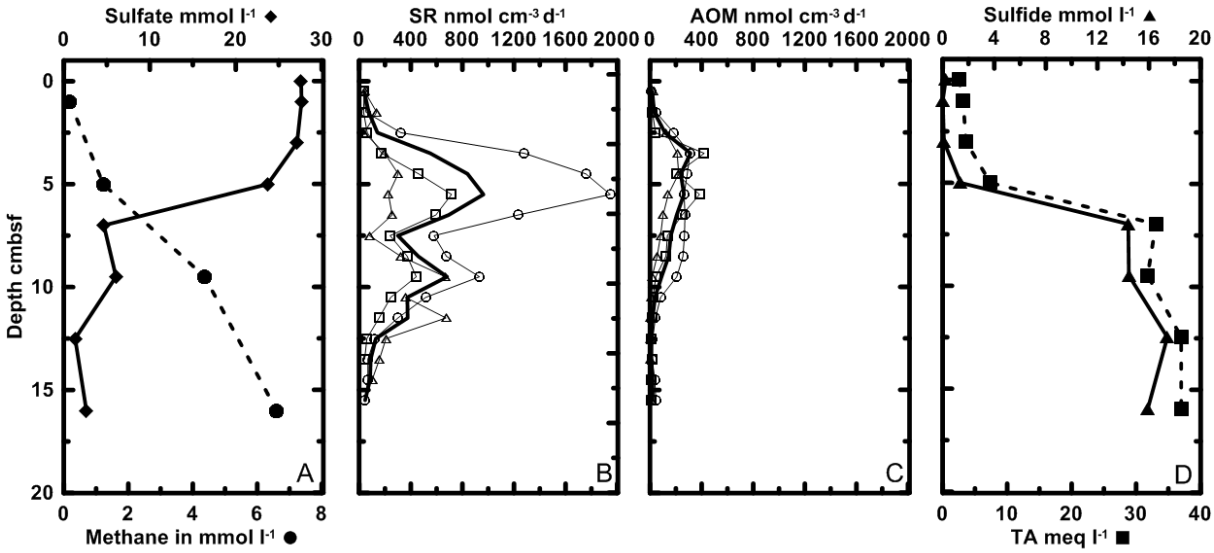

Figure 3: Porewater profiles of SO210-St25 and turnover rates at 689 m water depth of a clam field. Shown are A) sulfate (dot) and methane (diamond) concentrations, B) three replicates of sulfate reduction and their average (bulk line), C) three replicates of AOM rates and their average (bulk line),D) sulfide and total alkalinity concentration in relation to the sediment depth below seafloor (bsf).

Above and below this zone, almost no AOM activity was detected (Fig. 3C). Areal rates integrated over 0-15 cmbsf were 57.03 ± 35.61 mmol m^{-2} d^{-1} for sulfate reduction and 16.93 ± 6.48 mmol m^{-2} d^{-1} for AOM. Sulfide and TA were almost constant in the upper part of the core (0.00 - 0.23 mmol l^{-1} and 2.5 - 3.6 meq l^{-1}, respectively) and increased rapidly to 14.4 mmol l^{-1} and 33.6 meq l^{-1}, respectively, below 5 cmbsf. The depth of these peaks coincided with sulfate depletion and the sulfate reduction maximum.

Tubeworm field: The sediment was bright brownish in the first three cmbsf and bright gray below, displaying a few black spots. Tubes were observed at least down to 13 cmbsf but decreased in abundance with depth. We cannot exclude a penetration depth of the tubes deeper than 13 cmbsf, since tube penetration was not determined in cores longer than 13 cm (porewater and rates). Signs of bioturbation (e.g., burrows) were detected in the entire sediment. The sediment was very fluffy in the upper part (down to 3 cmbsf) and much harder and clayish below. Sulfate concentration remained constant within the first 7.5 cmbsf (~28.0 mmol l^{-1}) and linearly decreased below this depth to reach 18.6 mmol l^{-1}at the bottom of the core (19 cmbsf) (Fig. 4A). Sulfate reduction was very low in the entire sediment core. In the first 5 cm, rates increased to a maximum of 3.3 ± 0.8 nmol cm^{-3} d^{-1} (Fig. 4B).

Below 7.5 cmbsf, sulfate reduction was constant between 1.4 – 2.6 nmol cm^{-3} d^{-1}. Methane oxidation was detected only in upper 5 cmbsf, with a maximum turnover of 228.8 ± 277.2 nmol cm^{-3} d^{-1} at the sediment-water interface (Fig. 4C), and was most likely coupled to aerobic rather than anaerobic processes (see discussion).

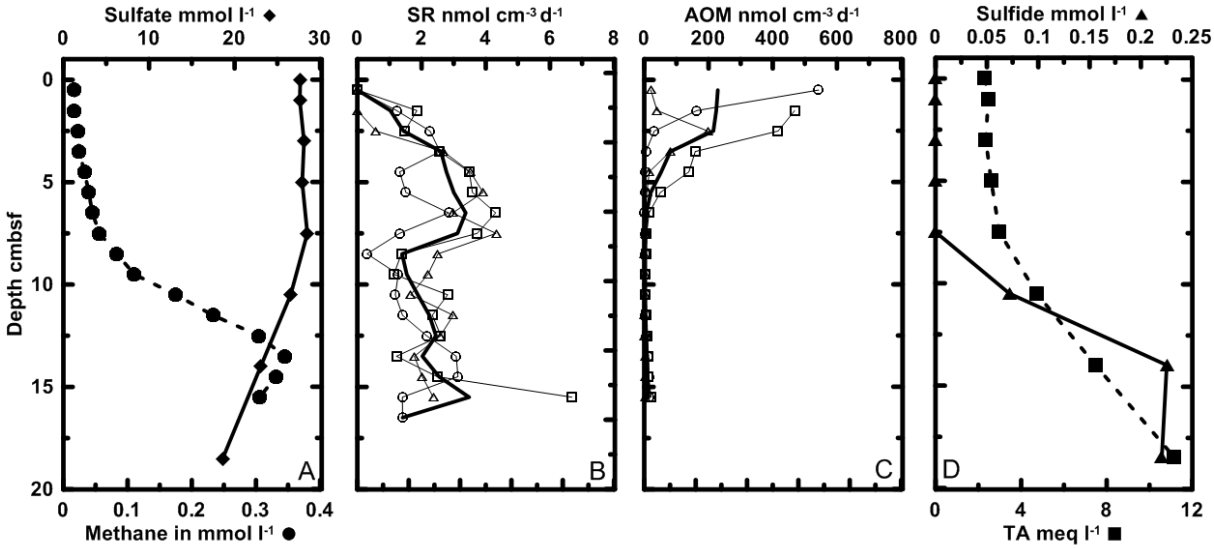

Figure 4: Porewater profiles of SO210-St88 and turnover rates at 688 m water depth of a tubeworm field. Shown are A) sulfate (dot) and methane (diamond) concentrations, B) three replicates of sulfate reduction and their average (bulk line), C) three replicates of AOM rates and their average (bulk line),D) sulfide and total alkalinity concentration in relation to the sediment in cm depth below seafloor (bsf).

Areal rates integrated over 0-15 cmbsf were much lower (0.31 ± 0.05 mmol m^{-2} d^{-1} and 8.80 ± 5.37 mmol m^{-2} d^{-1} for sulfate reduction and methane oxidation, respectively) compared to the bacterial mat and the clam field. Sulfide was not detected in the upper 7.5 cmbsf and also TA remained constant at seawater levels of 2.3 meq l^{-1}. At the depletion depth of sulfate, sulfide increased simultaneously with TA to reach a maximum concentration of 0.22 mmol l^{-1} and 11.2 meq l^{-1}, respectively, at the bottom of the core.

SLOT Experiment:

In the following geochemical gradients and methane out-flow parameters are described for each habitat. Subsequently, turnover rates and additional sediment parameters determined directly after the last measuring time point are described.

Geochemical gradients and in/outflow budgets:

Bacterial mat habitat: At the beginning of the experiment (4 d), sulfate and bromide gradients revealed no depth gradient in the low flow regime core (LFC) of the bacterial mat core (29 mmol l^{-1} sulfate and ~0.0 µmol l^{-1} bromide between 0-20 cmbsf, Fig. 3A). Sulfide concentration was high at the top (up to~4750 µmol l^{-1}) and fluctuated between 842-1455 µmol l^{-1} below 2 cm sediment depth (Fig. 5B). Total alkalinity (TA) ranged from 5 to 6 meq l^{-1}. The redox potential was about -250 mV in the first cm of the sediment and decreased to -350 mV at 12 cmbsf. At the sediment-water interface, a high pH of 8.5 was detected. Inside the sediment, pH ranged from 8.0 to 8.3.

After 54 d, sulfate and bromide concentration profiles still revealed no gradient (Fig. 5D). Sulfide ranged between 800 and 1200 µmol l^{-1} over the top 16 cm. The high sulfide peak at the top of the sediment disappeared. TA was 5.7 meq l^{-1} at top of the sediment and increased to 6.1 meq l^{-1} at a sediment depth of 16 cm (Fig. 5E). In the upper part of the sediment, the pH was around 8.0 and increased to a maximum of 8.2 at the bottom of the core (Fig. 5F).

After 107 d, bromide, which was used as tracer for the seepage medium, was detectable in the lower part of the core (10-20 cmbsf) indicating seepage medium intrusion. The bromide gradient was mirrored by the sulfate concentrations (reduction to 20 mmol l^{-1} at the bottom). Sulfide concentrations were decreased below 700 µmol l^{-1}. In the upper part of the sediment sulfide ranged between 236 and 624 µmol l^{-1}. Below 8 cmbsf, sulfide decreased almost linearly down to 40 µmol l^{-1}at the bottom of the core. TA was at 4.3 meq l^{-1} at the top of the core and increased almost linearly to 5.9 meq l^{-1}. In the entire sediment column pH declined to around 7.5.

Directly before experiment termination (138 d), sulfate and bromide profiles were dropped down slightly, compared to the profiles from 48 d (compare Fig. 3G and J). This artifact can resulted from porewater sampling or a may be pumping error and is also observed at the parallel cores of the in vitro experiments. Sulfide was almost below 400 µmol l^{-1}, with a maximum at 6 cmbsf (421 µmol l^{-1}). Between 12 and 16 cm sediment depth, sulfide showed a minimum (209 µmol l^{-1}), before it again increased to reach 335 µmol l^{-1} at the bottom of the core. At the top of the core TA was

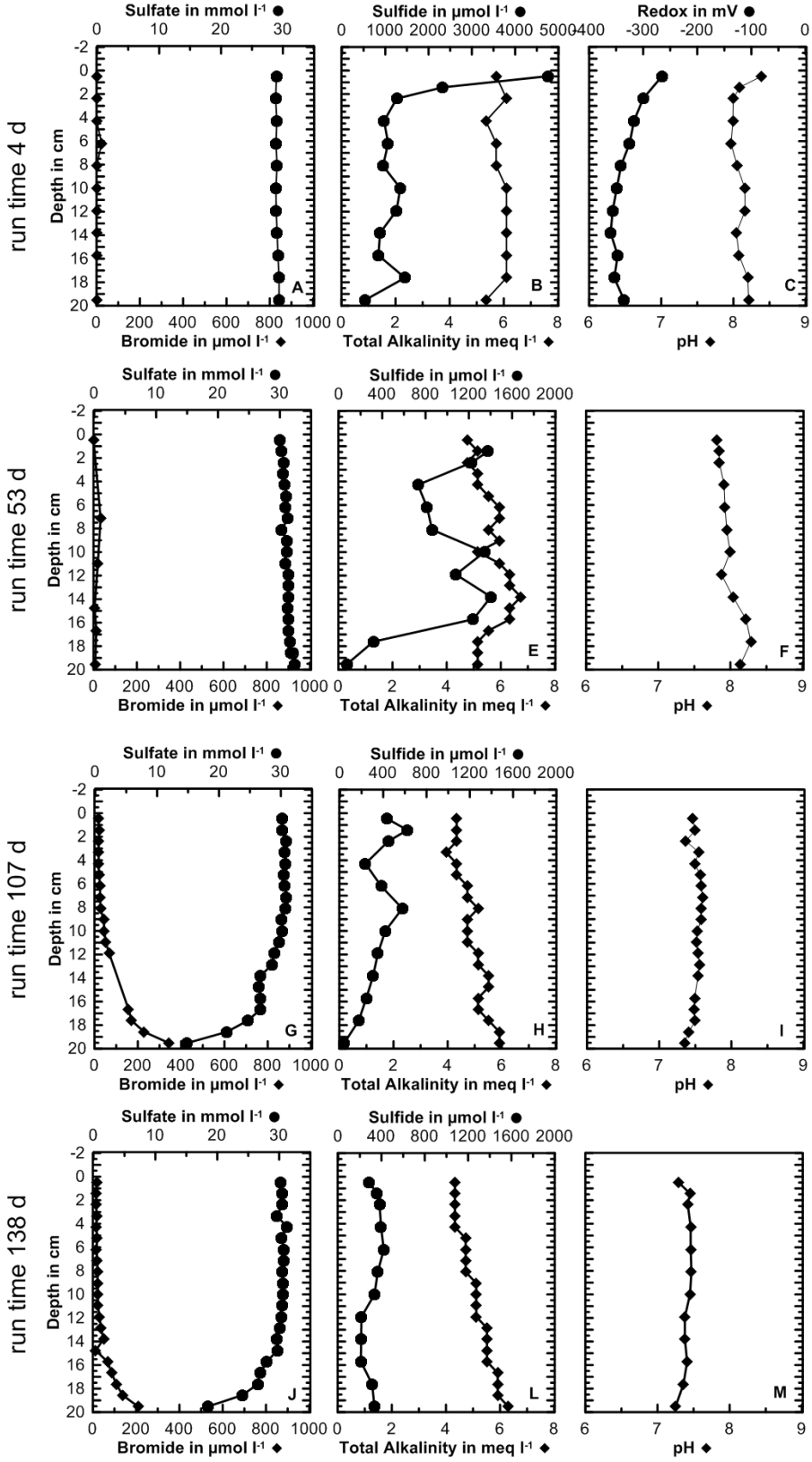

Figure 5: Geochemical gradients in the Low Flow Core (LFC) core of the bacterial mat (SO210-St42) during the experiment. Shown are: bromide (tracer) sulfate concentrations, sulfide and total alkalinity concentrations(B, E, H), as well as pH (C, F, I) and redox potential (C), to different run time of the experiment.

4.3 meq l^{-1} and increased stepwise to 6.3 meq l^{-1} at the bottom of the core. The pH stayed around 7.5 at the upper sediment and a bit lower (7.3) below 12 cm sediment depth (Fig. 5M).

Methane concentration determined in the outflow of the system increased from 0.2 to 3.2 µmol l^{-1} over the entire runtime (138 d) (Fig. 7A).

In contrast to the LFC, sulfate was already decreased (20 mmol l^{-1}), and accordingly the bromide concentration was increased (253 µmol l^{-1}), at the bottom of the high flow regime core (HFC) after 4 d. Sulfide was 1475 µmol l^{-1} at the top, decreased between 2 and 8 cm (781 – 1140 µmol l^{-1}) and increased again in the lower part of the core to reach a maximum of 2273 µmol l^{-1} at 14 cmbsf. TA increased from the top

(5.3 meq l^{-1}) to the bottom (6.9 meq l^{-1}) (Fig. 6B). At the upper part of the sediment, pH was lower (7.8-7.9) (Fig. 6C) than in the LFC, with lower increase at the very top (0-1 cm, 8.0), while in the lower part pH increased at the same depth like sulfide (pH 8.4, 12- 21 cm). Redox potential was strongly reduced at values between -347 and -406 mV in the entire core.

After 53 d runtime, bromide, i.e., the seepage medium, had ascended to 8 cm sediment depth and reached concentrations of 711 µmol l^{-1} at the bottom of the core (Fig. 6D). Sulfate mirrored this profile and was depleted down to 4.2 mmol l^{-1} at the bottom of the core. Sulfide was high at the top of the sediment (1798 µmol l^{-1}) and decreased rapidly down to around 600 µmol l^{-1} at 2 cmbsf, from where concentrations further decreased to the core bottom (254 µmol l^{-1}) (Fig. 6E). TA was 5.5 meq l^{-1} at the top of the core, reached a minimum at 3 cmbsf (4.8 meq l^{-1}) and increased to 6.7 meq l^{-1} at 10 cmbsf. In the entire core, pH was between 7.8 and 8.0 (Fig. 6F).

After 107 d run time, bromide had reached the sediment-water interface (~100 µmol l^{-1}) and remained constant within the first 5 cm (Fig. 6G). Below 5 cmbsf, bromide increased with sediment depth to 630 µmol l^{-1} at the bottom. Sulfate was around 28 mmol l^{-1} in the upper 5 cm and depleted to 6.2 mmol l^{-1} at the bottom of the core. Sulfide was between 710 and 1023 µmol l^{-1}, except for some minima (Fig. 6H). At the bottom, sulfide had only 375 µmol l^{-1}. TA reached concentrations of 4.7 meq l^{-1} (0-5 cmbsf) and 5.5 – 5.9 meq l^{-1} (5-20 cmbsf). Similar to sulfide, TA was

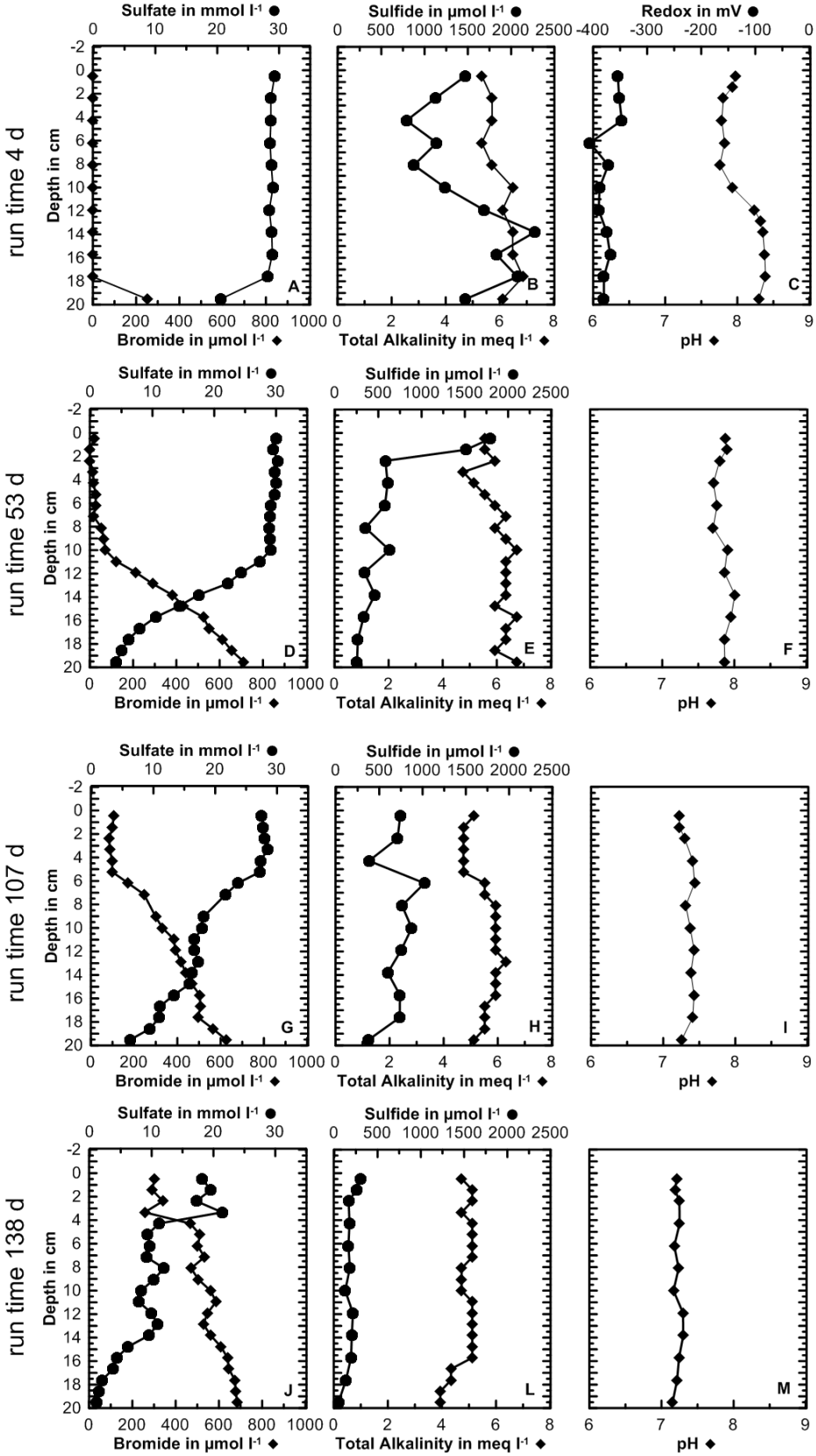

Figure 6: Geochemical gradients in the High Flow Core (HFC) of the bacterial mat (SO210-St42) during the experiment. Shown are: bromide (tracer) sulfate concentrations(A, D, G), sulfide and total alkalinity concentrations(B, E, H), as well as pH (C, F, I) and redox potential(C), to different run time of the experiment.

lower (5.1 meq l^{-1}) at the bottom. The pH was decreased to 7.2 – 7.4 over the entire core (Fig. 6I).

Directly before experiment termination (138 d), bromide reached 300 µmol l^{-1} at the top and increased to 685 µmol l^{-1} at the bottom (Fig. 6J). The profile was mirrored by sulfate with only 18.1 mmol l^{-1} at the top and 1 mmol l^{-1} at the bottom. Sulfide concentrations were generally strongly reduced (160 – 300 µmol l^{-1}). In the bottom part (16 – 20 cm sediment depth) sulfide further decreased down to 47 µmol l^{-1}. TA was between 4.9 and 5.1 meq l^{-1}, and was depleted in the bottom part (3.9 meq l^{-1}) similar to sulfide. pH further decreased to 7.2- 7.3 (Fig. 6M).

Similar to the LFC, methane concentrations in the outflow of the HFC increased from 0.6 to 3.6 µmol l^{-1} over the entire run time (138 d) (Fig. 7B).

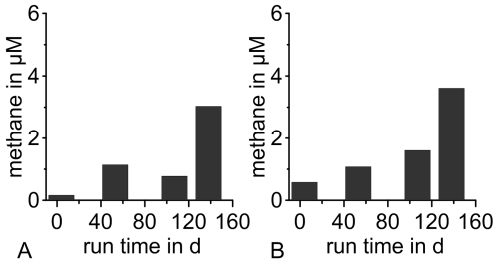

Figure 7: Methane concentration of the outflow (), calculated efflux of methane, and calculated AOM rates from the difference of in- and out-flow of Low Fluid Core (LFC) and High Fluid Core (HFC) of the bacterial mat (SO210-St42) during the experiment.

Clam field habitat:

In profile of the LFC of the clam field habitat had like the bacterial mat constant sulfate concentrations (~29 mmol l^{-1}) and almost no bromide, at the beginning (11 d run time) of the experiment (Fig. 8A). Sulfide was high (1022-1621 µmol l^{-1}) at the upper part of the core and decreased below 6 cm down to 492 µmol l^{-1} at the bottom(Fig. 8B). Beside a minimum of 5.3 meq l^{-1} between 3 and 6 cm sediment depth, TA was constant between 5.9 and 6.1 meq l^{-1}. At the beginning, pH was less than in the bacterial mat cores (8.1) and decreased slightly to the bottom (7.8) (Fig. 8C).

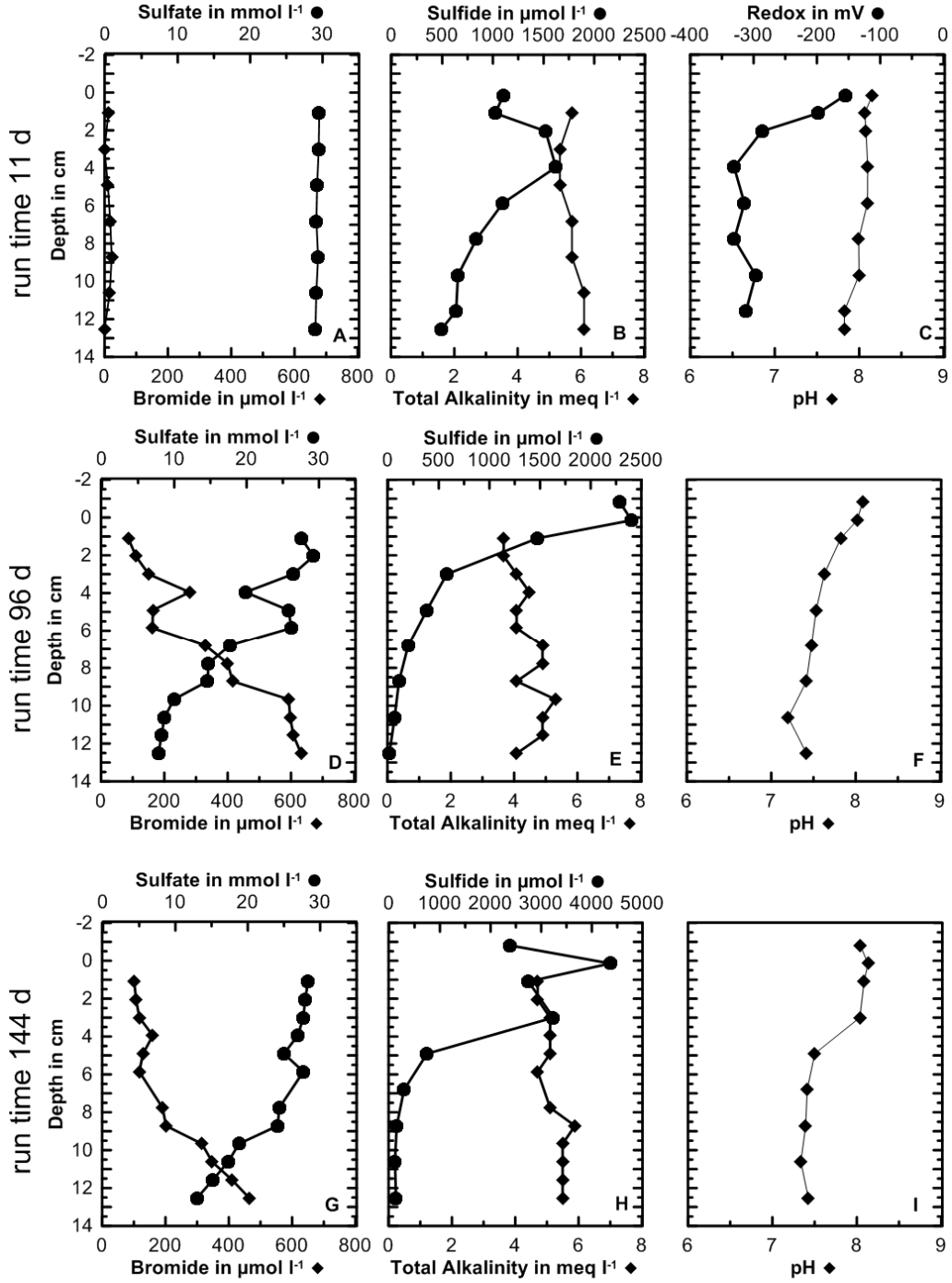

Figure 8: Geochemical gradients in the Low Flow Core (LFC) core of the clam field (SO210-St25) during the experiment. Shown are: bromide (tracer) sulfate concentrations (A, D, G), sulfide and total alkalinity concentrations (B, E, H), as well as pH (C, F, I) and redox potential (C), to different run time of the experiment.

After 96 d, bromide increased rapidly inside the sediment core and ascended up to the surface of the sediment core (10% of the inflow concentration). Accordingly, sulfate was depleted to 90% of the inflow concentration at the top of the sediment. The SMTZ was located between 6 and 10 cm sediment depth (Fig. 8D). Bromide increased from 163 to 593 µmol l^{-1} while sulfate depleted from 26 to 10 mmol l^{-1}. At

the bottom 632 µmol l^{-1} bromide and 7.8 µmol l^{-1} sulfate was reached. In general bromide was mirrored quit well by sulfate at this time. Uncommon, the outflow concentration of the LFC changed to only 24 mmol l^{-1} sulfate were (in contrast to 29-30 mmol l^{-1}, data not shown).

Sulfide was very high after 96 d at the top of the core (2288 µmol l^{-1}) and decreased concave down to almost zero (13 µmol l^{-1}) at the bottom of the core (Fig. 8E). In tendency, TA increased with increasing depth from 3.7 meq l^{-1} at the top, up to 5.3 meq l^{-1}. At the bottom lower concentrations (4.1 meq l^{-1}) were measured. Like before pH was around 8.1 at the top of the core but decreased stronger down to the bottom to 7.4 interrupted by a local minimum of 7.2 at 9 cm sediment depth (Fig. 8F).

Directly before experiment termination, 144 d after the start, bromide reached the top (101 µmol l^{-1}) and increased to the bottom to 465 µmol l^{-1}, while sulfate decreased from the top (28.3 mmol l^{-1}) to the bottom (13.0 mmol l^{-1}). Similar to LFC of the bacterial mat site the profiles were dropped down, probably by the same reason (see above). Between 0 and 3 cm even in the overlaying water, sulfide was very high (2386 – 4365 µmol l^{-1}) and decreased in a concave down shape to 133 µmol l^{-1} at the bottom of the core. TA was 4.7 meq l^{-1} at the top and increased to 5.5 meq l^{-1} to the bottom interrupted by a maximum of 5.8 meq l^{-1} at 9 cm sediment depth. At the upper part with high sulfide concentrations, pH was between 8.0 and 8.1 and between 7.3 - 7.5 below 3 cm sediment depth.

Methane concentrations in the outflow sample were almost zero at the beginning (11 d), increased to 3.6 µmol l^{-1} after 96 d and declined again to 1.3 µmol l^{-1} after the final time of 144 d (Fig. 10A).

In the HFC of the clam field, bromide was already at the beginning (11 d), increased (112 µmol l^{-1}) and sulfate depleted (26.2 µmol l^{-1}) at the bottom. Sulfide was around 100 µmol l^{-1} at the top, elevated to more than 600 µmol l^{-1} between 3 and 5 cm sediment depth, and was very low (30 - 40 µmol l^{-1}) at the lower part of the core. At the bottom, with increased bromide and lower sulfate concentrations, sulfide was increased to 714 µmol l^{-1}. TA was almost constant between 5.7 and 6.4 meq l^{-1} and pH was slightly decreased from 8.3 at the top to 7.9 at the bottom; similar to the LFC at the beginning.

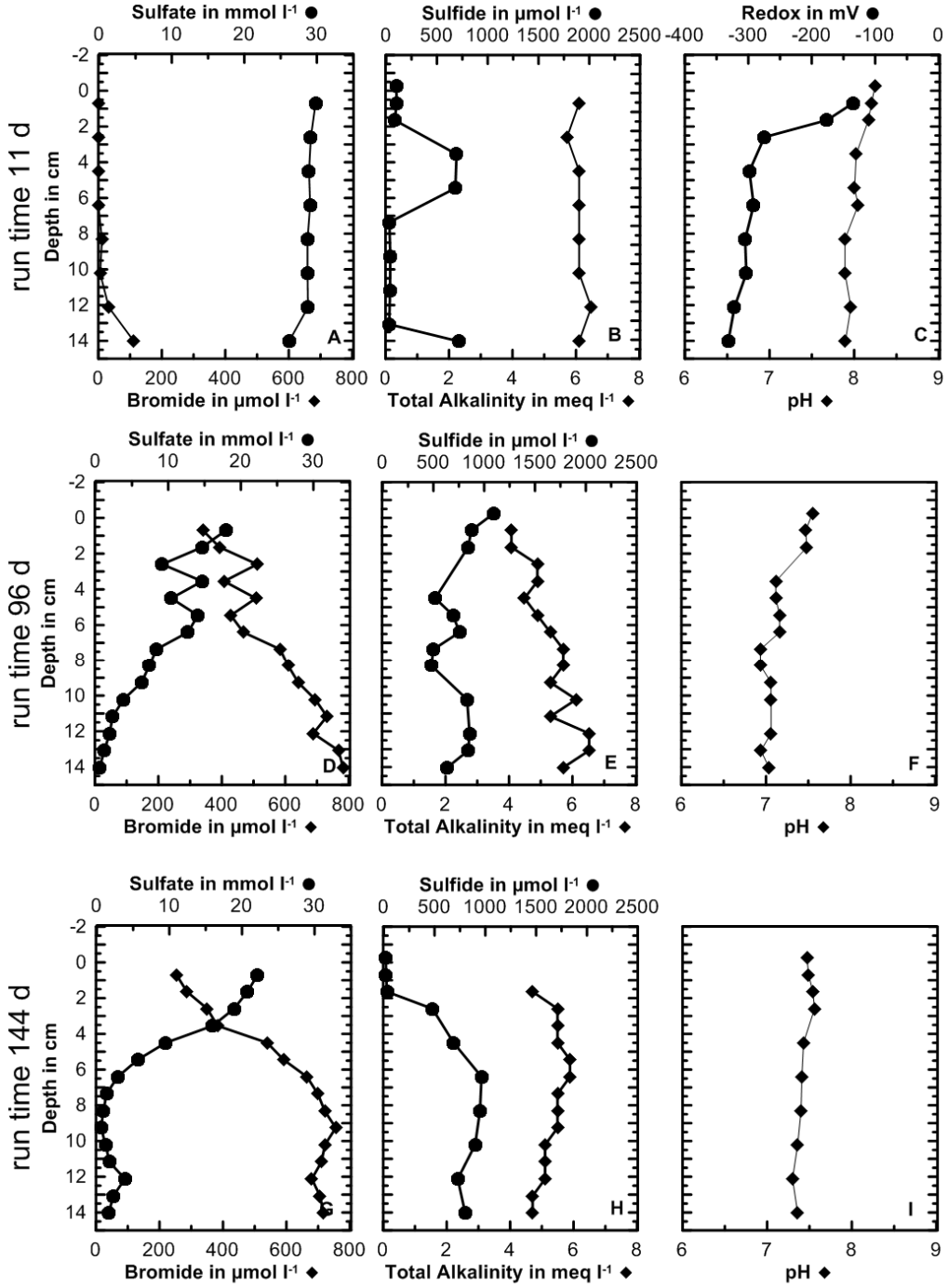

Figure 9: Geochemical gradients in the High Flow Regime (HFC) of the clam field (SO210-St25) during the experiment. Shown are: bromide (tracer) sulfate concentrations (A, D, G), sulfide and total alkalinity concentrations (B, E, H), as well as pH (C, F, I) and redox potential (C), to different run time of the experiment

Similar to the LFC, after 96 d bromide was increased in the entire sediment and up to 40% of the in-flowed bromide reached the sediment surface (340 µmol l^{-1}). Only 18 mmol l^{-1} of the sulfate remained at this time at the top of the sediment. Bromide and sulfate alternated between the first 6 cm sediment depth between 340 -

614 µmol l^{-1} and 9.2 – 18.0 mmol $l^{-1}$for bromide and sulfate respectively. Below 6 cm bromide increased while sulfate decreased almost to the inflow concentration of the seepage medium (782 µmol l^{-1} and 0.5 mmol l^{-1} for bromide and sulfate, respectively). Similar to the LFC, outflow concentration of the sulfate decreased to only 14.8 mmol l^{-1} sulfate and increased to 352 µmol l^{-1} bromide (data not shown). At this time sulfide concentrations were elevated over the entire sediment column (480 – 875 µmol l^{-1}) as well as in the overlaying water (1096 µmol l^{-1}). TA increase from the top (4.7 meq l^{-1}) to the bottom (5.7 meq l^{-1}) with a maximum (6.5 meq l^{-1}) between 11 and 13 cm sediment depth. Decreased pH values were detected with 7.5 at the top of the sediment and constant between 6.9-7.1 below.

At the end of the experiment (144 d), bromide reached concentrations of 250 µmol l^{-1} at the top of the sediment, and increased in a concave down shape to 700 – 750 µmol l^{-1} in the lower part of the core (7-15 cm). Sulfate mirrored this profile with 22.2 mmol l^{-1} at the top and 1.6 mmol l^{-1} at the bottom. These dropped profiles were observed before in LFCs of the bacterial mat and Clam field (see above). Sulfide was very low in the upper 2 cm (20 µmol l^{-1}) and increased rapidly to concentrations of 730 – 950 µmol l^{-1} in the lower part of the sediment with high bromide concentrations (7-15 cm). TA increased from the top (4.7 meq l^{-1}) to a maximum of 5.8 meq l^{-1} at 5 – 7 cm, and decreased back to 4.7 meq l^{-1} at the bottom of the core. pH was now higher and decreased from 7.5 (top) to 7.3 (bottom).

Methane concentration in the outflow of the HFC of the clam field sediment was around 0.4 µmol l^{-1} after 11 d. After 96 d methane concentrations reached 313 µmol l^{-1} and corresponded to the inflow concentrations under respect of the dilution factor of the seawater medium. At the end of the experiment (144 d), methane concentrations were declined again to 1.9 µmol l^{-1}.

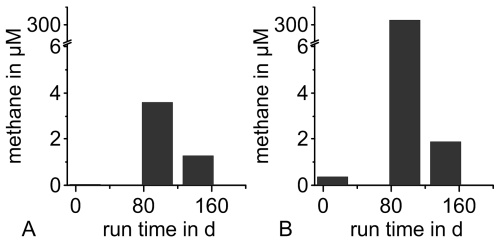

Fig. 10: Methane concentration of the outflow (), calculated efflux of methane, and calculated AOM rates from the difference of in- and out-flow of Low Fluid Core (LFC) and High Fluid Core (HFC) of the clam field (SO210-St25) during the experiment.

Tubeworm field habitat:

Cores of the tubeworm field were measured and sampled for the first time 19 d after the experiment had started. In the LFC bromide concentrations were already around 200 µmol l^{-1} at the bottom and detectable bromide was ascended up to 4 cm sediment depth. Sulfate was depleted only below 16 cm (25.8 mmol l^{-1} at the bottom), and constant above (29 mmol l^{-1}). In the overlaying water 83 µmol l^{-1} sulfide was detected, while inside the core only very low sulfide concentrations (10 – 19 µmol l^{-1}) were measured. TA increased from the top (4.6 meq l^{-1}) to the bottom (6.2 meq l^{-1}) with a maximum of 6.6 meq l^{-1} at 16 cm sediment depth. In the overlaying water, pH was at 8.2, in the upper sediment at 7.5 and decreased further to 7.2 at 4 cm sediment depth. Below 9 cm pH increased slightly to 7.5 at the bottom of the core. Redox potential was positive and above 200 mV in the overlaying water at the sediment surface (the first cm), and strongly altering between -22 and -155 mV in the rest of the core.

At the next time step after 101 d runtime, bromide had already reached the surface (56 µmol l^{-1}) and increased downwards to 560 µmol l^{-1} at the bottom of the core. Sulfate was only in the first two cm at the old level (29.1 mmol l^{-1}) and decreased downwards to 6.6 mmol l^{-1} at the bottom. Both, bromide and sulfate profiles show some fluctuations, and mirrored each other very well. There was almost no sulfide (4 – 9 µmol l^{-1}) detected in the core. TA increased from 3.5 meq l^{-1} at the top to 5.5 meq l^{-1} at the bottom. A very low pH (7.0 – 6.8) was measured in the entire sediment.

At the end of the experiment, 151 d after the start, bromide and sulfate profiles have not changed much, and were only flattened, probably by the same artifact as the parallel cores (see above). Sulfide was still very low (11 – 21 µmol l^{-1}), and the TA profile was like before, increasing from the top (3.7 meq l^{-1}) to the bottom (5.7 meq l^{-1}). The pH level was higher than before between 7.1 – 7.4.

Outflow methane concentrations of LFC of the tubeworm field sediment was already 3.9 µmol l^{-1} at the beginning (19 d) and increased massively after 101 d to 67.2 µmol l^{-1}. At the end of the experiment (151 d) methane outflow was reduced down to 1.0 µmol l^{-1}.

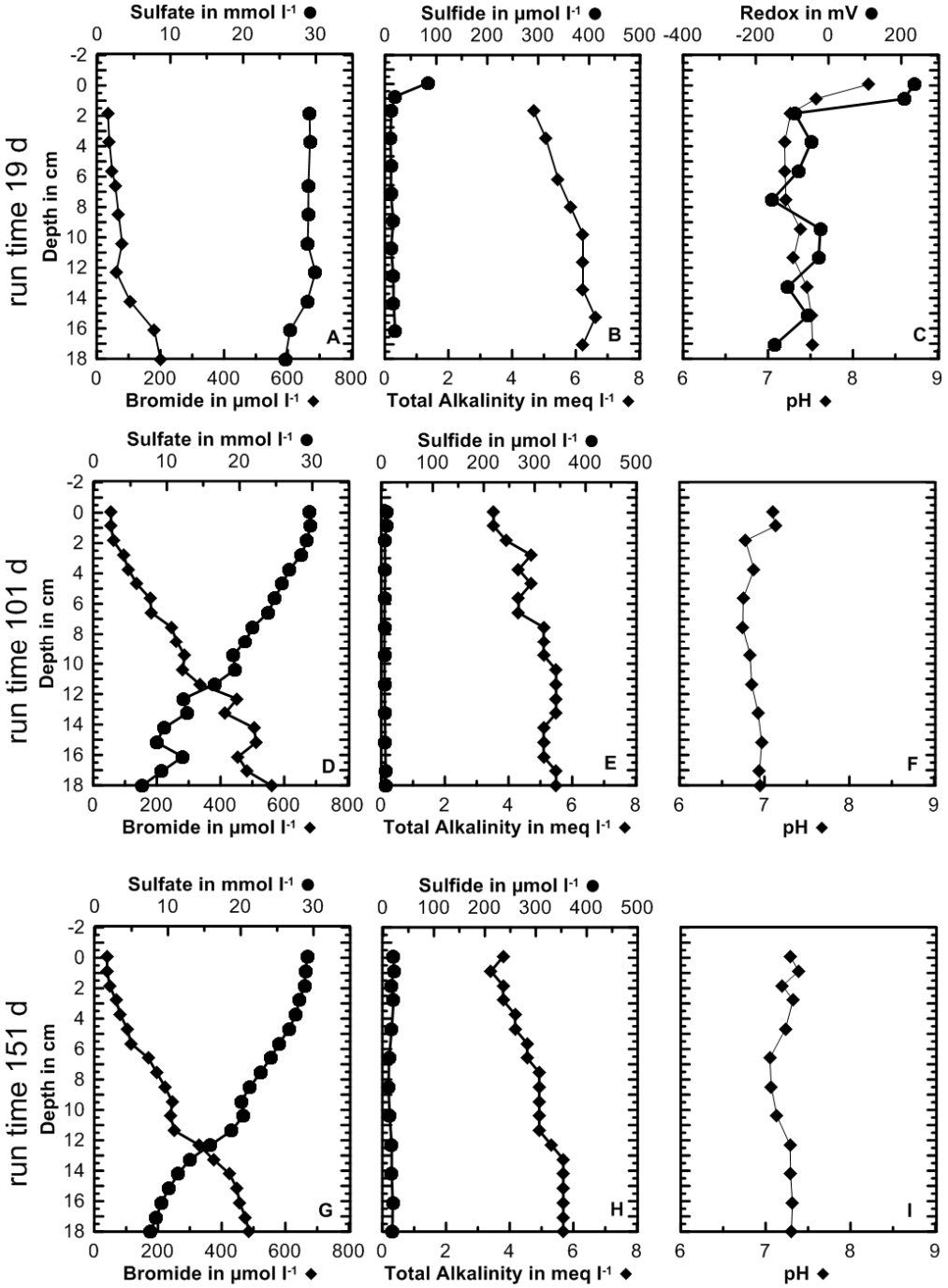

Figure 11: Geochemical gradients in the Low Flow Core (LFC) core of the tubeworm field (SO210-St88) during the experiment. Shown are: bromide (tracer) sulfate concentrations (A, D, G), sulfide and total alkalinity concentrations (B, E, H), as well as pH (C, F, I) and redox potential (C), to different run time of the experiment.

At the beginning of the experiment (19 d) in the HFC, bromide reached already the surface (70 µmol l^{-1}) and 308 µmol l^{-1} at the bottom of the core. Sulfate was around 28.6 mmol l^{-1} in the upper part and depleted slightly below 9 cm sediment depth to 26.9 mmol l^{-1} at the bottom. Like the LFC, sulfide was low at the upper part of the sediment (25 - 30 mmol l^{-1}). Below 5 cm sulfide concentrations increased rapidly to

the maximum of 455 µmol l^{-1} between 9 and 12 cm, and decreased to the bottom down to 213 µmol l^{-1}. TA was high and increased strongly from 5.1 to 8.6 meq l^{-1} with

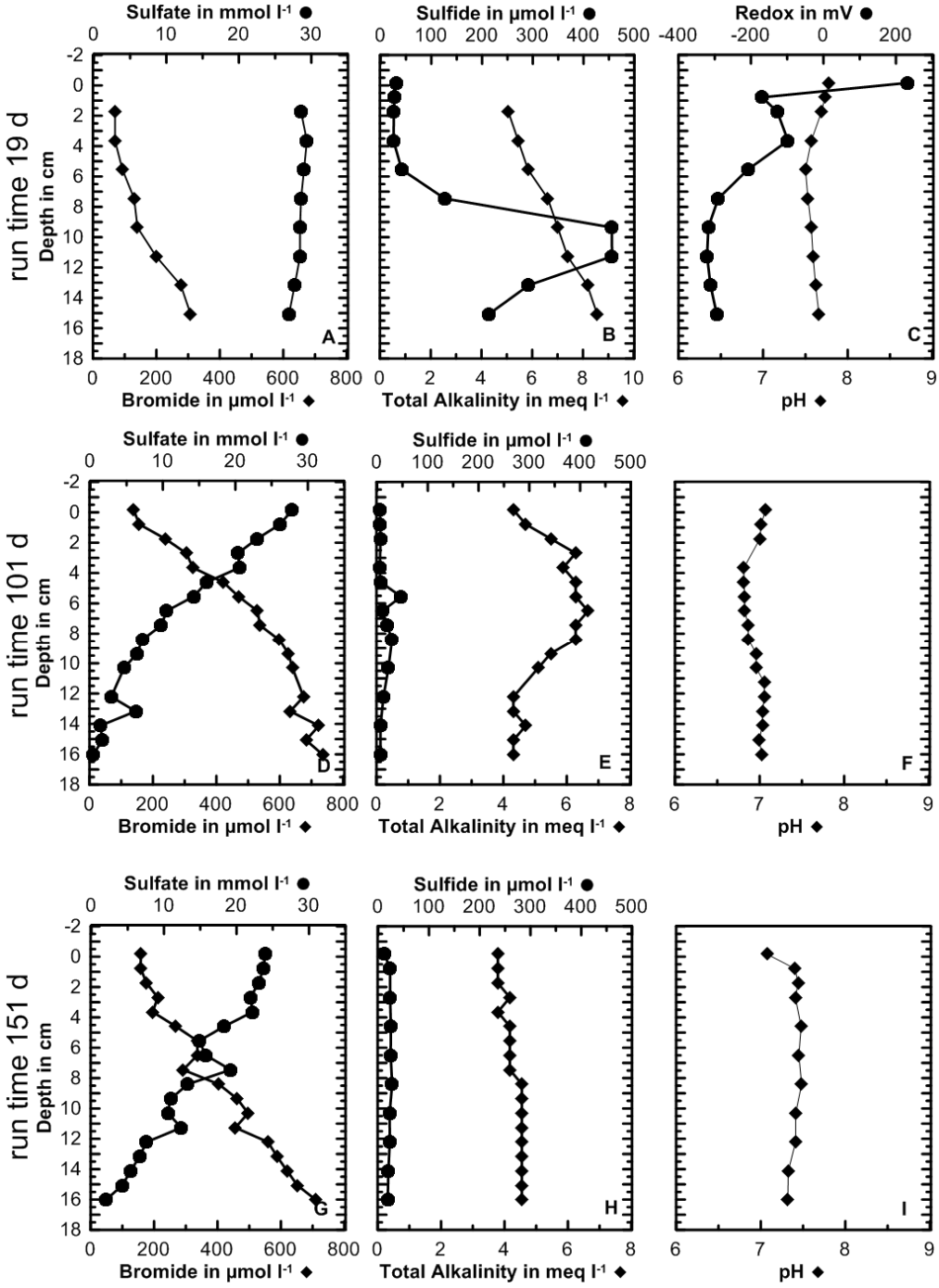

Figure 12: Geochemical gradients in the High Flow Core (HFC) of the tubeworm field (SO210-St88) during the experiment. Shown are: bromide (tracer) sulfate concentrations (A, D, G), sulfide and total alkalinity concentrations (B, E, H), as well as pH (C, F, I) and redox potential (C), to different run time of the experiment.

depth. Similar to the LFC, redox potential was positive in the overlaying water (200 mV), but decreased rapidly down to -100 - -170 mV and continued decreasing

slightly with increasing sulfide concentrations down to -320 mV (11 cm). Again pH was higher at the top (7.8) and decreased inside the sediment to 7.5 (9 cm) before it slightly increased again (7.7 at the bottom).

After 101 d bromide increased from the top (140 µmol l^{-1}) to the bottom (735 µmol l^{-1}) in a concave down shaped profile, and was mirrored by sulfate (27.9 mmol l^{-1} at the top, 0.4 mmol l^{-1} at the bottom). Sulfide was still low between 5 and 50 mmol l^{-1} and had a maximum between 5 and 6 cm. TA was 4.3 meq l^{-1} at top and bottom and showed an increased interval between 2 and 9 cm with a maximum of 6.7 meq l^{-1} at 5.5 cm sediment depth. Like the LFC at the same time period, pH was low between 6.8 and 7.1.

After 151 d, at the end of the experiment, bromide and sulfate were mirrored again. Bromide reached 160 µmol l^{-1} at the top and increased to the bottom to 710 µmol l^{-1}. Sulfate was only 24 mmol l^{-1} and decreased down to 2 mmol l^{-1} at the bottom. Similar to the parallel cores, profiles dropped down by an artifact (see above). Sulfide was constantly low at ~20 µmol l^{-1}. TA increased downwards from 3.7 meq l^{-1} (top) to 4.6 meq l^{-1} without the increased interval from before. Low pH values persisted only in the overlaying water (7.0), while in the sediment pH was increased to 7.3 - 7.5.

Methane concentration in the outflow of the HFC was similar to the LFC. After 20 d methane concentration reached 5.7 µmol l^{-1}, increased to 61.5 µmol l^{-1} after 101 d and reduced down to 1.0 µmol l^{-1} at the end (151 d) of the experiment.

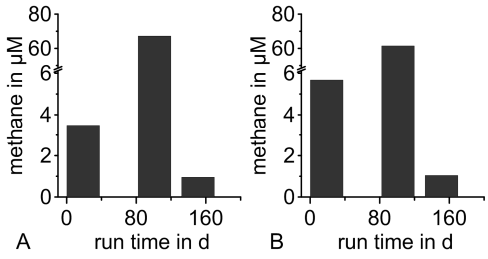

Figure 13: Methane concentration of the outflow (), calculated efflux of methane, and calculated AOM rates from the difference of in- and out-flow of Low Fluid Core (LFC) and High Fluid Core (HFC) of the tubeworm field (SO210-St88) during the experiment.

Sediment parameters and microbial turnover rates after experiment termination:

Bacterial mat:

Methane concentration of the LFC were 27 µmol l^{-1} at the top of the core and increased with depth to 106 µmol l^{-1} at the bottom of the core. AOM rates were around 0.9 nmol cm^{-3} d^{-1} in the first 4 cm and increased below to 5.16 nmol cm^{-3} d^{-1}. In contrast, maximum sulfate reduction rates were more than ten times higher with a maximum at the top of the sediment (70.40 nmol cm^{-3} d^{-1}). While sulfate concentrations stayed constant (30.5 mmol l^{-1}) in the upper part, sulfate reduction rates decreased with sediment depth (9.57 nmol cm^{-3} d^{-1} at the bottom) displaying a concave down profile.

In the HFC, AOM rates were comparably higher, but followed a similar profile (1.02 nmol cm^{-3} d^{-1} at the top, 70.0 nmol cm^{-3} d^{-1} at the bottom). Also methane concentrations (43 µmol l^{-1}at top, 112 µmol l^{-1} at bottom) and sulfate reduction rates (85.56 nmol cm^{-3} d^{-1} at top, 1.17 nmol cm^{-3} d^{-1} at the bottom) were similar to the LFC. Only sulfate concentrations were generally lower and depleted steadily with sediment depth.

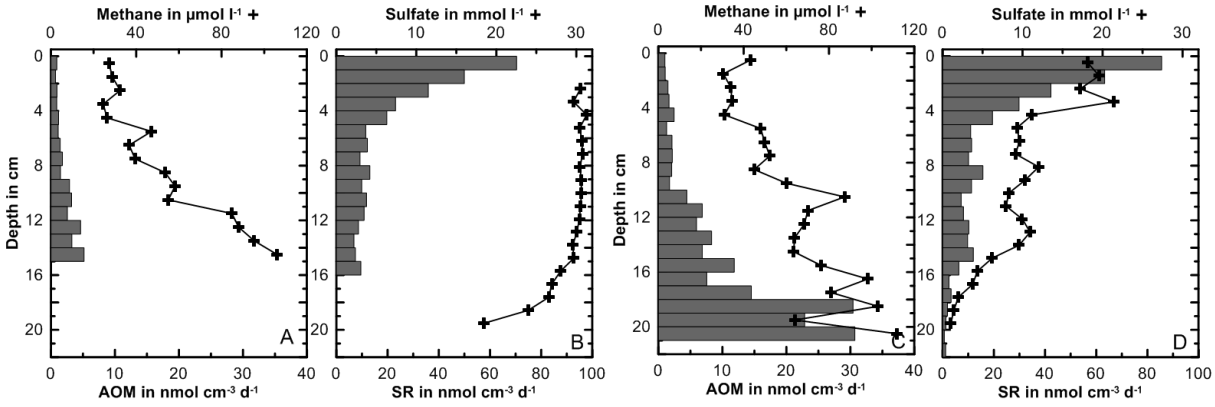

Figure 14: Rate measurement and porewater profiles in the Low Fluid Core (LFC, A-B) and High Fluid Core (HFC, C-D) of the bacterial mat (SO210-St42) after the experiment. Shown are A) AOM rates (bars) and methane concentration (solid line), B) sulfate reduction rates (bars) and sulfate concentrations (solid line).

Integrated areal rates of AOM were 0.32 mmol m^{-2} d^{-1} for the LFC and 1.67 mmol m^{-2} d^{-1} for the HFC core, respectively. Integrated areal rates of sulfate reduction were 3.10 and 3.64 mmol m^{-2} d^{-1} for the LFC and HFC core, respectively.

TC was almost 2% w/w in reference cores taken during fieldwork (Fig. 15A), and consisted mostly of organic carbon (TOC) in the upper 12 cm (Fig. 15B). Below 12 cm TC was enhanced due to an increase in TIC, while TOC was depleted to 0.9-1.2% w/w. Carbon contents measured after experimentation in the LFC and HFC were basically identical to the reference cores. Atomic C/N ratio in the reference core was around 9 and increased slightly to a maximum of 10.5 at the bottom (Fig. 15B). In the experimental cores, C/N ratios were higher in the entire sediments to the maximum of 11.4 in the LFC and 12.1 in the HFC. TS of the reference core started with 0.6% w/w at the top and increase with depth to ~1.5% w/w (Fig. 15C). In the experimental cores, TS was higher in the upper 13 cm of the LFC up to 2% w/w, while the TS content of the HFC was similar to the reference core. TN decreased from the top (0.23% w/w) to the bottom (~0.1% w/w) and was similar between reference and experimental cores, whereas the lowest 6 cm of the HFC exhibited higher TN content (2.40% w/w). In the reference core, porosity decreased with depth from 0.77 to a minimum of 0.58. In the LFC sediments porosity was generally lower (0.73-0.54), while values were similar to the reference core in the HFC.

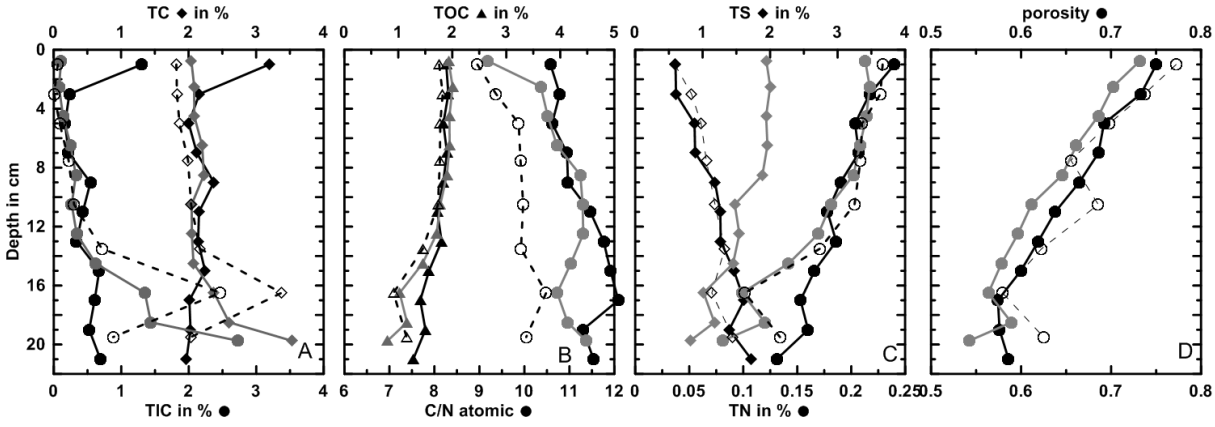

Figure 15: Solid phase of *ex situ* data (open symbols, dotted lines) and Low Fluid Core (LFC, grey) and High Fluid Core (HFC, black) of the bacterial mat (SO210-St42) after the experiment. Shown are total carbon (TC, A, diamonds), total inorganic carbon (TIC, A, circles), total organic carbon (TOC, B, triangle), total sulfur (TS, C, circle), total nitrogen (TN, C, diamonds) in mass percentage, as well as atomic C/N ratios (B, circle), and porosity (D).

Clam field habitat: On account of abundant shells and shell fractures, it was difficult to press the sub-cores for the rate measurements into the sediment. For this reason, sub-cores for turnover rates were shorter, and no sulfate reduction rates for the HFC were measured.

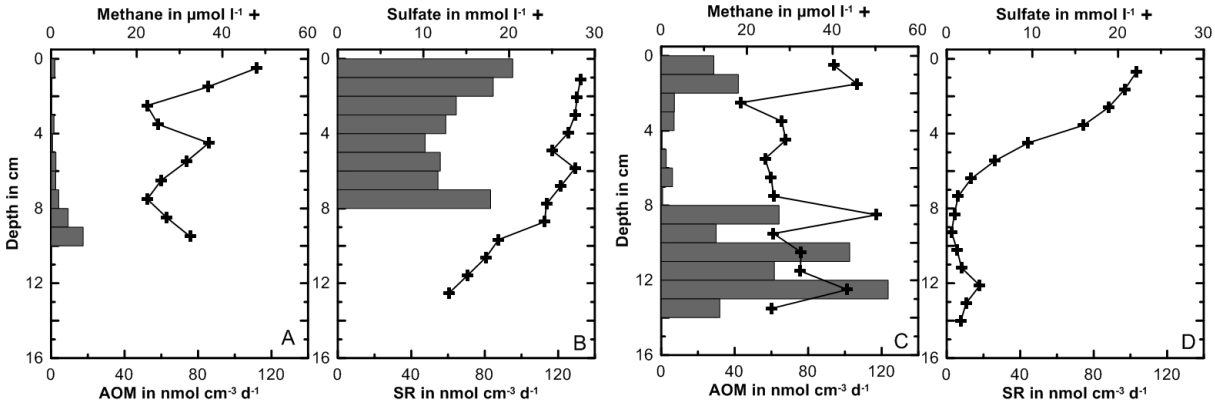

Figure 16: Rate measurement and porewater profiles in the Low Fluid Core (LFC, A-B) and High Fluid Core (HFC, C-D) of the clam field (SO210-St25) after the experiment. Shown are A) AOM rates (bars) and methane concentration (solid line), B) sulfate reduction rates (bars) and sulfate concentrations (solid line).

Methane concentrations ranged between 18 and 50 µmol l^{-1} in both cores and were on average the same without a clear trend. AOM rates of the LFC increased from the top (2.09 nmol cm^{-3} d^{-1}) to the bottom (17.47 nmol cm^{-3} d^{-1}) with a minimum (0.18 nmol cm^{-3} d^{-1}) between 1 and 3 cm sediment depth. AOM of the entire sediment column was 0.41 mmol m^{-2} d^{-1}. In the HFC AOM rates were much higher. High AOM rates were determined at the first 4 cm (7.00-42.00 nmol cm^{-3} d^{-1}) and below 8 cm sediment depth (29.92 – 123.55 nmol cm^{-3} d^{-1}). The integrated areal rate was more than ten times higher than the rate of the LFC (5.09 mmol m^{-2} d^{-1}). Sulfate reduction rate core of the LFC was only 8 cm long, with constant high turnover rates between 47.51 – 95.26 nmol cm^{-3} d^{-1}. The integrated areal rate of these 8 cm was 5.44 mmol m^{-2} d^{-1}.

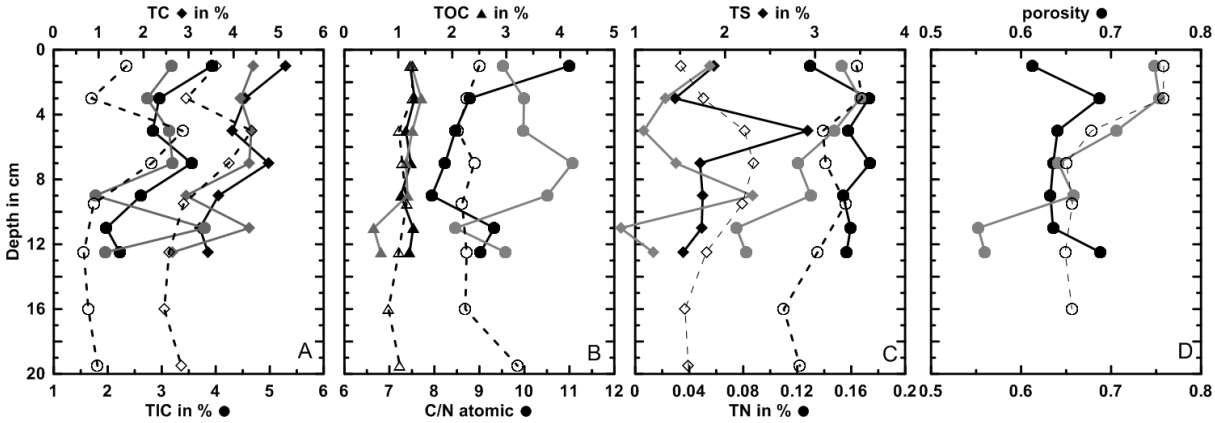

Figure 17: Solid phase of *ex situ* data (open symbols, dotted lines) and Low Fluid Core (LFC, grey) and High Fluid Core (HFC, black) of the clam field (SO210-St25) after the experiment. Shown are total carbon (TC, A, diamonds), total inorganic carbon (TIC, A, circles), total organic carbon (TOC, B, triangle), total sulfur (TS, C, circle), total nitrogen (TN, C, diamonds) in mass percentage, as well as atomic C/N ratios (B, circle), and porosity (D).

While TOC content of the reference core was constant (0.82-1.26% w/w mean 1.08% w/w) over the entire depth (Fig. 17B), TIC (3.39% w/w), and TC (4.40% w/w), were higher in the SMTZ compared to contents above and below (1.56-1.81 and 2.46-2.89% w/w for TIC and TC, respectively, Fig. 17A). After the experiment TOC content was similar in both cores, while TIC was in general higher (3.19 and 3.93% w/w for the LFC and HFC compared to 2.34% of the reference core) especially in the top 4 cm. The LFC showed a peak (3.80% w/w TIC) at 11 cm sediment depth. Ratios of organic carbon and nitrogen were constant around 9 and increased only at 20 cm to 9.8, in the reference core. In the LFC as well as the top of the HFC, C/N was higher (up to 11.1 and 11.0, respectively) after the experiment (Fig. 17B). In the reference core, the sulfur content was increased inside the SMTZ to 2.32% w/w compared to ~1.6% w/w above and below. Different to the increased TIC layer (4-8 cmbsf), the increased TS horizon was wider from 2 to 11 cmbsf (Fig. 17C). In the experiment cores, TS showed a totally different distribution and was generally decreased in both cores. The LFC showed a peak at 9 cm (2.31% w/w) and the HFC at 5 cm (2.92% w/w). TN was 0.16% w/w at the top and decreased by trend to 0.12% w/w at the bottom of the core. In the LFC of the experiment, TN decreased faster below 6 cm to 0.08% w/w at the bottom. In the HFC, TN was 0.12% w/w at the top layer and around 0.16% w/w below.

Porosity was 0.76 in the upper 4 cm, decreased at the horizon with increased TIC (4-8 cmbsf) to 0.65 and stayed constant down to 20 cmbsf in all three cores (LFC, HFC, and reference core).

Tubeworm field habitat: In the LFC of the tubeworm field habitat, 62 µmol l^{-1} methane were measured at the top of the core. Below, methane concentrations increased from 33 µmol l^{-1} (1.5 cm sediment depth) to 86 µmol l^{-1} at the bottom of the sediment core. In the HFC of the same habitat, methane concentrations increased from 28 to 95-103 µmol l^{-1} at 11 - 13 cm sediment depth.

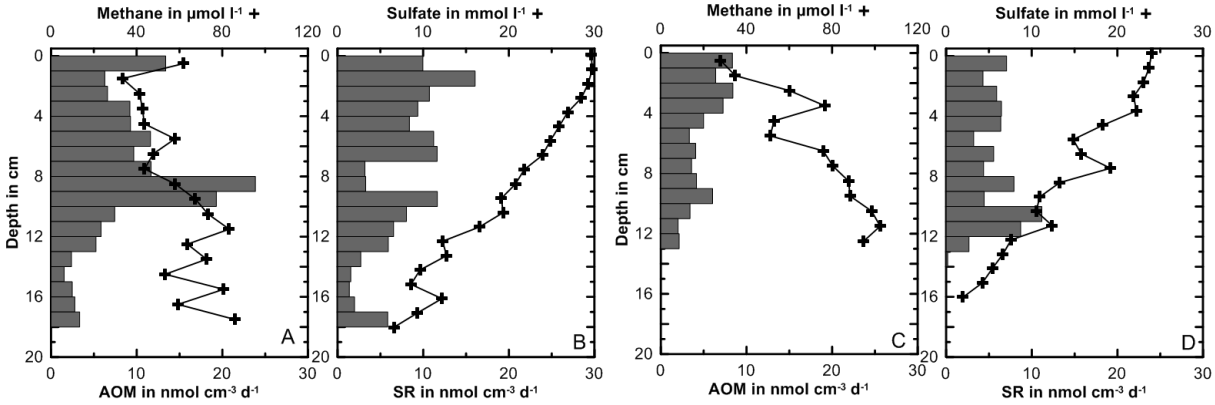

Figure 18: Rate measurement and porewater profiles in the Low Fluid Core (LFC, A-B) and High Fluid Core (HFC, C-D) of the tubeworm field (SO210-St88) after the experiment. Shown are A) AOM rates (bars) and methane concentration (solid line), B) sulfate reduction rates (bars) and sulfate concentrations (solid line).

AOM rates of the LFC range in the first ten cm from 6.28 – 23.86 nmol cm^{-3} d^{-1}, with a maximum at 8 – 9 cm sediment depth. Below (10-18 cm) AOM rates were lower (1.53 nmol cm^{-3} d^{-1} and 5.84 nmol cm^{-3} d^{-1}). In general, in the HFC less AOM were detected. AOM rates decreased from 8.36 nmol cm^{-3} d^{-1} at the top to 2.14 nmol cm^{-3} d^{-1} at the lowest layer. Integrated areal rates were 1.52 mmol m^{-2} d^{-1} and 0.64 mmol m^{-2} d^{-1} for the LFC and HFC, respectively.

Sulfate reduction rates were highest in the upper ten cm of the LFC (3.19 – 16.05 nmol cm^{-3} d^{-1}) and less below (1.38 - 6.54 nmol cm^{-3} d^{-1}), according to AOM rates, else wise not so pronounced. In the HFC sulfate reduction were lower and ranged from 0.18 – 11.18 nmol cm^{-3} d^{-1}. Integrated areal rates were in the ranged of AOM rate with 1.29 and 0.78 mmol m^{-2} d^{-1} for the LFC and HFC, respectively.

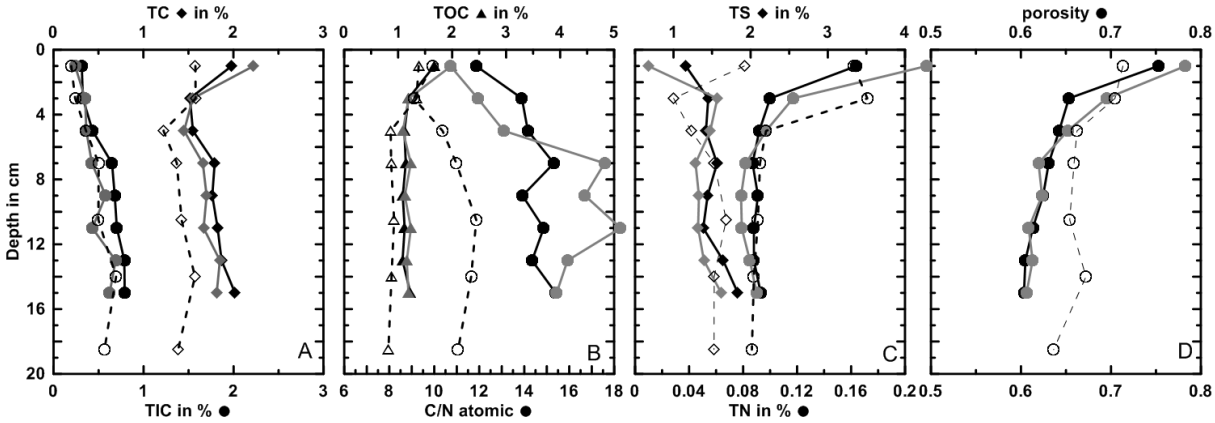

Figure 19: Solid phase of *ex situ* data (open symbols, dotted lines) and Low Fluid Core (LFC, grey) and High Fluid Core (HFC, black) of the tubeworm field (SO210-St88) after the experiment. Shown are total carbon (TC, A, diamonds), total inorganic carbon (TIC, A, circles), total organic carbon (TOC, B, triangle), total sulfur (TS, C, circle), total nitrogen (TN, C, diamonds) in mass percentage, as well as atomic C/N ratios (B, circle), and porosity (D).

TC content of the reference core was constant between 1.22 – 1.58% w/w and slightly increased in both cores after the experiment (1.45-2.22% w/w, Fig. 19A). TIC increased slightly with the depth from 0.2 to 0.69, in all three cores. TOC of the reference core was 1.38% w/w at the top and around 0.9% w/w below 4 cmbsf (Fig. 19B). Measurements after the experiment were slightly higher in both cores (1.09-1.98% w/w). C/N ratios were between 9.1 and 11.9 with a maximum at 10 cmbsf. After the experiment, the C/N ratios were extremely increased (10.72-18.28 and 11.86-15.39 for the LFC and HFC, respectively) in both cores. C/N ratios of the LFC were most elevated between 6-12 cm, while the profile of the HFC followed the trend from before. The TS content of the reference core was 1.92% at the top, decreased to 1.00% at 2 cmbsf and then increased again. Below 6 cmbsf TS was constant around 1.55% w/w. After the experiment, TS was less at the top (0.67 and 1.16% w/w for the LFC and HFC, respectively) and between 1.32 and 1.64% w/w below 2 cm sediment depth in both cores. TN was around 0.16% w/w in the upper 4 cm and around 0.09% w/w below in the reference core. After the experiment TN was similar to the reference core distributed, with 0.22 and 0.16% w/w at the top for the LFC and HFC respectively and a faster decrease. Below 4 cm TN contents were like before (~0.09% w/w) in both cores. Porosity of the reference core was 0.71 at the top and decreased with depth to 0.64. After the experiment in both sediment cores porosity was higher above (0.75-0.78) and lower below 2 cm (~0.6) in both cores.

Discussion

Bacterial mat habitat: The high efficiency of young seeps

The area of the bacterial mat represents probably a seep site in an early stage, since no authigenic carbonates were found in this area or in the sediments. At the black spots, bacterial mats have not colonized, and at areas with oxidized sediment and dark layer below, sulfidic fluids have not reached the sediment-water interface, yet. All this indicate a relatively young seep site.

The SMTZ of the bacterial mat site (SO210-St42) was very shallow and showed moderate to high turnover rates (24.2 ± 4.01 and 20.5 ± 0.33 mmol m^{-2} day^{-1} for sulfate reduction and AOM, respectively), both common for bacterial mat sites (e.g., Krause et al. 2013; Niemann et al. 2006; Treude et al. 2003). These turnover rates, which were mostly driven by methane (AOM : SR = 0.85), are a result of fluid and methane flux. With respect to the porewater profiles and the shallow SMTZ of the field data, higher fluid flux than the referred 0.03 - 0.18 cm yr^{-1} (Scholz et al. 2013) can be assumed. Considering a steady-state situation at this seep, the methane flux would have to be at least equal to the methane turnover rate. At the given water depth (700 m), salinity (35 psu) and temperature (4°C) of the site a maximum of 108.2 mmol l^{-1} methane should be soluble in the porewater (after Tishchenko et al. 2005). Considering this saturated methane concentration, a fluid flow of ~7 cm yr^{-1} would be necessary to reach equilibrium between methane flux and integrated areal rates of AOM. Compared to these natural conditions, the fluid flow applied in our experiments was much higher (LFC: 118.1 cm yr^{-1}; HFC: 232.4 cm yr^{-1}).

Nevertheless, the efficiency of the benthic methane filter was sustained, regarding the outflow methane concentration. Methane efflux in both cores (LFC and HFC) increased only slightly over the experiment and reached maximally 1.9 and 1.3% of the inflow methane flux, respectively, while more than 98% were consumed by the benthic methane filter. During the experiment, the depth of the SMTZ was assumed to be roughly at the same depth as the sulfate-bromide transition zone, since bromide served as indicator for the methane-loaded seepage medium. In LFC, the presumable SMTZ never exceeded above 14 cmbsf, while in the HFC, it moved up to 4 cmbsf at the end of the experiment (144 d). Looking at the bromide concentrations, the mixing ratio between seawater medium and seepage medium can be calculated.

At the end of the experiment, 38% of the medium at the sediment-water interface is exchanged by seepage medium (calculated from bromide concentration) (Fig. 6J). This fraction correlated with the ratio between pumping rate of seepage and seawater media, and indicated that the entire seepage front had reached the sediment surface, i.e., the fluid regime was close to steady-state system conditions. Considering this situation, further increase in methane effluxes was not expected since the rate of methane supply would remain constant over time.

Radiotracer determinations of turnover rates after experimentation in both SLOT cores showed an atypical reverse distribution of sulfate reduction (maximum at the top) and AOM (maximum at the bottom) (Fig. 14), which was different from the field core, where both processes overlapped at the top of the core (Fig. 2). While organoclastic sulfate reduction at the top of the core is common in sediments below oxygen minimum zones (Bohlen et al. 2011), at the bottom of the HFC higher AOM rate than sulfate reduction was reached. This is a surprising phenomenon and rises an open question for future efforts.

AOM rates determined with radiotracers (0.32 and 1.67 mmol m^{-2} d^{-1} for LFC and HFC, respectively) were lower than the applied methane flux (6.4 mmol m^{-2} d^{-1}, Table 3). By subsampling sediment for AOM determination got lost in the LFC. Considering the profile of AOM rates (Fig. 14A), this might be the most active sediment layer regarding AOM, leading to an underestimation of the areal rates in this core. Because, methane concentrations of the outflow increased only slightly during the experiment, integrated areal rates of both cores might be underestimated in general.

Integrated areal rates of sulfate reduction was more than two times higher in the HFC and ten times higher in the LFC compared to the AOM rates, and could be a result of organoclastic sulfate reduction. This assumption is supported by increased C/N ratios compared to the field core, especially in the LFC, which is a hint for advanced organic matter degradation (Whiticar 2002). Organoclastic sulfate reduction of the *ex situ* data was a little higher (~3.70 mmol m^{-2} d^{-1}) than in the LFC (2.78 mmol m^{-2} d^{-1}) and HFC (1.97 mmol m^{-2} d^{-1}). Reduced methane concentration provoked by final porewater sampling with rhizones could be an additional reason (Steeb et al. 2014).

Sulfide concentrations show fluctuations and a loss of sulfide during the experiment. Lower sulfide concentrations in the HFC despite higher methane oxidation when

compared to the LFC, is most likely the result of a flushing effect caused by the high fluid flow, while more sulfide could accumulate in LFC. Sulfate reduction were highest close to the sediment surface (Fig. 14A and C). Accordingly, higher sulfide concentrations were detected at the sediment-water interface. Other explanations of sulfide loss during the experiment are sulfide oxidation and precipitation. Since no oxygen was supplied, which was confirmed by the redox potential and the oxygen indicator, sulfide oxidation was possible only with nitrate as electron acceptor (de Beer et al. 2006; Billerbeck et al. 2006; Preisler et al. 2007). In the media only around 4 µmol l^{-1} nitrate were available, which appears not enough to supply considerable sulfide oxidation. However, Beggiatoa and Thioploca, both chemoautotroph bacteria, are able to accumulate and store nitrate in their vacuoles to oxidize sulfide (Fossing et al. 1995; Preisler et al. 2007). Thioploca has an immense potential to oxidize sulfide and is ubiquitous at the continental margin of Chile, especially in the Bay of Conception, and can create long sheets inside the sediment, which enable sulfide oxidation over the entire sediment core (Fossing et al. 1995; Schulz et al. 1996). Sulfide oxidation with nitrate increases the pH (Glud et al. 2004; Preisler et al. 2007, De Beer) which was observed in the first half of the experiment (0-53 d) in both cores and over the entire sediment depth.

Sulfide precipitation reduces the sulfide concentration of the porewater and increases the sulfur content of the solid phase. Indications of sulfide precipitation are increased TS content, observed in the upper 10 cm of the LFC (up to 1.2%), and decreased pH values (Preisler et al. 2007), observed at the end of the experiment. In the HFC, ongoing flushing avoid high sulfide accumulation in the porewater and results in lower sulfide concentrations by similar sulfate reduction rates.

The high similarity of AOM replicates (n=3) of the field data considering magnitude (SD of integrated AOM areal rates = 0.33) and depth distribution (Fig. 2C), indicate a homogenous sediment matrix with consistent fluid and methane flow. Accordingly, fluids ascended very consistently within both cores of the experiment, which was visible from the porewater profiles of the ascending bromide and the evasive sulfate (Fig. 5A, D ,G ,J and Fig. 6A, D ,G ,J). In the young seep of the bacterial mat site, sediments show a very low content of TIC and TS, compared to presumably older seep sediments (clam and tubeworm field) of this study as wells as other known seeps (e.g., Mound 11, Mound 12, Quepos Slide, unpublished data S. Krause, P.

Steeb). Probably, the seep is still too young to accumulate metal sulfide and authigenic carbonates precipitates thereby preserving the high homogeneity of the sediment matrix. Given less cemented pore space, less fluid channeling is expected increasing the reactive surface useable for the benthic methane filter (Sommer et al. 2006; Wankel et al. 2012). This still "pristine" character of the seepage site might be the reason for the high efficiency and adaptability of the benthic methane filter in this habitat.

Clam field habitat: From fluid pulses to sulfide flushing

Sediments from the clam field site showed a kinked porewater profile (Fig. 3A), which is an effect ascribed to porewater irrigation. Since no living clams were found and no bioturbation was detected by a Pb-210 dating method (unpublished data), polychaets located down to 6 cm depth might be responsible for this irrigated layer. Microbial turnover rates of clam field sediments in the irrigated as well as in the SMTZ layer were differed between AOM and sulfate reduction, in the field data. Sulfate reduction was very high (up to 2000 nmol cm^{-3} d^{-1}), showed a high variability over depth, and only ~30% of it appeared to be coupled to AOM. Consequently, we assume that the majority of sulfate reduction was coupled to organic matter degradation with a high heterogeneity (SD for sulfate reduction ± 35.61 mmol m^{-2} d^{-1}, 62%, n=3). Plenty of dead clams may have fueled the high organic matter degradation by sulfate reduction and caused the high heterogeneity.

During the *in vitro* experiment, sulfide production created high sulfide concentrations of up to 4000 µmol l^{-1} in the LFC. Nevertheless, sulfate reduction might have been fueled by different carbon sources. In the LFC, sulfate reduction was around 5.44 mmol m^{-2} d^{-1}, and was most likely mainly driven by organic matter degradation, since radiotracer measurements of AOM accounted for only one tenth of sulfate reduction. The C/N ratio in the LFC was higher after incubation when compared to the field data. Contrarily, radiotracer AOM rates (5.09 mmol m^{-2} d^{-1}) of the HFC were higher than in any other core of the experiments, and integrated areal rates reached similar magnitudes as the methane flux from below. Unfortunately, sulfate reduction was not measured in this core.

Field AOM rates (16.9 mmol m^{-2} d^{-1}) are moderate to high compared to reported turnover rates from clam fields (Treude et al. 2003). The HFC of the clam field

revealed a high adaptability of these sediments, which oxidize almost all delivered methane after ~150 d of adaption.

Fluid pulse and the efficiency of the benthic methane filter in the clam field habitat:

In both cores of the clam field habitat, seepage media ascended rapidly before the 96 d runtime (compare bromide and sulfate concentrations, Fig. 8D and Fig. 9D). This rapid ascend might have been caused by bubble rising and related porewater and sediment turbation, or by obstructed fluid flow followed by a spontaneous release and pulse in fluid flow. Since no bubbles were observed, an increased fluid flow instead of bubble rising is assumed to be the cause. Most likely, fluids were obstructed by either clam shells or alternatively by a layer of cemented sediment in the original SMTZ . In this layer (5-9 cm sediment depth), porosity decreased to around 0.1 while TS and TIC were increased, probably a result of sulfide and carbonate precipitation, respectively (Fig. 17A, C, D). When porewater pressure became too high, the obstruction was released and fluids moved upwards in a single pulse. This spontaneous fluid flow probably irrigated the porewater profiles and changed the solid phase conditions inside the sediment. In the LFC, the methane containing fluid was released in the upper part of the sediment. A strong increase in sulfide concentrations indicates the oxidation of the methane at the top of the core. Almost all methane was oxidized and the calculated efflux was only 0.07 mmol m^{-2} d^{-1}. In contrast, the fluid release of the HFC was much higher and partly bypassed the microbial benthic methane filter into the overlying water body and the outflow. Increased sulfide concentrations between 500 and 1100 µmol l^{-1} indicated high methane oxidation rates. After the fluid pulse porewater profiles were disarrayed and the sulfide was partially washed. A high fraction of the methane was released into the overlaying water body and the outflow. Under assumed constant flow conditions, the calculated methane efflux would be equal to the methane flux and all methane would be emitted at this time. However, the fluid release and increased fluid flow at this point event changed the dilution between seawater and seepage medium (previous dilution factor 3.5). Based on the bromide concentration, 44% of the outflow originated from the seepage medium and a dilution factor of 2.3 is assumed. If we use this new dilution factor to calculate the efflux, around 71% (efflux 5.911 mmol m^{-2} d^{-1}) of the contained methane was emitted from the sediment.

Around 50 d later, directly before the end of the experiment, porewater profiles were "re-arranged" in both cores: methane efflux was reduced to 0.018 and 0.022 mmol m^{-2} d^{-1} , respectively, and a SMTZ was formed between 8 – 13 cm for the LFC and between 0 - 6 cm for the HFC.

Fate of Clams:

Although sulfide sufficient was available to feed the symbiont clams, only dead clams were found and ^{210}Pb dating showed no hints for bioturbation since the past 100 years (V. Liebetrau, unpubl. data). Bioturbation of sediments is a common feature of active clams fields (Wallmann et al. 1997). It is therefore enigmatic what caused the death of these clams. We provide here two possible explanations. In the first explanation, we assume, the clam field was an active seep site with high methane flux and therefore sufficient sulfide supply to feed the clams. Over time the methane flux was dying together with the starving clams. An earthquake reactivated the seep site and AOM activity of the benthic methane filter. Until today no clams have re-colonized this seep site.

In the second explanation, we assume high sulfide concentrations had poisoned the clams. If a pulse of methane was received, AOM coupled sulfate reduction might have lead to a fast accumulation of sulfide and thereby killed the clams by excessive sulfide supply. Fast pulses of methane flux can be induced by earthquakes (Torres and McManus 2002; Hensen et al. 2004; Aiello 2005; Henrys et al. 2006; Mau et al. 2007; Praeg et al. 2009; Meister et al. 2011) and explain the high methane concentration (up to 2 µmol l^{-1}) of the bottom water. Cracks in the seafloor and other indications for earthquake activity were found next to the area of the clam field habitat, (Linke 2011). The high sulfide concentrations of this habitat might be not lethal, since living clams were reported in sediments with sulfide concentrations up to 20 mmol l^{-1} sulfide (Barry et al. 1997). However, the experiments have shown that very high sulfide concentrations can accumulate in the sediments, by both organic matter degradation and methane driven sulfate reduction. Spontaneous fluid pulses, like in the experiment, can transport the sulfide to the surface in very short time periods and disable the migration of clams that were poisoned by high sulfide concentrations.

Tubeworm field habitat: From aerobic to anaerobic benthic methane filter

In contrast to the bacterial mat and clam field, sediments of the tubeworm field showed lower turnover rates in sulfate reduction and methane oxidation, although they were higher than rates at diffusive sites of the Chilean continental margin (Treude et al. 2005b). Methane oxidation in the upper 5 cm of sediment, decoupled from sulfate reduction, is indicative for an aerobic methane oxidation. Tubeworm tubes allow oxygen to penetrate much deeper compared to low penetration depth of several mm in sediments without tubes (Beer et al. 2006). Accordingly, sulfide and TA were much lower and increased below the horizon (7.5 cm) of methane oxidation.

During the experiment, fluid flow was channeled through the worm tubes and fluid seeped out of the sediment very fast. During this time, methane bypassed the microbial methane filter and a very high methane efflux (1.263 and 1.368 mmol m^{-2} d^{-1} for the LFC and HFC, respectively) was detected after 101 d runtime in both cores. At this time, sediments from the tubeworm field exhibited a less efficient microbial benthic methane filter, because oxygen, the most important electron acceptor, was not available in the SLOT system. After 151 d, the methane efflux decreased to a level similar to the efflux of the bacterial mat. Radiotracer measurements showed a high coupling of sulfate reduction and AOM at the end of the experiment, quite surprising after a completely uncoupled methane oxidation in the field data. Around 117% of the sulfate reduction were accounted to AOM in the LFC and at least 82% in the HFC. Anaerobic methanotrophs can obviously colonize worm tubes after 151 d. A highly effective microbial benthic methane filter was the result at the end of the experiment, under low as well as high flow conditions.

Sulfide concentrations were very low in both cores of the tubeworm field, although sulfate reduction was present in the sediment cores (Fig. 18A). Sulfate reduction rates of the laboratory experiments were considerably higher than in the field measurements. Since sulfide was produced, but not detected in significant concentrations, a sink for sulfide must exist within the system. Sulfide oxidation is not plausible, because oxygen was not available and an pH increase as a result of oxidation by nitrate was not observed. Sulfide precipitation reduces the pH (Preisler et al. 2007)of the porewater, however, no elevated TS content was detected after the experiment (Fig. 19C).

Since sulfate reduction, coupled to AOM, occurred mostly inside the worm tube walls, sulfide was most likely unable to accumulate under the high flow-through conditions.

Summary and conclusion:

In the present study, we report for the first time AOM and sulfate reduction rates of different habitats in the recently discovered Concepción Methane Seep Area at the continental margin off Chile. Additionally, the response of the sediments and the efficiencies of the microbial benthic methane filters in response to increased fluid flow and methane in a recently developed sediment flow through system (SLOT) were studied.

A young seep site covered with bacterial mats showed an active and highly efficient benthic microbial methane filter retarding methane fluxes almost completely. After increased fluid and methane flux in the experiment, methane efflux increased only minor under moderate (here “low”) and high flow conditions. AOM and sulfate reduction showed an uncommon distribution, with highest methane turnover at the bottom and highest sulfate reduction at the top. Produced sulfide seems to be consumed by chemolithotrophic bacteria, like Beggiatoa or Thioploca.

Sediments of the clam field showed high sulfide concentrations at the SMTZ at 5-10 cmbsf. This habitat was much more heterogeneous than the bacterial mat and had lower turnover rates of AOM. Contrary, sulfate reduction was much higher and its variability was most likely a result of the heterogeneous distribution of organoclastic sulfate reduction. The in- vitro experiments demonstrated, that high sulfide concentrations can accumulate caused by high methane flux, and those can spontaneously released to the sediment surface. This process could explain the high sulfide concentrations in the sediments at the field site, the dead clams, as well as the high methane concentrations in the bottom water of this seep. Earthquakes might be one trigger to open new fluid pathways, induce higher methane flux and trigger the such spontaneous releases.

The tubeworm field was characterized by a microbial benthic methane filter with aerobic methane oxidation at the top of the sediments. While turnover rates of methane were low to moderate, sulfate reduction rates were much lower and more in

the range of diffusive systems. In the laboratory experiments, the benthic methane filter first needed to adapt to the new anoxic conditions in the water column. High amounts of methane were emitted from the sediments until the benthic microbial methane filter had switched from originally aerobic to anaerobic processes. In the end, turnover rates of AOM and sulfate reduction were increased, highly coupled, and a very efficient benthic methane filter was established.

Acknowledgments

We thank Captain Mallon and the crew of RV "Sonne" for support during the “Chiflux” cruise (SO210). Furthermore, we thank the team the ROV "KIEL 6000" for providing access to push cores at the cold seeps. Special thanks goes to B. Domeyer, A. Bleyer, R. Suhrberg, and U. Lomnitz for porewater analyzes. F. Valdés is thanked for the identification of the seep fauna. K. Kretschmer is thanked for support during system maintenance. K. Kretschmer and J. Farkas are thanked for turnover rate determination in the radioisotope lab. R. Schmitz-Streit is thanked for scientific input and helpful discussions. This project was financed through the Collaborative Research Centre (SFB) 574 "Volatiles and Fluids in Subduction Zones" funded by the German Research Foundation (DFG).

References

Aiello, I. 2005. Fossil seep structures of the Monterey Bay region and tectonic/structural controls on fluid flow in an active transform margin. Palaeogeogr. Palaeoclimatol. Palaeoecol. **227**: 124–142.

Angermann, D., J. Klotz, and C. Reigber. 1999. Space-geodetic estimation of the Nazca-South America Euler vector. Earth Planet. Sci. Lett. **171**: 329–334.

Archer, D. 2007. Methane hydrate stability and anthropogenic climate change. Biogeosciences **4**: 521–544.

Arntz, W., and E. Fahrbach. 1991. El Nino Klimaexperiment der Natur, Birkhäuser, Basel.

Barry, J., R. Kochevar, and C. Baxter. 1997. Water chemistry and physiology on the distribution of vesicomyid clams at cold seeps in Monterey Bay: Implications for patterns of chemosynthetic community. Limnol. Oceanogr. **42**: 318–328.

De Beer, D., E. Sauter, H. Niemann, N. Kaul, U. Witte, M. Schlüter, and A. Boetius. 2006. In situ fluxes and zonation of microbial activity in surface sediments of the Håkon Mosby Mud Volcano. Limnol. Oceanogr. **51**: 1315–1331.

Billerbeck, M., U. Werner, L. Polerecky, E. Walpersdorf, D. deBeer, and M. Huettel. 2006. Surficial and deep pore water circulation governs spatial and temporal scales of nutrient recycling in intertidal sand flat sediment. Mar. Ecol. Prog. Ser. **326**: 61–76.

Boetius, A., K. Ravenschlag, C. J. Schubert, D. Rickert, F. Widdel, A. Gieseke, R. Amann, B. B. Jørgensen, U. Witte, O. Pfannkuche, and B. B. Jorgensen. 2000. A marine microbial consortium apparently mediating anaerobic oxidation of methane. Nature **407**: 623–626.

Bohlen, L., A. W. Dale, S. Sommer, T. Mosch, C. Hensen, A. Noffke, F. Scholz, and K. Wallmann. 2011. Benthic nitrogen cycling traversing the Peruvian oxygen minimum zone. Geochim. Cosmochim. Acta **75**: 6094–6111.

Borowski, W. S. 2004. A review of methane and gas hydrates in the dynamic, stratified system of the Blake Ridge region, offshore southeastern North America,.

Borowski, W. S., C. K. Paull, and I. W. Ussler. 1999. Global and local variations of interstitial sulfate gradients in deep-water, continental margin sediments: Sensitivity to underlying methane and gas hydrates. Mar. Geol. **159**: 131–154.

Burwicz, E., L. Rüpke, and K. Wallmann. 2011. Estimation of the global amount of submarine gas hydrates formed via microbial methane formation based on numerical reaction-transport modeling and a novel parameterization of Holocene sedimentation. Geochim. Cosmochim. Acta **75**: 4562–4576.

Cline, J. 1969. Spectrophotometric determination of hydrogen sulfide in natural waters. Limnol. Oceanogr. **14**: 454–458.

Coffin, R., J. Pohlman, J. Gardner, R. Downer, W. Wood, L. Hamdan, S. Walker, R. Plummer, J. Gettrust, and J. Diaz. 2007. Methane hydrate exploration on the mid Chilean coast: A geochemical and geophysical survey. J. Pet. Sci. Eng. **56**: 32–41.

Ferdelman, T. G., C. Lee, S. Pantoja, J. Harder, B. M. Bebout, and H. Fossing. 1997. Sulfate reduction and methanogenesis in a Thioploca-dominated sediment off the coast of Chile. Geochim. Cosmochim. Acta **61**: 3065–3079.

Fossing, H., V. Gallardo, and B. Jørgensen. 1995. Concentration and transport of nitrate by the mat-forming sulphur bacterium Thioploca. Nature **374**: 714–715.

Geersen, J., J. H. Behrmann, D. Völker, S. Krastel, C. R. Ranero, J. Diaz-Naveas, and W. Weinrebe. 2011. Active tectonics of the South Chilean marine fore arc (35 S–40 S). … **30**, doi:10.1029/2010TC002777

Glud, R. N., S. Rysgaard, T. Fenchel, and P. H. Nielsen. 2004. A conspicuous H2S-oxidizing microbial mat from a high-latitude Arctic fjord (Young Sound, NE Greenland). Mar. Biol. **145**: 51–60.

Grasshoff, K., M. Erhardt, K. Kremling, and C. Revised. 1983. Methods of seawater analysis, Wiley-VCH, Weinheim.

Grevemeyer, I., N. Kaul, and J. L. Diaz-Naveas. 2006. Geothermal evidence for fluid flow through the gas hydrate stability field off Central Chile – transient flow related to large subduction zone earthquakes? Geophys. J. Int. **166**: 461–468.

Hamdan, L. J., P. M. Gillevet, M. Sikaroodi, J. W. Pohlman, R. E. Plummer, and R. B. Coffin. 2008. Geomicrobial characterization of gas hydrate-bearing sediments along the mid-Chilean margin. FEMS Microbiol. Ecol. **65**: 15–30.

Henrys, S., M. Reyners, I. Pecher, S. Bannister, Y. Nishimura, and G. Maslen. 2006. Kinking of the subducting slab by escalator normal faulting beneath the North Island of New Zealand. Geology **34**: 777.

Hensen, C., K. Wallmann, M. Schmidt, C. R. Ranero, and E. Suess. 2004. Fluid expulsion related to mud extrusion off Costa Rica—A window to the subducting slab. Geology **32**: 201.

Hester, K. C., and P. G. Brewer. 2009. Clathrate Hydrates in Nature. Ann. Rev. Mar. Sci. **1**: 303–327.

Iriarte, J., G. Pizarro, V. Troncoso, and M. Sobarzo. 2000. Primary production and biomass of size-fractionated phytoplankton off Antofagasta, Chile (23–24 S) during pre-El Niño and El Niño 1997. J. Mar. Syst. **26**: 37–51.

Ivanenkov, V. N., and Y. I. Lyakhin. 1978. Determination of total alkalinity in seawater, p. 110–114. *In* O.K. Bordovsky and V.N. Ivanenkov [eds.], Methods of Hydrochemical Investigations in the Ocean. Nauka Publ. House.

Iversen, N., and B. B. Jørgensen. 1985. Anaerobic methane oxidation rates at the sulfate-methane transition in marine sediments from Kattegat and Skagerrak (Denmark). Limnol. Oceanogr. **30**: 944–955.

Jørgensen, B. B. 1978. A comparison of methods for the quantification of bacterial sulfate reduction in coastal marine sediments. Geomicrobiol. J. 37–41.

Joye, S. B., A. Boetius, B. N. Orcutt, J. P. Montoya, H. N. Schulz, M. J. Erickson, and S. K. Lugo. 2004. The anaerobic oxidation of methane and sulfate reduction in sediments from Gulf of Mexico cold seeps. Chem. Geol. **205**: 219–238.

Judd, A., M. Hovland, and L. Dimitrov. 2002. The geological methane budget at continental margins and its influence on climate change. Geofluids **2**: 109–126.

Kallmeyer, J., T. G. Ferdelman, A. Weber, H. Fossing, and B. B. Jørgensen. 2004. A cold chromium distillation procedure for radiolabeled sulfide applied to sulfate reduction measurements. Limnol. Oceanogr. Methods **2**: 171–180.

Klaucke, I., W. Weinrebe, P. Linke, D. Kläschen, and J. Bialas. 2012. Sidescan sonar imagery of widespread fossil and active cold seeps along the central Chilean continental margin. Geo-Marine Lett. , doi:10.1007/s00367-012-0283-1

Knittel, K., A. Lemke, and K. Lochte. 2003. Activity , Distribution , and Diversity of Sulfate Reducers and Other Bacteria in Sediments above Gas Hydrate (Cascadia Margin , Oregon). 269–294.

Krause, S., P. Steeb, C. Hensen, V. Liebetrau, A. W. Dale, M. Nuzzo, and T. Treude. 2014. Microbial activity and carbonate isotope signatures as a tool for identification of spatial differences in methane advection: a case study at the Pacific Costa Rican margin. Biogeosciences **11**: 507–523.

Kukowski, N., and O. Oncken. 2006. Subduction Erosion - the “Normal” Mode of Fore-Arc Material Transfer along the Chilean Margin?, p. 217–236. *In* O. Oncken, G. Chong, G. Franz, P. Giese, H.-J. Götze, V.A. Ramos, M.R. Strecker, and P. Wigger [eds.], The Andes Achtive Subduction orogeny. Springer Berlin Heidelberg New York.

Kvenvolden, K. A. 1993. Gas Hydrates - Geological Perspective and Global Change. Rev. Geophys. **31**: 173–187.

Lamy, F., D. Hebbeln, and G. Wefer. 1998. Terrigenous sediment supply along the Chilean continental margin: modern regional patterns of texture and composition. Geol. Rundschau **87**: 477–494.

Levin, L. A. 2005. Ecology of cold seep sediments: interactions of fauna with flow, chemistry and microbes. Ocean. Mar. Biol. Ann. Rev. **43**: 1–46.

Liebetrau, V., A. Eisenhauer, and P. Linke. 2010. Cold seep carbonates and associated cold-water corals at the Hikurangi Margin, New Zealand: New insights into fluid pathways, growth structures and geochronology. Mar. Geol. **272**: 307–318.

Linke, P. 2011. Cruise Report SO210 Chiflux - Identification and investigation of fluid flux, mass wasting and sediments in the forearc of the central Chilean subduction zone Valparaiso - Valparaiso, 23.09.-01.11.2010.

Lucassen, F., M. Wiedicke, and G. Franz. 2010. Complete recycling of a magmatic arc: evidence from chemical and isotopic composition of Quaternary trench sediments in Chile (36°–40°S). Int. J. Earth Sci. **99**: 687–701.

Luff, R., and K. Wallmann. 2003. Fluid flow, methane fluxes, carbonate precipitation and biogeochemical turnover in gas hydrate-bearing sediments at Hydrate Ridge, Cascadia Margin: numerical modeling and mass balances. Geochim. Cosmochim. Acta **67**: 3403–3421.

Mau, S., G. Rehder, I. G. Arroyo, J. Gossler, and E. Suess. 2007. Indications of a link between seismotectonics and CH 4 release from seeps off Costa Rica. Geochemistry, Geophys. Geosystems **8**: 1–13.

Mau, S., H. Sahling, G. Rehder, E. Suess, P. Linke, and E. Soeding. 2006. Estimates of methane output from mud extrusions at the erosive convergent margin off Costa Rica. Mar. Geol. **225**: 129–144.

Meister, P., M. Gutjahr, M. Frank, S. M. Bernasconi, C. Vasconcelos, and J. A. McKenzie. 2011. Dolomite formation within the methanogenic zone induced by tectonically driven fluids in the Peru accretionary prism. Geology **39**: 563–566.

Melnick, D., and H. P. Echtler. 2006. Inversion of forearc basins in south-central Chile caused by rapid glacial age trench fill. Geology **34**: 709.

Morales, C. E., J. L. Blanco, M. Braun, H. Reyes, and N. Silva. 1996. Chlorophyll-a distribution and associated oceanographic conditions in the upwelling region off northern Chile during the winter and spring 1993. Deep Sea Res. Part I Oceanogr. Res. Pap. **43**: 267–289.

Niemann, H., T. Lösekann, D. de Beer, M. Elvert, T. Nadalig, K. Knittel, R. Amann, E. J. Sauter, M. Schlüter, M. Klages, J. P. Foucher, and A. Boetius. 2006. Novel microbial communities of the Haakon Mosby mud volcano and their role as a methane sink. Nature **443**: 854–8.

Niggemann, J., T. G. Ferdelman, B. A. Lomstein, J. Kallmeyer, and C. J. Schubert. 2007. How depositional conditions control input, composition, and degradation of organic matter in sediments from the Chilean coastal upwelling region. Geochim. Cosmochim. Acta **71**: 1513–1527.

Praeg, D., S. Ceramicola, R. Barbieri, V. Unnithan, and N. Wardell. 2009. Tectonically-driven mud volcanism since the late Pliocene on the Calabrian accretionary prism, central Mediterranean Sea. Mar. Pet. Geol. **26**: 1849–1865.

Preisler, A., D. de Beer, A. Lichtschlag, G. Lavik, A. Boetius, and B. B. Jørgensen. 2007. Biological and chemical sulfide oxidation in a Beggiatoa inhabited marine sediment. ISME J. **1**: 341–53.

Revsbech, N., and B. Jørgensen. 1986. Microelectrodes: their use in microbial ecology. Adv. Microb. Ecol **9**.

Saffer, D. M., and H. J. Tobin. 2011. Hydrogeology and Mechanics of Subduction Zone Forearcs: Fluid Flow and Pore Pressure. Annu. Rev. Earth Planet. Sci. **39**: 157–186.

Sahling, H., S. V Galkin, A. Salyuk, J. Greinert, H. Foerstel, D. Piepenburg, and E. Suess. 2003. Depth-related structure and ecological significance of cold-seep communities—a case study from the Sea of Okhotsk. Deep Sea Res. Part I Oceanogr. Res. Pap. **50**: 1391–1409.

Sahling, H., D. Rickert, R. W. Lee, P. Linke, and E. Suess. 2002. Macrofaunal community structure and sulfide flux at gas hydrate deposits from the Cascadia convergent margin, NE Pacific. Mar. Ecol. Prog. Ser. **231**: 121–138.

Scholz, F., C. Hensen, M. Schmidt, and J. Geersen. 2013. Submarine weathering of silicate minerals and the extent of pore water freshening at active continental margins. Geochim. Cosmochim. Acta **100**: 200–216.

Schubert, C. J., and B. Nielsen. 2000. Effects of decarbonation treatments on d 13 C values in marine sediments. 55–59.

Schulz, H. N., B. B. Jørgensen, H. a Fossing, and N. B. Ramsing. 1996. Community Structure of Filamentous, Sheath-Building Sulfur Bacteria, Thioploca spp., off the Coast of Chile. Appl. Environ. Microbiol. **62**: 1855–62.

Sellanes, J., C. Neira, E. Quiroga, and N. Teixido. 2010. Diversity patterns along and across the Chilean margin: a continental slope encompassing oxygen gradients and methane seep benthic habitats. Mar. Ecol. **31**: 111–124.

Sellanes, J., E. Quiroga, and V. a. Gallardo. 2004. First direct evidence of methane seepage and associated chemosynthetic communities in the bathyal zone off Chile. J. Mar. Biol. Assoc. UK **84**: 1065–1066.

Sommer, S., O. Pfannkuche, P. Linke, R. Luff, J. Greinert, M. Drews, S. Gubsch, M. Pieper, M. Poser, and T. Viergutz. 2006. Efficiency of the benthic filter: Biological control of the emission of dissolved methane from sediments containing shallow gas hydrates at Hydrate Ridge. Global Biogeochem. Cycles **20**: 1–14.

Steeb, P., P. Linke, and T. Treude. 2014. A sediment flow-through system to study the impact of shifting fluid and methane flow regimes on the efficiency of the benthic methane filter. Limnol. Oceanogr. Methods **12**: 25–45.

Suess, E. 2010. Marine Cold Seeps, p. 188–198. *In* K.N. Timmis [ed.], Handbook of Hydrocarbon and Lipid Microbiology. Springer Berlin Heidelberg.

Thamdrup, B., and D. E. Canfield. 1996. Pathways of carbon oxidation in continental margin sediments off central Chile. Limnol. Oceanogr. **41**: 1629–50.

Tishchenko, P., C. Hensen, K. Wallmann, and C. S. Wong. 2005. Calculation of the stability and solubility of methane hydrate in seawater. Chem. Geol. **219**: 37–52.

Torres, M., and J. McManus. 2002. Fluid and chemical fluxes in and out of sediments hosting methane hydrate deposits on Hydrate Ridge, OR, I: Hydrological provinces. Earth Planet. … **201**: 525–540.

Treude, T., A. Boetius, K. Knittel, K. Wallmann, and B. Barker Jørgensen. 2003. Anaerobic oxidation of methane above gas hydrates at Hydrate Ridge, NE Pacific Ocean. Mar. Ecol. Prog. Ser. **264**: 1–14.

Treude, T., M. Krüger, A. Boetius, and B. Jørgensen. 2005a. Environmental control on anaerobic oxidation of methane in the gassy sediments of Eckernfoerde Bay(German Baltic). Limnol. Oceanogr. **50**: 1771–1786.

Treude, T., J. Niggemann, J. Kallmeyer, P. Wintersteller, C. J. Schubert, A. Boetius, and B. B. Jørgensen. 2005b. Anaerobic oxidation of methane and sulfate

reduction along the Chilean continental margin. Geochim. Cosmochim. Acta **69**: 2767–2779.

Treude, T., C. R. Smith, F. Wenzhoefer, E. Carney, A. F. Bernardino, A. K. Hannides, M. Krueger, and A. Boetius. 2009. Biogeochemistry of a deep-sea whale fall: sulfate reduction, sulfide efflux and methanogenesis. Mar. Ecol. Prog. Ser. **382**: 1–21.

Tryon, M. D., K. M. Brown, and M. E. Torres. 2002. Fluid and chemical fluxes in and out of sediments hosting methane hydrate deposits on Hydrate Ridge, OR, II: Hydrological provinces. Earth Planet. Sci. Lett. **201**: 541–557.

Völker, D., F. Scholz, and J. Geersen. 2011. Analysis of submarine landsliding in the rupture area of the 27 February 2010 Maule earthquake, Central Chile. Mar. Geol. **288**: 79–89.

Wallmann, K., P. Linke, E. Suess, G. Bohrmann, H. Sahling, M. Schloter, D. Anke, S. Lammers, J. Greinert, and N. V. O. N. Mirbach. 1997. Quantifying fluid flow , solute mixing , and biogeochemical turnover at cold vents of the eastern Aleutian subduction zone. **61**: 5209–5219.

Wallmann, K., E. Pinero, E. Burwicz, M. Haeckel, C. Hensen, A. Dale, and L. Ruepke. 2012. The Global Inventory of Methane Hydrate in Marine Sediments: A Theoretical Approach. Energies **5**: 2449–2498.

Wankel, S. D., M. M. Adams, D. T. Johnston, C. M. Hansel, S. B. Joye, and P. R. Girguis. 2012. Anaerobic methane oxidation in metalliferous hydrothermal sediments: influence on carbon flux and decoupling from sulfate reduction. Environ. Microbiol. **14**: 2726–40.

Whiticar, M. J. 2002. Diagenetic relationships of methanogenesis , nutrients, acoustic turbidity , pockmarks and freshwater seepages in Eckernförde Bay. Mar. Geol. **182**: 29–53.

Widdel, F., and F. Bak. 2006. Gram-negative mesophilic sulfate-reducing bacteria, p. 3352–3378. *In* M. Dworkin, S. Falkow, E. Rosenberg, K.-H. Schleifer, and E. Stackebrandt [eds.], The Prokaryotes. Springer US.

Zapata-Hernández, G., J. Sellanes, A. R. Thurber, L. A. Levin, F. Chazalon, and P. Linke. 2014. New insights on the trophic ecology of bathyal communities from the methane seep area off Concepción, Chile (~36° S). Mar. Ecol. **35**: 1–21.

Chapter 6

Summary and conclusion

The presented thesis combines observations and laboratory experiments on the efficiency of the benthic methane filter. Inside the benthic filter advectively delivered methane from deeper reservoirs is oxidized with diffusively transported sulfate from seawater. The fluid flow controls the methane flux as well as the penetration of sulfate into the sediment, and therefore, represents a key factor for the efficiency of the benthic methane filter. Most of the studies on the benthic methane filter include observations at seep sites with constant fluid flow under steady state conditions. To investigate the efficiency under non-steady state conditions I developed a Sediment-Flow-Through system (SLOT) to perform experiments on intact benthic filters of different seep sediments. The SLOT system mimics the fluid regime of a cold seep and enables to monitor in- and outflow as well as geochemical profiles inside the sediments.

In chapter 2 the developed SLOT system is described in detail and methods for monitoring the experiments are summarized. For the first time, long-term experiments were performed with two intact sediment cores from Eckernförde Bay. Tenfold different fluid and methane fluxes of the two parallel sediment cores were reflected by the AOM rates whereas the efflux of the higher fluid and methane flux was only double of the lower fluid and methane flux. The benthic filters of both cores were highly efficient over the duration of the experiment and oxidized ~90% of the delivered methane. Monitoring of the porewater profiles and parameters revealed other seep related processes, such as sulfide oxidation by nitrate and precipitation of sulfide and carbonates. The chapter closes with an evaluation of the SLOT system and a comparison to previous flow-through systems.

Chapter 3 provides a case study of spatial differences in fluid flux of two neighbored Costa Rican mounds and their adapted benthic methane filters (Krause et al. 2014). The study contains field data of microbial turnover rates of AOM, sulfate reduction, numerical model application, and isotopic signatures of the carbonate archives. Both mounds differ in fluid and methane flux and origin. The one magnitude higher fluid and methane flux of mound 11 is reflected by six times higher AOM rates of the benthic methane filter, compared to Mound 12. Isotope signatures of ^{18}O, ^{13}C, and 87Sr/86Sr of the carbonates indicate a mixed composition of deep-sourced and shallow fluids and methane source at Mound 11 in contrast to seawater sourced carbonate precipitating fluids and shallow biotic methane source at Mound 12.

Chapter 4 combines field data with SLOT experiments. Radiotracer determinations, methane turnover rates and numerical modeling constrain a highly effective benthic methane filter at the Quepos Slide offshore Costa Rica. The sediment cores originate from bacterial mat habitats inside an oxygen minimum zone with integrated areal rates of AOM from 12.87 (SD=5.98) to 45.15 (SD=11.48) mmol m^{-2} d^{-1} and around

98% of the delivered methane is oxidized. The SLOT experiments were performed under similar fluid and methane flux as the experiments described in chapter 2, with parallel cores under high and low flow conditions. The highly adaptable benthic methane filter showed a response time of 150-170 days and demonstrates that increased fluid and methane flux is compensated by the benthic methane filter in this high active and heterogeneous region.

The fifth chapter provides field data and SLOT experiments of three different habitats to determine the efficiency and adaptability of the benthic methane filters from a recently discovered seep area at the continental slope of Chile. The experiments differed from the previous experiments of chapter 2 and 4, in time (140 -150 d), fluid flux and methane flux. The low flow conditions are similar to the high flow conditions of the previous experiments (10.6 – 137.8 cm y^{-1}) and the high flow conditions were performed with a doubled fluid flow (112.7 – 132.3 cm y^{-1}). Sediments from a probably young seep site, covered with bacterial mats, showed a very homogenous benthic methane filter with high adaptability to increased fluid flux. Sediments from a clam field demonstrate how heterogeneous fluid flow through the sediment column results in higher efficiency of the benthic filter. Additionally, discussions about the habitat history are provided. Sediments from a pogonophoran field demonstrate how an established aerobic methane filter can change into an efficient anoxic methane filter within 150 days. Furthermore, the experiment constrains how pogonophoran tubes can channel fluids and change the seepage behavior.

Chapter 3 describes two mounds under steady state conditions and how large differences in fluid and methane flux affect the efficiency and AOM activity of the benthic methane filter. Chapter 2, 4, and 5 provide the first estimation how the transition between these fluid conditions happen and how the transition affects the efficiency of the benthic microbial methane filter based on experiments. The response time of the benthic methane at seep sites was found to be between 150 and ~400 d. However, natural seep systems differ in some points and conditions from the experiment setup. In the following section some of the main factors and their possible effects on the benthic methane filter are discussed.

Evaluation of the SLOT experiment results

Seep site sediments differ from the experimental setup of the SLOT experiments in, e.g., pressure, methane flux, and transport mechanism. Some of the main differences to natural conditions, and therefore restrictions of the results, are discussed here.

Compared to natural seep sites, the methane flux in the SLOT experiments was low, based on the low methane concentration (Treude et al. 2003; de Beer et al. 2006). Higher methane solubility is only achieved in high pressure systems (Yamamoto 1976; Tishchenko et al. 2005), which is beyond the scope of the presented studies. Pressurized systems need an advanced setup (Deusner et al. 2010; Zhang et al. 2010) and different methods to monitor the experiments. Since there is a direct relation between methane concentration and AOM activity (Nauhaus et al. 2002;

Deusner et al. 2010), higher methane flux on the base of higher methane concentration might be largely compensated by the activity of the microbes.

The results of the SLOT experiments are restricted to advective transport of dissolved methane. In systems with diffusion as the dominant transport mechanism, methane is almost completely oxidized by AOM (Borowski 2004; Suess 2010). Since diffusion is a very slow transport process beyond cm scales, changes in diffusive methane flux can easily be compensated by AOM. In contrast, free gas can be transported very fast by the rise of methane bubbles. Rising methane bubbles would bypass the system, since only dissolved methane is available for microbes (Luff and Wallmann 2003). Furthermore, bubbles lead to changed porewater profiles and higher sulfate availability by sediment irrigation (Boetius and Suess 2004).

The experiments focused on AOM and were carried out under strict anoxic conditions. Aerobic methane oxidation at natural seep sites can enhance the efficiency of the benthic methane filter. However, most of the methane at seep sites is oxidized by AOM, and consequently, aerobic methane oxidation plays a minor role in these sediments (Linke et al. 2005; Krüger et al. 2005).

By the generation of new fluid paths through the sediment, based on e.g. new fault creation or gas hydrate dissolution, new cold seeps can form. These new seep sites have at first to establish a benthic methane filter and an adequate microbial population. Based on the long doubling time of the ANME (Girguis et al. 2005; Nauhaus et al. 2007; Meulepas et al. 2009), there might be a high lag phase of years or even decades (Dale et al. 2008) until an efficient benthic methane filter has established.

Adaption to new fluid and methane flux conditions

How fast benthic methane filters can adapt to the new fluid flow conditions depends on the difference to the previous steady state conditions.

For an increased methane flux a higher methane turnover is necessary to oxidize the entire methane. The activity of the microbes increases with methane availability (Nauhaus et al. 2002; Deusner et al. 2010). However, there might be a lag phase until the microbial activity is increased. Samples with highest ex-situ AOM rates, the Quepos Slide sediments (chapter 4) and bacterial mats from Chile (chapter 5), showed fastest adaptation and highest efficiency. An increase of the population density might take much longer, since the doubling time of ANME is several month (Girguis et al. 2005; Nauhaus et al. 2007; Meulepas et al. 2009).

Under steady state conditions the highest abundance of methanotrophs is located in the SMTZ (Knittel et al. 2005). Changing fluid flux shifts the SMTZ and the methanotrophs might not longer be in the focus of the SMTZ. Consequently, the methanotrophs need a prolonged period of time to adapt to these new conditions. Sediments of the SLOT experiments differ in several cm and shifted less than 10 cm.

These low differences in the AOM zone might be no problem, since the SMTZ depth can vary seasonally (Treude et al. 2005).

Sediment heterogeneity and filter efficiency

In sediment cores with a heterogeneous sediment matrix, as the clam and pogonophoran field sediments from Chile (chapter 5), a much higher methane efflux was observed, in contrast to sediments with a more homogenous sediment matrix as sediments from Eckernförde bay (chapter 2), the bacterial mat from Quepos Slide (chapter 4), and the bacterial mat of the young seep site (chapter 5). Much more obvious in experiments with sediments from the North Alex Mud Volcano (unpublished data, P. Steeb), which was performed in parallel to the experiments with Eckernförde bay and Quepos Slide sediments.

The North Alex Mud Volcano (NAMV) is a seep site/area at the Nile deep sea fan in the Mediterranean Sea (Omoregie et al. 2009; Feseker et al. 2010). The sediment core from the center of the NAMV was characterized by clayish sediments with clams and authigenic carbonates. Bromide concentrations, as a tracer for the ascending fluid, indicate a fast seepage with high fluctuations mirrored by the sulfate profile (Appendix Fig. 6S). The methane efflux was six times higher than the emissions from the parallel Eckernförde bay sediment under similar fluid and methane flux (Appendix Fig. 8S).

The fluctuations of the porewater profiles, especially for the inert tracer bromide, can be explained by preferential fluid paths, induced by the heterogeneity of the sediment (Torres et al. 2002). Channeled fluids and lateral heterogeneity of fluid flux may be much closer to natural conditions and were observed in other flow-through systems before (Wankel et al. 2012). Inside these fluid channels, the sulfate availability might be limited and therefore decrease the AOM activity. By the low hydrological residence time based on the higher fluid velocity, methane loaded seepage medium bypasses the benthic filter which results in a lower filter areal efficiency.

The tubes of the pogonophoran habitat (chapter 5) provide biogenic preferential fluid paths, whereas in the NAMV and clam field sediments preferential fluid paths were reinforced by increased fluid flux. In older seep systems pores might be cemented over time by carbonate or sulfide precipitation, and support the development of preferential fluid paths. In contrast to the sediments with uniform fluid front the difference in methane efflux of the sediments with channelized fluids indicate the heterogeneity of the sediment matrix as a major issue for the adaptability of the benthic methane filter to increased fluid flux.

Fluid and methane flux variations and adaptability of the benthic methane filter

Fluid pulses or new, as fluid paths serving, created faults, formed by earthquakes (Hensen et al. 2004; Aiello 2005; Henrys et al. 2006; Praeg et al. 2009; Meister et al. 2011) are point events with rapidly changed fluid flux. Fluid pulses represent situations similar to the carried out SLOT experiments and might be compensated

within the response time of 150 – 400 days. New fluid paths create new seeps where at first a benthic methane filter has to establish (Dale et al. 2008). Due to earthquake triggered slope failures (Ranero et al. 2008; Manga et al. 2009) a probably existing benthic methane filter can be removed and consequently a new one has to establish.

Fluid flux increase over several days to weeks (Tryon et al. 2002; Füri et al. 2010) is faster than the response time of the benthic filter and leads to additional methane efflux. Downward flow by released pore pressure, on the base of tidal variations (Boles et al. 2001; LaBonte et al. 2007), or at clam fields (Tryon et al. 2002) can increase the efficiency of the benthic filter by increased sulfate flux into the sediment. Lag phases, due to disrupt methane supply during this time, endure the microbes easily (Wegener and Boetius 2009; Deusner et al. 2010). Seasonal variations (Treude et al. 2005; Berndt et al. 2014) are within the response time of the benthic methane filter and therefore an interesting aim for further studies. If seasonal methane flux is related to flares and the release of free gas (Berndt et al. 2014), large amounts of methane might bypass the benthic methane filter.

Climate change can cause seafloor warming and therefore dissociate gas hydrates (Kvenvolden 1993), open new fluid paths, and potentially increase the methane flux. Since global warming will take years to decades, the benthic methane filter can react to increased methane flux or even establish a new microbial benthic methane filter above new fluid paths. However, some regions as the Arctic Ocean are affected stronger by temperature change, and the shallow gas hydrates of this region can dissociate (Buffett and Archer 2004; Biastoch et al. 2011). Depending on ocean currents and gas hydrate depth, the benthic methane filter at the Arctic ocean might be strongly challenged in the future.

Kutterolf et al. (2008) described long-term mud extrusion variations of several thousand years. In this time periods the methanotrophs grow according to the methane supply and the efficiency of the benthic methane filter persists.

Future perspectives:

To investigate the effects of different fluid regimes on the development and distribution of the microbial community, several samples (CARD-FISH, DNA/RNA, Biomarker) were taken before and after the experiments. Interesting questions are:

What was the effect on the microbial abundance?

Has the microbial community reacted to a shifting SMTZ?

Are there preferences of different ANME types for different fluid flows?

Furthermore, it would be interesting to use a mathematical model of the transient fluid regime and extrapolate the results to higher methane fluxes. Budgeting of methane emissions during the transition time can help to estimate and regionalize the additional methane emissions of a changing environment.

References:

Aiello, I. 2005. Fossil seep structures of the Monterey Bay region and tectonic/structural controls on fluid flow in an active transform margin. Palaeogeogr. Palaeoclimatol. Palaeoecol. **227**: 124–142.

De Beer, D., E. Sauter, H. Niemann, N. Kaul, U. Witte, M. Schlüter, and A. Boetius. 2006. In situ fluxes and zonation of microbial activity in surface sediments of the Håkon Mosby Mud Volcano. Limnol. Oceanogr. **51**: 1315–1331.

Berndt, C., T. Feseker, T. Treude, K. Krastel, V. Liebetrau, H. Niemann, V. Bertrics, I. Dumke, K. Dünnbier, B. Ferre, C. Graves, F. Gross, K. Hissmann, V. Hühnerbach, S. Krause, K. Lieser, J. Schauer, and L. Steinle. 2014. Temporal Constrains on Hydrate-Controlled Methane Seepage off Svalbard. Science (80-.). 1.

Biastoch, A., T. Treude, and L. Rüpke. 2011. Rising Arctic Ocean temperatures cause gas hydrate destabilization and ocean acidification. Geophys. Res. … **38**: 1–5.

Boetius, A., and E. Suess. 2004. Hydrate Ridge: a natural laboratory for the study of microbial life fueled by methane from near-surface gas hydrates. Chem. Geol. **205**: 291–310.

Boles, J. R., J. F. Clark, I. Leifer, and L. Washburn. 2001. Temporal variation in natural methane seep rate due to tides, Coal Oil Point area, California. J. Geophys. Res. Ocean. **106**: 27077–27086.

Borowski, W. S. 2004. A review of methane and gas hydrates in the dynamic, stratified system of the Blake Ridge region, offshore southeastern North America,.

Buffett, B., and D. Archer. 2004. Global inventory of methane clathrate: sensitivity to changes in the deep ocean. Earth Planet. Sci. Lett. **227**: 185–199.

Dale, A. W., P. Van Cappellen, D. R. Aguilera, and P. Regnier. 2008. Methane efflux from marine sediments in passive and active margins: Estimations from bioenergetic reaction–transport simulations. Earth Planet. Sci. Lett. **265**: 329–344.

Deusner, C., V. Meyer, and T. G. Ferdelman. 2010. High-pressure systems for gas-phase free continuous incubation of enriched marine microbial communities performing anaerobic oxidation of methane. Biotechnol. Bioeng. **105**: 524–33.

Feseker, T., K. R. Brown, C. Blanchet, F. Scholz, M. Nuzzo, A. Reitz, M. Schmidt, and C. Hensen. 2010. Active mud volcanoes on the upper slope of the western Nile deep-sea fan—first results from the P362/2 cruise of R/V Poseidon. Geo-Marine Lett. **30**: 169–186.

Füri, E., D. R. Hilton, M. D. Tryon, K. M. Brown, G. M. McMurtry, W. Brückmann, and C. G. Wheat. 2010. Carbon release from submarine seeps at the Costa Rica fore

arc: Implications for the volatile cycle at the Central America convergent margin. Geochemistry, Geophys. Geosystems **11**, doi:10.1029/2009GC002810

Girguis, P., A. Cozen, and E. DeLong. 2005. Growth and population dynamics of anaerobic methane-oxidizing archaea and sulfate-reducing bacteria in a continuous-flow bioreactor. Appl. Environ. Microbiol. **71**: 3725–3733.

Henrys, S., M. Reyners, I. Pecher, S. Bannister, Y. Nishimura, and G. Maslen. 2006. Kinking of the subducting slab by escalator normal faulting beneath the North Island of New Zealand. Geology **34**: 777.

Hensen, C., K. Wallmann, M. Schmidt, C. R. Ranero, and E. Suess. 2004. Fluid expulsion related to mud extrusion off Costa Rica—A window to the subducting slab. Geology **32**: 201.

Knittel, K., T. Lo, A. Boetius, R. Kort, and R. Amann. 2005. Diversity and Distribution of Methanotrophic Archaea at Cold Seeps †. **71**: 467–479.

Krause, S., P. Steeb, C. Hensen, V. Liebetrau, A. W. Dale, M. Nuzzo, and T. Treude. 2014. Microbial activity and carbonate isotope signatures as a tool for identification of spatial differences in methane advection: a case study at the Pacific Costa Rican margin. Biogeosciences **11**: 507–523.

Krüger, M., T. Treude, H. Wolters, K. Nauhaus, and A. Boetius. 2005. Microbial methane turnover in different marine habitats. Palaeogeogr. Palaeoclimatol. Palaeoecol. **227**: 6–17.

Kutterolf, S., V. Liebetrau, T. Mörz, A. Freundt, T. Hammerich, and D. Garbe-Schönberg. 2008. Lifetime and cyclicity of fluid venting at forearc mound structures determined by tephrostratigraphy and radiometric dating of authigenic carbonates. Geology **36**: 707.

Kvenvolden, K. A. 1993. Gas Hydrates - Geological Perspective and Global Change. Rev. Geophys. **31**: 173–187.

LaBonte, A. L., K. K. M. Brown, and M. M. D. Tryon. 2007. Monitoring periodic and episodic flow events at Monterey Bay seeps using a new optical flow meter. J. Geophys. Res. **112**: 1–14.

Linke, P., K. Wallmann, E. Suess, C. Hensen, and G. Rehder. 2005. In situ benthic fluxes from an intermittently active mud volcano at the Costa Rica convergent margin. Earth Planet. Sci. Lett. **235**: 79–95.

Luff, R., and K. Wallmann. 2003. Fluid flow, methane fluxes, carbonate precipitation and biogeochemical turnover in gas hydrate-bearing sediments at Hydrate Ridge, Cascadia Margin: numerical modeling and mass balances. Geochim. Cosmochim. Acta **67**: 3403–3421.

Manga, M., M. Brumm, and M. L. Rudolph. 2009. Earthquake triggering of mud volcanoes. Mar. Pet. Geol. **26**: 1785–1798.

Meister, P., M. Gutjahr, M. Frank, S. M. Bernasconi, C. Vasconcelos, and J. A. McKenzie. 2011. Dolomite formation within the methanogenic zone induced by tectonically driven fluids in the Peru accretionary prism. Geology **39**: 563–566.

Meulepas, R. J. W., C. G. Jagersma, J. Gieteling, C. J. N. Buisman, A. J. M. Stams, and P. N. L. Lens. 2009. Enrichment of anaerobic methanotrophs in sulfate-reducing membrane bioreactors. Biotechnol. Bioeng. **104**: 458–70.

Nauhaus, K., M. Albrecht, M. Elvert, A. Boetius, and F. Widdel. 2007. In vitro cell growth of marine archaeal-bacterial consortia during anaerobic oxidation of methane with sulfate. Environ. Microbiol. **9**: 187–96.

Nauhaus, K., A. Boetius, M. Krüger, and F. Widdel. 2002. In vitro demonstration of anaerobic oxidation of methane coupled to sulphate reduction in sediment from a marine gas hydrate area. Environ. Microbiol. **4**: 296–305.

Omoregie, E. O., H. Niemann, V. Mastalerz, G. J. de Lange, A. Stadnitskaia, J. Mascle, J.-P. Foucher, and A. Boetius. 2009. Microbial methane oxidation and sulfate reduction at cold seeps of the deep Eastern Mediterranean Sea. Mar. Geol. **261**: 114–127.

Praeg, D., S. Ceramicola, R. Barbieri, V. Unnithan, and N. Wardell. 2009. Tectonically-driven mud volcanism since the late Pliocene on the Calabrian accretionary prism, central Mediterranean Sea. Mar. Pet. Geol. **26**: 1849–1865.

Ranero, C. R., I. Grevemeyer, H. Sahling, U. Barckhausen, C. Hensen, K. Wallmann, W. Weinrebe, P. Vannucchi, R. von Huene, and K. McIntosh. 2008. Hydrogeological system of erosional convergent margins and its influence on tectonics and interplate seismogenesis. Geochemistry Geophys. Geosystems **9**, doi:10.1029/2007GC001679

Suess, E. 2010. Marine Cold Seeps, p. 188–198. *In* K.N. Timmis [ed.], Handbook of Hydrocarbon and Lipid Microbiology. Springer Berlin Heidelberg.

Tishchenko, P., C. Hensen, K. Wallmann, and C. S. Wong. 2005. Calculation of the stability and solubility of methane hydrate in seawater. Chem. Geol. **219**: 37–52.

Torres, M., J. McManus, D. Hammond, M. A. de Anglis, K. Hesschen, S. Colbert, M. D. Tryon, K. Brown, and E. Suess. 2002. Fluid and chemical fluxes in and out of sediments hosting methane hydrate deposits on Hydrate Ridge, OR, I: Hydrological provinces. Earth Planet. Sci. Lett. **201**: 525–540.

Treude, T., A. Boetius, K. Knittel, K. Wallmann, and B. Barker Jørgensen. 2003. Anaerobic oxidation of methane above gas hydrates at Hydrate Ridge, NE Pacific Ocean. Mar. Ecol. Prog. Ser. **264**: 1–14.

Treude, T., M. Krüger, A. Boetius, and B. Jørgensen. 2005. Environmental control on anaerobic oxidation of methane in the gassy sediments of Eckernfoerde Bay(German Baltic). Limnol. Oceanogr. **50**: 1771–1786.

Tryon, M., K. Brown, and M. Torres. 2002. Fluid and chemical flux in and out of sediments hosting methane hydrate deposits on Hydrate Ridge, OR, II: Hydrological processes. Earth Planet. Sci. Lett. **201**: 541–557.

Wankel, S. D., M. M. Adams, D. T. Johnston, C. M. Hansel, S. B. Joye, and P. R. Girguis. 2012. Anaerobic methane oxidation in metalliferous hydrothermal sediments: influence on carbon flux and decoupling from sulfate reduction. Environ. Microbiol. **14**: 2726–40.

Wegener, G., and A. Boetius. 2009. An experimental study on short-term changes in the anaerobic oxidation of methane in response to varying methane and sulfate fluxes. Biogeosciences **6**: 867–876.

Yamamoto, S. 1976. Solubility of methane in distilled water and seawater. J. Chem. … **2**: 3–5.

Zhang, Y., J.-P. Henriet, J. Bursens, and N. Boon. 2010. Stimulation of in vitro anaerobic oxidation of methane rate in a continuous high-pressure bioreactor. Bioresour. Technol. **101**: 3132–8.

Danksagung

Zunächst möchte ich mich bei meiner Betreuerin Tina Treude bedanken. Sie hatte die Idee zu der Arbeit, zu dieser Art von Sedimentdurchflusssystem, zur Entwicklung der Anlage und von ihr stammt auch der Name der Anlage (SLOT). Tina hat es mir ermöglicht mich mit diesem spannenden Ökosystem zu befassen und mir sowohl die Grundlagen mariner Biogeochemie als auch praktische und methodische Arbeiten an Bord und im Labor nahegebracht. Auch in andere Aspekte der Wissenschaft wie beispielsweise Review, Anträge schreiben und administrative Aufgaben ermöglichte sie mir einen Einblick.

Peter Linke möchte ich für seinen Rat und seine Hilfe danken. Er wies mich immer wieder auf Publikationen hin und konnte mir oft weiterhelfen, wenn ich benötigte Informationen nicht gefunden habe. Insgesamt habe ich viel von seiner Erfahrung profitieren können.

Ruth Schmitz-Streit danke ich für Tipps und Lösungen für praktische Probleme und ihren Rat in molekularbiologischen Fragen.

Besonderer Dank gilt Bettina Domeyer, die die vielen Proben mit Ionen Chromatographie gemessen hat. Auf Bettina, ebenso wie auf Anke Bleyer, war auch Verlaß, wenn es um andre Analysen ging oder wenn wieder mal etwas fehlte und ich kurzfristig Verbrauchsmaterial brauchte.

Herzlich möchte ich Kerstin Kretschmer danken, die mir bei vielen Kleinigkeiten geholfen hat und vor allem dafür, dass sie immer wieder als „Babysitter“ für meine Anlage eingesprungen ist.

Meinem „Schreibtischnachbarn“ Stefan Krause möchte ich für die vielen Diskussionen, Rat und Hilfe im Labor, beim Formulieren oder Präsentationen danken. Danken möchte ich ihm außerdem für Unterhaltungen, Witze und eine tolle Zeit. Für all dies möchte ich auch Vicky Bertrics danken, die das Ende meiner Arbeit leider nicht mehr erleben konnte.

Volker Liebetrau danke ich für die vielen Diskussionen, welche sich von kleinen Details bei der Probenaufbereitung bis hin zum großen wissenschaftlichen Kontext erstreckten.

Auch danken möchte ich den vielen Technikern, insbesondere unserer Laborleiterin Gabi Schüssler, für die viele Hilfe und guten Rat. Auch Peggy Wefers hat mir viel bei Fragen geholfen und konnte mir einiges am Gaschromatographen erklären. Im gleiche Maße möchte ich Julia Hommer danken, die mir besonders am Anfang der Arbeit geholfen hat. Julia Farkas danke ich für die Hilfe im Labor.

Marion Liebetrau danke für die viele Hilfe bei organisatorischen und administrativen Fragen.

Sonakshi, Johanna, Jessi und Skadi sei gedankt für Hilfe bei vielen kleinen Fragen oder für Diskussionen, die immer wieder auftraten.

Einen Großteil meiner Versuche habe ich im Gebäude 15A durchgeführt. Allen „Insassen“ danke ich für Hilfe, Werkzeug, Kaffee und Ablenkung, besonders erwähnt sei an dieser Stelle Jürgen Schauer, der etwas Abwechslung in lange Mikrosensor-Abende gebracht hat. Auch dem restlichen Team vom Technik- und Logistik-Zentrum möchte ich für die viele Hilfe danken, insbesondere Asmus Petersen, Dirk Wehrend, Mike Lange, Wolfgang Queisser und Klaus Steffen.

Dank gilt ebenfalls den vielen Technikern, Wissenschaftlern, Crew-Mitgliedern und anderen, die mir am GEOMAR oder auf den Ausfahrten SO206 und SO210 geholfen haben.

Gedankt sei auch meiner Vorgängerin Stefanie Reischke, für ihre Vorarbeit, Probennahme und natürlich dafür, dass sie mir die Arbeit überlassen hat.

Zum Schluß, aber keinesfalls minder, möchte ich meiner Freundin Claudia Volosciuk für ihre Hilfe, Anteilnahme, Aufmunterungen und vieles mehr danken.

Supplementary

Supplementary to Chapter 3: Differences in microbial methane turnover and carbonate isotopy between two neighboring mounds along the Pacific Costa Rican continental margin.

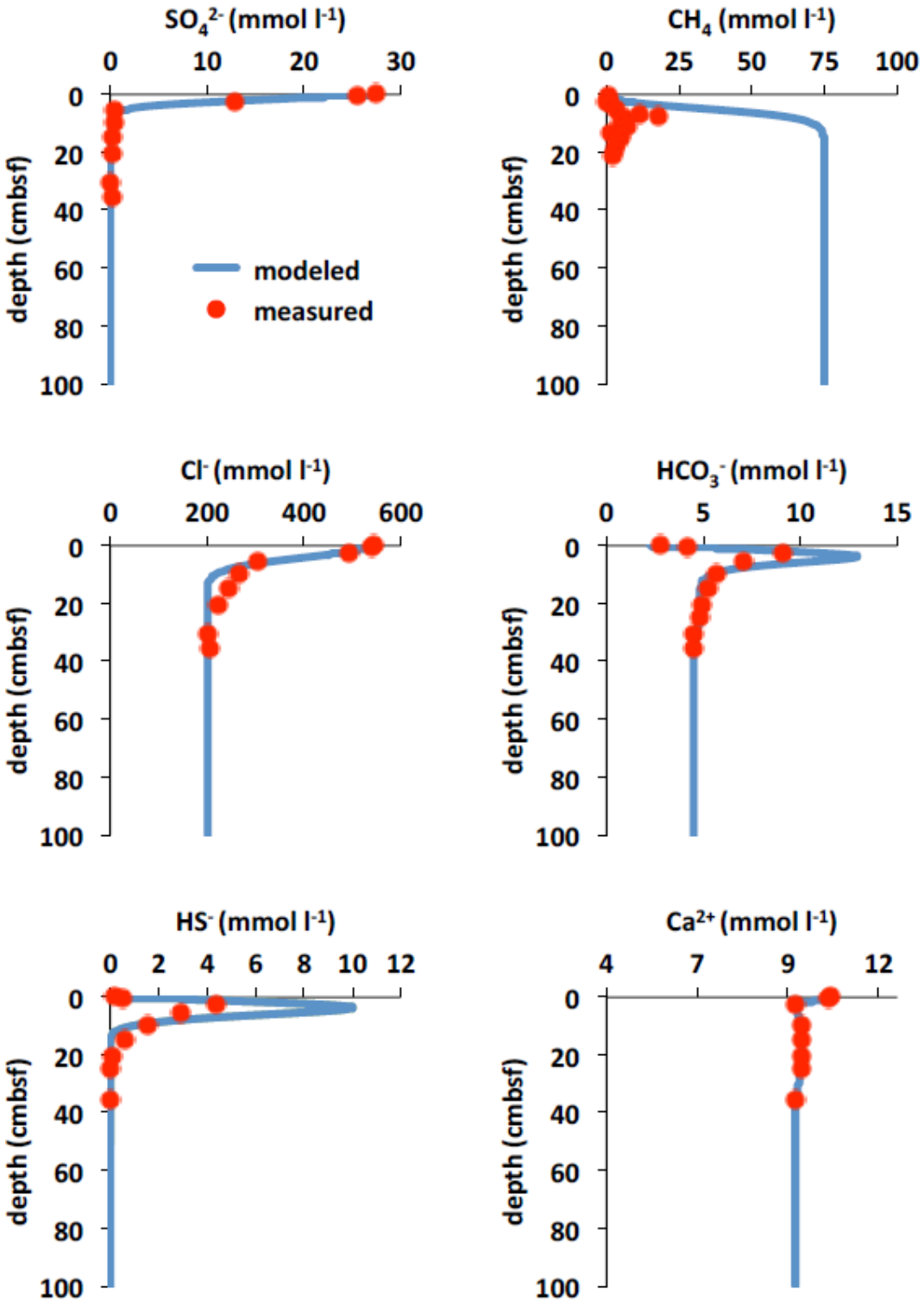

Figure 1S: Measured porewater data obtained from SO206-39 (Multi Corer) at Mound 11 during cruise SO206 and modeled vertical profile. Top left - sulfate (SO_4^{2-}), top right - methane (CH_4), middle left – chloride (Cl^-), middle right – bicarbonate (HCO_3^-), bottom left – sulfide (HS^-), bottom right – calcium (Ca^{2+}).

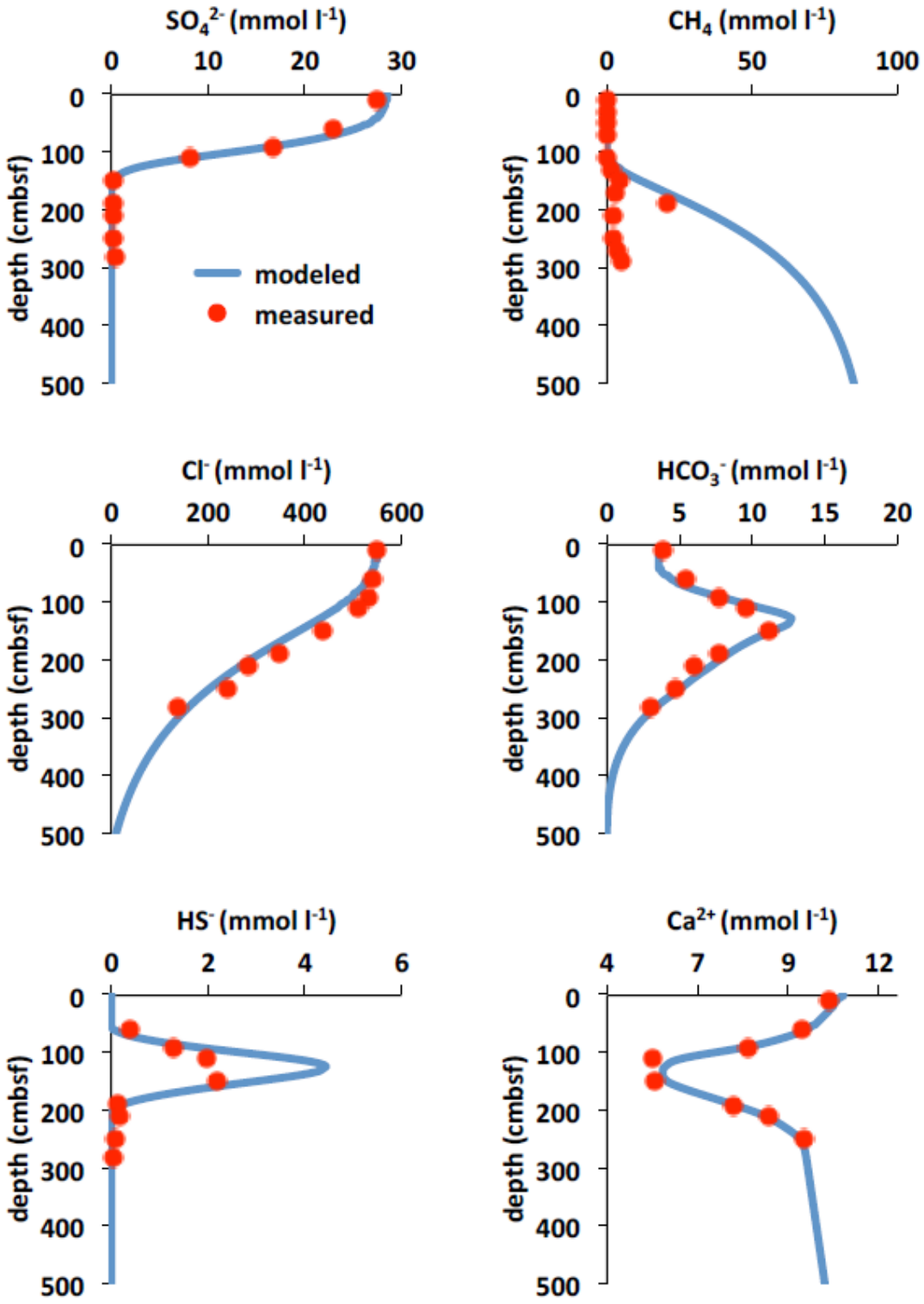

Figure 2S. Measured porewater data obtained from SO206-50 (Gravity corer) at Mound 11 during cruise SO206 and modeled vertical profile. Top left - sulfate (SO_4^{2-}), top right - methane (CH_4), middle left – chloride (Cl^-), middle right – bicarbonate (HCO_3^-), bottom left – sulfide (HS^-), bottom right – calcium (Ca^{2+}).

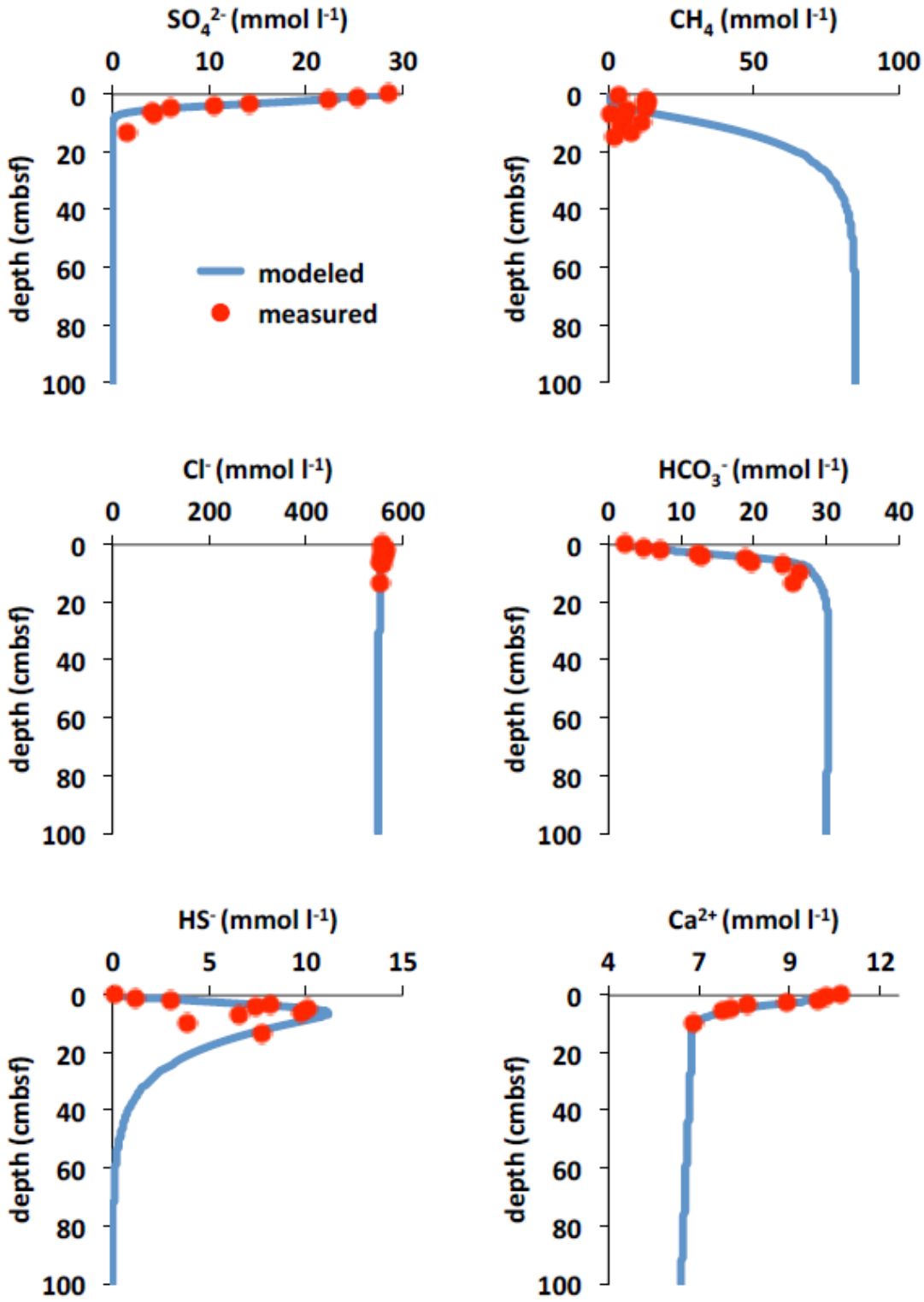

Figure 3S: Measured porewater data obtained from SO206-44 (Multi Corer) at Mound 12 during cruise SO206 and modeled vertical profile Top left - sulfate (SO_4^{2-}), top right methane (CH_4), middle left – chloride (Cl^-), middle right – bicarbonate (HCO_3^-), bottom left – sulfide (HS^-), bottom right – calcium (Ca^{2+}).

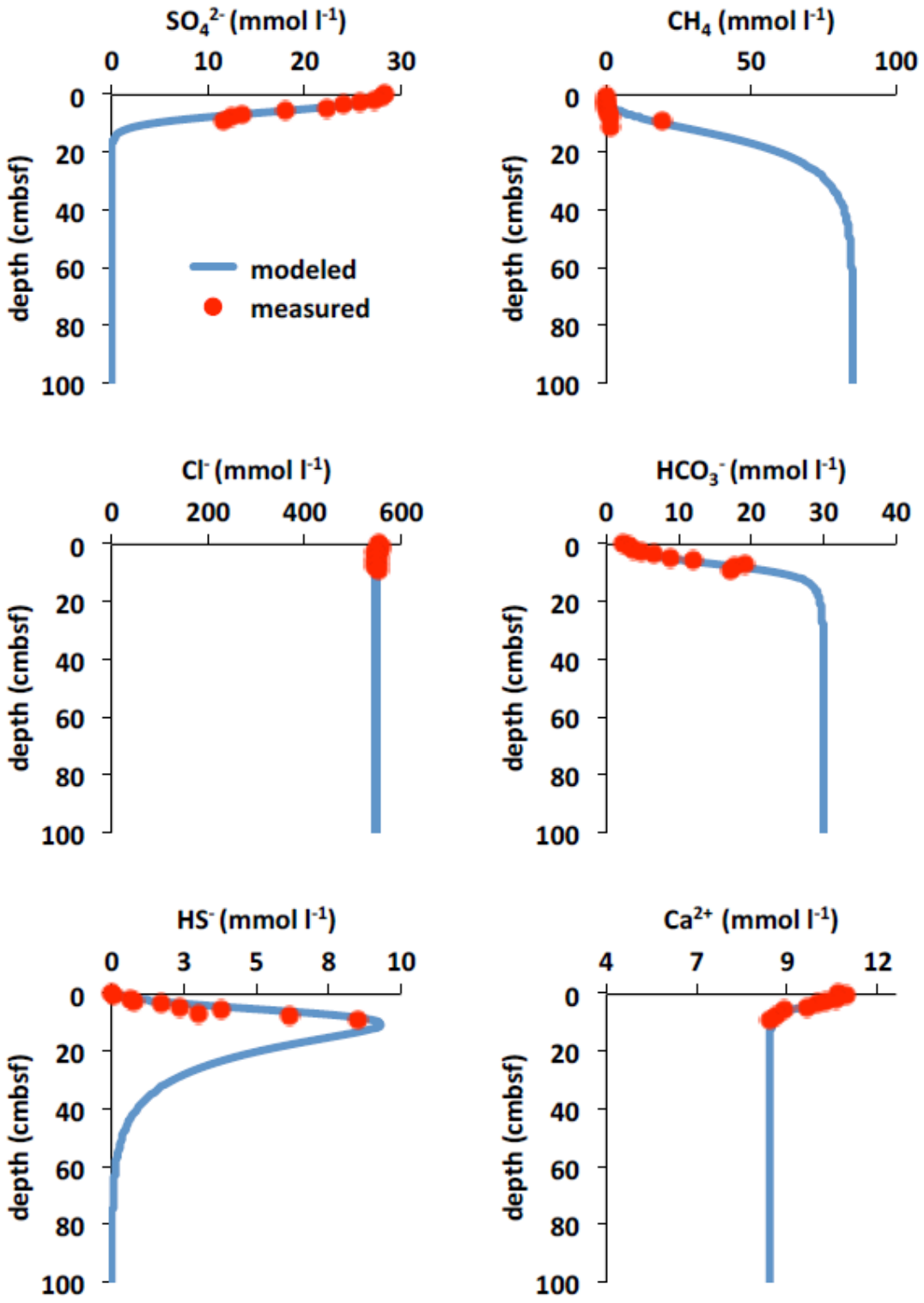

Figure 4S: Measured porewater data obtained from SO206-46 (Multi Corer) at Mound 12 during cruise SO206 and modeled vertical profile. Top left - sulfate (SO_4^{2-}), top right - methane (CH_4), middle left – chloride (Cl^-), middle right – bicarbonate (HCO_3^-), bottom left – sulfide (HS^-), bottom right – calcium (Ca^{2+}).

Supplementary to Chapter 6: Summary and conclusion

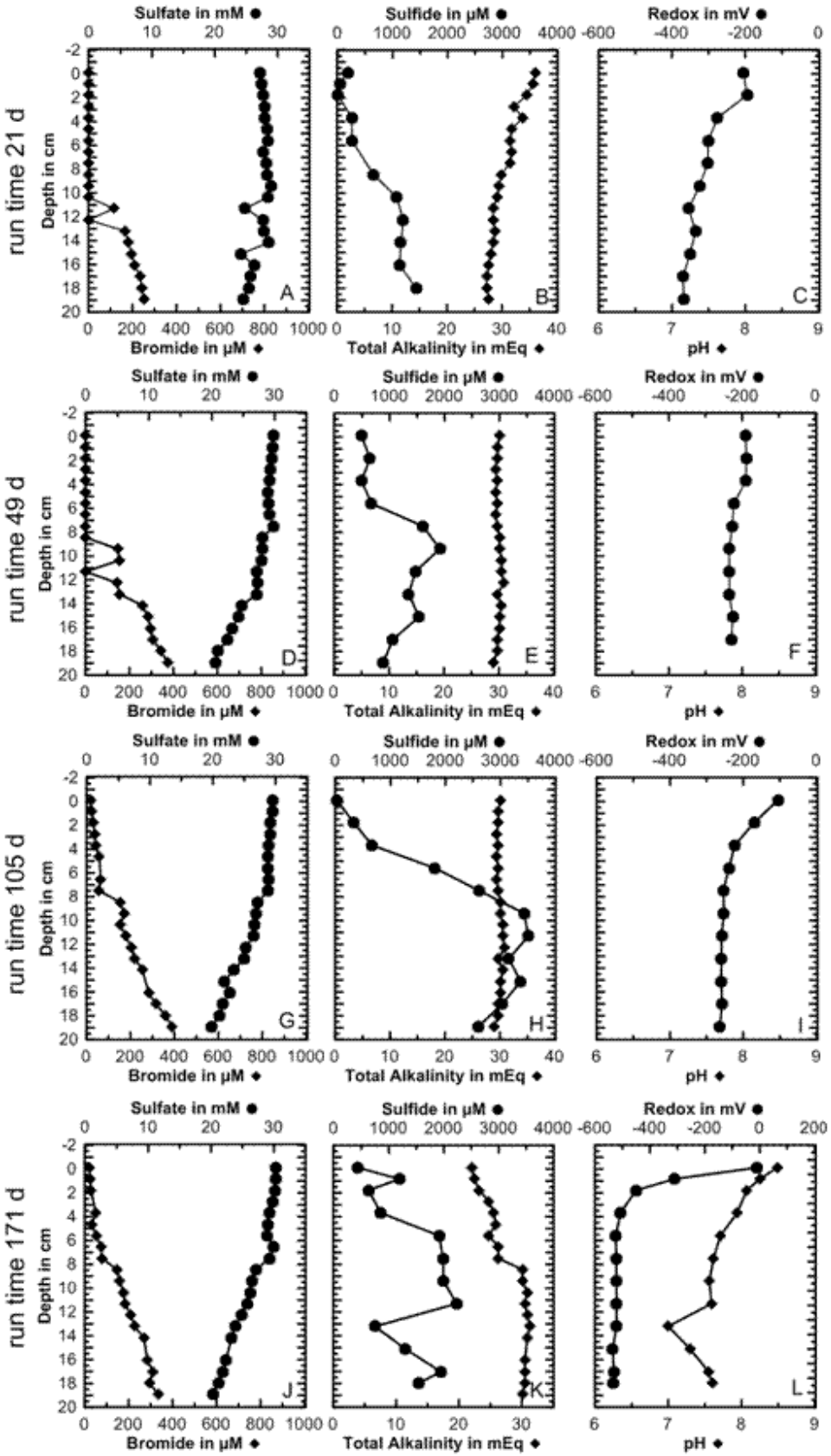
run time 21 d
run time 49 d
run time 105 d
run time 171 d
Depth in cm
Sulfate in mM
Sulfide in µM
Redox in mV
Bromide in µM
Total Alkalinity in mEq
pH
A
B
C
D
E
F
G
H
I
J
K
L

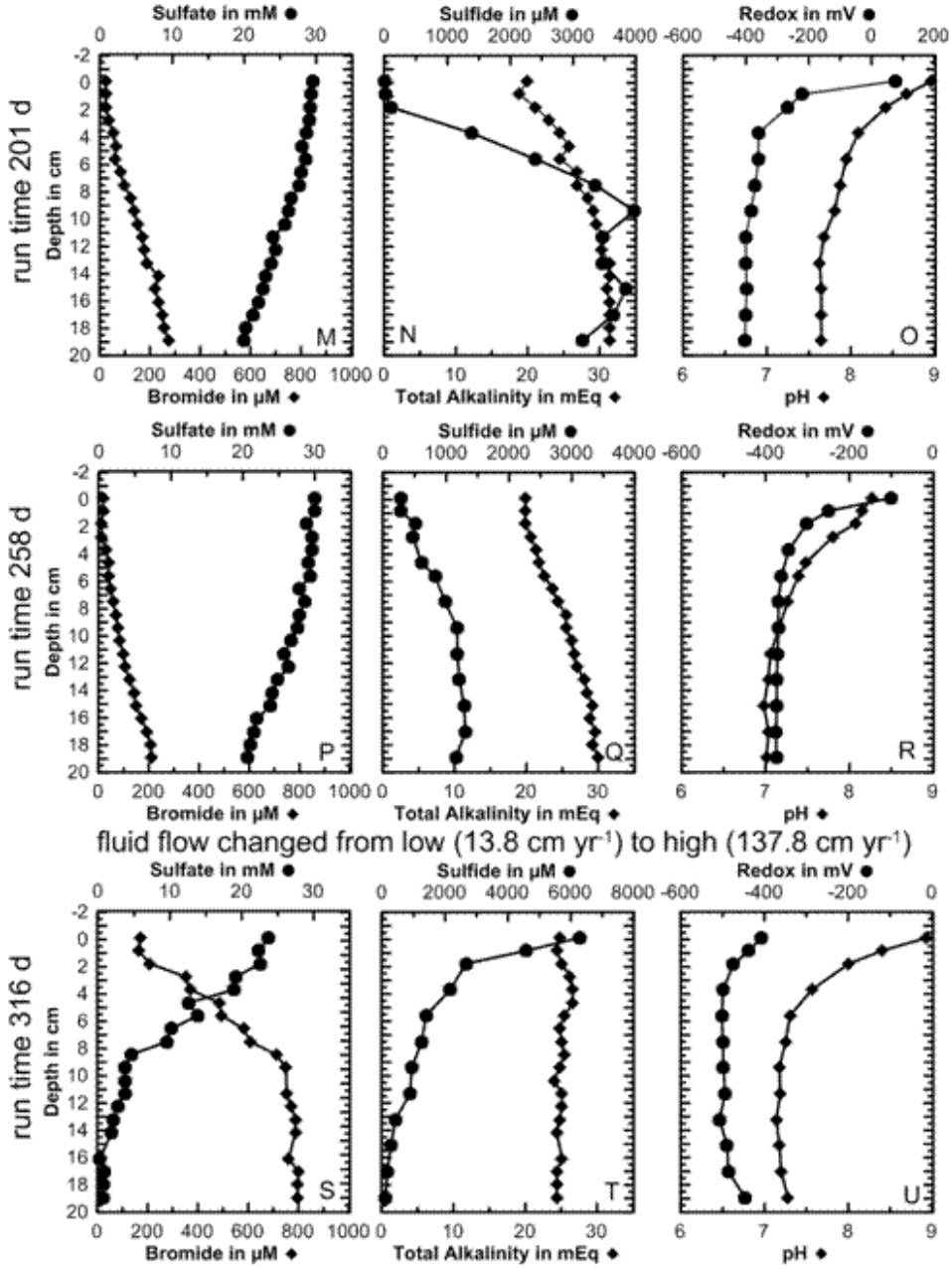

Figure 5S: Gradients of sulfate, the tracer bromide; sulfide, total alkalinity (TA; B, E, H, L, O, S), and redox (C, F, I, L, O, R, U), and pH profiles (L, O, R, U), to onward runtime of the experiment of the Low Flow Core (LFC) from the center of the North Alex Mud Volcano (PE298-Muc 10).

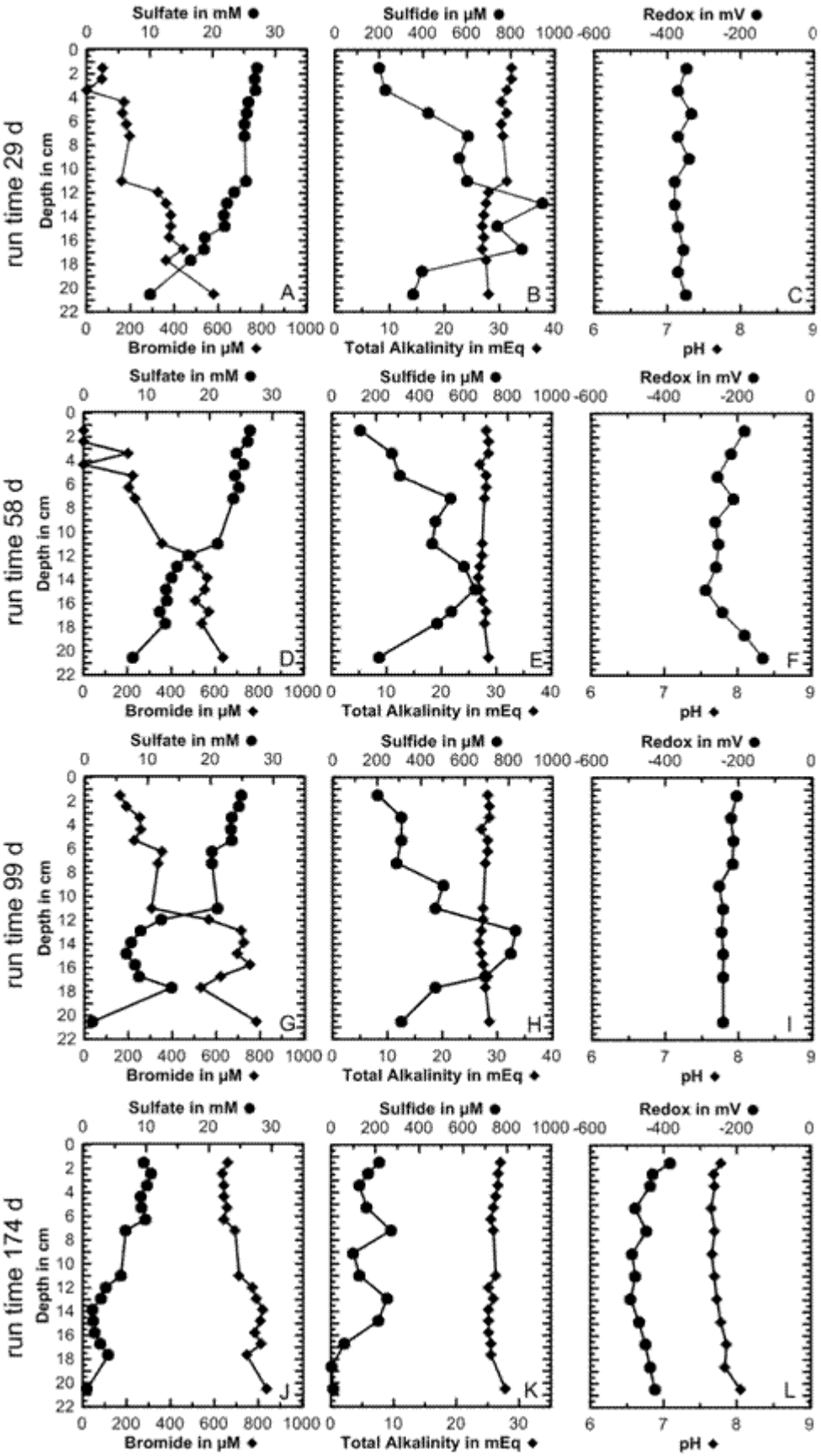
run time 29 d
run time 58 d
run time 99 d
run time 174 d
Depth in cm
Sulfate in mM ●
Sulfide in µM ●
Redox in mV ●
Bromide in µM ◆
Total Alkalinity in mEq ◆
pH ◆
A
B
C
D
E
F
G
H
I
J
K
L

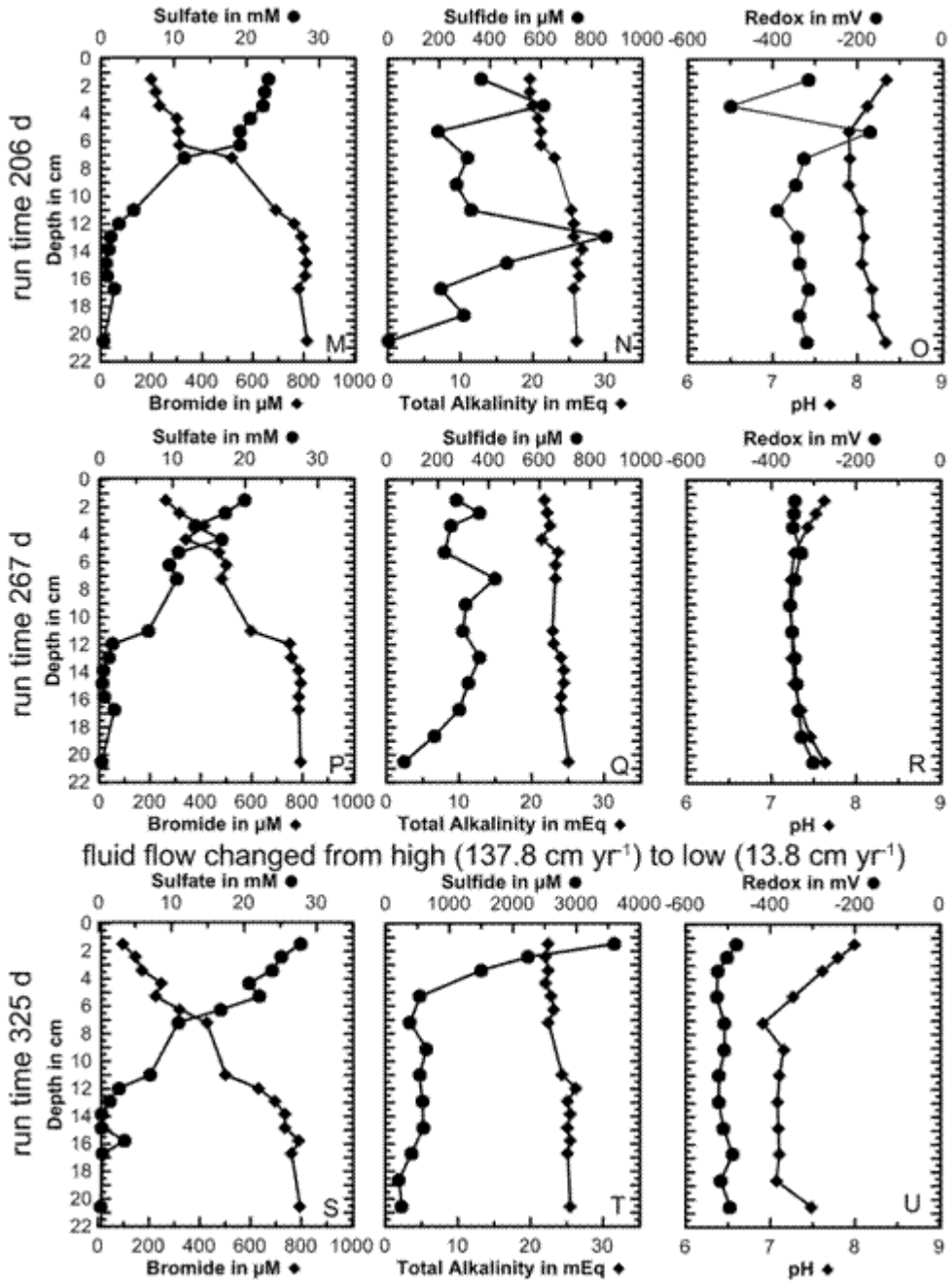

Figure 6S: Gradients of sulfate, the tracer bromide; sulfide, total alkalinity (TA; B, E, H, L, O, S), and redox (C, F, I, L, O, R, U), and pH profiles (L, O, R, U), to onward runtime of the experiment of the High Flow Core (HFC) from the center of the North Alex Mud Volcano (PE298-Muc 4).

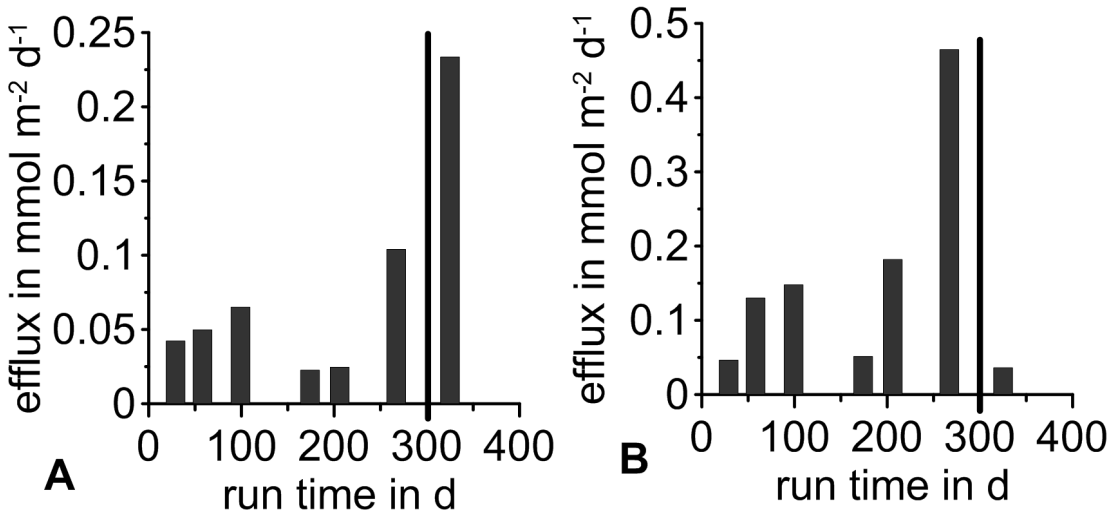

Figure 7S: Methane efflux of the LFC (A) and HFC (B) from the center of North Alex Mud Volcano. Vertical line show the swapping time.